

ANALYSIS OF ELECTRON
CORRELATION EFFECTS IN STRONGLY
CORRELATED SYSTEMS

INAUGURAL-DISSERTATION
TO OBTAIN THE ACADEMIC DEGREE
DOCTOR RERUM NATURALIUM (DR. RER. NAT.)

SUBMITTED TO
THE DEPARTMENT OF BIOLOGY, CHEMISTRY AND PHARMACY
OF FREIE UNIVERSITÄT BERLIN

BY
CHRISTIAN STEMMLE
FROM LAUCHHAMMER

2019

This work was prepared under supervision of
Prof. Dr. Beate Paulus

from
NOVEMBER 2014
until
JULY 2019

1. Gutachter: Prof. Dr. Beate Paulus
 2. Gutachter: PD Dr. Denis Usvyat
- Disputation am: 25. Oktober 2019

Abstract

To explore new approaches for wave function based correlation methods in chemistry, the electron correlation effects of different model systems are analyzed by means of Quantum Information Theory (QIT) and the Method of Increments (MoI). Data for the QIT is obtained based on calculations employing the Density Matrix Renormalization Group (DMRG) and Full Configuration Interaction Quantum Monte Carlo (FCIQMC) methods. The investigation covers standard model systems for strong correlation, such as the dissociation of N_2 and N_2^+ , as well as polyacetylene, Be_6 rings and the cobalt fluorides CoF_2 , CoF_3 and CoF_4 . The latter represent challenging open-shell, transition metal containing compounds that may be systematically extended to linear chains. The observations stimulate a novel approach to select the configuration space in multi-reference calculations, promising reduced computational scaling for strongly correlated systems with large active spaces. Furthermore, a correspondence between entropies (QIT) and increments (MoI) is demonstrated, which suggests the related methods may be combined to exploit their different advantages. Finally, the correlation analysis of the cobalt fluorides yields valuable insights to extent the study to longer, linear chains.

Zusammenfassung

Auf der Suche nach neuen Ansätzen für Elektronen-Korrelationsmethoden in der Chemie werden die Korrelationseffekte verschiedener Modelle mit Hilfe von Quanteninformationstheorie (QIT) und der Inkrementenmethode (MoI) untersucht. Die QIT Daten basieren dabei auf Ergebnissen der Dichtematrix Renormierungsgruppe (DMRG) und der Full Configuration Interaction Quanten Monte Carlo (FCIQMC) Methoden. Die untersuchten Systeme umfassen ein Standardmodell für starke Korrelation, die Dissoziation von N_2 und N_2^+ , sowie Polyacetylen, Be_6 Ringe und die Cobaltfluoride CoF_2 , CoF_3 und CoF_4 . Letztere stellen herausfordernde, offen-schalige Übergangsmetallverbindungen dar, welche sich systematisch zu linearen Ketten erweitern lassen. Die Beobachtungen regen einen neuen Ansatz zur Auswahl von Elektronen Konfigurationen in Multireferenz-Methoden an, und versprechen besonders für stark korrelierte Systeme eine Reduzierung des Rechenaufwandes. Darüber hinaus wird die Vergleichbarkeit von Entropien (QIT) mit den Inkrementen (MoI) demonstriert. Dies ermöglicht eine Übertragbarkeit der Ergebnisse und erlaubt dadurch die Stärken beider Ansätze auszunutzen. Die Analyse der Korrelationseffekte in den Cobaltfluoriden liefert außerdem wertvolle Informationen um die Untersuchungen auf längere, lineare Ketten auszuweiten.

Acknowledgments

A long term scientific project like this thesis is always accompanied by many people. Although I cannot name all of them here, I would like to thank everyone who have helped me during this time.

Foremost I would like to thank Prof. Dr. Beate Paulus for supervision of this work as well as support during my master studies before. She always granted me the freedom and support to follow my own scientific interests. I would also like to express my gratitude to PD Dr. Denis Usvyat for being to the second referee of this thesis. I am furthermore very grateful to Örs Legeza, Ph.D, from the Wigner Research Centre for Physics in Budapest for the collaboration and invitation of a short research stay to learn about his DMRG code. Likewise, I want to thank Prof. Ali Alavi, Ph.D, from the Max Planck Institute for Solid State Research in Stuttgart, who invited me to learn about the FCIQMC method. Both methods are a vital part of this thesis.

Special thanks is also due to the many people of the theory group I met over the years. They always provided a nice and helpful working environment. I would like to name in particular Dr. Matthias Berg and Dr. Edoardo Fertitta who helped me a lot getting started, as well as my long time office colleagues Kai Töpfer and Davood Alizadeh Sanati for many interesting discussions and helpful advice.

Furthermore I am grateful to the International Max Planck Research School (IMPRS) of the Fritz Haber Institute of the Max Planck Society their for financial support as well as the organization of regular block courses, discussion meetings and workshops broadening my scientific knowledge. Computing time and technical support provided by the high performance computing facilities of the Zentraleinrichtung für Datenverarbeitung (ZEDAT) at Freie Universität Berlin is gratefully acknowledged as well.

Contents

1	Introduction	1
2	Theoretical Background	7
2.1	The Schrödinger Equation	7
2.1.1	The Molecular Hamiltonian	10
2.1.2	The Born-Oppenheimer Approximation	11
2.1.3	Electronic Structure Theory	12
2.2	The Orbital Picture	12
2.2.1	Spin of Electrons	13
2.2.2	The Hartree-Fock Method	15
2.2.3	Atomic Orbital Basis Sets	19
2.2.4	Electron Correlation	20
2.2.5	Second Quantization	21
2.2.6	The Configuration Interaction Method	22
2.2.7	Weak and Strong Correlation	27
2.2.8	Multi-Configurational Self-Consistent Field	29
2.2.9	Unitary Transformation of Orbitals	30
2.3	Density Matrices	31
2.3.1	Pure and Mixed States	33
2.3.2	Reduced Density Matrices	33
2.4	Beyond Standard Quantum Chemistry	37
2.4.1	Density Matrix Renormalization Group	37
2.4.2	The Method of Increments	44
2.4.3	Quantum Monte Carlo	45
2.5	Quantifying Electron Correlation	49
2.5.1	Quantum Entanglement	50
2.5.2	Quantum Information Theory	51

2.5.3	Increments vs. Entropies	55
3	Molecular Model Systems	57
3.1	Dissociation of N_2/N_2^+	57
3.2	Polyacetylene	61
3.3	Be_6 Rings	61
3.4	Cobalt Fluorides	63
4	Results	69
4.1	QIT Analysis exemplified on the Dissociation of N_2/N_2^+	69
4.2	Entropy Based Configuration Selection in MCSCF and MRCI	77
4.2.1	Construction of Configurations based on 2-RDMs	79
4.2.2	Used Models and Computational Details	83
4.2.3	Reference Calculations	85
4.2.4	Results for ρ_{ij} based selection	89
4.2.5	Results for ϕ_{ij} based selection	93
4.2.6	Summary	102
4.3	Combining DMRG with the Incremental Approach	104
4.3.1	Polyacetylene	104
4.3.2	Be_6 Rings	110
4.3.3	Open Shell CoF_2	114
4.3.4	Summary	118
4.4	Analysis of Cobalt Fluorides	121
4.4.1	Basis Set Dependence and Orbital Entropies	121
4.4.2	Diagonalized 2-Orbital Reduced Density Matrices ϕ_{ij}	133
4.4.3	Summary	134
5	Conclusion and Outlook	139
	Bibliography	141
	Appendix	151

List of Figures

2.1	Weak and Strong Correlation	29
2.2	Matrix Product State	41
2.3	Effective Hamiltonian (DMRG)	42
2.4	MoI Expansion	45
2.5	Shannon Entropy	52
3.1	N ₂ : MO diagram	59
3.2	N ₂ /N ₂ ⁺ : CI vector	60
3.3	N ₂ /N ₂ ⁺ : Potential Energy Surfaces	60
3.4	Leading configurations in Be ₆ rings	62
3.5	Co chains	64
3.6	Co 3d orbitals in CoF ₂	65
4.1	N ₂ : Orbital Occupations	70
4.2	N ₂ : Entropy and Mutual Information	71
4.3	N ₂ : Diagonalized 2-RDMs	74
4.4	N ₂ /N ₂ ⁺ : 1π and 3σ orbitals	75
4.5	Construction of Configurations	80
4.6	CoF ₂ : FCIQMC 1-Orbital Entropies	84
4.7	Polyacetylene: Orbital Isosurfaces	106
4.8	Polyacetylene: 1- and 2-Orbital Correlation Measures	107
4.9	Polyacetylene: CCSD-MoI Increments	109
4.10	Be ₆ : 1-Orbital Increments	111
4.11	Be ₆ (<i>R</i> = 2.2 Å): 1- and 2-Orbital Correlation Measures	112
4.12	Be ₆ (<i>R</i> = 3.5 Å): 1- and 2-Orbital Correlation Measures	113
4.13	CoF ₂ (PM): 1-Orbital Increments and Entropies	118
4.14	CoF ₂ (PM): Mutual Information	119
4.15	CoF ₂ canonical vs. local	127

A.1	CoF ₂ local orbitals #1 to #8	152
A.2	CoF ₂ local orbitals #9 to #16	153
A.3	CoF ₂ local orbitals #17 to #24	154
A.4	CoF ₂ local orbitals #25 to #32	155
A.5	CoF ₂ local orbitals #33 to #40	156
A.6	CoF ₂ local orbitals #41 to #48	157
A.7	CoF ₂ local orbitals #49 to #56	158
A.8	CoF ₂ local orbitals #57 to #60	159
A.9	CoF ₂ orbitals #1 to #8	160
A.10	CoF ₂ orbitals #9 to #16	161
A.11	CoF ₂ orbitals #17 to #24	162
A.12	CoF ₂ orbitals #25 to #32	163
A.13	CoF ₂ orbitals #33 to #40	164
A.14	CoF ₂ orbitals #41 to #48	165
A.15	CoF ₂ orbitals #49 to #56	166
A.16	CoF ₂ orbitals #57 to #60	167
A.17	CoF ₂ (min. basis at F) orbitals #1 to #8	168
A.18	CoF ₂ (min. basis at F) orbitals #9 to #16	169
A.19	CoF ₂ (min. basis at F) orbitals #17 to #24	170
A.20	CoF ₂ (min. basis at F) orbitals #25 to #32	171
A.21	CoF ₂ (min. basis at F) orbitals #33 to #40	172
A.22	CoF ₂ (min. basis at F) orbitals #41 to #42	173
A.23	CoF ₃ orbitals #1 to #8	174
A.24	CoF ₃ orbitals #9 to #16	175
A.25	CoF ₃ orbitals #17 to #24	176
A.26	CoF ₃ orbitals #25 to #32	177
A.27	CoF ₃ orbitals #33 to #40	178
A.28	CoF ₃ orbitals #41 to #48	179
A.29	CoF ₃ orbitals #49 to #56	180
A.30	CoF ₃ orbitals #57 to #64	181
A.31	CoF ₃ orbitals #65 to #72	182
A.32	CoF ₃ orbitals #73 to #73	183
A.33	CoF ₄ <i>D</i> _{4h} orbitals #1 to #8	184
A.34	CoF ₄ <i>D</i> _{4h} orbitals #9 to #16	185
A.35	CoF ₄ <i>D</i> _{4h} orbitals #17 to #24	186

A.36 CoF ₄ D _{4h} orbitals #25 to #32	187
A.37 CoF ₄ D _{4h} orbitals #33 to #40	188
A.38 CoF ₄ D _{4h} orbitals #41 to #48	189
A.39 CoF ₄ D _{4h} orbitals #49 to #56	190
A.40 CoF ₄ D _{4h} orbitals #57 to #64	191
A.41 CoF ₄ D _{4h} orbitals #65 to #72	192
A.42 CoF ₄ D _{4h} orbitals #73 to #80	193
A.43 CoF ₄ T _d orbitals #1 to #8	194
A.44 CoF ₄ T _d orbitals #9 to #16	195
A.45 CoF ₄ T _d orbitals #17 to #24	196
A.46 CoF ₄ T _d orbitals #25 to #32	197
A.47 CoF ₄ T _d orbitals #33 to #40	198
A.48 CoF ₄ T _d orbitals #41 to #48	199
A.49 CoF ₄ T _d orbitals #49 to #56	200
A.50 CoF ₄ T _d orbitals #57 to #64	201
A.51 CoF ₄ T _d orbitals #65 to #72	202
A.52 CoF ₄ T _d orbitals #73 to #80	203
A.53 CoF ₄ T _d orbitals #81 to #86	204
A.54 CoF _n QIT data	205

List of Tables

3.1	Thermochemistry of Cobalt Fluorides	63
3.2	CoF _n : T_1 and D_1 diagnostics	64
4.1	Characteristic Eigenvectors of ρ_{ij}	73
4.2	Combination of Occupation Patterns	81
4.3	CoF ₂ : Reference Energies	85
4.4	CoF ₄ : Reference Energies	86
4.5	CoF ₂ : Energies of S_i -based Selection	87
4.6	CoF ₄ : Energies of S_i -based Selection	87
4.7	CoF ₂ : ρ_{ij} Threshold Parameters	92
4.8	CoF ₂ : ρ_{ij} MCSCF Results	93
4.9	CoF ₂ : ρ_{ij} MRCI Results	94
4.10	CoF ₄ : ρ_{ij} Threshold Parameters	94
4.11	CoF ₄ : ρ_{ij} MCSCF Results	95
4.12	CoF ₄ : ρ_{ij} MRCI Results	95
4.13	CoF ₂ : ϕ_{ij} Threshold Parameters	97
4.14	CoF ₂ : ϕ_{ij} MCSCF Results	98
4.15	CoF ₂ : ϕ_{ij} MRCI Results	98
4.16	CoF ₄ : ϕ_{ij} Threshold Parameters	99
4.17	CoF ₄ : ϕ_{ij} MCSCF Results	100
4.18	CoF ₄ : ϕ_{ij} MRCI Results	101
4.19	Polyacetylene: Reference Energies	105
4.20	Polyacetylene: MoI Energies	105
4.21	Be ₆ : Correlation Energies	111
4.22	Correlation Energies of the isolated Ions	122
4.23	Correlation Energies of CoF _n at different basis sets	123
4.24	CoF _n : Assignment of 3d Orbitals	125

4.25	CoF _n : DMRG results	127
4.26	CoF ₂ (cc-pVDZ): QIT data	128
4.27	CoF ₂ (Co cc-pVDZ; F minimal): QIT data	129
4.28	CoF ₃ : QIT data	130
4.29	CoF ₄ D_{4h} : QIT data	131
4.30	CoF ₄ T_d : QIT data	132
4.31	CoF ₂ : $\phi_{ij,\alpha}$	135
4.32	CoF ₃ : $\phi_{ij,\alpha}$	136
4.33	CoF ₄ D_{4h} : $\phi_{ij,\alpha}$	137
4.34	CoF ₄ T_d : $\phi_{ij,\alpha}$	138

1 Introduction

The underlying physical laws necessary for the mathematical theory of a large part of physics and the whole of chemistry are thus completely known, and the difficulty is only that the exact application of these laws leads to equations much too complicated to be soluble. It therefore becomes desirable that approximate practical methods of applying quantum mechanics should be developed, which can lead to an explanation of the main features of complex atomic systems without too much computation.

Paul Dirac, 1929 [1]

With the Schrödinger Equation [2] the theoretical foundation to describe and predict all of chemistry is, in principle, complete. A more general version of it including special relativity was later introduced by Dirac [3] and is also capable of correctly describing heavy elements like gold, mercury or lead. However, the added complexity in the Dirac Equation is huge and a lot of chemistry is appropriately describe by the Schrödinger Equation.

Although knowing the required equations for over 90 years by now, we still struggle solving them. The difficulty lies in having to solve high-dimensional differential equations in connection with the pairwise interaction (Coulomb force) of all involved particles. A numerical exact method is known as Full Configuration Interaction (FCI) method [4]. Its exponential scaling however makes practical application impossible, even with the drastic improvements of computational resources over the last couple of decades in mind. Only the smallest molecular systems with only a handful of electrons can be treated by this approach. Thus, the desire to developed approximate methods, as Dirac stated already in 1929, is today just as valid as in the past.

Today a large amount of methods is available for treating chemical problems on a theoretical basis. The probably most popular family of methods is called Density Functional Theory (DFT) [5] and is capable of dealing with most systems of interest at reasonable computational cost. Although being able to achieve high precision (i.e. a small statistical error), DFT methods tend to lack accuracy (i.e. a large systematic error), which makes it difficult to judge on the quality of the results. If available, data from experiments or higher levels of theory may be used evaluate different DFT methods and chose the most appropriate one. But the predictive capabilities of DFT alone are limited. Additionally, there are issues with a class of systems called strongly correlated, where multiple dominant contributions need to be described appropriately. This is typically encountered if partially occupied, close-degenerate orbital levels are present, for example in transition metals or dissociation processes.

Another approach are the highly systematic *correlations methods*, which usually rely on the Hartree-Fock (HF) method [6, 7, 8] as a starting point. In HF a systematic approximation is made to cope with the problematic electron-electron interaction. It asserts a structure on the electronic wave function which only applies to a non-interacting system (no Coulomb repulsion between electrons), but keeps the interaction in the equations that need to be solved: Each electron is described by its own *one-electron wave function*, called *orbital*, and the anti-symmetrized product of all orbitals corresponds to the *many-electron wave function*. In its physical interpretation this leads to each electron perceiving the others only in an averaged way, hence this theory is also known as *mean field theory*.

In the real system however, the probability densities of two electrons would try to avoid spatial overlap, i.e. the correlated pair-density of two electrons being close to each other is small. The HF method however, does only account for the average interaction between electrons and therefore cannot describe the correlated probabilities of two or more electrons. This error is known as *electron correlation* and the above mentioned FCI method provides an exact solution, by expanding the many-electron wave function in a basis of *electron configurations*. Those are obtained by constructing all possible permutations of the available electrons in the space of *occupied* and *virtual* orbitals as obtained from HF. The number of permutations (configurations) is given by $\binom{M}{N} = \frac{M!}{N!(M-N)!}$, where N and M are the number of electrons and spin orbitals respectively, and is responsible for the steep exponential

computational scaling. Different systematic truncations to that expansion are possible and lead to different subsets of correlation methods where the trade-off between accuracy and computational cost can be easily controlled. This results in both, high accuracy and high precision, however at the cost of higher computational scaling compared to DFT.

The power of wave function based correlation methods thus lies in obtaining accurate results where DFT fails. In order to reduce the high computational scaling, and apply this methods to larger systems, one may systematically study the correlation effects and their origin in terms of the orbitals. A better understanding of the structure of the electronic wave function may lead to new approaches for accurate treatment of strongly correlated systems large in size.

One of the most prominent standard approaches in the field of wave function based correlation methods is coupled cluster theory. Inclusion of so called Single and Double amplitudes as well as a perturbative correction for the Triple amplitudes is typically abbreviated as CCSD(T) [9] and often referred to as the “gold standard of quantum chemistry”. In most cases it yields chemical accuracy ($< 1 \frac{\text{kJ}}{\text{mol}}$) while its computational scaling with $\mathcal{O}(N^7)$ allows application to small to medium sized molecules. Its major drawback, besides the still quite large computational scaling, is its dependence on a reasonable HF starting point, i.e. a single reference configuration. This is typically referred to by the term *single-reference approach*, and systems that are adequately treated by such approaches are called *weakly correlated*. This means, if the HF wave function is a qualitatively reasonable description, then CCSD(T) will typically yield a quantitatively sensible correction.

The remaining cases, that are not qualitatively well described by HF, are the already mentioned *strongly correlated* systems. Instead of the single electron configuration considered by HF, multiple configurations with similar weights in the FCI wave function are required for a qualitative description. This is typically achieved by selecting an active space of orbitals. Within these active space orbitals all possible configurations are considered, similar to FCI. However, the occupation for orbitals outside of the active space is kept fixed, reducing the number of possible permutations to generate configurations. The weights of the considered configurations are then simultaneously optimized together with the orbitals in a Complete Active Space Self-Consistent Field (CASSCF) calculation, thus avoiding the bias of the

HF method towards only a single configuration. In a second step, the resulting set of orbitals and list of configurations forms the starting point for a *multi-reference* calculation.

The focus of this work is to consider the step regarding the active space, which aims to describe the strong correlation contribution. Its computational scaling is in principle similar to the FCI method, just with a smaller number of electrons and orbitals. Considering larger systems, for example transition metal complexes, requiring large active spaces thus makes this approach unfeasible. A systematic analysis of strong correlation effects may lead to new insights allowing for new (systematic) approximations regarding the active space. The ultimate aim is to reduce the number of configurations required to treat strong correlation.

In principle, this may be achieved by two approaches. First, one may reduce the number of configurations by imposing certain conditions on them. Reducing the active space would be a special case as it corresponds to fixing the occupation of specific orbitals in all configurations. Typically one starts by considering core orbitals, which are energetically below the valence orbitals, as closed, i.e. doubly occupied in all configurations. Similar, virtual orbitals high in energy are excluded from the active space by fixing their occupation to be empty. Assigning the remaining orbitals however remains a delicate process as not all valence orbitals are always necessary in the active space. The actual choice may critically influence the quality of the calculation. Besides defining an active space, the number of configurations can be reduced by the Restricted Active Space Configuration Interaction (RASCI) approach, where excitations are selected based on the number of excited electrons [10]. A special case of RASCI within the full space of orbitals is Configuration Interaction with Single and Double (CISD) excitations, where the number of electrons in the set of all virtual orbitals may not exceed two.

The second approach is to use a different set of orbitals which will lead to a different set of configurations. Examples include localized orbitals [11, 12] or natural orbitals. The new set of configurations may be more efficient in the sense, that a smaller number of configurations may yield similar accuracy. In fact, it has been demonstrated that it is possible to optimize orbitals to minimize the number of configurations required [13].

Many further strategies to solve the CI problem are currently pursued in quantum chemistry and related fields. The Density Matrix Renormalization Group (DMRG) [14, 15] introduces a memory efficient representation of the CI vector and iteratively optimizes it by considering different subsets of orbitals. This effectively avoids diagonalizing a very large Hamiltonian by diagonalizing many small effective Hamiltonians instead. The accuracy of the CI vector is easily controlled by a numerical parameter called number of blockstates. While it excels for strong correlation effects, it becomes inefficient for weak correlation which would require a very large number of blockstates. As an extension to DMRG, the obtained coefficients for single and double excitations may be fed into a so called Tailored Coupled Cluster (TCC) ansatz [16]. The Method of Increments (MoI) [17, 18] expands the FCI energy in terms of n -body contributions. Here the overall system is split into different centers and the contribution of each individual center is calculated independently. Correlation effects due to the combination of two or more centers are then accounted for by *incremental* corrections, but typically decay quite fast with the number of centers combined. Quantum Monte Carlo (QMC) [19] combines a family of methods which stochastically sample the wave function instead of explicitly considering all possible contributions. This approach has recently been combined with the CI formalism in the Full Configuration Interaction Quantum Monte Carlo (FCIQMC) method [20]. Here, the configuration space is stochastically sampled by random walkers. This allows treatment of larger configuration spaces than the established deterministic methods are capable of and accounts for both, weak and strong, correlation.

Two further methods for strong correlation are Dynamical Mean Field Theory (DMFT) [21] and Density Matrix Embedding Theory (DMET) [22]. In DMFT a many-body lattice problem (e.g. a solid single crystal) is mapped to a single-site problem with effective parameters to describe the interaction with an environment (or bath). DMET can be considered an intermediate between DMRG and DMFT. It partitions a large system into a local fragment and its environment using density matrices in a similar way as DMRG does. While a computationally cheap low-level method can be used to treat the environment, the local fragment can be described by a more accurate high-level method. DMFT and DMET will not be further considered here.

Furthermore, different combinations of the above approaches are possible. For example in CASSCF the CI problem may be solved by DMRG [23, 24, 25, 26] or

FCIQMC [27] where conventional CI solvers exceed their capabilities. Or a large active space can be screened by an approximate DMRG calculation, based on which a smaller active space may be selected and then treated with a standard CASSCF approach.

To improve the selection of orbitals and configurations one may systematically investigate the correlation effects and relate the results to “chemical intuition”. A useful tool here is Quantum Information Theory (QIT) [28] which can be used to quantify the importance of either individual or groups of orbitals and their occupation patterns within the CI vector. The analysis may only be performed after a successful CI calculation, but insights may be translated to larger systems. A central advantage of QIT however is, that the results do not require a highly accurate description of the CI vector. For example in connection with DMRG, the QIT measures quickly converge for quite small numbers of blockstates. This has already been exploited in order to estimate the correlation contributions of individual orbitals, as measured by the von Neumann entropy. This data can then be used to set up an iterative scheme for automated active space selection [29].

These ongoing developments and advances of improved methods to deal with larger active spaces allow for testing of more complex chemical systems. The focus of this work is therefore to consider larger chemical systems and investigate their correlation effects. Insights about how orbitals are correlated with each other may then provide new approaches for the accurate treatment of large, strongly correlated systems.

2 Theoretical Background

This chapter will cover the theoretical concepts used in this thesis. Starting from the Schrödinger equation the emergence of the orbital picture in Hartree-Fock theory will be discussed. Next, different approaches on how to recover the electron correlation energy will be presented. Finally, it is discussed how electron correlation may be systematically analyzed in terms of orbital contributions. Most of the concepts are taken from, if not stated otherwise, the (standard) text books by Tannor [30], Szabo and Ostlund [31] and Helgaker, Jorgensen, and Olsen [32].

2.1 The Schrödinger Equation

The fundamental equation for non-relativistic quantum mechanics is the time-dependent Schrödinger equation [2]

$$i\hbar\frac{\partial}{\partial t}\Psi(\vec{R}, t) = \hat{H}\Psi(\vec{R}, t). \quad (2.1)$$

Here $i = \sqrt{-1}$ is the imaginary unit, $\hbar = \frac{h}{2\pi}$ is the reduced Planck constant. The physical or chemical system of interest is generally defined by the Hamilton operator, or *Hamiltonian*, \hat{H} which covers all energy contributions and interactions of the different particles of the system. In its most general form it depends on time t and the spatial coordinates \vec{R} . The *wave function* $\Psi(\vec{R}, t)$ describing the state of the system is obtained as a solution of the above differential equation for a given Hamiltonian. All quantum mechanically accessible information, i.e. physical and chemical properties of the system, are encoded in the wave function and can be calculated as expectation values with their corresponding operator. For example

the total energy of the system is given by

$$E_{\text{total}}(t) = \int \Psi^*(\vec{R}, t) \hat{H} \Psi(\vec{R}, t) dV \quad (2.2)$$

$$= \langle \Psi(\vec{R}, t) | \hat{H} | \Psi(\vec{R}, t) \rangle \quad (2.3)$$

where the integral $\int dV$ covers the whole universe. In practice however, only the close environment on the microscopical scale of molecules and (sub)atomic particles needs to be considered, as the wave function quickly converges to zero for distances larger than that. The second line denotes the abbreviated Dirac notation for these kind of integrals. It implies the integral and introduces the ket vector $|\Psi(\vec{R}, t)\rangle$ representing the wave function in the Hilbert space as well as the bra vector $\langle \Psi(\vec{R}, t)|$ representing the dual vector of $|\Psi(\vec{R}, t)\rangle$.

For time-independent Hamiltonians, i.e. closed system with a constant total energy, the product ansatz can be applied which factorizes the wave function into a spatial part $\psi(\vec{R})$ and time-dependent part $\theta(t)$

$$\Psi(\vec{R}, t) = \psi(\vec{R})\theta(t). \quad (2.4)$$

This allows reordering of the Schrödinger equation as

$$i\hbar \frac{\partial}{\partial t} \theta(t) = \frac{\hat{H}\psi(\vec{R})}{\psi(\vec{R})} = \text{const.} \equiv E. \quad (2.5)$$

One can thus formulate a time-independent Schrödinger equation

$$\hat{H}\psi(\vec{R}) = E\psi(\vec{R}) \quad (2.6)$$

$$\hat{H}|\psi(\vec{R})\rangle = E|\psi(\vec{R})\rangle \quad (2.7)$$

where multiplication by $\langle \psi(\vec{R})|$ from the left side leads to

$$\langle \psi(\vec{R}) | \hat{H} | \psi(\vec{R}) \rangle = E \langle \psi(\vec{R}) | \psi(\vec{R}) \rangle = E \quad (2.8)$$

where the normalization constraint of the wave function

$$\langle \psi(\vec{R}) | \psi(\vec{R}) \rangle \equiv 1 \quad (2.9)$$

has been used. If the product ansatz of Eq. (2.4) is applied to the expectation value in Eq. (2.3), the time-dependent part $\theta(t)$ may be separate as the time-independent Hamiltonian does not act on it. Using normalization of $\theta(t)$ one obtains

$$E_{\text{total}}(t) = \langle \psi(\vec{R})\theta(t) | \hat{H} | \psi(\vec{R})\theta(t) \rangle \quad (2.10)$$

$$= \langle \psi(\vec{R}) | \hat{H} | \psi(\vec{R}) \rangle \langle \theta(t) | \theta(t) \rangle \quad (2.11)$$

$$= \langle \psi(\vec{R}) | \hat{H} | \psi(\vec{R}) \rangle \quad (2.12)$$

which identifies the constant E in Eq. (2.8) with the total energy E_{total} of the system.

Furthermore, the time-dependent part of Eq. (2.5) can be written as

$$i\hbar \frac{\partial}{\partial t} \theta(t) = E\theta(t) \quad (2.13)$$

which may be solved by direct integration

$$\theta(t) = \exp\left(-i\frac{E}{\hbar}t\right). \quad (2.14)$$

The more general case of a time-dependent Hamiltonian can be treated by separating the variables in Eq. (2.1) and direct integration on each side

$$\begin{aligned} \int_{\Psi(\vec{R},0)}^{\Psi(\vec{R},t)} \frac{d\Psi(\vec{R},t)}{\Psi(\vec{R},t)} &= \int_0^t \frac{1}{i\hbar} \hat{H} dt' \\ \ln \frac{\Psi(\vec{R},t)}{\Psi(\vec{R},0)} &= \frac{1}{i\hbar} \hat{H}t \\ \Psi(\vec{R},t) &= \exp\left(-\frac{i}{\hbar} \hat{H}t\right) \Psi(\vec{R},0). \end{aligned} \quad (2.15)$$

This result can be used to simulate the time evolution of quantum systems, based on a starting point $\Psi(\vec{R}, t = 0)$. Thus one first needs to solve the time-independent Schrödinger equation Eq. (2.7), which will be discussed in more detail below.

2.1.1 The Molecular Hamiltonian

Chemistry is typically concerned with molecules, their properties and how different molecules interact with each other or external fields (e.g. electromagnetic fields). As molecules are built from atomic nuclei and electrons, which are quantum mechanical objects, an accurate theoretical description of chemistry requires application of the Schrödinger equation. The main contributions to the molecular Hamiltonian are given by the kinetic energy (\hat{T}) of each particle and the Coulomb interaction (\hat{V}) between all combinations of pairs of particles. It is thus given by

$$\hat{H}^{\text{mol}}(\vec{R}, \vec{r}) = \hat{T}_n(\vec{R}) + \hat{T}_e(\vec{r}) + \hat{V}_{nn}(\vec{R}) + \hat{V}_{ne}(\vec{R}, \vec{r}) + \hat{V}_{ee}(\vec{r}) \quad (2.16)$$

where \vec{R} and \vec{r} denote the 3-dimensional coordinates for all atomic nuclei and electrons respectively. Using atomic units, the different operators are the nuclear kinetic energy

$$\hat{T}_n(\vec{R}) = -\sum_{\alpha}^M \frac{1}{2m_{\alpha}} \nabla_{\vec{R}_{\alpha}}^2, \quad (2.17)$$

the electron kinetic energy

$$\hat{T}_e(\vec{r}) = -\sum_i^N \frac{1}{2} \nabla_{\vec{r}_i}^2, \quad (2.18)$$

the nuclear-nuclear Coulomb interaction

$$\hat{V}_{nn}(\vec{R}) = \frac{1}{2} \sum_{\alpha}^M \sum_{\beta}^M \frac{Z_{\alpha} Z_{\beta}}{R_{\alpha\beta}}, \quad (2.19)$$

the nuclear-electron Coulomb interaction

$$\hat{V}_{ne}(\vec{R}, \vec{r}) = -\sum_{\alpha}^M \sum_i^N \frac{Z_{\alpha}}{r_{\alpha i}}, \quad (2.20)$$

and finally the electron-electron Coulomb interaction

$$\hat{V}_{ee}(\vec{r}) = \frac{1}{2} \sum_i^N \sum_j^N \frac{1}{r_{ij}}. \quad (2.21)$$

In the above equations M and N are the total number of atoms and electrons respectively, which are indexed by Greek and Latin small letters respectively. Their physical properties of relevance are the electron mass m_e and atomic mass m_{α} (in

units of m_e) as well as electron charge $q = -e$ and nuclear charge Z_α (both in units of the elementary charge e). The distances between two particles are denoted by $R_{\alpha\beta} = |\vec{R}_\alpha - \vec{R}_\beta|$, $r_{\alpha i} = |\vec{R}_\alpha - \vec{r}_i|$ and $r_{ij} = |\vec{r}_i - \vec{r}_j|$.

2.1.2 The Born-Oppenheimer Approximation

The coupling of nuclear and electronic coordinates due to the different Coulomb interactions constitutes a major problem for an analytic solution of the differential equation Eq. (2.7). One of the most central approximations in theoretical chemistry, the Born-Oppenheimer Approximation (BOA), sidesteps (part of) this problem by decoupling the nuclear and electronic movement. Its central argument is that the nuclei are much heavier than the electrons and therefore will react to electronic movement only on a rather long time scale. On the other hand, the light electrons will follow the nuclear movement almost instantaneously. One may therefore use a product ansatz to split the wave function into an electronic part $\Phi(\vec{r}; \vec{R})$ and a nuclear part $X(\vec{R})$ [33]

$$\Psi(\vec{R}, \vec{r}) = \Phi(\vec{r}; \vec{R})X(\vec{R}), \quad (2.22)$$

where the semicolon indicates parametric dependence. The electronic system is solved independently for a fixed set of parameters for the nuclear coordinates. Freezing the nuclear coordinates means the nuclear kinetic energy \hat{T}_n becomes zero, the nuclear repulsion term \hat{V}_{nn} will be constant and the electron-nuclear attraction \hat{V}_{ne} only depends on the electronic coordinates. The only problematic term left is then the electron-electron interaction \hat{V}_{ee} .

The electronic Schrödinger equation then reads

$$\hat{H}^{\text{el}}(\vec{R}, \vec{r}) \Phi(\vec{r}; \vec{R}) = E_{\text{el}}(\vec{R})\Phi(\vec{r}; \vec{R}) \quad (2.23)$$

with

$$\hat{H}^{\text{el}}(\vec{R}, \vec{r}) = \hat{T}_e(\vec{r}) + \underbrace{\hat{V}_{nn}(\vec{R})}_{\text{const.}} + \hat{V}_{ne}(\vec{r}; \vec{R}) + \hat{V}_{ee}(\vec{r}). \quad (2.24)$$

The electronic eigenenergy $E_{\text{el}}(\vec{R})$ is then used in the nuclear Schrödinger equation

as a potential depending on the nuclear coordinates

$$\hat{H}^{\text{nuc}}(\vec{R})\Phi(\vec{R}) = E_{\text{nuc}}\Phi(\vec{R}) \quad (2.25)$$

where

$$\hat{H}^{\text{nuc}} = \hat{T}_n(\vec{R}) + E_{\text{el}}(\vec{R}). \quad (2.26)$$

2.1.3 Electronic Structure Theory

The remaining task of electronic structure theory is now to solve the electronic Schrödinger equation Eq. (2.23) for a specific set of nuclear coordinates \vec{R} . The resulting electronic wave function $\Phi(\vec{r})$ then describes how the electrons are arranged around the atoms, thus represents the *electronic structure* of the molecular system. The central challenge here is treating the electron-electron interaction \hat{V}_{ee} which couples all electrons together. The problem is similar to the nuclear-electronic coupling, however applying an approximation similar to the BOA is not justified anymore as same particles are treated here. Applying a product ansatz to separate all electronic coordinates from each other is thus strictly speaking not allowed. The standard approach in wave function based correlation methods however is to first ignore that issue (cf. Section 2.2.2) and to correct for it in a second step (cf. Section 2.2.4).

An alternative, popular method is to avoid dealing with the $3N$ -dimensional electronic wave function, where N is the number of electrons. Instead the description works with the 3-dimensional electron density which has a uniquely assigned eigenenergy as well, as proven by the Hohenberg-Kohn theorems [5]. However the exact mapping (functional) is unknown and finding improved approximations to it is a matter of active research. The associated family of methods is called *Density Functional Theory* (DFT) and not further covered within this thesis.

2.2 The Orbital Picture

Orbitals are a well known tool for describing chemistry and are used to construct simplified models. For example in Frontier molecular orbital theory [34], the High-

est Occupied Molecular Orbital (HOMO) and Lowest Unoccupied Orbital (LUMO) are used to describe reaction mechanisms. Another example are the Woodward-Hoffmann rules [35], which can be used to explain and predict the chemistry of pericyclic reactions. It should be pointed out however, that the concept of orbitals is the result of an approximation which lacks quantitative accuracy, and often even gives qualitatively wrong results. Correction of this error is therefore crucial for both, predicting new chemistry and confirming experimental results based on theoretical approaches. In the following the origin (cf. Section 2.2.2) and the attempts for correcting this error (cf. Section 2.2.4) will be described in more detail.

2.2.1 Spin of Electrons

Spin is an intrinsic quantum mechanical property of particles, with no classical analog. It behaves like spatial angular momentum, but is its own degree of freedom with its own set of quantum numbers. It is described by the commutator relations

$$[\hat{s}_x, \hat{s}_y] = i\hat{s}_z \quad (2.27)$$

$$[\hat{s}_y, \hat{s}_z] = i\hat{s}_x \quad (2.28)$$

$$[\hat{s}_z, \hat{s}_x] = i\hat{s}_y. \quad (2.29)$$

Additionally, each individual component does commute with \hat{s}^2

$$\hat{s}^2 = \hat{\vec{s}} \cdot \hat{\vec{s}} = \hat{s}_x^2 + \hat{s}_y^2 + \hat{s}_z^2. \quad (2.30)$$

One can thus choose a set of simultaneous eigenfunctions of \hat{s}^2 and one of the components, usually \hat{s}_z .

$$\hat{s}^2|s, m_s\rangle = s(s+1)|s, m_s\rangle \quad (2.31)$$

$$\hat{s}_z|s, m_s\rangle = m_s|s, m_s\rangle \quad (2.32)$$

where s is the *total* spin quantum number and m_s the *projected* spin quantum number. For single electrons, the total spin quantum number is always $s = \frac{1}{2}$, while the projected spin quantum number $m_s = \pm\frac{1}{2}$ distinguishes α and β spin.

Instead of working with \hat{s}_x and \hat{s}_y , one may use the more convenient ladder operators

\hat{s}_+ and \hat{s}_- defined as

$$\hat{s}_+ = \hat{s}_x + i\hat{s}_y \quad (2.33)$$

$$\hat{s}_- = \hat{s}_x - i\hat{s}_y. \quad (2.34)$$

They have a more intuitive action on the spin eigenfunctions, by increasing or decreasing the m_s quantum number

$$\hat{s}_+|\alpha\rangle = 0 \quad (2.35)$$

$$\hat{s}_-|\alpha\rangle = |\beta\rangle \quad (2.36)$$

$$\hat{s}_+|\beta\rangle = |\alpha\rangle \quad (2.37)$$

$$\hat{s}_-|\beta\rangle = 0. \quad (2.38)$$

Together with the commutator relations of Eqs. (2.27) to (2.29), \hat{s}^2 can be expressed in terms of the ladder operators as

$$\hat{s}^2 = \hat{s}_+\hat{s}_- - \hat{s}_z + \hat{s}_z^2. \quad (2.39)$$

For many electron systems, the overall quantum numbers for total spin S and projected spin M can be obtained from the individual quantum numbers of each electron by using

$$\hat{S}_z = \sum_i \hat{s}_{z,i} \quad (2.40)$$

$$\hat{S}_\pm = \sum_i \hat{s}_{\pm,i} \quad (2.41)$$

where the index i labels the electrons, and the sum goes over all all electrons in the system. The total spin operator can then be evaluated in terms of its components

$$\hat{S}^2 = \hat{S}_+\hat{S}_- - \hat{S}_z + \hat{S}_z^2. \quad (2.42)$$

The two possible spin states of each electron need to be considered in the quantum mechanical description of molecule, but is not implicitly included in the Schrödinger equation. Instead it is added as a further property of each electron and the electronic

coordinates are thus represented as

$$\vec{x}_i = (\vec{r}_i, \zeta_i) \quad (2.43)$$

where ζ_i is the spin coordinate of the i -th electron. Accordingly, \vec{x} represents the combined electronic coordinates \vec{x}_i for all N electrons of the system. A common short hand notation for \vec{x}_i is to only write the index i , e.g. $\hat{h}(1)$ for the one-electron Hamiltonian depending only on electron $i = 1$.

2.2.2 The Hartree-Fock Method

The Slater determinant

The derivation of the Hartree-Fock methods starts by first ignoring the electron-electron interaction \hat{V}_{ee} completely, which allows expressing the many-electron wave function $\Phi(\vec{x})$ as a product of one-electron wave functions $\chi(\vec{x})$, called *orbitals*. This is known as the *Hartree product* [6, 7]

$$\Phi(\vec{x}) \approx \prod_i^N \chi_i(\vec{x}_i). \quad (2.44)$$

It was later pointed out by Slater [8, 36] that this approach violates the Pauli principle [37], which requires the many-electron wave function to be anti-symmetric when swapping two electronic coordinates. A convenient fix for that is to exploit the anti-symmetric structure of determinants, resulting in the commonly used *Slater determinant*

$$\Phi(\vec{x}) \approx \Psi(\vec{x}) = \frac{1}{\sqrt{N!}} \begin{vmatrix} \chi_1(\vec{r}_1, \zeta_1) & \chi_2(\vec{r}_1, \zeta_1) & \dots & \chi_N(\vec{r}_1, \zeta_1) \\ \chi_1(\vec{r}_2, \zeta_2) & \chi_2(\vec{r}_2, \zeta_2) & \dots & \chi_N(\vec{r}_2, \zeta_2) \\ \vdots & \vdots & & \vdots \\ \chi_1(\vec{r}_N, \zeta_N) & \chi_2(\vec{r}_N, \zeta_N) & \dots & \chi_N(\vec{r}_N, \zeta_N) \end{vmatrix}. \quad (2.45)$$

The Fock operator

In the Hartree-Fock method, the Slater determinant is used as an ansatz for the wave function in the electronic Schrödinger equation, including the electron-electron interaction. The approximation here lies in assuming that the structure of the wave function for the non-interacting system may be directly translated to the interacting system. This is the crucial step that on the one hand allows the use of orbitals as a model, on the other hand introduces a non-negligible error. This error is known as *electron correlation* and covered in detail in Section 2.2.4.

The Hartree-Fock equations are thus derived by plugging the Slater determinant from Eq. (2.45) into the time independent Schrödinger equation (Eq. (2.23)) and applying the Slater-Condon-Rules [36, 38] to resolve the integrals in terms of spin orbitals. In the resulting equations each spin-orbital is then expressed as an eigenfunction of the *Fock operator* \hat{f}

$$\hat{f}|\chi_a\rangle = \varepsilon_a|\chi_a\rangle \quad (2.46)$$

with

$$\hat{f}(1) = \underbrace{-\frac{1}{2}\nabla_1^2 - \sum_{\alpha} \frac{Z_{\alpha}}{r_{1\alpha}}}_{\hat{h}(1)} + \underbrace{\sum_j \hat{J}_j(1) - \hat{K}_j(1)}_{\hat{v}^{\text{HF}}(1)} \quad (2.47)$$

where $\hat{h}(1)$ is a one-particle Hamiltonian only depending on the electron itself, and $\hat{v}^{\text{HF}}(1)$ is an effective one-electron potential. \hat{J} and \hat{K} are the *coulomb* and *exchange* operators respectively and describe the interactions of any electron with all the other electrons in the system.

$$\hat{J}_j(1)\chi_i(1) = \left[\int \chi_j^*(2) \frac{1}{r_{12}} \chi_j(2) d2 \right] \chi_i(1) \quad (2.48)$$

$$\hat{K}_j(1)\chi_i(1) = \left[\int \chi_j^*(2) \frac{1}{r_{12}} \chi_i(2) d2 \right] \chi_j(1) \quad (2.49)$$

In terms of expectation values the coulomb and exchange integrals

$$J_{ij} = \langle \chi_i(1)\chi_j(2) | \frac{1}{r_{12}} | \chi_i(1)\chi_j(2) \rangle = \langle ij | ij \rangle \quad (2.50)$$

$$K_{ij} = \langle \chi_i(1)\chi_j(2) | \frac{1}{r_{12}} | \chi_j(1)\chi_i(2) \rangle = \langle ij | ji \rangle \quad (2.51)$$

are obtained. The term on the right hand side is an abbreviation called *physicists' notation*. Note that self interaction of electrons is canceled out, since both integrals become identical for $i = j$.

The Hartree-Fock ground state energy is then given by

$$E_{\text{HF}} = \sum_i \langle i | \hat{h} | i \rangle - \frac{1}{2} \sum_{ij} (\langle ij | ij \rangle - \langle ij | ji \rangle) + \hat{V}_{nn} \quad (2.52)$$

where the sums go over all occupied spin orbitals χ_i .

The task to carry out now is to find an appropriate set of spin orbitals χ_i describing the molecular system. This is typically done by applying the *variational principle* which states that all possible trial wave functions have a higher ground state energy than the exact solution. Thus minimization of the energy in Eq. (2.52) with respect to the spin orbitals χ_i yields a solution, which is optimal with respect to the total energy.

Spatial orbitals

As electrons are commonly found to form pairs with opposing spins, one may construct *restricted* orbitals where two molecular spin orbitals χ_i and χ_j may share their spatial part and only differ in their spin contribution (cf. Section 2.2.1).

$$\chi(\vec{r}, \zeta) = \begin{cases} \phi(\vec{r}) \alpha(\zeta) \\ \phi(\vec{r}) \beta(\zeta) \end{cases} \quad (2.53)$$

Especially for closed shell systems, i.e. no unpaired electrons, this approach is commonly used to simplify the equations. The Fock operator of Eq. (2.47) can then be modified to

$$\hat{f}^c(1) = \hat{h}(1) + \sum_j^{N/2} 2\hat{J}_j(1) - \hat{K}_j(1) \quad (2.54)$$

where the sum goes over the $\frac{N}{2}$ occupied molecular orbitals and each coulomb integral occurs twice due to double occupation, while exchange integral vanishes between α and β spin orbitals. However for open shell system this restriction yields qualitatively wrong results, as unpaired electrons will introduce a spin polarization. Using

unrestricted orbitals one may account for the spin polarization, which will lower the ground state energy, at the cost of the HF wave function no longer being an eigenfunction of the \hat{S}^2 operator. Two Fock operators, one for α and one for β spin orbitals, will then need to be considered

$$f^\alpha(1) = h(1) + \sum_j^{N^\alpha} [2\hat{J}_j^\alpha(1) - \hat{K}_j^\alpha(1)] + \sum_i^{N^\beta} J_i^\beta(1) \quad (2.55)$$

$$f^\beta(1) = h(1) + \sum_j^{N^\beta} [2\hat{J}_j^\beta(1) - \hat{K}_j^\beta(1)] + \sum_i^{N^\alpha} J_i^\alpha(1). \quad (2.56)$$

Linear Combination of Atomic Orbitals

The integro-differential equation in Eq. (2.46) can be solved numerically by expanding the orbitals in a basis set [39] of atomic orbitals φ_i (cf. Section 2.2.3).

$$\phi_j = \sum_{i=1}^K C_{ij} \varphi_i \quad (2.57)$$

This is known as Linear Combination of Atomic Orbitals (LCAO). Alternatives, for example plane waves, are possible as well but not considered here. Substituting the expansion of Eq. (2.57) into Eq. (2.46) and using the spatial molecular orbitals from Eq. (2.53) one can derive the *Roothaan equations* for closed shell systems

$$\mathbf{FC} = \mathbf{SC}\boldsymbol{\varepsilon} \quad (2.58)$$

with the Fock matrix \mathbf{F}

$$F_{ij} = \langle \phi_i | f^c | \phi_j \rangle, \quad (2.59)$$

the overlap matrix \mathbf{S}

$$S_{ij} = \langle \phi_i | \phi_j \rangle \quad (2.60)$$

and molecular orbital coefficients matrix \mathbf{C} from Eq. (2.57). The diagonal matrix $\boldsymbol{\varepsilon}$ holds the molecular orbital eigenvalues (or orbital energies) ε_j .

Eq. (2.58) is a generalized eigenvalue problem and can be solved by standard numerical methods. Due to the electron-electron interaction the Fock matrix \mathbf{F} depends on all the molecular orbitals (cf. Eq. (2.47)). Therefore the matrix to diagonalize

directly depends on its own eigenvectors. The problem may thus be solved *self-consistently* by starting with an initial guess for \mathbf{C} and iteratively constructing and diagonalizing $\mathbf{F}(\mathbf{C})$ until a converged results is obtained.

For the unrestricted case, two separate Fock matrices for α and β spin orbitals need to be constructed and diagonalized in each iteration.

2.2.3 Atomic Orbital Basis Sets

One of the most popular approaches to parameterize molecular orbitals in HF calculations is to expand them in a basis set of atomic orbitals. Originating from the analytic solution of the Hydrogen atom, which may be generalized to Hydrogen-like atoms with an arbitrary, effective nuclear charge, these solutions are adapted for all elements across the periodic table.

Exploiting spherical symmetry of an atom, orbitals are expressed in spherical coordinates (r, θ, ϕ) with radius r , polar angle θ and azimuth angle ϕ . The orbitals may be factorized into a radial part and an angular part. The latter can be represented in the basis of the spherical harmonics, independent of the chemical elements. For the radial part different basis sets are possible and used. One common choice are Gaussian Type Orbitals (GTO) of the form

$$\varphi^{GTO}(\alpha, \vec{r} - \vec{R}) = \left(\frac{2\alpha}{\pi}\right)^{\frac{3}{4}} e^{-\alpha|\vec{r}-\vec{R}|^2} \quad (2.61)$$

centered at the coordinates \vec{R} of a given atom and with the Gaussian orbital exponent α . Note that the GTO includes a e^{-r^2} term, while the actual analytic solutions of the Hydrogen atom decay only with e^{-r} dependence. However, this slight modifications allows for fast analytic evaluation of integrals over these functions, while for the e^{-r} functions costly numerical approaches are required. To reduce the error introduced by this approximation many primitive GTOs are linearly combined resulting in contracted GTOs

$$\varphi_{\mu}^{cGTO}(\vec{r} - \vec{R}) = \sum_{p=1}^L d_{p\mu} \varphi_p^{GTO}(\alpha_{p\mu}, \vec{r} - \vec{R}). \quad (2.62)$$

A GTO basis set for a certain calculation is then defined by specifying the expansion coefficients $d_{p\mu}$ and orbital exponents $\alpha_{p\mu}$ together with the angular momentum quantum number l for each orbital shell of each atom.

In a minimal basis set there is one contracted GTO for each orbital shell (1s, 2s, 2p *etc.*) that is occupied by electrons. More complete basis sets are obtained by introducing additional basis functions, eventually approaching the complete basis set limit for which numerical exact results may be obtained. Different types of additional basis functions can be considered: a *split valence* basis set uses multiple basis function for valence orbitals, e.g. a *double zeta* basis set uses two contracted GTOs per shell. However, just a single basis function is supplied for core orbitals, as those do not change much in different molecular arrangements, leading to negligible errors. Furthermore, *augmented* basis sets include *diffuse* basis functions with small exponent α to describe electron density further apart from the nucleus, e.g. for bond breaking or anions. And *polarized* functions with higher angular momentum l allow to shift electron density due to polarization by bonding partners neighboring the atom or due to the presence of external electromagnetic fields.

2.2.4 Electron Correlation

The use of orbitals is a systematic approximation and lies at the core of the Hartree-Fock method. Although this approximation has much less justification than the in principle similar Born-Oppenheimer Approximation (cf. Section 2.1.2), it does yield surprisingly well results, and sometimes gives qualitatively correct trends. On a quantitative level however, chemical accuracy is typically considered to be on the order of 1 kJ/mol, which is beyond the capabilities of HF.

The physical interpretation of the error in HF is that each electron only feels the interaction of other electrons on average, i.e. by their probability distribution. They are unaware of each others instantaneous locations and thus a high pair density $\rho(\vec{r}_1, \vec{r}_2)$ (the *correlated* probability density) of being located close to each other ($|\vec{r}_1 - \vec{r}_2| \approx 0$) is possible. In reality however the pair density of such situations should be small, due to the electron-electron interaction, which is therefore insufficiently described at the HF level. Accordingly, the *correlation energy* E_{corr} is defined as the

difference between the HF solution and the exact non-relativistic solution.

$$E_{\text{corr}} = E_{\text{exact}} - E_{\text{HF}} \quad (2.63)$$

2.2.5 Second Quantization

Before considering ways to calculate the electron correlation energy, a brief introduction into creation and annihilation operators will follow. They originate from the second quantization formalism of quantum field theory and are commonly used for the mathematical representation of the Fock space, i.e. the set of configurations serving as a basis set for Configuration Interaction and related methods in the following sections.

Consider an electron configuration

$$|k\rangle = \left| \prod_{I=1}^M k_I \right\rangle = |k_1 k_2 \cdots k_M\rangle \quad (2.64)$$

which corresponds to a Slater-Determinant constructed from the spin orbitals χ_I . The occupation of that orbital is given by $k_I = \{0, 1\}$. One then defines the *creation* operator

$$\hat{a}_I^\dagger |k_1 k_2 \cdots 0_I \cdots k_M\rangle = \delta_{k_I, 0} \prod_{J=1}^{I-1} (-1)^{k_J} |k_1 k_2 \cdots 1_I \cdots k_M\rangle \quad (2.65)$$

which will create an electron in the previously unoccupied spin orbital χ_I , while the *annihilation* operator

$$\hat{a}_I |k_1 k_2 \cdots 1_I \cdots k_M\rangle = \delta_{k_I, 1} \prod_{J=1}^{I-1} (-1)^{k_J} |k_1 k_2 \cdots 0_I \cdots k_M\rangle \quad (2.66)$$

will remove an electron from the corresponding occupied orbital. Due to the Kronecker δ , creating electrons in occupied orbitals, or annihilating electrons in unoccupied orbitals yields 0. And the term $(-1)^{k_J}$ ensures the wave function is anti-symmetric with respect to the exchange of two electrons, i.e. the Pauli-Principle is

satisfied. As a consequence they also fulfill the anti-commutator relations

$$\hat{a}_I^\dagger \hat{a}_J^\dagger + \hat{a}_J^\dagger \hat{a}_I^\dagger = 0 \quad (2.67)$$

$$\hat{a}_I \hat{a}_J + \hat{a}_J \hat{a}_I = 0 \quad (2.68)$$

$$\hat{a}_I^\dagger \hat{a}_J + \hat{a}_J \hat{a}_I^\dagger = \delta_{IJ}. \quad (2.69)$$

The expectation value of successive application of the annihilation operator and the creation operator on the same orbital results in the occupation number of that orbital. Thus one can define the occupation number operator

$$\hat{n}_I = \hat{a}_I^\dagger \hat{a}_I. \quad (2.70)$$

Using the above operators, one can express the molecular electronic Hamiltonian in spin orbital basis as

$$\hat{H} = \sum_{IJ} h_{IJ} \hat{a}_I^\dagger \hat{a}_J + \frac{1}{2} g_{IJKL} \hat{a}_I^\dagger \hat{a}_K^\dagger \hat{a}_L \hat{a}_J + \hat{V}_{\text{nn}} \quad (2.71)$$

where h_{IJ} corresponds to the one-particle Hamiltonian of HF transformed into molecular orbital basis and g_{IJKL} are the electron repulsion integrals in molecular orbital basis.

$$h_{IJ} = \langle I | -\frac{1}{2} \nabla^2 - \sum_{\alpha} \frac{Z_{\alpha}}{r_{\alpha}} | J \rangle \quad (2.72)$$

$$g_{IJKL} = \langle IK | \frac{1}{r_{12}} | LJ \rangle \quad (2.73)$$

This means, that as input for all correlation methods relying on the HF orbitals, only the integrals h_{IJ} and g_{IJKL} as well as the nuclear repulsion energy \hat{V}_{nn} are needed. In practice, those values are commonly stored in so called **FCIDUMP** files, which serve as an interface between different quantum chemistry codes.

2.2.6 The Configuration Interaction Method

One way to correct for the HF approximation and recover E_{corr} is to use HF as a starting point. As HF does not only yield *occupied* molecular orbitals, but a large number of *virtual* molecular orbitals as well, electron configurations other than

the HF configuration can be constructed. Each configuration yields its own Slater determinant and considering all possible combinations of distributing N electrons in M spin orbitals, a total of $\binom{M}{N}$ determinants can be obtained. This set of a determinants forms a many-electron basis set, in which the electronic wave function may be expanded.

Configuration State Functions

Besides the direct use of Slater determinants as a basis, one may also construct spin adapted basis states as linear combinations of Slater determinants, called Configuration State Functions (CSFs). Their advantage is, that they are simultaneous eigenfunctions of the total spin operator \hat{S}^2 and projected spin operator \hat{S}_z , while Slater determinants are eigenfunctions of the projected spin only.

As an example, the CSF for a two electron system is considered, where both electrons occupy different spatial orbitals. As closed shell orbitals do not contribute to the overall spin quantum numbers, this may be generalized to any system with two unpaired electrons. A single electron always has the total spin quantum number $s = \frac{1}{2}$ and projected spin quantum number $m_s = \pm\frac{1}{2}$, corresponding to α or β spin. The spin multiplicity $2S + 1$ of a single electron system therefore yields a doublet ($2 \times \frac{1}{2} + 1 = 2$). In a two electron system, both electrons may have same projected spin ($\alpha(\zeta_1)\alpha(\zeta_2)$ or $\beta(\zeta_1)\beta(\zeta_2)$) or opposite spin ($\alpha(\zeta_1)\beta(\zeta_2)$ or $\beta(\zeta_1)\alpha(\zeta_2)$). Combining situations with total spin flip two Slater determinants can be constructed

$$|\Psi_1\rangle = |\alpha\alpha\rangle \quad (2.74)$$

$$|\Psi_2\rangle = |\alpha\beta\rangle \quad (2.75)$$

where explicit writing of the spin coordinates ζ_i as well as the spatial part of the orbitals has been omitted. The two Slater determinants are eigenfunctions of the projected spin operator

$$\hat{S}_z|\alpha\alpha\rangle = 1|\alpha\alpha\rangle \quad (2.76)$$

$$\hat{S}_z|\alpha\beta\rangle = 0|\alpha\beta\rangle. \quad (2.77)$$

And for the total spin operator one obtains

$$\hat{S}^2|\alpha\alpha\rangle = 2|\alpha\alpha\rangle \quad (2.78)$$

$$\hat{S}^2|\alpha\beta\rangle = |\alpha\beta\rangle + |\beta\alpha\rangle. \quad (2.79)$$

This means the first Slater determinant $|\Psi_1\rangle = |\alpha\alpha\rangle$ may directly be considered a CSF. On the other hand, the second Slater determinant $|\Psi_2\rangle = |\alpha\beta\rangle$ is not an eigenfunction of the \hat{S}^2 operator. Suitable eigenfunctions of \hat{S}^2 may be constructed as linear combinations of Slater determinants, e.g.

$$|^1\Psi\rangle = \frac{1}{\sqrt{2}}(|\alpha\beta\rangle - |\beta\alpha\rangle) \quad (2.80)$$

$$|^3\Psi\rangle = \frac{1}{\sqrt{2}}(|\alpha\beta\rangle + |\beta\alpha\rangle). \quad (2.81)$$

Application of the \hat{S}^2 operator will then yield the eigenvalue $S(S+1) = 0$ for $|^1\Psi\rangle$, i.e. a pure spin singlet, and $S(S+1) = 2$ for $|^3\Psi\rangle$, i.e. a pure spin triplet.

Full Configuration Interaction

Expanding the electronic wave function $|\Phi\rangle$ in the basis of all configurations $\{|i\rangle\}$ yields the ansatz for the Full Configuration Interaction (FCI) [4] wave function.

$$|\Phi\rangle = |\text{FCI}\rangle = \sum_i c_i |i\rangle \quad (2.82)$$

The set of all coefficients c_i is called the Configuration Interaction (CI) vector and the basis functions $|i\rangle$ may either refer to Slater determinants or CSFs. Constructing and diagonalizing the electronic Hamiltonian Eq. (2.24) in this basis yields a numerically exact solution, provided the HF basis set is large enough to approach the (one-electron) basis set limit. However, the exponential scaling due to the large number of $\binom{M}{N}$ determinants makes this approach unfeasible for any system with more than just a couple of electrons.

The many-electron basis depends on the choice of the one-electron basis, i.e. the set of molecular orbitals. The latter can for example be the canonical orbitals as directly obtained from HF. Alternatively, it is possible to use orbitals optimized for many

configurations at once (cf. Section 2.2.8) or localized orbitals (cf. Section 2.2.9).

Truncations to the FCI wave function

Various systematic truncations to the ansatz in Eq. (2.82) constitute the field of *wave function based correlation methods* and allow for a controlled choice between accuracy and computational cost. Although being more reliable in accuracy, applications are still limited to fairly small systems and are no where close to the computational performance of Density Functional Theory.

The standard approaches to truncate the FCI expansion in Eq. (2.82) start by classifying all configurations as excitations from the HF ground state configuration. A Single excitation is a configuration that is obtained by removing one electron from the occupied orbital space and placing it in one of the virtual orbital. Similar Double, Triple, Quadruple *etc.* excitations are define. Although the term “excitation” may suggest so, this is not a dynamic process, but merely a term used for classification purposes.

The CI wave function

$$|\text{FCI}\rangle = \left(1 + \sum_{A,I} \hat{X}_I^A + \sum_{\substack{A>B \\ I>J}} \hat{X}_{IJ}^{AB} + \dots \right) |\text{HF}\rangle \quad (2.83)$$

can thus be expressed in terms of excitation operators

$$\hat{X}_I^A = C_I^A \hat{a}_A^\dagger \hat{a}_I \quad (2.84)$$

$$\hat{X}_{IJ}^{AB} = C_{IJ}^{AB} \hat{a}_A^\dagger \hat{a}_B^\dagger \hat{a}_I \hat{a}_J \quad (2.85)$$

⋮

where \hat{a}_A^\dagger and \hat{a}_I are the *creation* and *annihilation* operators in the framework of second quantization (cf. Section 2.2.5).

In most cases HF provides a quite reasonable starting point, thus the HF configuration has the largest weight in the CI vector. Additionally, electron configurations that are more similar to the HF configuration are then typically more important as

well, i.e. the weights have a decreasing trend going from single to double to triple excitations and so on. Thus it is reasonable to truncate the CI expansion after a certain level of excitations. For example in CISD all triple excitations and beyond are neglected. One may add further excitation levels if needed, but the gain of additional accuracy is at the expense of much higher computational effort.

Size consistency

Unfortunately, the above CI truncation is not size-consistent, i.e. the CISD energy of a non-interacting dimer is not equal to the sum of the two monomers calculated independently. In the dimer case the CI truncation will neglect quadruple excitations that can be obtained by combining double excitations of the monomers. A popular alternative to CI is Coupled Cluster (CC) theory, where an exponential ansatz for the excitation expansion is used.

$$|\text{CC}\rangle = \exp \left(\sum_{A,I} \hat{X}_I^A + \sum_{\substack{A>B \\ I>J}} \hat{X}_{IJ}^{AB} + \dots \right) |\text{HF}\rangle \quad (2.86)$$

Expanding this ansatz in a Taylor series yields a truncation scheme similar to Eq. (2.83), but a couple of additional *disconnected* excitations are included, which makes CC size-consistent and therefore favorable. The thus resulting excitation operators and associated coefficients in CC are called *amplitudes* and have a slightly different meaning compared to CI. In general however, a CC wave function may be cast as a CI wave function, but it does not fall into a truncation scheme like CISD. In the exact limit, both methods correspond to FCI.

The *gold standard* of quantum chemistry is considered to be the truncation after the double amplitudes and including a perturbative correction for triples: CCSD(T) [9]. It yields chemical accuracy at the complete basis set limit for most systems, but has a quite costly computational scaling of $\mathcal{O}(N^7)$.

Alternatively, for truncated CI wave functions (e.g. CISD) the Davidson correction

$$E_{\text{corr}}^{\text{D}} = E_{\text{corr}} \frac{1 - c_{\text{ref}}^2}{c_{\text{ref}}^2} \quad (2.87)$$

may be applied to achieve size consistency, where c_{ref} is the coefficient of the reference wave function. It is based on the assumption that the correlation contribution to the wave function is small and is furthermore justified empirically.

2.2.7 Weak and Strong Correlation

Although being quite successful for a large number of molecular systems, Coupled Cluster does not always yield the required accuracy. Being a *single-reference* method, it can only consider excitations that are based on just one reference configuration. In these cases a very large number of configurations with very small individual weights are covered quite well. This type of correlation is called *weak* or *dynamical* correlation.

However, there is another class of systems where no single major configuration can be identified. Examples include open-shell systems (e.g. radicals) or transition metal complexes with many (close) degenerate d orbitals. Here a smaller number of configurations with similar weights are encountered. These configurations are responsible for what is called *static* or *strong* correlation and typically differ only in a small set of orbitals. It is therefore feasible to recover strong correlation by defining a space of active orbitals for which all possible configurations are formed. All orbitals lower in energy than the active space orbitals are kept closed, i.e. doubly occupied, while virtual orbitals higher in energy than the active space orbitals are empty in all configurations. A CI calculation based on this approach is called Complete Active Space Configuration Interaction (CASCI) and recovers strong correlation, but no weak correlation effects.

An actual strict definition to separate strong and weak correlation does not exist, and a certain configuration may contribute to both types. The classification used here is closely related to Bartlett and Stanton [40] and Bartlett and Musiał [41] who considered next to dynamic (weak) and static (strong) correlation also an intermediate type called *non dynamic* correlation. Furthermore the situation depends on the type of orbitals used as a one-electron basis set. A unitary transformation of the molecular orbitals, e.g. performing a localization procedure (cf. Section 2.2.9), may switch a system from a singly-reference to a multi-reference problem, or *vice*

versa.

Both situations, weak and strong correlation, are compared in Fig. 2.1. The weakly correlated system (blue crosses) has a leading configuration with its coefficient close to 1, while the next largest coefficient is one order of magnitude smaller. On the other hand, the strongly correlated system (red circles) has a number of coefficients of similar magnitude at ≈ 0.2 . As a side note, the data shown in Fig. 2.1 is obtained from CASSCF (cf. Section 2.2.8) calculations, thus it does not represent a CI vector including all dynamic correlations. However, since there is no strict separation between both and a CAS approach will always cover some dynamic correlation, the general differences are sufficiently represented.

A CASCI calculation based on HF orbitals suffers from a bias of the orbitals towards the HF configuration. This is not of relevance for weak correlation, where the HF configuration is the single most important configuration (cf. Fig. 2.1). For static correlation where many configurations are of similar importance however, this bias may not be an optimal solution anymore. Although this bias will vanish in the FCI limit, it is unfeasible to consider the large number of configurations needed. Therefore, one typically combines the CASCI approach with the Multi-Configurational Self-Consistent Field (MCSCF) approach (cf. 2.2.8), where the CI vector and molecular orbitals are optimized simultaneously. The resulting method is called Complete Active Space Self-Consistent Field (CASSCF) and will balance the orbitals to better describe all of the major configurations.

To additionally recover weak correlation one has to generate excitations into all the virtual orbital, as is done in single-reference methods. However, generating excitations for each of the configurations responsible for strong correlation will yield different sets of configurations, which may partially overlap. Therefore a single-reference approach, which will only yield one of these sets of configurations, will miss a number of potentially important configurations for dynamical correlation. To recover dynamical correlation, it is therefore crucial to generate excitations for many configurations. This is known as the *multi-reference* approach.

Accurate calculations on strongly correlated systems are one of the hardest challenges in theoretical chemistry. The standard approach is to perform a state-averaged CASSCF calculation to qualitatively describe the static correlation con-

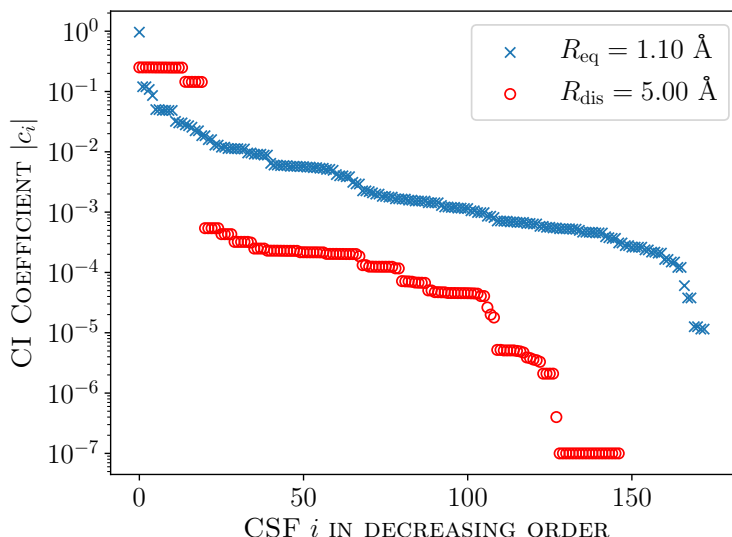


Figure 2.1: CI vector for a weakly (blue crosses) and strongly (red circles) correlated system. Data represents the CI vectors for the N_2 ground state at equilibrium distance ($R_{\text{eq}} = 1.1 \text{ \AA}$) and dissociation limit ($R_{\text{dis}} = 5.0 \text{ \AA}$), both calculated at the CASSCF(10,8)/aug-cc-pV5Z level.

tributions. Additional dynamic correlation is then recovered in a second step by a multi-reference approach which may be based on different schemes. Based on the simple CI truncation scheme Single and Double excitations may be generated for each reference configuration leading to the Multi-Reference Configuration Interaction method (MRCI-SD). Similar Coupled Cluster theory can be extended to Multi-Reference Coupled Cluster (MRCC) theory [42]. In CASPT2 [43, 44] and NEVPT [45, 46, 47] a perturbation theory based correction is added to a CASSCF or CASCI reference.

2.2.8 Multi-Configurational Self-Consistent Field

Multi-Configurational Self-Consistent Field (MCSCF) [48] describes a method where the molecular orbital coefficients C_{ij} from Eq. (2.57) are optimized simultaneously with the CI coefficients c_i from Eq. (2.82). This leads to a complex mathematical optimization problem, as the CI coefficients for the many-electron basis (configurations), depend on the molecular orbital coefficients for the one-electron basis (orbitals). Furthermore the energy of the targeted electronic state, which is min-

imized, depends on both sets of coefficients. Therefore when changing one set of coefficients the other set of coefficients will no longer be optimal, making the method numerically challenging.

Thus only a relative small set of configurations may be considered and a suitable CI truncation scheme has to be chosen. The most common variant is the Complete Active Space Self-Consistent Field (CASSCF) where an active space of orbitals is chosen within which all possible configurations are considered (cf. 2.2.7). It is also possible to restrict the excitation degree within the active space, which is called Restricted Active Space (RAS).

2.2.9 Unitary Transformation of Orbitals

The expectation value of any operator \hat{O} in its basis $|\varphi\rangle$

$$\langle\hat{O}\rangle = \langle\varphi|\hat{O}|\varphi\rangle \quad (2.88)$$

may be expanded by inserting any unitary operator $\hat{\kappa}$ with $\hat{\kappa}^\dagger\hat{\kappa} = \mathbb{1}$

$$\langle\hat{O}\rangle = \langle\varphi|\hat{\kappa}^\dagger\hat{\kappa}\hat{O}\hat{\kappa}^\dagger\hat{\kappa}|\varphi\rangle. \quad (2.89)$$

By defining the transformed basis and operator

$$\hat{\kappa}|\varphi\rangle = |\tilde{\varphi}\rangle \quad (2.90)$$

$$\hat{\kappa}\hat{O}\hat{\kappa}^\dagger = \hat{O}_\kappa \quad (2.91)$$

respectively, the transformed expectation value remains identical to the original one.

$$\langle\hat{O}\rangle = \langle\tilde{\varphi}|\hat{O}_\kappa|\tilde{\varphi}\rangle \quad (2.92)$$

$$= \langle\hat{O}_\kappa\rangle \quad (2.93)$$

Thus, if $|\varphi\rangle$ represents a set of molecular orbitals, one may introduce any unitary transformation κ resulting in a different set of orbitals, without changing the value

of any observable $\langle \hat{O} \rangle$, provided the operator is transformed accordingly.

The geometrical interpretation is easy to see in the 2- or 3-dimensional Cartesian space, \mathbb{R}^2 and \mathbb{R}^3 respectively. Here a unitary transformation corresponds to a rotation of the basis vectors along a certain axis. Any object represented in this basis changes its representation in the new, rotated basis. But the object itself remains unchanged. Due to this analogy, unitary transformations of orbitals are often called *orbital rotations*.

This degree of freedom may be exploited in quantum chemical calculations by defining additional criteria for the molecular orbitals as needed. For example, the orbitals typically obtained from a Hartree-Fock calculations are the eigenfunction of the Fock operator (cf. Eq. (2.46)) and thus diagonalize the Fock matrix \mathbf{F} . They are called *canonical orbitals*. After a CI or MCSCF calculation the orbitals may be transformed to *natural orbitals*, for which the one-particle reduced density matrix (cf. Section 2.3)) is diagonal.

Another important application is *orbital localization*. Here the otherwise delocalized, i.e. over the whole system distributed, orbitals are spatially contracted to cover only part of the system, e.g. an atom or molecular bond. Examples for such localization schemes are the method by Foster-Boys [11], where the spatial extend of orbitals is minimized or the approach by Pipek and Mezey [12] who maximize the amount of partial charges due to each orbital on the nuclei.

A further approach related to DMRG and QIT (cf. Sections 2.4.1 and 2.5.2 respectively) is the minimization of all orbital entropies [13] to allow for a compact, and thus easy to truncate, CI vector.

2.3 Density Matrices

Density matrices are an alternative representation of a wave function Ψ and thus represent a quantum state. The density matrix in its general form relates to the probability density ρ

$$\rho = |\Psi\rangle\langle\Psi|. \quad (2.94)$$

Considering $|\Psi\rangle$ as a vector, the above equation defines an outer product, thus yielding a matrix for ρ . In this form ρ explicitly depends on all (electronic) coordinates Ψ does depend on.

The wave function may be recovered from the density matrix, by applying it to any arbitrary, normalized wave function $|\tilde{\Psi}\rangle$. Representing that wave function as a linear combination of an orthonormal basis set

$$|\tilde{\Psi}\rangle = \sum_i c_i |\psi_i\rangle \quad (2.95)$$

one can write

$$\rho|\tilde{\Psi}\rangle = |\Psi\rangle\langle\Psi| \sum_i c_i |\psi_i\rangle \quad (2.96)$$

$$= |\Psi\rangle \sum_i c_i \langle\Psi|\psi_i\rangle \quad (2.97)$$

where $\langle\Psi|\psi_i\rangle$ is the complex conjugate version of projecting $|\Psi\rangle$ onto the basis functions $|\psi_i\rangle$, thus yielding the coefficients c_i^* . Together with the normalization constraint $\sum_i c_i^* c_i = 1$ this yields

$$\rho|\tilde{\Psi}\rangle = |\Psi\rangle \sum_i c_i c_i^* \quad (2.98)$$

$$= |\Psi\rangle. \quad (2.99)$$

Integration over all the coordinates of $\Psi(\vec{x}_1, \vec{x}_2 \dots \vec{x}_N)$ recovers the norm of the wave function, and can be denoted by the inner product

$$N = \int |\Psi\rangle\langle\Psi| = \langle\Psi|\Psi\rangle \quad (2.100)$$

$$= \int \Psi(\vec{x}_1, \vec{x}_2 \dots \vec{x}_N) \Psi^*(\vec{x}_1, \vec{x}_2 \dots \vec{x}_N) d\vec{x}_1 d\vec{x}_2 \dots d\vec{x}_N. \quad (2.101)$$

2.3.1 Pure and Mixed States

A quantum state can be either a *pure state*

$$|\Psi\rangle = |\psi_i\rangle \quad (2.102)$$

or a *mixed state*, i.e. a superposition of pure states

$$|\Psi\rangle = \sum_i c_i |\psi_i\rangle. \quad (2.103)$$

The density matrix is then given by

$$\rho = \sum_i c_i^* c_i |\psi_i\rangle \langle \psi_i| \quad (2.104)$$

where $p_i = c_i^* c_i$ gives the probability of observing $|\Psi\rangle$ to be in state $|\psi_i\rangle$ when measured.

Mixed states can for example arise as a statistical distribution if the system under study is in a thermal equilibrium above 0 K. There many quantum states are populated simultaneously. Another example for mixed states is considering subsystems. Even though the full system may be in a pure state, an artificial split into subsystems can lead to entanglement (cf. Section 2.5.1) between the subsystems. This is of large relevance in electronic structure theory, where the electronic wave function is usually split into subsystems of orbitals.

2.3.2 Reduced Density Matrices

Reduced Density Matrices (RDMs) are obtained by partial integration over the full density matrix in Eq. (2.101), i.e. integration over some of the coordinates is omitted. This corresponds to averaging over the respective coordinate, and thus RDMs do not cover all the information of the full density matrix. Therefore a full reconstruction of $|\Psi\rangle$, as shown in Eqs. (2.96) to (2.99), is no longer possible. They contain however important information at the level of the omitted integrations.

For example for the calculation of the expectation value of the Hamiltonian, only

the 1- and 2-particle RDMs are required. This is because it only involves one- and two-particle operators (recall that the Coulomb interaction is always just between two electrons i and j ; cf. Eq. (2.21)). Another application for RDMs is the splitting of a system into different subsystems.

In practice there are two different kinds of RDMs, which differ in the way the integration is done. Both will be presented in the following.

Particle Reduced Density Matrices

The first kind of RDMs are defined in terms of expectation values with respect to the wave function in second quantization. They are related to the number of *particles* the operator is acting on. A detailed description of this type of RDMs is given in the book by Helgaker, Jorgensen, and Olsen [32].

In second quantization a Hermitian operator including 1- and 2-electron contributions is given by

$$\hat{O} = \sum_{IJ} O_{IJ} \hat{a}_I^\dagger \hat{a}_J + \frac{1}{2} \sum_{IJKL} O_{IJKL} \hat{a}_I^\dagger \hat{a}_J^\dagger \hat{a}_K \hat{a}_L + O_0 \quad (2.105)$$

The expectation value can then be expressed as

$$\langle \Psi | \hat{O} | \Psi \rangle = \sum_{IJ} O_{IJ} \bar{\rho}_{IJ} + \frac{1}{2} \sum_{IJKL} O_{IJKL} \bar{\rho}_{IJKL} + O_0 \quad (2.106)$$

where the *1-particle RDM*

$$\bar{\rho}_{IJ} = \langle \Psi | \hat{a}_I^\dagger \hat{a}_J | \Psi \rangle \quad (2.107)$$

and the *2-particle RDM*

$$\bar{\rho}_{IJKL} = \langle \Psi | \hat{a}_I^\dagger \hat{a}_J^\dagger \hat{a}_K \hat{a}_L | \Psi \rangle \quad (2.108)$$

have been used. The bars over $\bar{\rho}$ indicate the use of spin orbitals. The last two equations can be related to the representation in coordinate space by [32]

$$\gamma_1(\vec{x}_1, \vec{x}'_1) = N \int \Psi(\vec{x}_1, \vec{x}_2 \dots \vec{x}_N) \Psi^*(\vec{x}'_1, \vec{x}_2 \dots \vec{x}_N) d\vec{x}_2 \dots d\vec{x}_N \quad (2.109)$$

$$= \sum_{IJ} \bar{\rho}_{IJ} \chi_I^*(\vec{x}'_1) \chi_J(\vec{x}_1) \quad (2.110)$$

for the 1-particle RDM and

$$\gamma_2(\vec{x}_1, \vec{x}_2, \vec{x}'_1, \vec{x}'_2) = \frac{N(N-1)}{2} \int \Psi(\vec{x}_1, \vec{x}_2, \vec{x}_3 \dots \vec{x}_N) \Psi^*(\vec{x}'_1, \vec{x}'_2, \vec{x}_3 \dots \vec{x}_N) d\vec{x}_3 \dots d\vec{x}_N \quad (2.111)$$

$$= \frac{1}{2} \sum_{IJKL} \bar{\varrho}_{IJKL} \chi_I^*(\vec{x}'_1) \chi_J(\vec{x}_1) \chi_K^*(\vec{x}'_2) \chi_L(\vec{x}_2) \quad (2.112)$$

for the 2-particle RDM. Thus they are partial integrations of Eq. (2.101), i.e. for the n -particle RDM, the integration over n coordinates is omitted. Additionally this directly highlights, how one can obtain the $n-1$ particle RDM, by integration over one of the electronic coordinates of the n -particle RDM.

The above definition for particle RDMs $\bar{\varrho}$ in spin orbital basis may be extended the spin-free version ϱ , i.e. in spatial orbital basis. For this an additional summation over the spin-indices needs to be introduced. For example

$$\varrho_{ij} = \sum_{\sigma} \langle \Psi | \hat{a}_{i\sigma}^{\dagger} \hat{a}_{j\sigma} | \Psi \rangle \quad (2.113)$$

$$\varrho_{ijkl} = \sum_{\sigma\tau} \langle \Psi | \hat{a}_{i\sigma}^{\dagger} \hat{a}_{j\tau}^{\dagger} \hat{a}_{k\tau} \hat{a}_{l\sigma} | \Psi \rangle \quad (2.114)$$

with $\sigma, \tau \in \{\alpha, \beta\}$.

Orbital Reduced Density Matrices

The other kind of RDMs considers the split of a combined quantum system into two subsystems, where one of the two subsystems, the environment, is traced out. This type of RDM is for example covered in the appendix of the book by Tannor [30].

In the context of quantum chemistry they are called *orbital* RDM, and the subsystems are groups of orbitals. Hence the summation is not over the electronic coordinates (as for the particle RDMs), but orbitals. For example the 1-orbital RDMs are obtained as the partial trace over all orbitals but orbital i .

$$\rho_i(\alpha_i, \alpha'_i) = \text{Tr}_{1, \dots, \hat{i}, \dots, d} |\Psi\rangle \langle \Psi| \quad (2.115)$$

Analogous, in the 2-orbital RDMs the trace over 2 orbitals i and j are omitted.

$$\rho_{ij}(\alpha_i, \alpha_j, \alpha'_i, \alpha'_j) = \text{Tr}_{1, \dots, \hat{i}, \dots, \hat{j}, \dots, d} |\Psi\rangle\langle\Psi| \quad (2.116)$$

Note that, while there is always just one n -particle RDM for a given state $|\Psi\rangle$, there are many orbital RDMs. Each possible combination of n orbitals yields its own orbital RDM, i.e. for a total of d orbitals, there are $\binom{d}{n}$ possible n -orbital RDMs.

The orbital RDMs can be related to the particle RDMs by recognizing that their matrix elements may be represented in terms of particle number operators. Consider a single spatial orbital i with basis states $|\phi_{\alpha_i=0}\rangle = |-\rangle$ (empty), $|\phi_{\alpha_i=1}\rangle = |\downarrow\rangle$ (spin down), $|\phi_{\alpha_i=2}\rangle = |\uparrow\rangle$ (spin up) or $|\phi_{\alpha_i=3}\rangle = |\uparrow\downarrow\rangle$ (double occupation). The diagonal elements of the corresponding 1-orbital RDM then represent the probability of these occupations, and are given by the expectation values of the following operators: $(1 - \hat{n}_{\uparrow}^{\alpha_i})(1 - \hat{n}_{\downarrow}^{\alpha_i})$ (empty), $(1 - \hat{n}_{\uparrow}^{\alpha_i})\hat{n}_{\downarrow}^{\alpha_i}$ (spin-up), $(1 - \hat{n}_{\downarrow}^{\alpha_i})\hat{n}_{\uparrow}^{\alpha_i}$ (spin-down) and $\hat{n}_{\uparrow}^{\alpha_i}\hat{n}_{\downarrow}^{\alpha_i}$ (double occupation) [49], where the superscript indicates on which orbital the operator is acting on. The off-diagonal elements are zero due to conservation of the quantum numbers for spin and particle number.

The *single electron* particle number operators $\hat{n}_{\uparrow}^{\alpha_i} = \hat{n}_{i\alpha}$ and $\hat{n}_{\downarrow} = \hat{n}_{i\beta}$ for spatial orbital i correspond to the diagonal elements of the 1-particle RDM in spin basis

$$\bar{\rho}_{II} = \langle \hat{a}_I^\dagger \hat{a}_I \rangle = \langle \hat{n}_{i\alpha} \rangle \quad (2.117)$$

$$\bar{\rho}_{JJ} = \langle \hat{a}_J^\dagger \hat{a}_J \rangle = \langle \hat{n}_{i\beta} \rangle \quad (2.118)$$

where I and J denote those two spin orbitals that correspond to spatial orbital i . The product $\hat{n}_{\uparrow}^{\alpha_i}\hat{n}_{\downarrow}^{\alpha_i}$ can be extracted from the 2-particle RDM

$$\bar{\rho}_{IJJ I} = \langle \hat{a}_I^\dagger \hat{a}_J^\dagger \hat{a}_J \hat{a}_I \rangle = \langle \hat{n}_{i\alpha} \hat{n}_{i\beta} \rangle \quad (2.119)$$

Thus all information required for the spatial 1-orbital RDMs ρ_i is included in the spin 2-particle RDM $\bar{\rho}_{pqrs}$. Similar the spatial 2-orbital RDMs may be extracted from the spin 4-particle RDM.

2.4 Beyond Standard Quantum Chemistry

This chapter has summarized so far the current standard approaches of wave function based correlation methods. These are readily implemented in a large number of (freely) available quantum chemistry packages. Beyond, there exists a number of alternative, promising ideas which give access to some further hard to treat molecular systems. Three such approaches are briefly introduced in the following. The Density Matrix Renormalization Group (DMRG) introduces a memory efficient representation of the CI vector and is a powerful method to study strongly correlated systems with large active spaces. Next, the Method of Increments (MoI) allows for a truncation at different levels of orbital correlations (1, 2, 3, *etc.* orbital correlations), which is especially useful in connection with localized orbital. And finally the Full Configuration Interaction Quantum Monte Carlo method, which stochastically samples the configuration space instead of an expensive deterministic treatment.

DMRG and FCIQMC may also be used in connection with MCSCF (cf. Section 2.2.8), where they are used as alternative CI solvers. The related methods are called DMRG-SCF [23, 24, 25, 26] and FCIQMC-SCF [27].

2.4.1 Density Matrix Renormalization Group

The Density Matrix Renormalization Group (DMRG) method was first introduced in 1992 by White [14, 15]. It is based on the renormalization group approach, which was first applied by Wilson [50] to solve the Kondo problem in solid state physics. Its basic idea is to split a physical system into subsystems and increase their size step by step, until the properties of interest are converged. In the context of quantum chemistry, DMRG splits the orbital space into small groups, usually of 2 orbitals, and optimizes those groups one after another while keeping the respective environment fixed. This allows for efficient treatment of large orbital spaces and for strongly correlated, 1-dimensional systems it usually achieves high accuracy. As a number of reviews describe the method in detail [49, 51, 52, 53, 54], only a summary will follow here.

In essence DMRG offers two key features. First, it allows for an efficient represen-

tation of the CI vector in the form of a *Matrix Product State* (MPS). Its numerical accuracy is controlled by a parameter called *number of blockstates* M , which is also known as *virtual dimensions* or *bond dimensions*. In its numerically exact limit $M \rightarrow \infty$ it corresponds to FCI, or CASCI in case of a truncated orbital space. The other extreme case with $M = 1$ yields the HF solution. The second feature is a reduced computational scaling compared to conventional FCI calculations. In FCI one constructs and diagonalizes the Hamiltonian for the whole configuration space. In DMRG an effective Hamiltonian for only a few orbitals is constructed and diagonalized. The remaining orbitals are kept fixed and represent the environment for which the current orbitals are optimized. This procedure is iteratively repeated for the various orbitals until convergence is achieved. Together, both properties allow to solve the CI problem by constructing and diagonalizing many smaller matrices instead of a single large matrix, while the numerical accuracy is controlled by the parameter M .

Singular Value Decomposition

The Singular Value Decomposition (SVD) is the mathematical tool allowing to factorize the CI vector into subsystems and controlling the accuracy when truncating the matrix dimensions of this split. It is defined as

$$\mathbf{M} = \mathbf{U}\boldsymbol{\sigma}\mathbf{V}^\dagger \quad (2.120)$$

where \mathbf{M} is a rectangular matrix with dimensions $(m \times n)$, which is factorized into the *left singular vectors* \mathbf{U} with dimensions $(m \times \min(m, n))$, *right singular vectors* \mathbf{V}^\dagger with dimensions $(\min(m, n) \times n)$ and the *singular values* $\boldsymbol{\sigma}$ with dimensions $(\min(m, n) \times \min(m, n))$.¹

The singular values $\boldsymbol{\sigma}$ may be multiplied into either \mathbf{U} or \mathbf{V}^\dagger , thus a factorization of \mathbf{M} into only two matrices is possible as well. This is also known as QR decomposition, which is numerically faster to calculate.

$$\mathbf{M} = \mathbf{Q}\mathbf{R} \quad (2.121)$$

¹The mathematical notation in this subsection follows the standard notation used to introduce the SVD and does not correspond to the notation in the rest of this thesis.

The SVD is closely related to the eigenvalue decomposition

$$\mathbf{M} = \mathbf{U}\boldsymbol{\lambda}\mathbf{U}^\dagger \quad (2.122)$$

for a square matrix \mathbf{M} (with shape $n \times n$) with eigenvectors \mathbf{U} and eigenvalues $\boldsymbol{\lambda}$.

A common approximation for both decompositions is to keep and store only a certain number M of the eigen- or singular values and its corresponding eigen- or singular vectors respectively. In case of the SVD the truncated matrices for \mathbf{U} , $\boldsymbol{\sigma}$, \mathbf{V}^\dagger will have dimensions of $(m \times \min(m, n, M))$, $(\min(m, n, M)) \times \min(m, n, M)$ and $(\min(m, n, M) \times n)$ respectively. After multiplication of these three matrices, \mathbf{M} will recover its original shape $(m \times n)$, but may deviate in its actual values depending on M . This step is also known as *low-rank tensor approximation*.

For a sufficiently small cutoff parameter M , the original Matrix \mathbf{M} can then be stored with less memory in the factorized form, while sacrificing accuracy. This is the core feature exploited in the MPS.

Matrix Product State

To achieve efficient storage of the CI wave function in computer memory, it is factorized into the Matrix Product State (MPS) by multiple application of the SVD.

To demonstrate the relationship between both, the procedure of factorizing the conventional CI wave function to the MPS is illustrated in Fig. 2.2. Starting from the CI wave function in its vector form, i.e. a tensor of order 1, it can easily be reshaped into a tensor $\mathbf{U}(\alpha_1, \dots, \alpha_d)$ whose order corresponds to the number of orbitals d . The CI wave function then becomes

$$|\Psi\rangle = \sum_{\alpha_1, \dots, \alpha_d} \mathbf{U}(\alpha_1, \dots, \alpha_d) |\phi_{\alpha_1}\rangle \otimes \dots \otimes |\phi_{\alpha_d}\rangle \quad (2.123)$$

where α_i labels the basis states of a single orbital, i.e. empty ($|\phi_{\alpha_i=0}\rangle = |-\rangle$), down-spin ($|\phi_{\alpha_i=1}\rangle = |\downarrow\rangle$), up-spin ($|\phi_{\alpha_i=2}\rangle = |\uparrow\rangle$) or double occupation ($|\phi_{\alpha_i=3}\rangle = |\uparrow\downarrow\rangle$).

Next, the tensor $\mathbf{U}(\alpha_1, \dots, \alpha_d)$ is factorized by successive application of the SVD.

Formally all indices, except the currently selected orbital i to be factorized of from the tensor, are grouped and combined into a single index, then the SVD is applied to the resulting rectangular matrix. One of the decomposed matrices ($\mathbf{A}_i(\alpha_i)$) is kept as part of the final MPS, representing the selected orbital. The other matrix describing the remaining orbitals is used for the next SVD. The process is repeated until each orbital is represented by its own matrix. A detailed description of this procedure can be found in the review by Schollwöck [52].

The original tensor $\mathbf{U}(\alpha_1, \dots, \alpha_d)$ can then be recovered as the product of all individual matrices without loss of any information.

$$\mathbf{U}(\alpha_1, \dots, \alpha_d) = \mathbf{A}_1(\alpha_1) \otimes \dots \otimes \mathbf{A}_d(\alpha_d) \quad (2.124)$$

Note that the size of the dimensions of the \mathbf{A}_i matrices of the MPS grows in powers of 4 towards the center of the orbital chain (cf. lower right part of Fig. 2.2). Thus in terms of memory, the resulting MPS is just as large the original tensor. Only the truncation by the number of blockstates M makes the MPS memory efficient. At its lower limit ($M = 1$) the MPS becomes very small in memory and the contraction back to the full tensors recovers the HF configuration only. Thus there is no entanglement between the orbitals (cf. Section 2.5.1). At its upper limit ($M \rightarrow \infty$) the FCI solution is recovered within numerical accuracy.

Historically, DMRG was formulated based on RDMs (cf. Section 2.3.2) which allow to separate a system into two subsystems. Details on this perspective are given in the review by Szalay et al. [49] and are briefly summarized here. The subsystem of current interest (A) is a set of selected orbitals, while the remaining orbitals form the environment (B). The wave function can then be expressed as

$$|\Psi\rangle = \sum_{\alpha_{(A)}} \sum_{\alpha_{(B)}} \mathbf{U}(\alpha_{(A)}, \alpha_{(B)}) |\phi_{\alpha_{(A)}}^{(A)}\rangle \otimes |\phi_{\alpha_{(B)}}^{(B)}\rangle \quad (2.125)$$

where $|\phi_{\alpha_{(A)}}^{(A)}\rangle$ and $|\phi_{\alpha_{(B)}}^{(B)}\rangle$ are the bases states for subsystems (A) and (B) respectively. It is possible to bring the last equation into the *Schmidt form* [55]

$$|\Psi\rangle = \sum_{m=1}^{r_{\text{Sch}}} \sqrt{\omega_m} |\xi_m^{(A)}\rangle \otimes |\xi_m^{(B)}\rangle \quad (2.126)$$

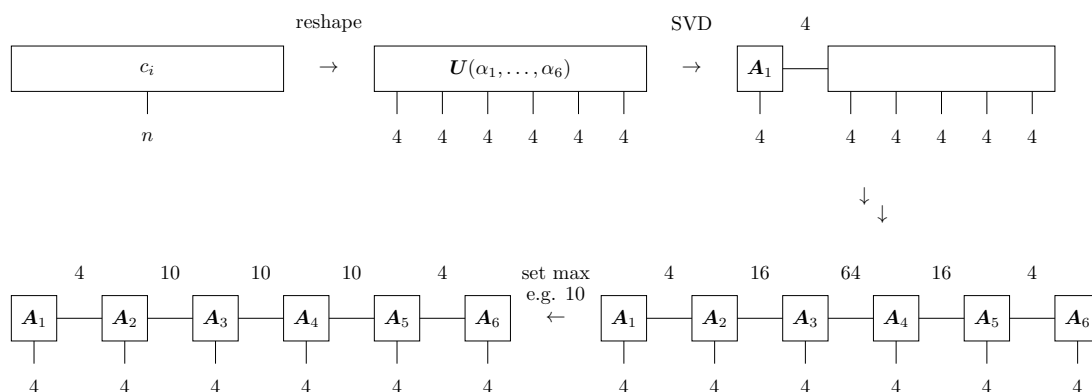


Figure 2.2: Construction of the MPS by successive application of the SVD. Each rectangle represents a tensor whose order corresponds to the number of lines connected to it. The connection of two tensors via their indices represents a matrix product. The number on an index line indicates the dimension along this index. The example factorizes a CI vector for 6 orbitals into 6 matrices in the MPS and then applies a truncation to $M = 10$ blockstates.

with $|\xi_m^{(A)}\rangle$ and $\xi_m^{(B)}\rangle$ being the orthonormal *Schmidt bases* and $\sqrt{\omega_m}$ the *Schmidt coefficients* which satisfy $0 \leq \sqrt{\omega_m} \leq 1$ and $\sum_m \sqrt{\omega_m} = 1$. The *Schmidt rank* r_{Sch} corresponds to the dimension of Hilbert space of the smaller subsystem ((A) or (B)). In essence, the Schmidt decomposition corresponds to the SVD from above, where the singular values correspond to $\sqrt{\omega_m}$ and the Schmidt rank r_{Sch} becomes the number of blockstates M .

The RDM for a subsystem of orbitals (A) is obtained by tracing the full density matrix over (B)

$$\rho^{(A)} = \text{Tr}_B |\Psi\rangle\langle\Psi| \quad (2.127)$$

which corresponds to the definition of the orbital RDMs in Eqs. (2.115) and (2.116). Together with the Schmidt form of Eq. (2.126) this leads to

$$\rho^{(A)} = \sum_{m=1} \sqrt{\omega_m} |\xi_m^{(A)}\rangle\langle\xi_m^{(A)}|. \quad (2.128)$$

This type of RDM is used to quantify entanglement (cf. Section 2.5.1) and it is easily obtained from the MPS by tracing $|\Psi\rangle\langle\Psi|$ over all orbital indices which are part of the environment (B) while skipping contraction over indices belonging to the

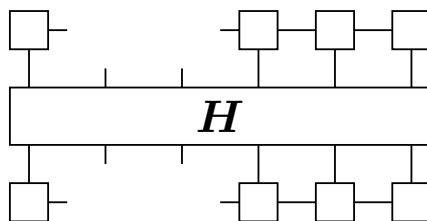


Figure 2.3: Contraction to the effective Hamiltonian by omitting 2 orbitals of the MPS in the bra- and ket-vector.

subsystem (A).

DMRG Algorithm

While the MPS itself is only a different representation of the CI vector, the term DMRG refers to an algorithm to optimize that MPS. Starting from some initial guess, the MPS is optimized iteratively for only a small subset of the orbitals. Usually 2 orbitals are optimized at once. The energy expectation value $\langle \Psi | \hat{H}^{\text{el}} | \Psi \rangle$ can be calculated by contracting the current MPS with the Hamiltonian. An effective Hamiltonian is constructed according to the usual expression for energy expectation value

$$\mathbf{H}_{\text{eff}} = \mathbf{U}^\dagger \mathbf{H} \mathbf{U} \quad (2.129)$$

but the summation over indices α_i and matrices \mathbf{A}_i of the orbitals to be optimized are omitted. A graphical representation of the effective Hamiltonian for orbitals 2 and 3 is presented in Fig. 2.3. In the 2-orbital case, the effective Hamiltonian then has maximum dimensions $((4M)^2 \times (4M)^2)$, which is usually much smaller than the Hamiltonian in the full CI space. Thus its diagonalization requires much less computational resources. The resulting eigenvector can then be factorized into the individual orbital matrices by the procedure described above, and the corresponding \mathbf{A}_i matrices in the MPS are replaced by the new ones.

The whole MPS is then optimized iteratively. Usually one starts at one end of the chain and works its way to the other end, until each orbital has been optimized at least once. As all orbitals are correlated with each other, the direction is then reversed and the algorithm sweeps back and forth through the chain until convergence

is reached.

The advantage of DMRG is thus to only diagonalize small matrices. However, one has to repeatedly construct effective Hamiltonians, diagonalize them and factorize the eigenvectors. Additionally the DMRG algorithm usually requires many iterations in order to transport the correlation information of orbitals from one end of the chain to the other. It is therefore desirable to locate orbitals strongly correlated with each other in close vicinity, while having weakly correlated orbitals sitting at the ends of the chain.

Another weakness of DMRG is dynamical correlation. This would require a large number of blockstates M as many configurations with minor individual contribution each need to be represented by the MPS. Furthermore the amount of correlation on each orbital and a larger number of pair correlations become important (cf. Figs. 4.8 and 4.9), which cannot efficiently be represented by the linear structure of the orbital chain. Static correlation however can be recovered very well and the truncation scheme is not biased towards any specific excitation class of configurations, as in the CISD scheme.

Different additional approaches are used to increase performance of the DMRG algorithm, most of them are described in the review by Szalay et al. [49]. For example the order in which the orbitals are factorized is a degree of freedom that can be optimized to place highly entangled orbitals close to each other, by calculating the Fiedler vector based on the mutual information (cf. Section 2.5.2) [49, 56]. Additionally more complex network topologies than linear chains may be considered and are subject to ongoing research [49, 57, 58, 59, 60]. Another optimization considers the construction of the initial guess for the MPS by the CI based Dynamically Extended Active Space (CI-DEAS) procedure [49, 61]. The number of blockstates M to keep can be adaptively controlled by the Dynamic Block State Selection (DBSS) approach [62, 63], where a user-defined truncation error is used. And the CI Hamiltonian may be efficiently stored and constructed in the Matrix Product Operator (MPO) form [49, 52], which is analogous to the MPS. DMRG may also be combined with coupled cluster in the so called Tailored Coupled Cluster (TCC) ansatz [16] where the coefficients for single and double excitations are extracted from the MPS and then used to “tailor” additional external amplitudes in a CC calculation.

2.4.2 The Method of Increments

The Method of Increments (MoI) was originally invented by Stoll [17, 18] in 1992. Its core idea is to expand the correlation energy in contributions of centers, where a center consists of one or more molecular orbitals. Exploiting orbital localization allows to assign each center to a single site of the system. One then starts by calculating the 1-center increments

$$\varepsilon_i = E_i - E_{\text{HF}} \quad (2.130)$$

which correlates only a single center of occupied orbitals with the whole virtual orbital space. Correlations between two centers i and j are not considered at this step. Instead, this is recovered in a second step by combining both centers in one calculation

$$\varepsilon_{ij} = E_{ij} - E_{\text{HF}} \quad (2.131)$$

and then calculating the 2-center increments by subtracting the already accounted for 1-center increments

$$\Delta\varepsilon_{ij} = \varepsilon_{ij} - \varepsilon_i - \varepsilon_j. \quad (2.132)$$

A graphical representation for calculating the 1- and 2-center energies is provided by Fig. 2.4, labeled as E_i^{occ} and E_{ij}^{occ} respectively. The procedure is then continued with the next level of increments, e.g. the 3-center increments are given by

$$\varepsilon_{ijk} = E_{ijk} - E_{\text{HF}} \quad (2.133)$$

$$\Delta\varepsilon_{ijk} = \varepsilon_{ijk} - \Delta\varepsilon_{ij} - \Delta\varepsilon_{ik} - \Delta\varepsilon_{jk} - \varepsilon_i - \varepsilon_j - \varepsilon_k. \quad (2.134)$$

and so on. The exact correlation energy at the FCI level is then recovered when performing the complete expansion until all centers are included in a single calculation.

$$E_{\text{corr}} = \sum_i \varepsilon_i + \sum_i \sum_{j>i} \Delta\varepsilon_{ij} + \sum_i \sum_{j>i} \sum_{k>j} \Delta\varepsilon_{ijk} + \dots \quad (2.135)$$

In practice however, the truncation is cut once converged to sufficient accuracy. This exploits the fact that multi-center correlations typically decrease the more centers are combined.

Using localized orbitals additionally allows for *a priori* selection of centers which

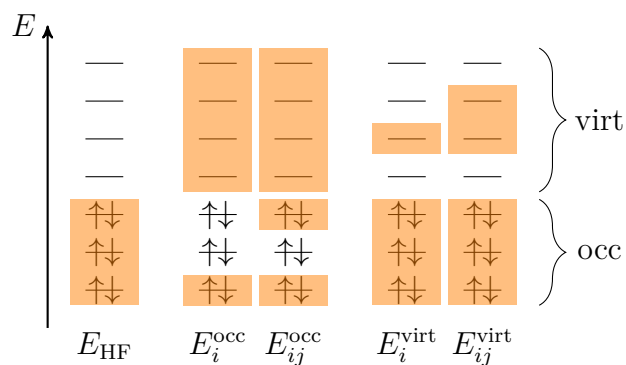


Figure 2.4: Molecular orbital scheme for the MoI expansion. Arrows indicate orbital occupation of the HF configuration, while the colored rectangles indicate the active space for each calculation, i.e. which orbitals are available for the construction of Slater determinants. Here it is assumed, that each center corresponds to a single orbital.

are spatially close to each other. Centers far away from each other typically result in negligible increments.

Another interesting approach has been recently presented by Eriksen, Lipparini, and Gauss [64], who did not develop the correlation energy in centers of occupied orbitals, but in centers of virtual orbitals instead, as indicated by E_i^{virt} and E_{ij}^{virt} in Fig. 2.4. The basic idea here is that the number of virtual orbitals is usually much larger than the number of occupied orbital. Thus correlating a small number of virtual orbitals (centers) with the whole occupied orbital space leads to much smaller active spaces for each individual increment. Although at the same time this leads to a much larger number of increments to be calculated, the reduced computational effort of the individual calculations outweighs their number. Additionally, neglecting a number of virtual increments can be considered.

2.4.3 Quantum Monte Carlo

Another class of methods, which can be found in various fields, is Monte Carlo Sampling. Instead of explicitly considering all possible contributions to a problem, they are randomly sampled and the final result is inferred from that data. For example the conventional approach for obtaining numerical integrals, is to split the argument space into a grid. For each grid point the contribution to the overall

area is approximated by a simple shape with known area law, e.g. rectangles. The overall result is then obtained by summing the contributions from each grid point. Especially for high dimensional functions, the number of grid points grows rapidly and becomes computationally costly to evaluate. Monte Carlo sampling reduces this computational cost by not considering every individual contribution, but by randomly choosing only a subset of them. Provided this subset is statistically representative of the whole set, the average contribution from each sampled grid point corresponds to the full solution.

Another common approach is to sample probability distributions by random walks. A walker, whose attributes define the state of a physical system, moves in a time dependent simulation through the space of all states. Depending on the transition probability between states, and a randomly chosen number, the walker may move from one state to another at each time step, or not. If a large enough number of walkers are used, and the system reaches equilibrium, then the overall distribution of all walkers will not change anymore, and the time-dependent simulation is converged.

In Diffusion Monte Carlo (DMC) [19] the imaginary-time Schrödinger equation for such a simulation is given by

$$\frac{\partial \Psi}{\partial \tau} = -\hat{H}\Psi \quad (2.136)$$

where $\tau = it$. The wave function $\Psi(\tau)$ at time step τ is proportional to the starting wave function $\Psi(\tau = 0)$

$$\Psi(\tau) \propto e^{-\tau \hat{H}} \Psi(\tau = 0) \quad (2.137)$$

For the initial wave function one may choose for example the Hartree-Fock ground state $\Psi(\tau = 0) = \Psi_{\text{HF}}$. In the long-limit the exponential term will project out all excited states and leave the electronic ground state Φ_0

$$\Phi_0 = \lim_{\tau \rightarrow \infty} e^{-\tau(\hat{H}-E_0)} \Psi_{\text{HF}}. \quad (2.138)$$

The proportionality constant $e^{\tau E_0}$ is introduced to keep the ground state from decaying as well.

Full Configuration Interaction Quantum Monte Carlo

Similar to DMC, in Full Configuration Interaction Quantum Monte Carlo (FCIQMC) the Schrödinger equation is propagated in imaginary time. However the wave function is represented in configuration space. The method will be briefly summarized in the following. For further details, please refer to the original publication by Booth, Thom, and Alavi [20].

In FCIQMC configurations are represented by walkers. And the amount of walkers N_i on each configuration corresponds to the coefficient c_i of the FCI method.

$$c_i \propto N_i \quad (2.139)$$

The use of determinants ensures the wave function is antisymmetric according to the Pauli principle. Furthermore, the walker population on each determinant may have a negative sign. The coupling between two determinants $|i\rangle$ and $|j\rangle$ via the Hamiltonian

$$K_{ij} = \langle i | \hat{H} | j \rangle - E_{\text{HF}} \delta_{ij} \quad (2.140)$$

gives the transition probability between the configurations (states) i and j , and thus determines the propagation of the (initial) walker distribution. Together with the imaginary-time Schrödinger equation Eq. (2.136) and using determinants as a basis set this yields a set of coupled differential equations

$$-\frac{dc_i}{d\tau} = (K_{ii} - S)c_i + \sum_{j \neq i} K_{ij}c_j \quad (2.141)$$

where S is an energy shift parameter which will control the population growth.

The above equation is solved by an algorithm that evolves a population of walkers until an equilibrium is reached. The algorithm consists of three steps for each iteration. First, each walker may spawn new child walkers on a coupled determinant with a certain probability. The second step considers cloning and death events of walkers on their current determinant. Those two steps are independent from walker populations on other determinants and may thus be executed in parallel without loss of performance due to communication overhead. The final iteration step sums over all walker contributions (spawned, cloned and old parents) and thus annihilates

populations with different sign on the same configuration.

The energy shift parameter S controls the total number of walkers. By definition it represents the correlation energy once a the walker population achieves equilibrium close to the electronic ground state. Values for S larger than the correlation energy will lead to an increase of the number of walkers, while a value smaller than the correlation energy decreases the number of walkers. An algorithm may therefore control the value of S such that the number of walkers is kept constant at a user defined target number. A typical FCIQMC calculation thus starts with some fixed value larger than the correlation energy, e.g. $S = 0$, and propagates the walker population until the predefined number of walkers is reached. The following iterations will then try to vary S such that the number of walkers is kept constant. Once an equilibrium distribution of walkers is reached, the energy shift will correspond to the correlation energy.

In practice however, exact equilibrium will not be reached. Instead the walker distribution will fluctuate around the exact solution. Accordingly, the energy shift will oscillate around the correlation energy, which can then be approximated as the mean energy shift over many iterations. Since the fluctuation in the walker distribution is not completely random, but each step directly depends on the previous iteration, the sampled data points are correlated and direct averaging may be biased. This can be avoided by performing a reblocking analysis [65] of the correlated data.

Another measure for the correlation energy is obtained by the projection

$$E(\tau) = \frac{\langle \Psi_{\text{HF}} | \hat{H} e^{-\tau \hat{H}} | \Psi_{\text{HF}} \rangle}{\langle \Psi_{\text{HF}} | e^{-\tau \hat{H}} | \Psi_{\text{HF}} \rangle} \quad (2.142)$$

which may be rearranged to [20]

$$E(\tau) = E_{\text{HF}} + \sum_{j \in \{\text{singles}, \text{doubles}\}} \langle j | \hat{H} | \Psi_{\text{HF}} \rangle \frac{N_j(\tau)}{N_{\text{HF}}(\tau)}. \quad (2.143)$$

It is fast to evaluate since it only depends on single and double excitations. The projected energy may be improved by choosing a different trial wave function than the HF configuration. Typically a small subspace of configurations is evaluated deterministically to yield such a trial wave function. Similar to the energy shift, the

projected energy will oscillate with the walker population and a mean value over many iterations needs to be considered for the final result.

The advantage of the FCIQMC approach lies in the amount of walkers. Although a critical amount of walkers which depends on the system under study is required, this is usually much smaller than the number of configurations that needs to be considered in the conventional FCI approach. The main reason is, that in FCIQMC not all determinants with minor contributions are populated by walkers in every time step. Instantaneously, only a subset of them is populated, however all of them remain accessible in the next propagation step [66]. An *a priori* choice of configurations to include is therefore not necessary. This is a feature common to FCIQMC and DMRG and an important ingredient for a black box method. In contrast to FCIQMC, DMRG will however still completely neglect small contributions due to the low-rank tensor approximation. DMRG is thus not suited for dynamic correlation unless a very large number of blockstates is kept, while FCIQMC is able to treat it.

An extension to FCIQMC is the initiator-FCIQMC method, which allows to reduce the number of walkers required [66, 67]. An additional rule is introduced, which classifies certain configurations as an initiator. Only initiators are allowed to spawn walker populations on previously unoccupied determinants. This allows to keep the overall sign of the wave function well-defined and controlled, which would otherwise result in large amount of noise in the walker population. A related, further extension introduces so called super-initiators [68], where all populations spawned by a super-initiator are considered initiators. Finally, the semi-stochastic extension [69, 70] divides the configuration space in two sets: Here, the stochastic error is reduced by exact, deterministic treatment of the first set covering the most important configurations, while treatment of the other set remains stochastic.

2.5 Quantifying Electron Correlation

While weak correlation can be very well treated using Coupled-Cluster methods, e.g. CCSD(T), strong correlation can be quite challenging. The necessity to treat multiple dominant configurations on the same foundation is typically met by the CASSCF method, i.e. choosing an active space of orbitals to construct the configu-

rations and then optimize them simultaneously with the orbital coefficients, which reduces the initial bias of the orbitals towards the HF starting point. Large, more complex systems however require large active spaces. And the computational scaling of the active space is in principle equivalent to the FCI method. Therefore each orbital that may be removed from the active space yields large computational savings. Measures to quantitatively determine the importance of each orbital to the (strong) correlation is therefore desirable.

2.5.1 Quantum Entanglement

In quantum mechanics a physical system is described by a wave function. If the system is composed of two (or more) particles, and those particles do not interact with each other, the particles may be considered individually. Each particle then has its own independent wave function and the total wave function for the combined system is given by the product of the single-particle wave functions. If the particles however do interact, e.g. electrons via the Coulomb force, those particles become *entangled*, and a simple product ansatz is insufficient for a correct description of the total system.

Entanglement can be represented by density matrices as already shown in Eq. (2.104). Each state $|\phi_i\rangle$ is then associated with a weight, or probability, $p_i = c_i^* c_i$, which is normalized to $\sum_i p_i = 1$. If only one state is populated, i.e. there is a single non-zero $p_i = 1$, the system is unentangled.

A general state may be split into subsystems according to Eq. (2.127), after defining the corresponding subsystems. Even if the overall state of the combined system is pure, the resulting RDMs for both subsystems may be in mixed states.

In the context of quantum chemistry, the combined system is the electronic state which is split into entangled orbitals. In HF theory these orbitals are considered to be unentangled, or pure, justifying the product ansatz for the wave function. The CI ansatz then introduces the possibility of the previously unentangled orbitals to be mixed, and therefore recovers the correlation energy. The term electron correlation however is defined as an energy (difference) (cf. Eq. (2.63)), while entanglement measures how pure or mixed a state is. Both concepts will be further elucidated in

the following.

Note that, while the correlation of electrons due to the Coulomb interaction is physical, orbital entanglement is not. Splitting the electronic wave function into orbitals is an abstract mathematical tool. And different splits (sets of orbitals) are possible, e.g. canonical, localized or natural orbitals (cf. Section 2.2.9). Thus the orbital picture is artificial and therefore entanglement between orbitals is artificial as well, i.e. it cannot be measured experimentally. As a consequence the analysis of correlation effects remains a purely theoretical tool.

2.5.2 Quantum Information Theory

The field of information theory was introduced by Shannon in 1948 [71, 72] and is a mathematical framework to study information in communication and data storage. It serves as a foundation for data compression as well as efficient encoding and transmission of messages. Information theory is thus crucial for many applications of modern information technology including mobile phones, money and trade transactions, the Internet in general or even communication with space probes where bandwidth is often very limited. It has been applied in various fields, including molecular information theory [73], linguistics [74] or black holes in astrophysics [75, 76].

The central quantity in information theory is the *Shannon entropy*

$$H(\mathbf{X}) = - \sum_{i=1}^n P(x_i) \log_b P(x_i) \quad (2.144)$$

where $\mathbf{X} = \{x_i\}$ is a set of discrete variables and $P(x_i)$ a classical probability distribution function. The basis b of the logarithm may be chosen arbitrarily, but typical choices are the natural ($b = e$), binary ($b = 2$) or decimal ($b = 10$) logarithm.

The Shannon entropy measures how much information with a certain occurrence of x_i is associated. Consider for example a coin toss, i.e. a binary random variable x_1 with probability $P(x_1)$ being equal to 1, and a second variable x_0 with probability $P(x_0) = 1 - P(x_1)$ being equal to 1. The corresponding Shannon entropy is plotted in

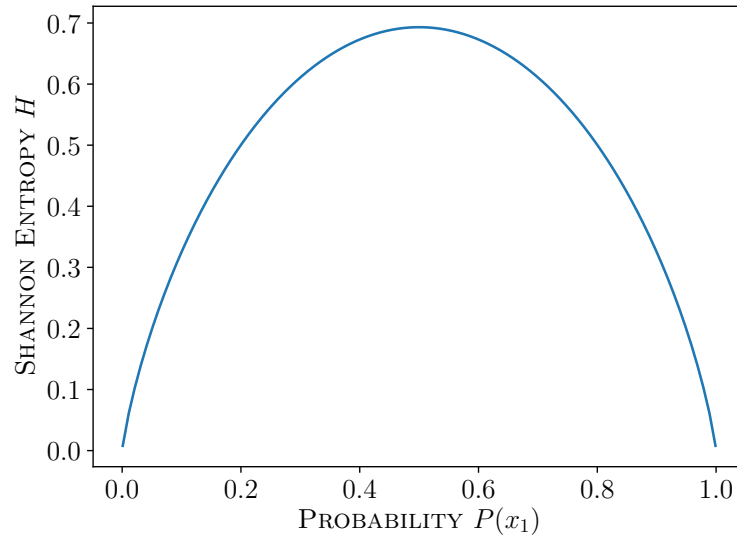


Figure 2.5: Shannon Entropy of a binary random variable x_1 with probability $P(x_1)$ being equal to 1. The maximum value $H = \ln 2$ corresponds to a fair coin toss, with heads and tail being equally likely ($P(x_1) = 0.5$). The minimum values $H = 0$ correspond to a rigged coin with two equal sides ($P(x_1) = 0$ or $P(x_1) = 1$), where the outcome is predefined.

Fig. 2.5 as a function of $P(x_1)$. For a fair coin toss maximum entropy with $H = \ln 2$ is reached, because both results, heads and tails, are equally likely ($P(x_1) = 0.5$) and impossible to predict. For a rigged coin with two equal side, either heads or tails, the entropy reaches $H = 0$ as the outcome is predefined and no information is obtained from the toss. Values in between would represent a magical coin, where increasing entropy means a gamble on the result of a toss would be increasingly harder to win.

The form of the Shannon entropy in Eq. (2.144) is very similar to the thermodynamic Gibbs entropy

$$S_G = -k_B \sum_i p_i \ln p_i \quad (2.145)$$

with the Boltzmann's constant k_B and the probability p_i of the i -th microstate. This connection may be interpreted as the amount of information available on the microstates a given macrostate is constituted of.

The actual functional form for the entropy has some degree of freedom. A more

general version is the Rényi entropy [77]

$$H_\alpha(\mathbf{X}) = \frac{1}{1-\alpha} \log \left(\sum_{i=1}^n P(x_i)^\alpha \right) \quad (2.146)$$

where α is a free parameter with $\alpha \geq 0$ and $\alpha \neq 1$. In the limit of $\alpha \rightarrow 1$ the Shannon entropy is obtained.

In quantum mechanics, information theory is used to quantify the entanglement of quantum states. Instead of a classical distribution function $P(x_i)$, a quantum state is described by a density matrix ρ (cf. Section 2.3). Accordingly, Quantum Information Theory (QIT) defines the von Neumann entropy [28, 78]

$$S(\rho) = -\text{Tr}(\rho \ln \rho) = -\sum_i \omega_i \ln \omega_i. \quad (2.147)$$

It measures how much an entangled state is distributed among its pure eigenstates $|\phi_i\rangle$ by considering the amplitudes (eigenvalues) ω_i .

In quantum chemistry, QIT can be used to quantify the entanglement of the orbitals in the molecular system. As mentioned before, this entanglement is related to the orbital picture (cf. Section 2.2.2), an artificial split of the many-electron wave function into subsystems. The CI wave function describes how to mix (entangle) these orbitals back together, to achieve a more physical description of the electronic state. It therefore depends on the choice of the one-electron basis from which the configuration space is constructed. Any unitary transformation (cf. Section 2.2.9) in the orbital space, will therefore result in different entropies.

A QIT analysis is thus based on a CI wave function, and a quantum chemical calculation is required first. Following the notation from the DMRG section (cf. Section 2.4.1) the CI vector may be reshaped into a tensor $\mathbf{U}(\alpha_1, \dots, \alpha_d)$ of order d , which corresponds to the number of (active) orbitals, labeled i and j in the following. Each index d_i goes over the four possible occupations a spatial orbital can adopt for the different electron configurations: $|-\rangle$, $|\downarrow\rangle$, $|\uparrow\rangle$ and $|\uparrow\downarrow\rangle$. Working with spin orbitals is possible as well and would give a tensor of order $2d$ with only two occupations each.

Next, the n -orbital RDMs are calculated by tracing over all but n orbitals. With the

above definition of $\mathbf{U}(\alpha_1, \dots, \alpha_d)$ in Eq. (2.123), the 1-orbital RDMs of Eq. (2.115) becomes

$$\rho_i(\alpha_i, \alpha'_i) = \sum_{\alpha_1, \dots, \alpha_i, \dots, \alpha_d} \mathbf{U}(\alpha_1, \dots, \alpha_i, \dots, \alpha_d) \overline{\mathbf{U}(\alpha_1, \dots, \alpha'_i, \dots, \alpha_d)}, \quad (2.148)$$

while the 2-orbital RDMs of Eq. (2.116) becomes

$$\rho_{ij}(\alpha_i, \alpha_j, \alpha'_i, \alpha'_j) = \sum_{\alpha_1, \dots, \alpha_i, \alpha_j, \dots, \alpha_d} \mathbf{U}(\alpha_1, \dots, \alpha_i, \alpha_j, \dots, \alpha_d) \overline{\mathbf{U}(\alpha_1, \dots, \alpha'_i, \alpha'_j, \dots, \alpha_d)}, \quad (2.149)$$

The entanglement of each orbital-RDM is then obtained by first diagonalizing it. In quantum chemistry the 1-orbital RDMs are already diagonal due to particle and spin quantum number conservation. Then the n -orbital von Neumann entropy [61, 79] is calculated from all eigenvalues $\{\omega\}$. For example the 1-orbital entropy S_i and 2-orbital entropy S_{ij} are given by

$$S_i = -\text{Tr}(\rho_i \ln \rho_i) = -\sum_{\alpha} \omega_{i,\alpha} \ln \omega_{i,\alpha} \quad (2.150)$$

$$S_{ij} = -\text{Tr}(\rho_{ij} \ln \rho_{ij}) = -\sum_{\alpha} \omega_{ij,\alpha} \ln \omega_{ij,\alpha} \quad (2.151)$$

where the summation index α enumerates the 4^n eigenvalues of each n -orbital RDM.

For an intuitive understanding consider the two extreme cases of no entanglement and maximum entanglement. In the first case only one of the four occupations is relevant, e.g. $\omega_{i,0} = 1$ and $\omega_{i,1} = \omega_{i,2} = \omega_{i,3} = 0$. Then Eq. (2.150) becomes $S_i = -1 \ln 1 - 3 \times (0 \ln 0) = 0$. On the other hand, maximum entanglement is reached when all possible occupations are of equal relevance, i.e. $\omega_{i,\alpha} = 0.25$ for all α , which gives $S_i = -4 \times 0.25 \times \ln 0.25 = \ln 4 \approx 1.39$. The von Neumann entropy thus quantifies the amount of entanglement between the subsystem represented by the corresponding RDM and the rest of the system (environment). This also means the amount of entanglement between two orbitals i and j is not covered by the 2-orbital entropy S_{ij} , while the two 1-orbital entropies S_i and S_j account for it. Thus the mutual information I_{ij} can be defined as [80]

$$I_{ij} = S_i + S_j - S_{ij}. \quad (2.152)$$

Furthermore one can define the *total correlation*

$$I_{\text{tot}} = \sum_i S_i \quad (2.153)$$

of the wave function [63, 81].

To consider any arbitrary number of orbitals and their entanglement, the concept of the mutual information may be generalized to the ξ -*correlation* [81]. Here ξ denotes a chosen subset of orbitals, e.g. for $\xi = \{i, j\}$ the ξ -correlation corresponds to the mutual information. The combined subsystem of all ξ is then represented by the RDM ρ_L and the individual one-orbital RDMs are ρ_X for $X \in \xi$. The ξ -correlation is then given by

$$C_\xi(\rho_L) = \sum_{X \in \xi} S(\rho_X) - S(\rho_L) \quad (2.154)$$

2.5.3 Increments vs. Entropies

As an alternative measure to QIT one can consider the energy increments introduced by the Methods of Increments (cf. Section 2.4.2). By assigning each orbital to its own center, the corresponding increments may be directly interpreted as correlation measures. The 1-orbital increments ε_i may thus be associated with the 1-orbital entropy S_i , while the 2-orbital increments $\Delta\varepsilon_{ij}$ correspond to the mutual information I_{ij} .

However, both measures have very different definitions and therefore cannot directly be related. Although the equations to obtain the mutual information and 2-orbital increments, cf. Eqs. (2.132) and (2.152) respectively, are quite similar and might suggest a deep relationship, the generalizations of these equations to higher order orbital correlations, cf. Eqs. (2.134) and (2.154) respectively, deviate from each other. Furthermore, the increment measures are in units of energy and are obtained by applying the same Hamiltonian to different truncations of the CI space. On the other hand, the entropy measures consider the distribution of state occupations in each subsystem by applying a logarithmic function, and are thus dimensionless. Finally, the “mixedness” of a state, does not directly relate to its energy expectation value and thus the occupation number of an orbital does not tell much about its

contribution to the correlation energy. A systematic connection between increments and entropies does therefore not exist.

Another important point is the setup of many individual calculations for the incremental approach, making each increment agnostic of the correlation effects of other increments on its level. For example $\Delta\varepsilon_i$ is not correlated with $\Delta\varepsilon_j$, this may only be recovered by considering 2-orbital increments. The entropies however may be extracted from a single calculation, correlating all orbitals at once (e.g. CASCI or DMRG), thus all 1-orbital entropies are correlated with each other. Nevertheless one may obtain entropies based on an incremental approach as well, again making them agnostic to each other. The advantage here would be of computational efficiency only.

A drawback of the original MoI scheme is the restriction to closed shell systems as it is unclear whether to assign singly occupied orbitals to the set of occupied or virtual orbitals. Application of the MoI to systems with only one unpaired electron has been summarized and demonstrated Müller and Paulus [82], where the expansion Eq. (2.135) has been modified. This however is not possible for more than a single unpaired electron. Although the individual incremental calculations may be setup and calculated, they will not yield a meaning full total correlation energy.

The second drawback of MoI is, that it does not provide a correlation measure for groups of orbitals consisting of occupied and virtual orbital at the same time. The expansion is either in terms of occupied orbitals, or in terms of virtual orbitals. For example the structure of the ε_{ij} matrix is block diagonal, with the off-diagonal block missing.

3 Molecular Model Systems

For the purpose of testing and analyzing new approaches for correlation methods, suitable model systems are required. Common model systems in the physics community are for example Heisenberg spin chains [83] or the Hubbard Model [84]. Their simplicity allows for systematic and controllable test cases where solutions on different levels of theory are easily accessible.

The focus of this thesis is to evaluate the application of existing wave function based correlation methods, as well as systematic approximations to them, to more realistic, chemical systems. As dynamically correlated systems are usually well describe by Coupled Cluster methods, the main interest here are strongly correlated systems. Within the scope of this work, the term *model* refers to the set of orbitals passed to the CI method, i.e. the one- and two-electron integrals in MO basis (cf. Eqs. (2.72) and (2.73) respectively), typically collected in a file called `FCIDUMP`. This chapter will therefore present the chosen model systems in their chemical background as well as which numerical parameter are used to yield the orbitals used for the calculations presented in Chapter 4.

3.1 Dissociation of N_2/N_2^+

The dissociation of N_2 is a common test case for strong correlation methods. Two examples that cover the application of new methods to N_2 are the FCIQMC method [20] and the DMRG based tailored coupled cluster approach (DMRG-TCCSD) [16].

Various studies investigated the electronic structure by means of *ab initio* calcula-

tions [85, 86, 87, 88]. A broad range of experimental studies using different spectroscopic approaches are available as well [88, 89, 90, 91, 92, 93].

The small number of atoms and the high symmetry of the system results in molecular orbitals that are easily interpreted. They may be classified as σ or π bonds as well as bonding or anti-bonding orbitals. A schematic molecular orbital diagram depicting those orbitals and the HF configuration is shown in Fig. 3.1. It is therefore a suitable system to study correlation effects and interpret them with respect to a basic chemical concept of bonding situations. Being a small system, in number of electrons, also allows for a highly accurate treatment with the standard multi-reference methods. N_2 is indeed a single-reference problem around equilibrium distance, i.e. the bonding regime, but strong correlation becomes increasingly important towards the limit of the dissociated fragments. This is evident from Fig. 3.2 (lower panel), which plots the CI coefficients and their magnitudes (see also Fig. 2.1).

While the N_2 is still a relatively simple system, a more complex electronic structure is found in the open-shell N_2^+ species. In its excited $B^2\Sigma_u^+$ one can even find a change of the leading configuration during bond stretching (cf. Fig. 3.2).

Optimized molecular orbitals are obtained on the CASSCF(10,8)/aug-cc-pV5Z and CASSCF(9,8)/aug-cc-pV5Z level, for N_2 and N_2^+ respectively, using MOLPRO [94, 95, 96]. As a reference covering strong and weak correlation simultaneously, subsequent MRCI-SD calculations have been performed and compared with DMRG results [97]. As the dissociation energies on the MRCI level agree with literature values [97], the obtained orbitals represent a data set of a realistic chemical systems.

The Potential Energy Surfaces (PES) for the three states under investigation, the N_2 ground state ($X^1\Sigma_g^+$), N_2^+ ground state ($X^2\Sigma_g^+$) and N_2^+ excited state ($B^2\Sigma_u^+$) as a function of the internuclear distance R are presented in Fig. 3.3. The major contributions to the CI vectors at the MRCI-SD level are plotted in Fig. 3.2. All three states show typical single-reference behavior at equilibrium distance and pronounced multi-reference character at the dissociation limit. The excited $B^2\Sigma_u^+$ state of N_2^+ is distinguished by a change of the leading configuration at $R \approx 1.4 \text{ \AA}$.

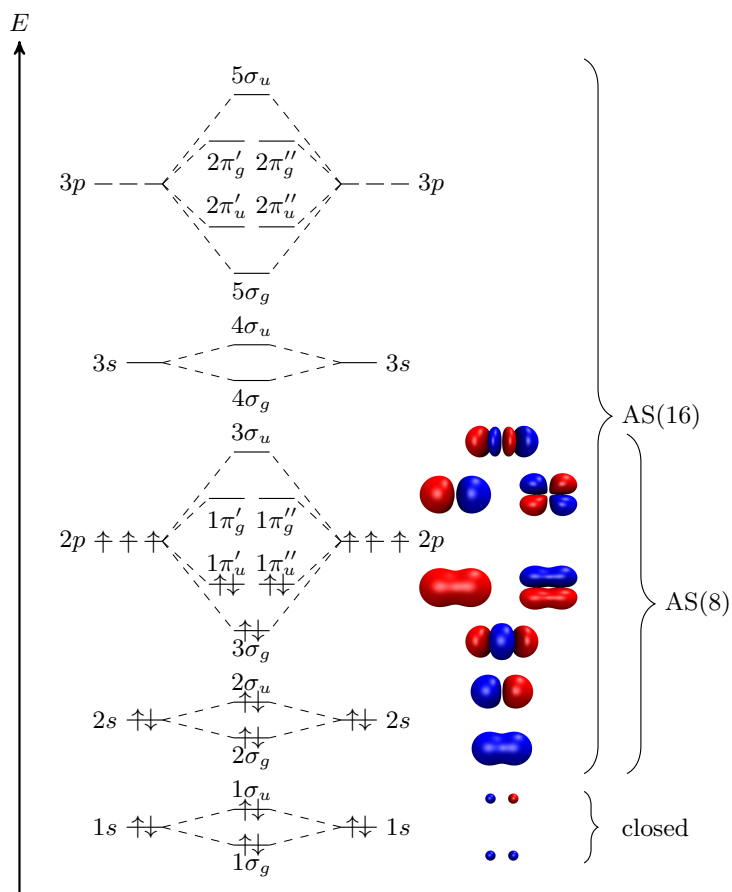


Figure 3.1: Schematic Molecular Orbital diagram showing the Hartree-Fock configuration of N_2 ($X^1\Sigma_g^+$) and its molecular orbitals. Figure adopted from Ref. [97].

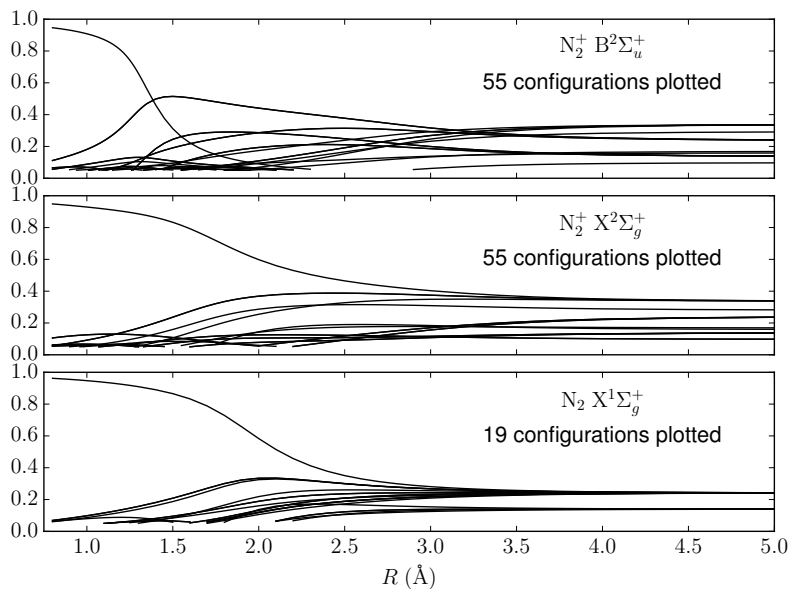


Figure 3.2: Leading contributions to the CI vector for N_2 ($X^1\Sigma_g^+$), N_2^+ ($X^2\Sigma_g^+$) and N_2^+ ($B^2\Sigma_u^+$) as a function of internuclear distance R . The plotted values are the absolute values of the MRCI coefficients $|c_i| \geq 0.05$. Figure adopted from Ref. [97].

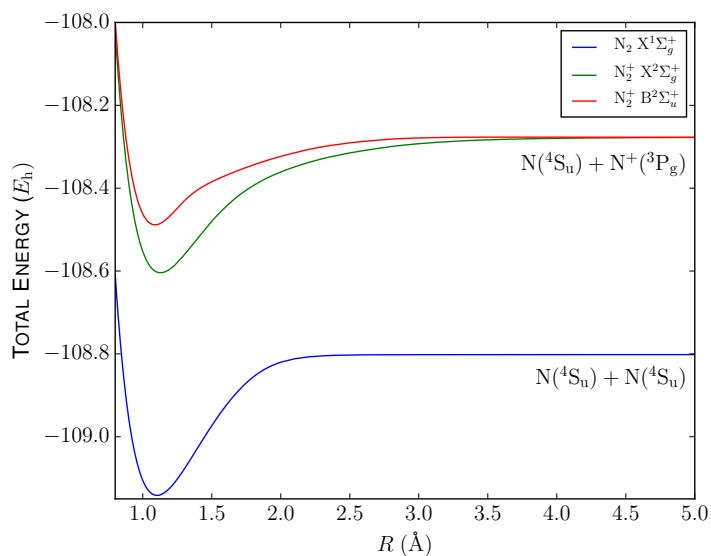


Figure 3.3: Potential Energy Surfaces (PES) for N_2 ($X^1\Sigma_g^+$), N_2^+ ($X^2\Sigma_g^+$) and N_2^+ ($B^2\Sigma_u^+$) as a function of internuclear distance R . Calculated on the CASSCF(10,8)/aug-cc-pV5Z and CASSCF(9,8)/aug-cc-pV5Z level for N_2 and N_2^+ respectively. The atomic states of the fragments are given for each dissociation limit. Figure adopted from Ref. [97].

3.2 Polyacetylene

The hexatriene (C_6H_8) molecule provides a simple model system including C–H and C–C σ bonds as well as C=C π bonds. Thus different bonding situations may be compared. A previous MoI study showed it is possible to distinguish between the different bonds by comparing the increments [98].

The linear structure of conjugated *trans*-polyacetylene may easily be extended to yield longer model systems, where similar results are to be expected. Here, the hexatriene is chosen, as it provides spatially separated double bonds while still being fairly small in number of orbitals. Localizing the occupied molecular orbitals yields a set of orbitals corresponding to the above mentioned bonds, thus allowing an intuitive chemical interpretation of the correlation effects.

For the calculations a geometry with all bond angles fixed at 120° is assumed. The bond distances are set to 145 pm for C–C bonds, 136 pm for C=C bonds and 109 pm for C–H bonds.

The model system is based on Hartree-Fock calculations using the cc-pVTZ basis set [99]. Pipek-Mezey [12] localization was applied for all occupied orbitals, while the virtual orbitals remain unchanged. Next an active space is selected, by excluding the 6 1s carbon core orbitals and then selecting all orbitals arising from the carbon 2sp and hydrogen 1s shells. This yields 32 electrons in 32 orbitals, i.e. a CAS(32,32).

3.3 Be₆ Rings

Beryllium features a close degeneracy between its doubly occupied 2s shell and empty 2p shell, a situation with potentially large correlation effects. Furthermore, the small number of electrons allows to construct molecular system of varying sizes, suitable for benchmark calculations with highly accurate methods.

One of such model systems are Be₆ rings in D_{6h} symmetry. Previous studies investigated its metal-insulator-transition during bond stretch by means of DMRG [100] and considered different basis sets and correlation methods for the incremental

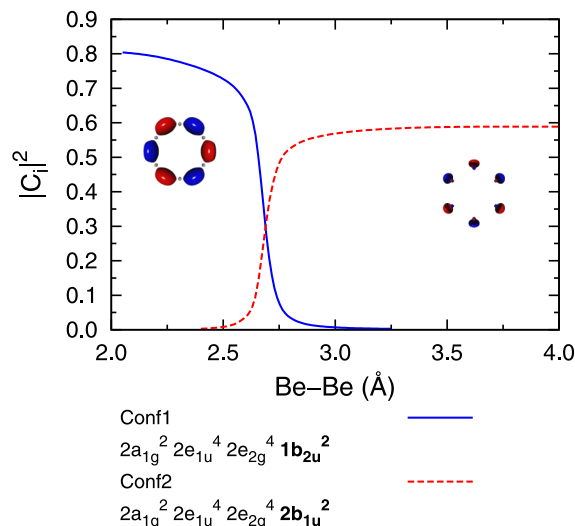


Figure 3.4: Weights of the two leading configurations of the ground state of the Be_6 ring calculated with a RAS(4,24) calculation employing a minimal basis set. The valence occupations are given beneath in terms of the molecular orbitals in D_{6h} symmetry. In the insets, depictions of the $1b_{2u}$ (left) and $2b_{1u}$ (right) orbitals are shown. Reprinted from Ref. [101], with the permission of AIP Publishing.

expansion [101]. The electronic ground state is dominated by 2 different configurations as shown in Fig. 3.4. The first configuration describes the equilibrium distance ($R = 2.2 \text{ \AA}$) and the other one the dissociation limit ($R = 3.5 \text{ \AA}$) [100].

The molecular orbitals for the model are based on Hartree-Fock calculation using the cc-pVDZ basis set [99]. Additionally, all occupied and all virtual molecular orbitals are localized according to the Foster-Boys scheme [11]. Due to the D_{6h} symmetry of the nuclear geometry, all localized orbitals show up in groups of 6 degenerate orbitals, which may be transformed into each other by applying C_6 rotations around the z axis perpendicular to the molecular plane. Especially for elongated internuclear distances R , this yields a strongly correlated system.

The active space is selected by excluding the $1s$ core orbitals of each Be atom, thus 6 occupied molecular orbitals with 12 electrons remain in the active space. Additionally, all localized virtual orbital will be considered.

Table 3.1: Thermochemistry for different decomposition pathways of CoF_4 and CoF_3 as calculated on CCSD(T)/aVTZ level of theory [102]. Energies in $\frac{\text{kJ}}{\text{mol}}$.

Reaction	Energy	ZPE corrected
$\text{CoF}_4 \longrightarrow \text{CoF}_2 + \text{F}_2$	280.1	271.7
$\text{CoF}_4 \longrightarrow \text{CoF}_3 + \text{F}$	141.0	133.5
$\text{CoF}_4 \longrightarrow \text{CoF}_3 + \frac{1}{2}\text{F}_2$	64.8	60.0
$\text{CoF}_3 \longrightarrow \text{CoF}_2 + \text{F}_2$	291.6	285.2
$\text{CoF}_3 \longrightarrow \text{CoF}_2 + \frac{1}{2}\text{F}_2$	215.3	211.7

3.4 Cobalt Fluorides

As a 3d transition metal cobalt tends to form various compounds with magnetic properties. Its atomic electron configuration is given as $[\text{Ar}]3d^74s^2$. Formally, for molecular $\text{Co}^{\text{IV}}\text{F}_4$ one thus obtains 5 unpaired electrons in the Co 3d shell. Indeed its electronic ground state is a high-spin sextet multiplet. Similar, CoF_3 and CoF_2 form high-spin quintet and quartet ground states respectively [102]. Matrix-isolated IR spectra of all three molecules have been successfully measured [103], while the cationic species have been detected in mass spectrometric experiments [103, 104].

All three compounds (CoF_2 , CoF_3 and CoF_4) have been previously calculated on the CCSD(T)/aVTZ and B3LYP/aVTZ levels [102] and show high-spin character, i.e. all electrons in the Co 3d shell are unpaired. The structure of CoF_2 has a linear geometry ($D_{\infty h}$) [102, 105], while CoF_3 is trigonal planar (D_{3h}) [102, 106, 107]. The CoF_4 minimum structure is reported to be tetrahedral (T_d) [102]. The decomposition of CoF_4 and CoF_3 under release of F or F_2 is endothermic in all cases [102], as shown in Table 3.1.

Molecular CoF_4 is the highest neutral fluoride [104, 108] and is therefore of potential interest as oxidation or fluorination reagent. Solid CoF_3 has an industrial application for the synthesis of fluorocarbons, where it is reduced to CoF_2 , and in a second step regenerated by F_2 [109].

The systems may also be considered as a prototype for 1-dimensional chains. Either $\text{Co}^{\text{II}}\text{O}$ or planar $\text{Co}^{\text{IV}}\text{O}_2$ chains are possible, as shown in Fig. 3.5. Both chains may be terminated by fluorine. The CoO_2 chains have been experimentally pre-

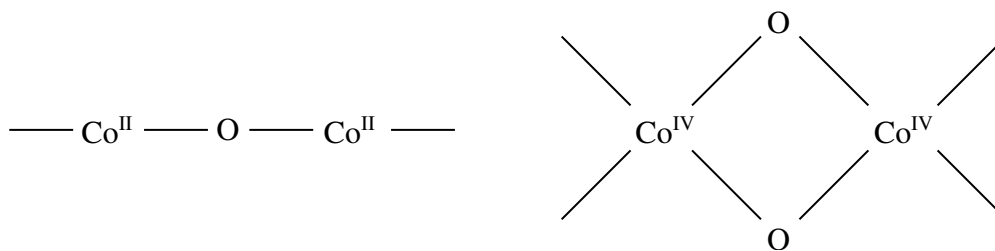


Figure 3.5: Structures for linear chains of $\text{Co}^{\text{II}}\text{O}$ and $\text{Co}^{\text{IV}}\text{O}_2$. The chains may be arbitrarily extended and terminated with fluorine.

Table 3.2: Correlation diagnostics (T_1 and D_1) for the CoF_n systems as obtained from RCCSD(T)/cc-pVDZ calculations.

	T_1	D_1
CoF_2 (${}^4\Delta_g$)	0.032	0.076
CoF_3	0.042	0.118
CoF_4 (D_{4h})	0.070	0.263
CoF_4 (T_d)	0.054	0.163

pared and studied on a Ir(100) surface [110, 111], where they showed ferromagnetic character.

The large number of singly occupied orbitals in these systems presents a challenge for standard correlation methods. However, the number of electrons in these system is still manageable and the range from CoF_2 to CoF_4 allows to pick and compare benchmark cases of varying size.

The reported Co–F bond lengths are in the range of 1.72 to 1.75 Å, depending on the species (CoF_2 , CoF_3 , CoF_4) and method (B3LYP, CCSD(T), exp.) [102]. For simplicity a fixed bond length of 1.73 Å is chosen for all cases studied in the following.

In Table 3.2 the T_1 and D_1 diagnostics, based on RCCSD(T) calculations, indicate the strongly correlated character of all four model systems. Commonly, T_1 and D_1 diagnostics larger than 0.02 and 0.05 respectively, are considered to be strongly correlated. Another threshold specifically intended for 3d transition metal containing compounds was suggested with 0.05 and 0.15 respectively [112]. The trend is clearly increasing with the number of F atoms, with the D_{4h} structure being the most

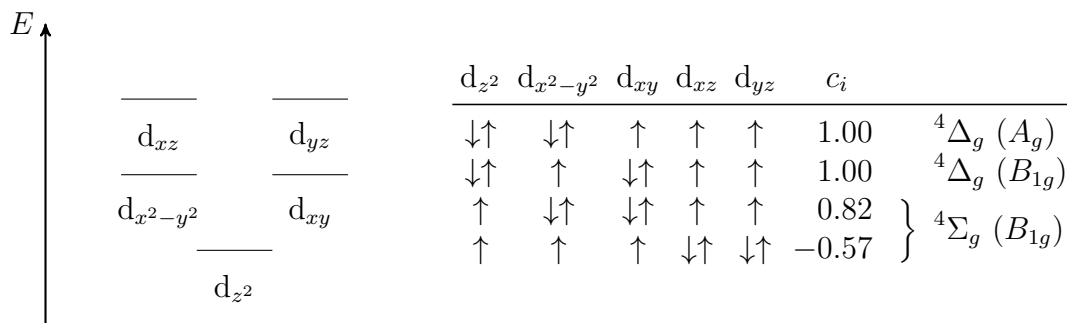


Figure 3.6: The Co 3d orbitals in the CASSCF(7,5) calculation of CoF_2 using the cc-pVDZ basis set. The energetic order is plotted to the left. The occupation patterns and CI coefficients c_i of the four included configurations and their corresponding electronic states are indicated to the right.

strongly correlated case. According to the thresholds for 3d transition metals, only CoF_4 is strongly correlated, but all systems clearly exceed the more conservative threshold.

CoF₂

The electronic ground state of CoF_2 is reported to be an ${}^4\Delta_g$ state with the first excited ${}^4\Sigma_g^-$ state about $5 mE_h$ higher in energy [105]. Due to reduction of the full $D_{\infty h}$ symmetry to its the abelian subgroup D_{2h} , the two degenerate ${}^4\Delta_g$ components fall into the A_g and B_{1g} IRREPs, while ${}^4\Sigma_g^-$ is B_{1g} . For a qualitatively reasonable set of orbitals a CASSCF(7,5) calculation with a state average of equal weights for the three mentioned components and using the cc-pVDZ basis set [99] is performed. The electronic states and a qualitative description of the Co 3d orbitals are summarized in Fig. 3.6. Calculations are performed with the MOLPRO software package [94, 113].

The CASSCF(7,5) yields the ${}^4\Sigma_g^-$ to be $4 mE_h$ lower in energy than the ${}^4\Delta_g$, i.e. energetically their order is reversed. This however can be corrected by MRCI or DMRG calculations. Furthermore the ${}^4\Sigma_g^-$ state is described by two configurations with coefficients 0.82 and -0.57 at CASSCF(7,5) level, while the two ${}^4\Delta_g$ components consist of a single configuration each.

The model for the CASCI calculations of CoF_2 is constructed by first excluding

all orbitals with eigenvalues below $-3 E_h$, which yields 11 core orbitals. It is then necessary to focus only on a single state (component) for the following discussions. The ${}^4\Sigma_g$ is already described by two leading configurations, which complicates the definition and correct assignment of further correlation contributions. Selecting only one of the two ${}^4\Delta_g$ may break symmetry of the degenerate 3d orbitals, but simplifies the model. Since in the B_{1g} IRREP the ${}^4\Sigma_g$ state is energetically close to the ${}^4\Delta_g$, it may cause some instabilities in the calculations. Therefore the A_g component is chosen here.

For an optional localization the remaining orbitals are then split into 3 sets: doubly occupied (closed) orbitals, singly occupied orbitals and empty (virtual) orbitals. The set of virtual orbitals corresponds to the CASSCF(7,5) virtual orbital space. For the singly occupied orbitals a total of three orbitals are required due to the spin quartet. Thus only three of the five active space orbitals can be selected, and the remaining two will be assigned to the doubly occupied closed orbital set. The three singly occupied orbitals are selected according to the A_g component of the ${}^4\Delta_g$ ground state (cf. Fig. 3.6). The active space will thus cover 23 electrons in 60 molecular orbitals. These three groups of orbitals are then localized in separate groups using the Pipek-Mezey scheme [12].

CoF₃ and CoF₄

In the trigonal planar arrangement (D_{3h}) of CoF₃ the Co 3d orbitals split into two doubly degenerate pairs and a non-degenerate d_{z^2} orbitals. This is similar to the linear CoF₂. However, due to the additional F⁻, the cobalt center is oxidized to Co₃⁺ and one less electron needs to be distributed among the 3d orbitals. Thus only the d_{z^2} orbital is occupied and the electronic ground state (A_1 in C_{2v}) is not degenerate.

For CoF₄ two structures are considered. The planar (D_{4h}) and tetrahedral (T_d) geometries are close in energy, with the latter being the ground state structure. The Co 3d orbitals split according to crystal field theory, i.e. in case of T_d there is a doubly degenerate pair (d_{z^2} , $d_{x^2-y^2}$) and a three-fold degenerate set (d_{xy} , d_{xz} , d_{yz}) higher in energy. In D_{4h} only two orbitals are degenerate (d_{xz} and d_{yz}). Since the number of 3d orbitals matches the number of unpaired electrons, all five of them

are singly occupied in the HF configurations of both structures.

The orbital space for the used models (FCIDUMP files) is constructed similar to CoF_2 . Based on ROHF calculations, for CoF_3 12 core orbitals are excluded from the (30,73) active space. It includes 13 orbitals doubly occupied and 4 orbitals singly occupied in the HF configuration. CoF_4 has 13 core orbitals being excluded and the (37,86) active space includes the 16 doubly and 5 singly occupied HF orbitals.

4 Results

4.1 QIT Analysis exemplified on the Dissociation of N_2/N_2^+

To help getting an intuitive understanding of the information available from a QIT analyses, the discussion starts with the fairly simple N_2 and its dissociation. In combination with the ground state and one excited state of N_2^+ , different chemical situations can be compared. The model system is described in more detail in Section 3.1. A detailed discussion of the results presented here has already been published previously [97], therefore only a summary will follow.

All information relevant for the electron correlation is encoded in the CI vector, as partially shown in Fig. 3.2. The drawback of visualizing the CI vector is, that it covers a large amount of configurations and is therefore difficult to grasp. The QIT analyses can be viewed as a tool to condense the information, making it easier to visualize and understand. Furthermore the perspective is shifted away from individual configurations, towards individual orbitals, i.e. the split into subsystem being responsible for electron correlation.

The QIT analyses is based on DMRG calculations using an active space of 16 orbitals, as indicated in Fig. 3.1, thus treating strong correlation only. Note that the energy levels are not to scale, or may even cross in their values, depending on the internuclear distance R . The overall qualitative picture including degeneracies, symmetries and approximate orbital shape however is depicted in sufficient accuracy. A more detailed characterization of the orbitals is covered by the original publication [97]. Although the large active space of 16 orbitals provides data for the QIT of higher lying orbitals, the discussion will be restricted to the orbitals related to the

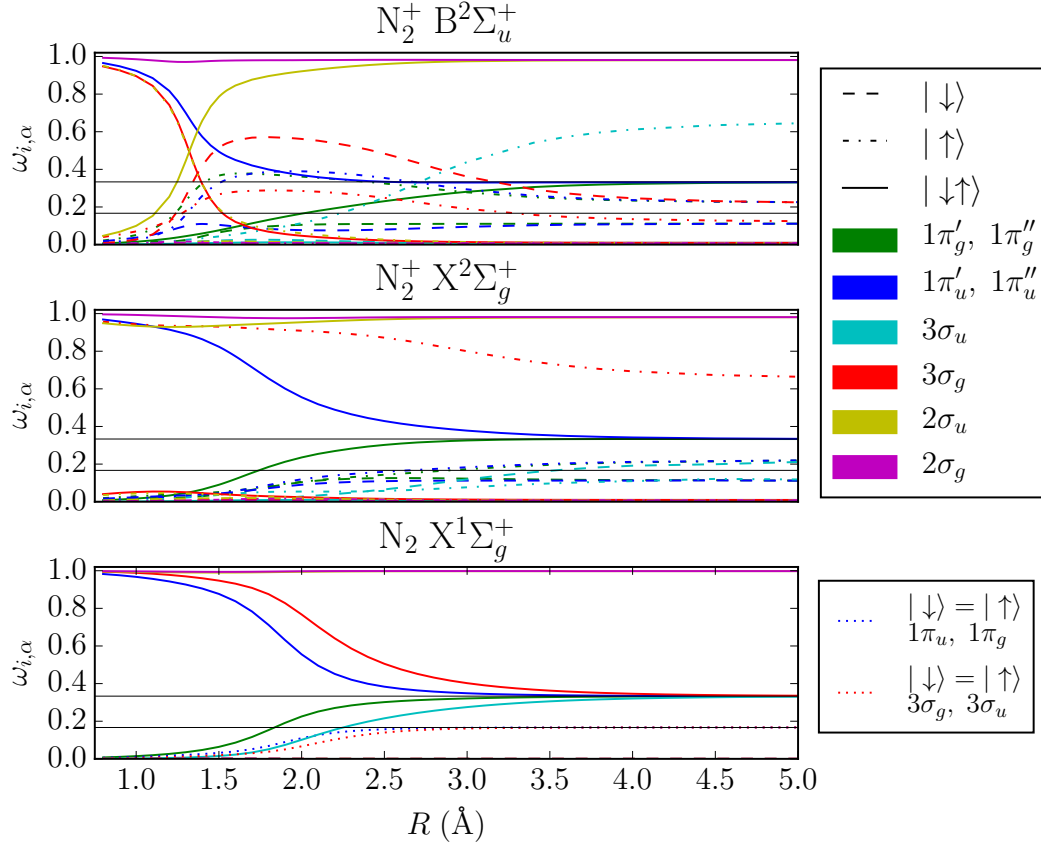


Figure 4.1: Orbital occupations $\omega_{i,\alpha}$ as a function of internuclear distance R . The line shapes indicate the eigenfunctions, while colors encode the molecular orbitals. For clarity, only three eigenvectors are included. The fourth eigenvector for the empty occupation $|-\rangle$ has been omitted and may be inferred based on the normalization constrained $\sum_{\alpha} \omega_{i,\alpha} = 1$. Figure adopted from Ref. [97].

2sp shell, as those are the most important contributions. The 1-orbital entropies and mutual information of the 3sp shell orbitals are much smaller.

Calculations are performed using the DMRG Budapest code [114] and $M = 4096$ blockstates, which is close to the numerical exact limit. As a reference to the DMRG energies, CASCI calculations using MOLPRO [94, 115, 116] have been performed as well and are in good agreement [97].

The first step of a QIT analysis is constructing the 1-orbital density matrices ρ_i and obtaining their eigenvalues $\omega_{i,\alpha}$ (cf. Eqs. (2.115) and (2.150)). In quantum chemistry these density matrices are already diagonal due to conservation of the spin and

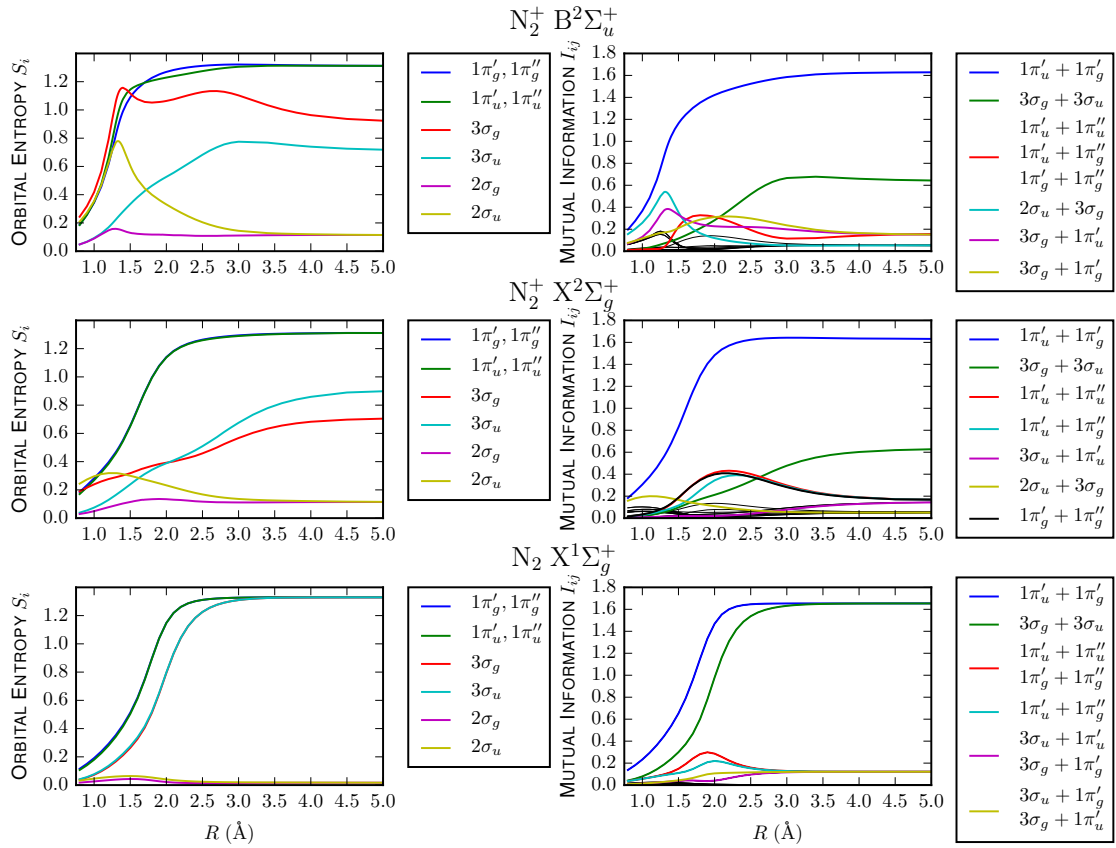


Figure 4.2: 1-orbital entropy S_i and mutual information I_{ij} . Smaller contributions to the mutual information which are not covered in the legend are indicated by thin black lines. Figure adopted from Ref. [97].

particle quantum numbers. Explicit diagonalization is therefore not necessary. The eigenvalues and eigenvectors are plotted in Fig. 4.1 as a function of internuclear distance R . They tell which occupation of each orbital yields the largest combined weight in the CI vector. The 1-orbital entropies further condenses this information by summing over the four eigenvalues of each orbital according to Eq. (2.150). Based on the eigenvalues $\omega_{i,\alpha}$ the 1-orbital entropies S_i in Fig. 4.2 (left panels) is easily understood. Thus they will be discussed together below. The discussion of 2-orbital correlations by means of the mutual information (cf. Eq. (2.152)) will follow after that.

First, note the degenerate values of $\omega_{i,\alpha}$ due to spin and spatial symmetries. In case of the singlet ground state of N_2 (lower panel) spin symmetry dictates identical spin-up and spin-down occupation for each orbital, they are thus depicted by a single line. This restriction is lifted for the doublet N_2^+ system. However, the degeneracy due to the spatial orbital symmetry of the $\pi'_{g/u}$ and $\pi''_{g/u}$ orbitals, as a result of lowering the full point group $D_{\infty h}$ to its largest abelian sub group D_{2h} , holds for all the states. Thus, in the plots, those orbitals share colors.

The plot for the N_2 ground state $X^1\Sigma_g^+$ is rather well structured and straight forward to understand. The $2\sigma_g$ and $2\sigma_u$ are almost exclusively doubly occupied, accordingly their 1-orbital entropy is very small. The latter does however show a small maximum around 1.5 Å. They do thus play a minor role in the bond breaking process. The story for the 3σ and 1π orbitals are very similar: While they exhibit at equilibrium distance mainly double and empty occupations for the bonding and anti-bonding MOs respectively, the two eigenvalues converge together at $1/3$ at dissociation limit. Additionally, the single electron occupations (spin-up and spin-down) evolve from negligible level to $1/6$. The distribution of the eigenvalues for each of these orbitals thus evolves from a very ordered one with low entropy to an almost uniform one with high entropy. The transition (maximum slope) for the 3σ orbitals is however slightly shifted towards larger internuclear distances R . This indicates that the π bonds break before the σ and relates to the larger overlap of atomic two p_z orbitals, oriented along the bond axis, compared to the p_x and p_y orbitals perpendicular to it. This observation has also previously been reported by Boguslawski et al. [117].

Note that orbital pairs of the corresponding bonding and anti-bonding orbital, i.e. $3\sigma_g$ and $3\sigma_u$ as well as the $1\pi_u$ and $1\pi_g$ pairs, have almost identical entropies ("close

Table 4.1: Assignment of the labels used in Figs. 4.3 and 4.4 to characteristic eigenvectors $\phi_{ij,\alpha}$ of the two-orbital density matrix ρ_{ij} . Further possible eigenvectors are the basis vectors itself, which are indicated by their corresponding label directly. Table adopted from Ref. [97].

$\phi_{ij,\alpha}$	$\langle S^2 \rangle$	label
$\frac{1}{\sqrt{2}}(-, \uparrow\downarrow\rangle + \uparrow\downarrow, -\rangle)$	0	$ \uparrow\downarrow, -\rangle_+$
$\frac{1}{\sqrt{2}}(-, \uparrow\downarrow\rangle - \uparrow\downarrow, -\rangle)$	0	$ \uparrow\downarrow, -\rangle_-$
$\frac{1}{\sqrt{2}}(\uparrow, \downarrow\rangle - \downarrow, \uparrow\rangle)$	0	singlet
$\frac{1}{\sqrt{2}}(\uparrow, \downarrow\rangle + \downarrow, \uparrow\rangle)$	2	} triplet
$ \uparrow, \uparrow\rangle$	2	
$ \downarrow, \downarrow\rangle$	2	

degenerate“). This relates to the eigenvalues $\omega_{i,\alpha}$ being very similar. The double occupation in the bonding orbital (almost) equals the empty occupation in the corresponding anti-bonding orbital, while spin-up and spin-down occupation are (almost) the same for both. The very small deviations are related to the higher lying virtual orbitals of the 3sp shell. The correlations to those orbitals are different for bonding and anti-bonding orbitals, but very small in magnitude.

The mutual information (right panels in Fig. 4.2) indicates which orbital pairs are entangled most with each other. Largest values are observed for pairs of corresponding bonding and anti-bonding orbitals in the 2p shell. Smaller contributions are related to other combinations of the same orbitals, while the $2\sigma_{g/u}$ of the 2s shell are negligible for the N_2 ground state.

For the N_2^+ states similar trends can be observed. But there are also obvious differences, related to the spin doublet. The degeneracy of the spin-up/spin-down occupations is lifted and the electron hole in the $3\sigma_g$ orbital is easily identified (cf. Fig. 4.1). This results in a drastically decreased overall entropy and mutual information for the $3\sigma_{g/u}$ orbitals (cf. Fig. 4.2), but at the same time allows for more entanglement with the $2\sigma_{g/u}$ orbitals. The N_2^+ ($B^2\Sigma_u^+$) additionally shows characteristics related to the change of the leading configuration.

Since the mutual information is constructed from the 2-orbital RDMs ρ_{ij} , according to Eqs. (2.151) and (2.152), more detailed information about 2-orbital entanglement is provided by investigating the eigenvalues $\omega_{ij,\alpha}$ and eigenvectors $\phi_{ij,\alpha}$ of the 2-

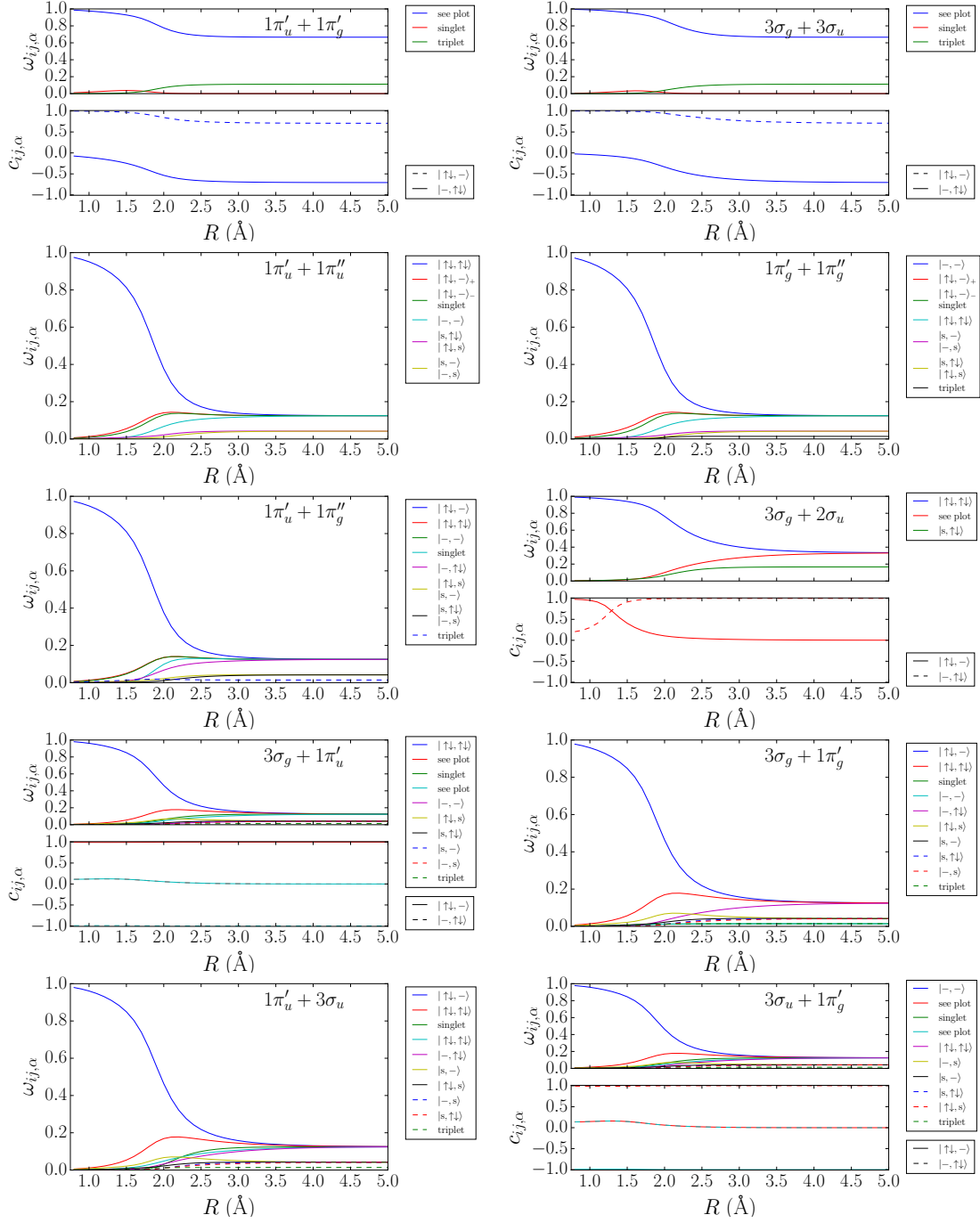


Figure 4.3: Eigenvalues $\omega_{ij,\alpha}$ of selected orbital pairs of the $\text{N}_2 \text{X}^1\Sigma_g^+$. The corresponding eigenvectors $\phi_{ij,\alpha}$ are indicated in the legend either in terms of the basis states, or the labels of the characteristic eigenvectors summarized in Table 4.1, where possible. The letter s in the label indicates either spin-up or spin-down and implies both options have identical values. If the eigenvectors changes with respect to the internuclear distance R , their coefficients $c_{ij,\alpha}$ are added as a plot below the corresponding eigenvalues. Figure adopted from Ref. [97].

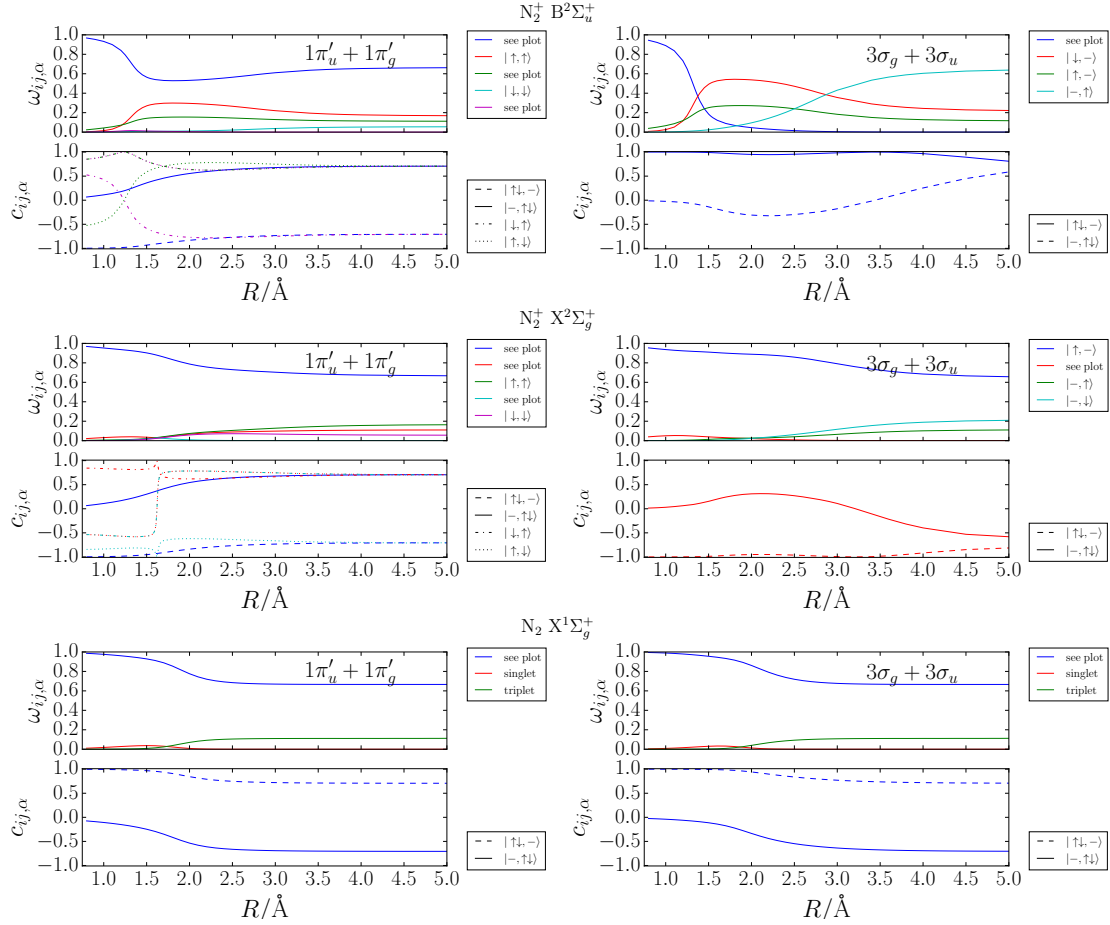


Figure 4.4: Largest eigenvalues $\omega_{ij,\alpha}$ and their corresponding eigenvectors $\phi_{ij,\alpha} = \sum_{\alpha} c_{ij,\alpha} |\phi_{\alpha_i}\rangle |\phi_{\alpha_j}\rangle$ of the two-orbital reduced density matrices, plotted over the internuclear distance R . Selected orbital pairs are $1\pi'_u + 1\pi'_g$ and $3\sigma_g + 3\sigma_u$, left and right columns respectively. The electronic states from top to bottom are $N_2^+ B^1\Sigma_u^+$, $N_2^+ X^1\Sigma_g^+$ and $N_2 X^1\Sigma_g^+$. Labels for eigenvectors which do not change with respect to R are assigned according to Table 4.1, s indicates \uparrow and \downarrow yield same results. For eigenvectors depending on R their nonzero coefficients are plotted. Figure adopted from Ref. [97].

orbital RMD directly. Graphical representation of this data however is difficult, due to the large amount of data points. However, studying the eigenfunctions $\phi_{ij,\alpha}$ a set of *characteristic* eigenfunctions which appear frequently is noticeable. Many of the eigenvectors directly correspond to the 16 basis states, formed by combining the four 1-orbital basis states ($|-\rangle$, $|\downarrow\rangle$, $|\uparrow\rangle$ and $|\uparrow\downarrow\rangle$) from the 2 orbitals. The remaining eigenfunctions are mostly linear combinations of two basis states, most of them with fixed coefficients over R . All of these characteristic eigenvectors may thus be labeled by the corresponding basis states directly, or as summarized in Table 4.1. Only a few occurring eigenvectors are not covered by this set of characteristic eigenfunctions and have varying coefficients with respect to R . In these cases the main coefficients are plotted over R , in addition to their eigenvalues $\omega_{ij,\alpha}$. The data for selected pairs of orbitals in the $\text{N}_2 \text{X}^1\Sigma_g^+$ state is plotted in Fig. 4.3.

The 2-orbital RDM eigenvalues $\omega_{ij,\alpha}$ show an interesting pattern. In the single-reference regime close to the equilibrium distance, all of the orbital pairs have a single major eigenvalue close to 1, while all other eigenvalues are close to zero. The corresponding eigenvectors resemble the occupations of the orbital pair in the Hartree-Fock configuration. At dissociation limit however, most orbital pairs show multiple degenerate eigenvalues between 0.1 and 0.2. The exception here are the bonding/anti-bonding orbital pairs in the 2p shell (top panels in Fig. 4.3), which already had come to attention with their large mutual information. For large R they show one eigenvalue with $\omega_{ij,\alpha} \approx 0.7$ with its eigenvector being a linear combination of two basis states ($\frac{1}{\sqrt{2}}(|-\rangle, \uparrow\downarrow\rangle - |\uparrow\downarrow, -\rangle) = |\uparrow\downarrow, -\rangle_-$). A second, smaller eigenvalue with three-fold degeneracy at $\omega_{ij,\alpha} \approx 0.1$ shows up as well, and is similar to the pattern of many degenerate eigenvalues for the other orbital pairs.

Thus, three different cases may be classified: First, a large eigenvalue $\omega_{ij,\alpha}$ with an eigenvector $\phi_{ij,\alpha}$ resembling a single occupation and in connection with a small to medium mutual information I_{ij} . This is observed for all orbital pairs at small R , and therefore connected to a single-reference problem with small total correlation. The other two cases are related to the multi-reference region at large R , where the total correlation is larger. Small to medium mutual information in connection with many similar eigenvalues $\omega_{ij,\alpha}$ is observed for most of the orbital pairs. These many eigenvalues represent many different occupations with similar weight in the CI vector, as is typically the case for dynamic correlation. The final cases is only found in the orbitals pairs with highest mutual information and has a single major

eigenvalue $\omega_{ij,\alpha}$ related to an eigenvector of few orbital pair occupations. This means certain occupation patterns are of very high relevance, i.e. a smaller number of configurations with large coefficient. This resembles strong correlation. This would identify the bonding/anti-bonding orbitals to be responsible for strong correlation.

The 2-orbital RDMs yield similar results for the two N_2^+ states. The orbital pairs related to strong correlation in the N_2 ground state are compared for all three considered states in Fig. 4.4. The remaining pairs are not shown here, but the complete data set is available in the supplementary information of the original work [97]. The 1π orbital pairs are very similar across the three states, however the degenerate triplet in N_2 splits into non-degenerate eigenvalues due to the spin doublet symmetry in N_2^+ . The $3\sigma_g + 3\sigma_u$ orbital pair look similar in their eigenvalue spectrum, but are very different in their related eigenvectors. In both N_2^+ states, the leading eigenvalues are connected to eigenvectors describing only a single orbital occupation, not a mixture like observed for the N_2 ground state. However, the next smaller two eigenvalues describe single electron excitations from the bonding orbital to the anti-bonding orbital. This suggest that the $3\sigma_g + 3\sigma_u$ orbital pair does contribute less to the strong correlation character in N_2^+ than for N_2 .

The above discussion suggest that it may be possible to identify strong correlation contributions by selecting orbital pairs with high mutual information and analyzing their 2-RDMs. If there is only a small number of eigenvalues with eigenvectors of few, but more than one, orbital occupation patterns, the corresponding orbital pair may be attributed to strong correlation. One may furthermore search for certain occupations related to strong correlation. For example in the 1π orbital pairs double ($|\uparrow\downarrow\rangle$) and empty ($|- \rangle$) occupations are more important than single electron occupations, while there are at most 2 electrons at a time in that orbital pair.

4.2 Entropy Based Configuration Selection in MCSCF and MRCI

The standard approach for treating strong correlation is to perform a CASSCF calculation. The scaling with the number of active space orbitals however is expo-

nential and only small systems may be considered. Selection of an appropriately active space is therefore crucial, however not an easy task. Recently Stein and Reiher [29] suggested and demonstrated an automated active space selection based on the 1-orbital entropies S_1 for MnO_4^- . They also discussed a mutual information I_{ij} based selection, but did not focus on it.

An alternative suggested here is to reducing the scaling of this method by not only selecting the active space orbitals, but further selecting specific configurations of that active space. This raises the question of which configuration to choose. One possible approach is to combine a DMRG calculation, which in essence tries to find the largest configurations of the active space without a biased preselection (e.g. based on the excitation degree) with the SCF step in MCSCF. In DMRG-SCF the DMRG method is used as a solver for the CI step in an CASSCF calculation. The drawback of this approach however, is that convergence in DMRG is slow and sometimes unstable as DMRG may get trapped in a local minimum. Furthermore there are many MCSCF iterations including a DMRG step.

Another approach might be to use DMRG to screen the configuration space. The most important configurations could be extracted from the MPS and used in a MCSCF calculation with a conventional CI solver. The problem however is, extracting the largest coefficients of the MPS is not that easy. Due to the SVD the coefficients are not stored explicitly, thus the MPS needs to be contracted to the full tensor from which the required information can then be obtained. Performing the full contraction in a single step would require large amounts of memory. In essence, this is the same problem the MPS was designed to avoid in the first place. Alternatively, each configuration may be sampled individually, but this approach deals with the same scaling problem the original CASCI/FCI approach suffers from and is therefore not feasible as well.

Motivated by the results of the previous section however, one may try to construct a list of configurations based on the QIT results. The idea is to find enough configurations to describe all strong correlation, but omit all configurations related to dynamical correlation. This list of configurations is then used to optimize the orbitals by a MCSCF approach. Naturally, the MCSCF energy will be worse than the CASSCF energy, as all dynamical correlation will be missing. A successive MRCI calculation may therefore be necessary.

4.2.1 Construction of Configurations based on 2-RDMs

All 1- and 2-orbital RDMs and related quantities (S_i , I_{ij} , $\omega_{ij,\alpha}$, *etc.*) are readily available from the Budapest DMRG code [114] and encode all information on the level of pair-correlations. Higher level correlations are not accessible as they require the corresponding higher order orbital RDMs. Implementation of those is in principle possible, but they would require increased computational resources. On the other hand, restricting to 2-orbital RDMs keeps their evaluation computationally feasible. Therefore the idea is to approximately reconstruct the most important configurations by selecting and appropriately combining the most important pair-correlations to yield a list of configurations.

This list of configurations represents a truncation of the CASCI vector, and their coefficients c_i may be obtained from the MPS. Using these coefficients, the quality of that truncation may be judged by its norm. Additionally, the configurations may be further restricted by choosing a threshold parameter c_{thresh} and keeping only those where $|c_i| \geq c_{\text{thresh}}$. Obtaining these coefficients from the MPS is usually feasible since only a small set of configurations is considered, and sampling of the full CASCI vector is avoided.

The basic idea is to identify orbitals and their occupations with major contributions, and then construct those configurations, which fulfill the occupation requirements based on this selection. How to identify these orbital pairs and their occupation patterns is a central question and two possible approaches will be presented below. The complete selection scheme is summarized in Fig. 4.5 and will be explained in detail below.

Once the pair correlations are identified, the corresponding orbital pair occupations will need to be combined to higher level correlations, until all orbitals are included. For example, assume the following two orbital pairs and occupations have been obtained: ij with occupations 20 and ab (where 2, a, b and 0 represent double, α -spin, β -spin and empty occupation respectively) as well as ik with occupations 20 and 02. Then in the orbital triple ijk all possible configurations including these pair occupations need to be considered. As summarized in Table 4.2, this leads to seven triple occupations: 200, 202, 002, ab0, 2b0, ab2, 0b2. The occupation patterns are

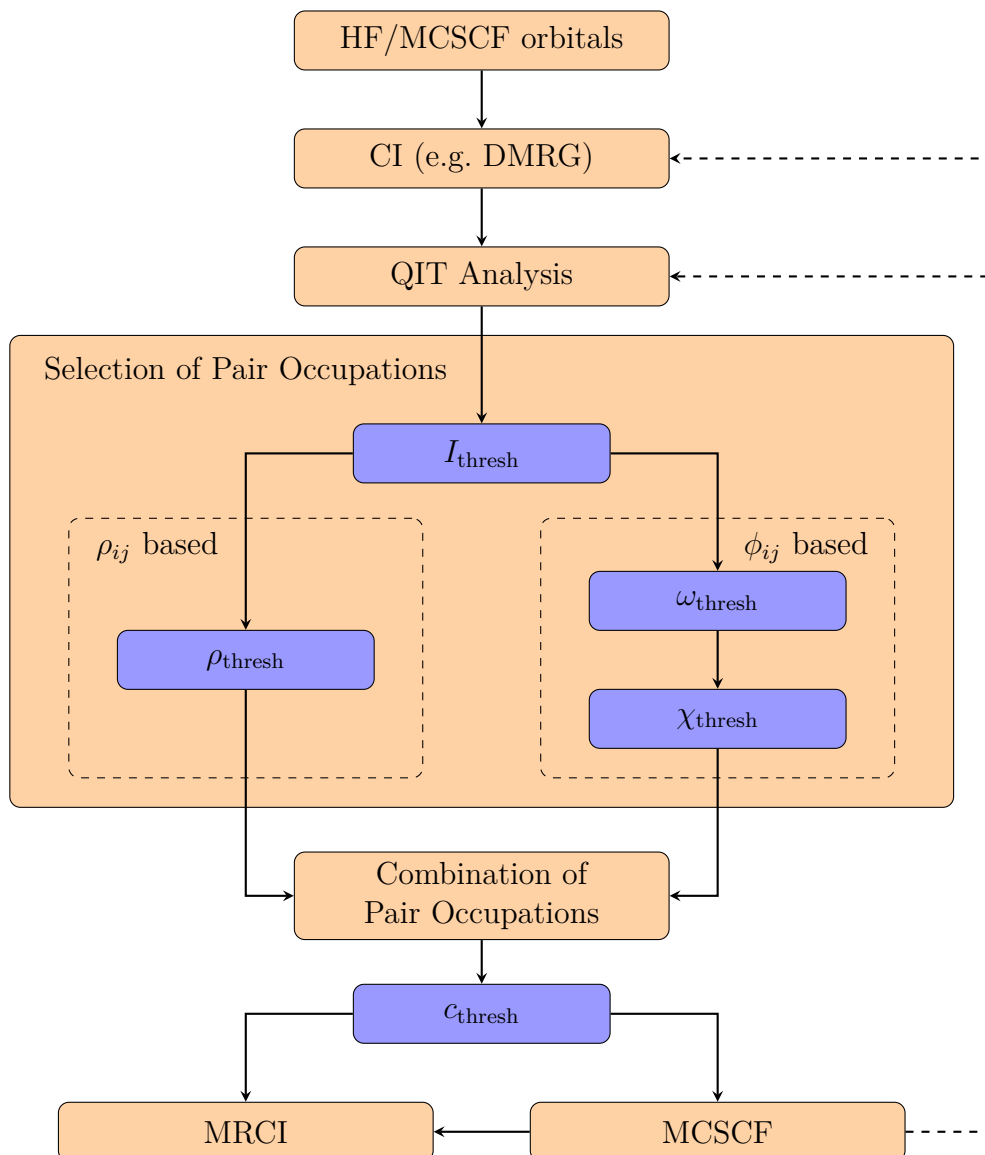


Figure 4.5: Construction of configurations based on the 2-RDMs. After obtaining the molecular orbitals an approximate CI calculation of qualitative accuracy is performed and the acquired CI vector is analyzed by QIT. The most important orbital pairs are selected by their mutual information and the relevant occupations of each pair are then identified by either the ρ_{ij} based selection (left path) or the ϕ_{ij} based selection (right path). After combining all identified relevant pair occupations (cf. Table 4.2) the list of obtained configurations may be screened by the CI vector, keeping only those with largest amplitude. The final list of configurations is then used in MCSCF and/or as the reference space for MRCI. The dashed arrow indicates a possible iterative optimization of the orbitals.

Table 4.2: Combination of selected occupation patterns of two orbital pairs ij and ik to occupation patterns of the resulting orbital triplet ijk . The characters 2, a, b and 0 represent double, α -spin, β -spin and empty occupation respectively.

ij	ik	\rightarrow	ijk
20	20	\rightarrow	200
20	02	\rightarrow	202, 002
ab	20	\rightarrow	ab0, 2b0
ab	02	\rightarrow	ab2, 0b2

then normalized such that the first unpaired orbital always has α spin and duplicates are removed. For the above example, the list is now 200, 202, 002, ab0, 2a0, ab2, 0a2. This process is then repeated until all orbital pairs are combined into a single list of “configurations”. At this point, the configurations are possibly not complete yet. Single orbitals that do not appear in any selected orbital pair have not been considered so far. Those uncorrelated orbitals will always adopt their occupation from the HF configuration, yielding a list of complete configurations. Finally, configurations not matching in number of electrons or IRREP of the state of interest can be discarded.

To select the orbital pairs a user-defined threshold for the mutual information I_{thresh} is proposed. To further select the occupation patterns of those orbital pairs, two different approaches are proposed and tested in the following. The first one is based on the 2-orbital RDMs (ρ_{ij} based) directly and aims to construct all major configurations, while the second one considers the eigenvalues $\omega_{ij,\alpha}$ and their corresponding eigenfunctions $\phi_{ij,\alpha}$ (ϕ_{ij} based) to classify and select only configurations related to static correlation.

Approach 1: ρ_{ij} based selection

Each matrix element $\rho_{ij}(\alpha_i, \alpha_j, \alpha'_i, \alpha'_j)$ relates to two occupations the orbital pair ij can adopt: α_i, α_j and α'_i, α'_j . It may be interpreted as the correlated appearance of those two occupations in the CI vector. Thus, the two occupations of each matrix element with amplitude above a value ρ_{thresh} are included. If only a single occupation

is obtained, i.e. the only matrix element above the threshold ρ_{thresh} is of the form $\rho_{ij}(\alpha_i, \alpha_j, \alpha_i, \alpha_j)$, it will correspond to the HF occupation of this orbital pair. It will therefore not be considered as a correlation and not included.

The construction of the configuration space is thus controlled by the parameters I_{thresh} and ρ_{thresh} , and optionally c_{thresh} .

Approach 2: ϕ_{ij} based selection

In the previous section, different patterns for the eigenvalues $\omega_{ij,\alpha}$ and $\phi_{ij,\alpha}$ -functions $|\phi_{ij,\alpha}\rangle$ of the 2-RDM for orbitals pairs attributed to strong and weak correlation have been observed. The essential difference is, how many states of the 16 occupation basis states $|\xi_\beta\rangle = \{|-, -\rangle, |\downarrow, -\rangle, \dots\}$ contribute to the 2-RDMs. The second approach will therefore try to capture those contributions.

First, all eigenvectors with eigenvalue $\omega_{ij,\alpha} \geq \omega_{\text{thresh}}$ are selected. The amount of contributing basis states $|\xi_\beta\rangle$ is then determined by calculating an entropy. For this, the absolute square of the eigenvector's coefficients $c_{\alpha\beta}^{ij}$

$$\chi_{\alpha\beta}^{ij} = |c_{\alpha\beta}^{ij}|^2 \quad (4.1)$$

is used, as this ensures all $\chi_{\alpha\beta}^{ij} \geq 0$ and $\sum_{\beta} \chi_{\alpha\beta}^{ij} = 1$. The entropy is then defined by

$$S_{\alpha}^{\chi} = \sum_{\beta} \chi_{\alpha\beta}^{ij} \ln \chi_{\alpha\beta}^{ij}. \quad (4.2)$$

Note that, S_{α}^{χ} is different from the 2-orbital entropy S_{ij} , which is obtained from the eigenvalues $\omega_{ij,\alpha}$. All eigenstates $|\phi_{ij,\alpha}\rangle$ with $S_{\alpha}^{\chi} \geq \chi_{\text{thresh}}$ are then selected, which will exclude all eigenvectors being mainly constituted of just a single basis state $|\xi_\beta\rangle$, i.e. unentangled occupations. All non-zero basis states $|\xi_\beta\rangle$ of the selected eigenvectors are then included as orbital occupations to construct the list of configurations. For some orbital pairs ij , the HF occupation of those two orbitals may turn out to be less important than other occupations. Depending on the selected thresholds ω_{thresh} and χ_{thresh} this may exclude important configurations (such as the HF configuration) from the list of generated configurations. To avoid this, it is checked whether the HF occupation for each considered orbital pair ij is included and added

if not.

In summary, this approach thus uses the three main parameters I_{thresh} , ω_{thresh} and χ_{thresh} as well as the optional c_{thresh} threshold to select the configuration space. Additionally, different values for the selection of the non-zero basis states $|\xi_{\beta}\rangle$ can be considered. Here however, a fixed value of 10^{-8} is used.

4.2.2 Used Models and Computational Details

The two proposed approaches are tested on two different model systems. The CoF_2 model is constructed as described in Section 3.4. The FCIDUMP is generated from the natural CASSCF(7,5) orbitals, where the state average includes both ${}^4\Delta_g$ components as well as the ${}^4\Sigma_g^-$ state. The second model considers the more strongly correlated CoF_4 in D_{4h} symmetry and uses the canonical orbitals of the ROHF ground state. The QIT analysis for both systems is based on a DMRG calculation using the Budapest Code [114] with the DBSS approach and density matrix cut-off of 1×10^{-5} and a maximum of 1024 block states. Convergence to the correct states proves difficult for DMRG. However the 1-orbital entropies may also be obtained from a FCIQMC calculation and thus be compared to the DMRG results for validation.

To obtain the 1-orbital entropies the 1-orbital RDMs in spatial orbital basis are required. Those in turn can be obtained from the 2-particle RDM in spin orbital basis as described in Section 2.3.2. The latter can be sampled without bias by propagating two independent walker populations [118]. Using 1×10^6 walkers in FCIQMC is sufficient for qualitative agreement of the 1-orbital entropies, however the energy is not converged at this point. This is similar to the entropies being insensitive to the number of blockstates in DMRG. Increasing the number of walkers will increase the overall correlation and therefore yield larger entropies, but qualitatively the results are very similar (cf. Fig. 4.6).

FCIQMC furthermore provides an estimate for the FCI energy, which here serves as a reference. All FCIQMC calculations are performed with the NECI code [70, 119, 120] in multiple steps: First a walker population of 1×10^6 was equilibrated and then stepwise increased over 1×10^7 to 1×10^8 walkers. Next the superinitiator

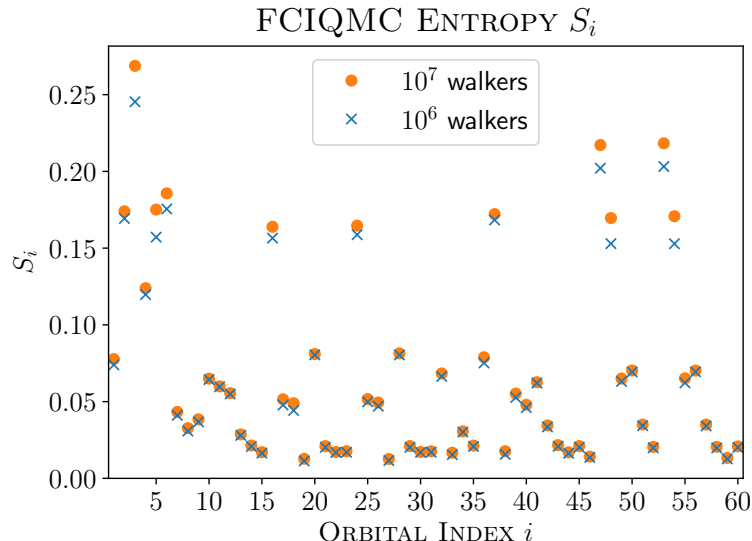


Figure 4.6: The 1-orbital entropies for the CoF_2 system as obtained by FCIQMC, using 1×10^6 (blue crosses) and 1×10^7 (orange circles) walkers in NECI’s double run mode.

method [68] is applied, where the number of superinitiators is increased stepwise until no further improvement in the FCIQMC energy can be observed.

The QIT analysis for the CoF_2 model is only performed for the A_g component of the ${}^4\Delta_g$ state. The other component as well as the excited ${}^4\Sigma_g^-$ state would yield their own CI vectors and therefore different QIT results. Targeting more than one state therefore introduces additional complexity and is thus not considered here. Instead focusing on the A_g component only facilitates convergence of the DMRG, as it cannot get trapped in the close lying excited ${}^4\Sigma_g^-$ state present in the B_{1g} IRREP. As a consequence the following CASSCF calculation are optimized for only a single state, i.e. have a different state average than the orbitals used in the DMRG calculation. For CoF_4 (D_{4h}) only a single state is considered from the beginning, so this issue does not show up.

Since both systems are calculated using their abelian subgroup D_{2h} instead of exploiting their full molecular symmetry, degeneracies in the MCSCF orbitals may be broken and thus result in qualitative differences. A subsequent MRCI calculation may in principle correct this issue, but only if it is close enough to the FCI solution which is invariant under orbital rotations. One may try to avoid such issues, for

Table 4.3: Energies (in E_h) for the CoF_2 model system obtained by different methods.

	Total Energy	E_{corr}	Std. Deviation
HF	-1580.389262		
FCIQMC	-1581.022206	-0.632861	3.2×10^{-5}
DMRG	-1580.807867	-0.418606	
RCCSD	-1581.007664	-0.618403	
UCCSD	-1581.008446	-0.619185	
RCCSD(T)	-1581.021331	-0.632070	
UCCSD(T)	-1581.022103	-0.632841	
CISD	-1580.939596	-0.550335	
CISD + David.	-1581.000822	-0.611560	

example by trying different state averages until the orbital symmetry is conserved. But this requires to add more configurations if the additional states are of different symmetry. Furthermore energies between different state averages are not directly comparable anymore. For simplicity this is avoided here, instead all data presented below has been checked for broken orbital symmetry and marked accordingly.

All HF, MCSCF and MRCI calculations are performed using the MOLPRO software package [94, 113]. The main contributions of the QIT data are presented and discussed in Section 4.4.2, together with CoF_3 and CoF_4 (T_d).

4.2.3 Reference Calculations

As a reference, the total energy of both models has been calculated by different methods and are shown in Tables 4.3 and 4.4 for CoF_2 and CoF_4 (D_{4h}) respectively. FCIQMC results are obtained using 1×10^8 walkers as well as 11 and 12 superinitiators for CoF_2 and CoF_4 respectively. The standard deviation after the reblocking analysis of the sampled correlation energy is given in the tables as well. Lowest energies are obtained by CCSD(T) and FCIQMC, which agree within $1 mE_h$ and $10 mE_h$ for CoF_2 and CoF_4 respectively. The differences may be related to the strong correlation character, which is more pronounced for CoF_4 (cf. Table 3.2). This also agrees with the CCSD(T) energies being much lower than FCIQMC for CoF_4 , which therefore should be considered unreliable. For both models DMRG yields consid-

Table 4.4: Energies (in E_h) for the CoF_4 D_{4h} model system obtained by different methods.

	Total Energy	E_{corr}	Std. Deviation
HF	-1779.019872		
FCIQMC	-1780.124419	-1.104546	4.9×10^{-4}
DMRG	-1779.719044	-0.699172	
RCCSD	-1780.087041	-1.067169	
UCCSD	-1780.092296	-1.072424	
RCCSD(T)	-1780.132355	-1.112482	
UCCSD(T)	-1780.137332	-1.117460	
CISD	-1779.896442	-0.876570	
CISD + David.	-1780.048175	-1.028303	

erably higher energies as it struggles with the dynamic correlation contributions. The difference between the CISD and FCIQMC results are supposed to give some rough idea about the missing contribution due to strong correlation. However this does not provide any exact measure since a strict definition of strong correlation is difficult. Overall the FCIQMC energy should provide the most reliable estimate to the true FCI energy of the models and will therefore serve as the reference for the following tests.

Next to the FCI energy, the active spaces and configurations selected based on the QIT data will be compared to the active spaces that may be obtained by choosing the highest correlated orbitals, based on the 1-orbital entropy S_i . The corresponding data is presented in Tables 4.5 and 4.6 up to the limit where the active space becomes too large for feasible calculations. The data includes CASSCF energies as well as MRCI-SD calculations based on the ROHF and CASSCF orbitals. Note that in case of CoF_2 the ‘‘ROHF’’ orbitals actually refer to CASSCF(7,5) orbitals as described in Section 3.4. Due to symmetry restrictions however, there is only a single configuration included in that active space to represent the targeted state. The difference to the actual ROHF orbitals is therefore only in the mentioned state averaging.

The active spaces are constructed by choosing those orbitals with largest 1-orbital entropy S_1 , according to a QIT analysis of the DMRG calculation. The number of orbitals is indicated by the first row. The actual active space may be slightly larger,

Table 4.5: Correlation Energies (in E_h) and CPU times for CASSCF and MRCI-SD calculations based on different active spaces selected based on the 1-orbital entropy S_i . Data is shown for the CoF_2 model system. Results being based on orbitals that do not reflect the expected degeneracies due to the molecular point group are indicated by a gray font color, while numbers printed in bold represent preserved symmetry.

# correlated orbitals	active space	CASSCF		MRCI@ROHF			MRCI@CASSCF		
		energy	time	energy	Davidson	time	energy	Davidson	time
2	(5,5)	-0.0158	<1 s	-0.5522	-0.6129	2 s	-0.5571	-0.6161	3 s
3	(7,6)	-0.0170	<1 s	-0.5524	-0.6132	6 s	-0.5582	-0.6169	7 s
7	(11,9)	-0.0210	<1 s	-0.5545	-0.6158	5 min	-0.5610	-0.6192	6 min
10	(15,11)	-0.0310	3 s	-0.5562	-0.6167	11 min	-0.5647	-0.6209	13 min
11	(17,12)	-0.0318	7 s	-0.5564	-0.6169	22 min	-0.5654	-0.6213	25 min
12	(19,13)	-0.0371	10 s	-0.5565	-0.6172	40 min	-0.4992	-0.5369	46 min
13	(19,14)	-0.0720	40 s	-0.5583	-0.6186	21 h	-0.4828	-0.5109	25 h
14	(19,15)	-0.0833	2 min						
16	(19,17)	-0.1562	4 h						

Table 4.6: Correlation Energies (in E_h) and CPU times for CASSCF and MRCI-SD calculations based on different active spaces selected based on the 1-orbital entropy S_i . Data is shown for the CoF_4 D_{4h} model system. Results being based on orbitals that do not reflect the expected degeneracies due to the molecular point group are indicated by a gray font color, while numbers printed in bold represent preserved symmetry.

# correlated orbitals	active space	CASSCF		MRCI@ROHF			MRCI@CASSCF		
		energy	time	energy	Davidson	time	energy	Davidson	time
4, 6	(9,7)	-0.0098	3 s	-0.8817	-1.0348	59 s	-0.8952	-1.0483	68 s
7	(11,8)	-0.0372	5 s	-0.8872	-1.0391	2 min	-0.9116	-1.0576	3 min
8	(13,9)	-0.0492	4 s	-0.8879	-1.0399	4 min	-0.9207	-1.0637	4 min
9	(15,10)	-0.0583	3 s	-0.9006	-1.0482	8 min	-0.9270	-1.0675	7 min
10	(17,11)	-0.0583	3 s	-0.9006	-1.0482	7 min	-0.9270	-1.0675	8 min
11	(19,12)	-0.0583	4 s	-0.9007	-1.0485	10 min	-0.8921	-1.0199	10 min
13	(21,13)	-0.0598	2 s	-0.9078	-1.0521	18 min	-0.8981	-1.0268	18 min
15	(25,15)	-0.0682	5 s	-0.9090	-1.0534	31 min	-0.8823	-1.0031	35 min
16	(27,16)	-0.0796	5 s	-0.9103	-1.0548	36 min	-0.8923	-1.0109	41 min
17	(29,17)	-0.0817	12 s	-0.9104	-1.0548	42 min	-0.8945	-1.0121	47 min
18	(29,18)	-0.1037	2 min						

as all singly occupied orbitals belonging to the three unpaired electrons are always included as well.

The data shows that the correlation energy for CASSCF decreases with the size of the active space, as expected. Likewise the MRCI energy based on the ROHF orbitals decreases systematically. The MRCI calculations based on CASSCF orbitals only decreases up to the (17,12) and (21,13) active space for CoF_2 and CoF_4 respectively and then suddenly increases when adding another orbital to the active space. The reason for the higher energies must be related to the CASSCF orbitals, since the MRCI@ROHF energies do not show this inconsistency. Although the CASSCF(17,11) and CASSCF(19,12) for CoF_4 yield almost identical energies, closer inspection of the orbitals reveals some significant difference in some orbitals: Two orbitals from the smaller active space with orbital energies of $-3.4 E_h$ and $-0.67 E_h$ are replaced in the larger active space by two orbitals with energies of $-2.1 E_h$ and $-1.97 E_h$. Thus there is one less core orbital available (considering a threshold of $-3 E_h$ to classify core orbitals). Adding the former core orbital to the active space will lower the MRCI energy significantly. Alternatively the core orbital may be frozen in the CASSCF. However, both approaches are inconsistent with the other calculations and will therefore not yield comparable energies.

In case of CASSCF(7,6) for CoF_2 the S_i based selection did not lead to a suitable active space. For one pair of degenerate orbitals only one of the two orbitals is included, leading to an overall symmetry breaking of the orbitals. Although the corresponding results follow the expected trends, they should not be considered being reliable.

The best energy estimates for CoF_2 with respect to the FCIQMC energy are obtained on the MRCI@CASSCF level using the (17,12) active space with $-0.5654 E_h$ (= 89.3 %) without Davidson correction and $-0.6213 E_h$ (= 98.2 %) including the Davidson correction. For CoF_4 the (17,11) active space yields $-0.9270 E_h$ (= 83.9 %) and $-1.0675 E_h$ (= 96.6 %) without and with Davidson correction respectively. However, even lower energies for the larger active spaces would have been expected. They suffer however from symmetry breaking in the CASSCF orbitals in case of CASSCF(27,16), CASSCF(29,17), CASSCF(29,18) and from core-valence orbital rotations in case of CASSCF(19,12) and CASSCF(21,13) and thus the resulting energies are based on qualitatively different orbitals.

4.2.4 Results for ρ_{ij} based selection

The tests for the ρ_{ij} and ϕ_{ij} based selection follow in principle the same procedure: First the DMRG based QIT data is analyzed, as described in Section 4.2.1, to identify orbital pair occupations which are then used to create a list of configurations that can be used as a reduced reference space for MRCI calculations. This list of configurations is used for orbital optimization (MCSCF) and compared to CASSCF using the same orbitals. MRCI calculations using only the reconstructed (selected) reference configurations as well as the full active space as reference space are then performed on all three sets of orbitals: the original ROHF orbitals (that were also used for the DMRG and QIT analysis), the MCSCF orbitals (optimized using the selected configurations only) as well as the CASSCF orbitals.

Different choices for the threshold parameters (I_{thresh} , ρ_{thresh} and c_{thresh}) are made such that the reconstruction of configurations as well as the MCSCF and MRCI calculations remain computationally feasible. If different tested values for the same threshold parameters yields the same results, only the tighter threshold value is presented in the following. The final choice of parameters is shown in Tables 4.7 and 4.10, together with the number of identified correlated orbitals, the number of resulting configurations that have been reconstructed, their norm in the DMRG wave function as well as the resulting active space. The label in the first column indicates corresponding results in the following tables. Note that the active space may deviate in its size from the number of correlated orbitals. On the one hand, the singly occupied orbitals are always added. On the other hand, removing configurations based on symmetry and number of electrons may only occasionally leave only one possible occupation for a certain orbital. Note furthermore that the number of configurations actually refers to the number of CON cards in the MOLPRO input, which only distinguishes between empty, single or double occupation for each orbital. The actual number of configurations, where α and β spin are distinguished, is thus somewhat larger. Empty fields always indicate a certain calculation did either not converge, or was not carried out due to high computational cost.

Tables 4.8, 4.9, 4.11 and 4.12 compare correlation energies, including the Davidson correction for CI calculations, and CPU times. Note that the CPU times are influenced by external factors, as resources may be shared with other jobs on the

same node. Furthermore, the number of iterations until each MCSCF calculation converges may be very different and affects the CPU time. Only the order of magnitude should therefore be considered.

Although only the size of the resulting active spaces is shown, it is obvious that they are different from the active space selection based on the 1-orbital entropy S_i in Tables 4.5 and 4.6. Here the active spaces have in general less electrons. i.e. the ρ_{ij} based selection prefers to include more virtual orbitals than the S_i based active space selection does.

Results for MCSCF and CASSCF calculations are given in Tables 4.8 and 4.11. The “CI@ROHF” column refers to CI calculations on the ROHF orbitals only considering the selected configurations. If the reconstruction of configurations is exact, i.e. corresponds to the MPS, this energy should correspond to the DMRG energy. In all cases, the correlation energy decreases when going from CI@ROHF over MCSCF to CASSCF, since the number of available optimization parameters for the electronic wave function is stepwise increased. Additionally, the energies in each column should decrease as the size of the active space and the norm is growing. This is true for most values, but there are two exceptions: The F2rho5 parameters yield much smaller energies than the F2rho6 do. Note that the latter has two more orbitals in its active space but a lower number of electrons. The MCSCF and CASSCF are thus not directly comparable. However the trend is in agreement with the slightly larger norm of F2rho5. Closer inspection of the MCSCF orbitals for F2rho5 reveals however that one of the core orbitals is rotated with one of the valence orbitals, resulting in a set of qualitatively very different orbitals. Accordingly, the corresponding MRCI@MCSCF results presented below yield comparatively bad energies. A similar issue was found for the F2rho7, F2rho8 and F2rho9 parameters, again only for the MCSCF orbitals.

The lowest energies are obtained for the largest selected active spaces. For CoF_2 those are F2rho7, F2rho8 and F2rho8, which are only different in the c_{thresh} parameters and thus result in the same active spaces. The resulting CASSCF(15,16) correlation energy is $-0.0705 E_h$. Compared to the S_i selected active spaces (cf. Table 4.5) of similar size (in number of orbitals) this is worse and required more CPU time. However, the F2roh4 CASSCF correlation energy ($-0.0522 E_h$) using a (11,11) active space is lower than the S_i based CASSCF(15,11) and CASSCF(19,13) corre-

lation energies ($-0.0310 E_h$ and $-0.0371 E_h$ respectively) at similar CPU time.

More promising results are obtained for CoF_4 . Here the CASSCF(21,17) (F4rho5, F4rho6, F4rho7) yields $-0.1412 E_h$, which is much lower than the $-0.0817 E_h$ obtained by the CASSCF(29,17) or even the $-0.1037 E_h$ of the CASSCF(29,18) calculations of the S_i based active space selection. It does however require more CPU time. Comparable CPU times are found for the CASSCF(19,13) (F4rho4) and CASSCF(21,13) (S_i based) calculations. They result in $-0.0645 E_h$ and $-0.0598 E_h$ respectively.

The MCSCF calculations are, in most cases, considerably faster than the CASSCF calculations due to the restricted number of configurations considered. Accordingly they result in a worse correlation energies. But still, they always recover a large portion ($>50\%$) of the corresponding CASSCF correlation energy. The main idea however, was to investigate how well a MRCI calculation will perform on these orbitals.

Various MRCI results are collected in Tables 4.9 and 4.12. The upper values only consider the selected, reconstructed configurations in the reference wave function, while in the lower part of the tables the whole set of configurations generated from the CAS as considered for the reference space. Obviously, the smaller reference space of selected configurations allows to perform MRCI calculations on much larger active spaces. For example the lowest correlation energy for the selected MRCI@MCSCF calculations is obtained for the F2rho6 parameters: $-0.5660 E_h$ ($=89.4\%$ of the FCIQMC reference) and $-0.6213 E_h$ ($=98.2\%$) with and without Davidson correction respectively. The best CAS MRCI@MCSCF results differ by less than $1 mE_h$ and took more than 10 times as much CPU time. Even the CAS MRCI@CASSCF, which should be the most reliable estimate, is only able to lower the correlation energy by $\approx 1 mE_h$. However, similar accuracy as for F2rho6 is obtained by the MRCI@CAS(17,12) (S_i based selection) at even less computational cost. Note that the MRCI@MCSCF results for F2rho5, F2rho7, F2rho8 and F2rho9, which are considerably worse than for F2rho6, are based on a qualitatively different set of orbitals, as already mentioned above. Furthermore the results demonstrate the greatly reduced computational cost due to the selected reference configuration, sacrificing accuracy in the order of $1 mE_h$.

Table 4.7: Selected threshold parameters for the ρ_{ij} based selection of configuration of the **CoF₂** model system. Additionally, the number of correlated orbitals that have been identified based on these parameters and the number of reconstructed configurations is given, together the norm of the corresponding CI vector in the MPS and active space of orbitals to allow for all reconstructed configurations. The labels in the first column indicate corresponding rows in the following tables.

label	I_{thresh}	ρ_{thresh}	c_{thresh}	# correlated orbitals	active space	# configurations	Norm
F2rho1	0.1	0.01	0	2	(5,5)	3	0.8785
F2rho2	0.01	0.1	0	2	(5,5)	2	0.8780
F2rho3	0.001	0.04	0	7	(9,8)	12	0.8995
F2rho4	0.01	0.03	0	10	(11,11)	36	0.9023
F2rho5	0.01	0.02	0	12	(13,12)	264	0.9053
F2rho6	0.001	0.03	0	23	(11,14)	60	0.9023
	0.001	0.02	0	30		880	0.9061
F2rho7	0.001	0.02	0.01	30	(15,16)	23	0.9054
F2rho8	0.001	0.02	0.001	30	(15,16)	58	0.9060
F2rho9	0.001	0.02	0.0001	30	(15,16)	149	0.9061

In general, similar observations are made for CoF₄ MRCI calculations. Although the correlation energy can be improve in the order of $10 mE_h$, they require much more CPU time compared to the S_i based active space selection. Furthermore the lower correlation energies are obtained at larger active spaces than the S_i based selection requires. Due to the above described issues in the CASSCF orbitals, direct comparison based on the available data is thus not possible. However, the ρ_{ij} based selection did lead to an active space more stable in the MCSCF/CASSCF calculations and thus resulting in improved MRCI energies. MRCI calculations with similar CPU times are on the order of $1 mE_h$ higher than the results of S_i based selection. In one case (F4rho6 MRCI@CASSCF) the selected configurations space leads to a lower energy at less CPU time, than the lowest CAS reference space (F4rho4 MRCI@CASSCF). For the MCSCF orbitals such a situation is not observed.

Based on the current results the ρ_{ij} based selection may yield improvement on the CASSCF results (lower energies, more stable orbitals) with respect to the S_i based active space selection. But this is strongly dependent on the system and choice of threshold parameters. More strongly correlated system seem to benefit more. On the MRCI level however, no significant improvement can be observed. Comparing the

Table 4.8: Resulting energies for applying the reconstructed configurations in a CI calculation based on the original orbitals (CI@ROHF) as well as optimizing the orbitals based on the reconstructed configurations only (MCSCF) and based on all active space configurations (CASSCF). Data is shown for the ρ_{ij} based selection of the **CoF₂** model system. Results being based on orbitals that do not reflect the expected degeneracies due to the molecular point group are indicated by a gray font color, while numbers printed in bold represent preserved symmetry.

label	CI@ROHF		MCSCF		CASSCF	
	energy	time	energy	time	energy	time
F2rho1	-0.0014	<1 s	-0.0021	<1 s	-0.0021	<1 s
F2rho2	-0.0014	<1 s	-0.0015	<1 s	-0.0021	<1 s
F2rho3	-0.0016	<1 s	-0.0016	<1 s	-0.0027	<1 s
F2rho4	-0.0026	<1 s	-0.0439	14 s	-0.0522	3 s
F2rho5	-0.0151	<1 s	-0.0540	26 s	-0.0580	7 s
F2rho6	-0.0041	<1 s	-0.0440	44 s	-0.0538	2 min
F2rho7	-0.0053	<1 s	-0.0482	7 s	-0.0705	44 min
F2rho8	-0.0157	<1 s	-0.0536	45 s	-0.0705	43 min
F2rho9	-0.0178	<1 s	-0.0494	34 s	-0.0705	55 min

selected set of configuration versus the full CAS configuration space calculations, similar MCSCF and MRCI energies may be obtained at much lower cost for the selected set of configurations. Again, this is strong depends on the chosen threshold parameters.

4.2.5 Results for ϕ_{ij} based selection

The application of the ϕ_{ij} based selection follows a similar scheme as the ρ_{ij} based selection above. For both test systems, CoF₂ and CoF₄, the selected threshold parameters I_{thresh} , ω_{thresh} , χ_{thresh} and c_{thresh} are summarized in Tables 4.13 and 4.16 while Tables 4.14, 4.15, 4.17 and 4.18 present the MCSCF and MRCI results.

Again, the constructed active spaces (cf. Tables 4.13 and 4.16) tend to prefer virtual orbitals over occupied ones, when compared to the S_i based selection (cf. Tables 4.5 and 4.6). Large threshold parameters lead to the same active space as for the ρ_{ij} based selection, however different configurations are constructed. Different active

Table 4.9: MRCI energies based on the ROHF, MCSCF and CASSCF orbitals. The upper rows consider the reconstructed/selected configurations for the reference space only. The lower rows consider the full active space as reference space. Data is shown for the ρ_{ij} based selection of the CoF_2 model system. Results being based on orbitals that do not reflect the expected degeneracies due to the molecular point group are indicated by a gray font color, while numbers printed in bold represent preserved symmetry.

label	MRCI@ROHF			MRCI@MCSCF			MRCI@CASSCF		
	energy	Davidson	time	energy	Davidson	time	energy	Davidson	time
selected reference configurations									
F2rho1	-0.5516	-0.6124	2 s	-0.5519	-0.6126	2 s	-0.5519	-0.6126	2 s
F2rho2	-0.5516	-0.6124	2 s	-0.5518	-0.6127	2 s	-0.5517	-0.6125	2 s
F2rho3	-0.5522	-0.6135	23 s	-0.5524	-0.6138	23 s	-0.5522	-0.6134	23 s
F2rho4	-0.5535	-0.6157	19 min	-0.5652	-0.6200	25 min	-0.5563	-0.6184	22 min
F2rho5	-0.5589	-0.6189	4 h	-0.5233	-0.5669	5 h	-0.5601	-0.6202	4 h
F2rho6	-0.5558	-0.6187	2 h	-0.5660	-0.6213	2 h	-0.5638	-0.6217	2 h
F2rho7	-0.5560	-0.6182	12 min	-0.5139	-0.5563	21 min	-0.5455	-0.6039	16 min
F2rho8	-0.5593	-0.6201	2 h	-0.5161	-0.5581	3 h	-0.5507	-0.6063	2 h
F2rho9	-0.5612	-0.6210	14 h	-0.5261	-0.5720	16 h	-0.5530	-0.6073	16 h
CAS reference configurations									
F2rho1	-0.5516	-0.6124	2 s	-0.5519	-0.6126	2 s	-0.5519	-0.6126	2 s
F2rho2	-0.5516	-0.6124	2 s	-0.5519	-0.6127	2 s	-0.5519	-0.6126	2 s
F2rho3	-0.5526	-0.6143	3 min	-0.5530	-0.6149	3 min	-0.5528	-0.6141	4 min
F2rho4	-0.5594	-0.6189	25 h	-0.5669	-0.6210	31 h	-0.5681	-0.6218	28 h
F2rho5	-0.5654	-0.6212	76 h	-0.5245	-0.5674	81 h	-0.5696	-0.6219	92 h

Table 4.10: Selected threshold parameters for the ρ_{ij} based selection of configuration of the CoF_4 D_{4h} model system. Additionally, the number of correlated orbitals that have been identified based on these parameters and the number of reconstructed configurations is given, together the norm of the corresponding CI vector in the MPS and active space of orbitals to allow for all reconstructed configurations.

label	I_{thresh}	ρ_{thresh}	c_{thresh}	# correlated orbitals	active space	# configurations	Norm
F4rho1	0.01	0.1	0	4	(9,7)	4	0.7814
F4rho2	0.01	0.05	0	13	(15,10)	16	0.8142
F4rho3	0.001	0.05	0	23	(15,10)	19	0.8142
F4rho4	0.01	0.04	0	15	(19,13)	32	0.8164
F4rho5	0.01	0.03	0	21	(21,17)	716	0.8273
F4rho6	0.01	0.03	0.01	21	(21,17)	29	0.8264
F4rho7	0.01	0.03	0.001	21	(21,17)	87	0.8273

Table 4.11: Resulting energies for applying the reconstructed configurations in a CI calculation based on the original orbitals (CI@ROHF) as well as optimizing the orbitals based on the reconstructed configurations only (MCSCF) and based on all active space configurations (CASSCF). Data is shown for the ρ_{ij} based selection of the **CoF₄** *D_{4h}* model system. Results being based on orbitals that do not reflect the expected degeneracies due to the molecular point group are indicated by a gray font color, while numbers printed in bold represent preserved symmetry.

label	CI@ROHF		MCSCF		CASSCF	
	energy	time	energy	time	energy	time
F4rho1	-0.0021	<1 s	-0.0098	<1 s	-0.0098	4 s
F4rho2	-0.0353	<1 s	-0.0485	3 s	-0.0501	2 s
F4rho3	-0.0354	<1 s	-0.0486	3 s	-0.0501	<1 s
F4rho4	-0.0372	<1 s	-0.0608	11 s	-0.0645	4 s
F4rho5	-0.0522	<1 s			-0.1412	10 min
F4rho6	-0.0427	<1 s	-0.0832	13 s	-0.1412	12 min
F4rho7	-0.0501	<1 s	-0.0970	4 min	-0.1412	10 min

Table 4.12: MRCI energies based on the ROHF, MCSCF and CASSCF orbitals. The upper rows consider the reconstructed/selected configurations for the reference space only. The lower rows consider the full active space as reference space. Data is shown for the ρ_{ij} based selection of the **CoF₄** *D_{4h}* model system. Results being based on orbitals that do not reflect the expected degeneracies due to the molecular point group are indicated by a gray font color, while numbers printed in bold represent preserved symmetry.

label	MRCI@ROHF			MRCI@MCSCF			MRCI@CASSCF		
	energy	Davidson	time	energy	Davidson	time	energy	Davidson	time
selected reference configurations									
F4rho1	-0.8816	-1.0345	29 s	-0.8951	-1.0481	34 s	-0.8950	-1.0481	44 s
F4rho2	-0.9004	-1.0566	2 min	-0.9200	-1.0629	2 min	-0.9004	-1.0566	2 min
F4rho3	-0.9061	-1.0505	3 min	-0.9200	-1.0630	3 min	-0.9005	-1.0568	2 min
F4rho4	-0.9078	-1.0527	23 min	-0.9225	-1.0638	26 min	-0.9068	-1.0623	23 min
F4rho6	-0.9165	-1.0614	4 h	-0.8669	-0.9831	4 h	-0.9314	-1.0780	4 h
F4rho7	-0.9182	-1.0624	44 h	-0.8594	-0.9720	43 h	-0.9355	-1.0804	42 h
CAS reference configurations									
F4rho1	-0.8817	-1.0348	44 s	-0.8952	-1.0483	49 s	-0.8952	-1.0483	69 s
F4rho2	-0.9218	-1.0648	8 min	-0.9214	-1.0643	7 min	-0.9218	-1.0648	8 min
F4rho3	-0.9071	-1.0516	8 min	-0.9214	-1.0643	6 min	-0.9218	-1.0648	7 min
F4rho4	-0.9107	-1.0562	17 h	-0.9263	-1.0679	20 h	-0.9313	-1.0732	20 h

spaces are obtained from tighter thresholds.

The CASSCF and MCSCF results are similar to the ρ_{ij} based selection. Again, for CoF_4 better CASSCF energies than for the S_i based active space selection can be obtained if similar numbers of orbitals in the active space are compared. Considering the CPU time mixed results are obtained. Similar, no clear trend is observed for CoF_2 . For example F2phi4 and F2phi6, with (9,13) and (11,12) active spaces respectively, yield significant lower energies ($-0.0537 E_h$ and $-0.0532 E_h$ respectively) than the S_i based (17,12) and (19,13) active spaces ($-0.0318 E_h$ and $-0.0371 E_h$ respectively). However the (11,18) active space of the F2phi7 parameters results in a much higher energy ($-0.1047 E_h$) than the S_i based (19,17) active space ($-0.1562 E_h$). CPU time for these calculations is comparable. The MCSCF results yield higher energies than their corresponding CASSCF calculation, at comparable CPU times. Unfortunately, most of the CoF_4 MCSCF calculations have issues with symmetry broken orbitals.

The lowest MRCI energy for CoF_2 (cf. Table 4.15) is obtained for the F2phi7 threshold parameters if only the selected reference configurations are used in connection with the MCSCF based on the selected reference calculations. Corresponding results using the full CAS reference space are not available due to high computational cost. However, this example yields lower energies at less CPU time compared to the full CAS reference space based on the F2phi3 parameters. The corresponding MRCI results based on the selected configuration reference space are only a couple of mE_h higher in energy, but significantly cheaper. In contrast to the ρ_{ij} based selection, using the MCSCF orbital for the selected reference space usually yields lower energies than using the CASSCF orbitals. However for the full CAS reference space the CASSCF orbitals tend to yield lower energies. Thus, the MRCI reference space should agree with the configuration space the orbitals have been optimized for.

Similar observations are made for CoF_4 in Table 4.18. Using the ϕ_{ij} selected configurations may yield similar energies at less CPU time and the MRCI reference space should agree with the configuration space the orbitals are optimized for. This time one may even observe lower energies at less CPU time for the selected reference space (F4phi4) compared to the full CAS reference space (F4phi3). This may either relate to the larger system (more orbitals) or more strongly correlated char-

Table 4.13: Selected threshold parameters for the ϕ_{ij} based selection of configuration of the **CoF₂** model system. Additionally, the number of correlated orbitals that have been identified based on these parameters and the number of reconstructed configurations is given, together the norm of the corresponding CI vector in the MPS and active space of orbitals to allow for all reconstructed configurations. The labels in the first column indicate corresponding rows in the following tables.

label	I_{thresh}	ω_{thresh}	χ_{thresh}	c_{thresh}	# correlated orbitals	active space	# configurations	Norm
F2phi1	0.1	0.01	0.01	0	2	(5,5)	3	0.8785
F2phi2	0.01	0.01	0.1	0	3	(5,6)	1	0.8673
F2phi3	0.001	0.1	0.01	0	10	(11,11)	100	0.9043
F2phi4	0.001	0.01	0.1	0	12	(9,13)	298	0.8674
F2phi5	0.01	0.02	0.01	0	11	(11,12)	280	0.9052
	0.01	0.01	0.01	0	17	(11,18)	14560	0.9058
F2phi6	0.01	0.01	0.01	0.01	17	(11,12)	23	0.9048
F2phi7	0.01	0.01	0.01	0.001	17	(11,18)	83	0.9058

acter of CoF₄. For the F4phi11 parameters the MRCI@MCSCF calculation results in significantly worse energies. The MCSCF orbitals are qualitatively as expected (no symmetry breaking), however the MCSCF is only 57% of the corresponding CASSCF energy, much less than in most other cases. A similar situation is observed for the F4phi6 case (MCSCF obtains 49% of the CASSCF energy), here however the MRCI@MCSCF is able to yield a very low correlation energy considering the required low CPU time. The exact reasons for the very different behavior of these two cases are unknown and would require a more detailed investigation.

In summary, the ϕ_{ij} based selection of configurations seems beneficial as a systematic approximation to the CI vector. Although, the effects are more pronounced for the CoF₄ case. The results of the active space selection however are unclear and depend on the specific case and suitable choice of threshold parameters.

Table 4.14: Resulting energies for applying the reconstructed configurations in a CI calculation based on the original orbitals (CI@ROHF) as well as optimizing the orbitals based on the reconstructed configurations only (MCSCF) and based on all active space configurations (CASSCF). Data is shown for the ϕ_{ij} based selection of the **CoF₂** model system. Results being based on orbitals that do not reflect the expected degeneracies due to the molecular point group are indicated by a gray font color, while numbers printed in bold represent preserved symmetry.

label	CI@ROHF		MCSCF		CASSCF	
	energy	time	energy	time	energy	time
F2phi1	-0.0014	<1 s	-0.0021	<1 s	-0.0021	<1 s
F2phi2	-0.0015	<1 s	-0.0017	<1 s	-0.0021	<1 s
F2phi3	-0.0058	<1 s	-0.0480	<1 s	-0.0522	2 s
F2phi4	-0.0030	<1 s	-0.0228	10 s	-0.0537	26 s
F2phi5	-0.0196	<1 s	-0.0505	11 s	-0.0532	6 s
F2phi6	-0.0050	<1 s	-0.0427	14 s	-0.0532	6 s
F2phi7	-0.0143	<1 s	-0.0557	3 h	-0.1047	3 h

Table 4.15: MRCI energies based on the ROHF, MCSCF and CASSCF orbitals. The upper rows consider the reconstructed/selected configurations for the reference space only. The lower rows consider the full active space as reference space. Data is shown for the ϕ_{ij} based selection of the **CoF₂** model system. Results being based on orbitals that do not reflect the expected degeneracies due to the molecular point group are indicated by a gray font color, while numbers printed in bold represent preserved symmetry.

label	MRCI@ROHF			MRCI@MCSCF			MRCI@CASSCF		
	energy	Davidson	time	energy	Davidson	time	energy	Davidson	time
selected reference configurations									
F2phi1	-0.5516	-0.6124	2 s	-0.5519	-0.6126	2 s	-0.5519	-0.6126	2 s
F2phi2	-0.5518	-0.6127	10 s	-0.5518	-0.6126	10 s	-0.5519	-0.6128	11 s
F2phi3	-0.5542	-0.6160	41 min	-0.5660	-0.6203	47 min	-0.5582	-0.6189	42 h
F2phi4	-0.5543	-0.6166	47 h	-0.5576	-0.6156	71 h	-0.5105	-0.5613	68 h
F2phi5	-0.5579	-0.6174	2 h	-0.5674	-0.6214	3 h	-0.5585	-0.6190	3 h
F2phi6	-0.5542	-0.6162	16 min	-0.5649	-0.6202	22 min	-0.5575	-0.6187	20 min
F2phi7	-0.5579	-0.6202	11 h	-0.5703	-0.6254	12 h	-0.5602	-0.6226	12 h
CAS reference configurations									
F2phi1	-0.5516	-0.6124	2 s	-0.5519	-0.6126	2 s	-0.5519	-0.6126	2 s
F2phi2	-0.5519	-0.6128	14 s	-0.5519	-0.6126	14 s	-0.5520	-0.6128	17 s
F2phi3	-0.5594	-0.6189	25 h	-0.5677	-0.6212	28 h	-0.5681	-0.6218	27 h

Table 4.16: Selected threshold parameters for the ϕ_{ij} based selection of configuration of the \mathbf{CoF}_4 D_{4h} model system. Additionally, the number of correlated orbitals that have been identified based on these parameters and the number of reconstructed configurations is given, together the norm of the corresponding CI vector in the MPS and active space of orbitals to allow for all reconstructed configurations. The labels in the first column indicate corresponding rows in the following tables.

label	I_{thresh}	ω_{thresh}	χ_{thresh}	c_{thresh}	# correlated orbitals	active space	# configurations	Norm
F4phi1	0.1	0.01	0.1	0	6	(9,7)	4	0.7814
F4phi1	0.01	0.1	0.1	0	4	(9,7)	4	0.7814
F4phi2	0.03	0.03	0.03	0	7	(13,11)	16	0.7992
F4phi3	0.1	0.01	0.01	0	8	(15,10)	16	0.8142
F4phi4	0.03	0.02	0.02	0	9	(15,12)	32	0.8146
F4phi5	0.02	0.02	0.03	0	11	(13,15)	144	0.8027
F4phi6	0.02	0.02	0.03	0.01	11	(13,15)	13	0.8024
F4phi7	0.02	0.02	0.03	0.001	11	(13,15)	38	0.8027
F4phi8	0.02	0.02	0.03	0.0001	11	(13,15)	73	0.8027
	0.02	0.02	0.02	0	13		3200	0.8236
F4phi9	0.02	0.02	0.02	0.01	13	(15,16)	37	0.8220
F4phi10	0.02	0.02	0.02	0.001	13	(15,16)	146	0.8235
	0.01	0.1	0.01	0	16		864	0.8269
F4phi11	0.01	0.1	0.01	0.01	16	(21,18)	27	0.8258
F4phi12	0.01	0.1	0.01	0.001	16	(21,18)	107	0.8269
	0.02	0.01	0.01	0	17		56658	0.8328
F4phi13	0.02	0.01	0.01	0.01	17	(21,20)	48	0.8305
F4phi14	0.02	0.01	0.01	0.001	17	(21,20)	228	0.8326

Table 4.17: Resulting energies for applying the reconstructed configurations in a CI calculation based on the original orbitals (CI@ROHF) as well as optimizing the orbitals based on the reconstructed configurations only (MCSCF) and based on all active space configurations (CASSCF). Data is shown for the ϕ_{ij} based selection of the CoF_4 D_{4h} model system. Results being based on orbitals that do not reflect the expected degeneracies due to the molecular point group are indicated by a gray font color, while numbers printed in bold represent preserved symmetry.

label	CI@ROHF		MCSCF		CASSCF	
	energy	time	energy	time	energy	time
F4phi1	-0.0021	<1 s	-0.0098	<1 s	-0.0098	3 s
F4phi2	-0.0104	<1 s	-0.0274	9 s	-0.0381	2 s
F4phi3	-0.0353	<1 s	-0.0485	4 s	-0.0501	2 s
F4phi4	-0.0389	<1 s	-0.0543	29 s	-0.0662	3 s
F4phi5	-0.0231	<1 s	-0.0563	60 s	-0.0888	3 min
F4phi6	-0.0199	<1 s	-0.0437	17 s	-0.0888	3 min
F4phi7	-0.0228	<1 s	-0.0516	3 min	-0.0888	3 min
F4phi8	-0.0231	<1 s	-0.0560	70 s	-0.0888	2 min
F4phi9	-0.0565	<1 s	-0.0808	10 s	-0.1156	16 min
F4phi10	-0.0688	<1 s	-0.0905	59 s	-0.1156	14 min
F4phi11	-0.0511	<1 s	-0.0811	14 s	-0.1430	2 h
F4phi12	-0.0595	<1 s	-0.0991	21 s	-0.1430	21 s
F4phi13	-0.0650	<1 s	-0.0947	28 s		
F4phi14	-0.0800	2 s	-0.1205	32 s		

Table 4.18: MRCI energies based on the ROHF, MCSCF and CASSCF orbitals. The upper rows consider the reconstructed/selected configurations for the reference space only. The lower rows consider the full active space as reference space. Data is shown for the ϕ_{ij} based selection of the $\text{CoF}_4 D_{4h}$ model system. Results being based on orbitals that do not reflect the expected degeneracies due to the molecular point group are indicated by a gray font color, while numbers printed in bold represent preserved symmetry.

label	MRCI@ROHF			MRCI@MCSCF			MRCI@CASSCF		
	energy	Davidson	time	energy	Davidson	time	energy	Davidson	time
selected reference configurations									
F4phi1	-0.8816	-1.0345	26 s	-0.8951	-1.0481	34 s	-0.8950	-1.0481	34 s
F4phi2	-0.8901	-1.0423	28 min	-0.9056	-1.0561	35 min	-0.8991	-1.0571	21 min
F4phi3	-0.9061	-1.0504	21 min	-0.9200	-1.0629	2 min	-0.9004	-1.0566	2 min
F4phi4	-0.9086	-1.0535	55 min	-0.9230	-1.0656	61 min	-0.9017	-1.0603	51 min
F4phi6	-0.9003	-1.0534	4 h	-0.9164	-1.0664	5 h	-0.9091	-1.0653	5 h
F4phi7	-0.9017	-1.0551	70 h	-0.9195	-1.0682	72 h	-0.9108	-1.0672	79 h
F4phi9	-0.9234	-1.0658	7 h	-0.9345	-1.0741	9 h	-0.9164	-1.0727	10 h
F4phi11	-0.9211	-1.0642	6 h	-0.8775	-0.9965	6 h	-0.9313	-1.0770	7 h
F4phi12	-0.9229	-1.0652	74 h	-0.9447	-1.0804	76 h	-0.9365	-1.0794	91 h
F4phi13	-0.9289	-1.0697	17 h	-0.8706	-0.9858	23 h			
CAS reference configurations									
F4phi1	-0.8817	-1.0348	40 s	-0.8952	-1.0483	52 s	-0.8952	-1.0483	52 s
F4phi2	-0.8970	-1.0498	5 d	-0.9107	-1.0609	6 d	-0.9145	-1.0650	4 d
F4phi3	-0.9071	-1.0516	7 min	-0.9214	-1.0643	7 min	-0.9218	-1.0648	7 min
F4phi4	-0.9156	-1.0589	11 d						

4.2.6 Summary

The selection of configurations based on QIT was tested for two different approaches and has been applied to two different model systems. Both selection schemes can lead to active spaces yielding lower CASSCF energies, but this depends strongly on the test case and choice of threshold parameters. This does imply that active space selection based on 1-orbital entropies S_i only, as recently demonstrated by Stein and Reiher [29], is not always the best approach.

Overall, the ϕ_{ij} based selection seems more promising than the ρ_{ij} based selection, especially for the CoF₄ system. The reason might be the larger size (more orbitals) or the more strongly correlated character of this system. Application to more test systems should elucidate these questions. In general, the here provided data is very limited and may thus not yield statistically reliable insights. Alternatively, further selection schemes based on the QIT data can be considered. The two approaches suggested here are rather arbitrary and better algorithms might be possible. The present investigation therefore only represents a first proof of principle. Further tests and more a detailed analysis are required to draw more rigorous conclusions.

It should also be noted, that the tested model systems are still rather abstract. Although motivated by real, existing molecules, the constructed models have not been validated against experimental data (e.g. thermodynamic stability). Additionally, using FCI (or FCIQMC) energies as a reference for the reached accuracy has limited relevance for experimentally available properties. The accuracy in the total energy does not necessarily correlate with the accuracy in various properties like dissociation energies, vibrational frequencies or magnetic properties. Extending the test cases to strongly correlated systems with available data for properties of interest would provide a more reliable foundation to validate the approximations on an empirical basis.

A drawback is that the QIT analysis requires an approximate CI solution. This may be obtained by DMRG, for which the QIT data is usually readily available, but not all systems are suitable for this method. Implementation of a QIT analysis for different methods is in principle possible, as here exemplary done for the 1-orbital entropies based on FCIQMC calculation, but not widely available. Additionally, the

restriction to the 2-RDMs limits accuracy and higher order correlations might provide a more reliable reconstruction of the CI vector. However, their implementation would require increased computational resources.

The selection scheme may be extended to higher order correlations. Extending the reconstruction of the CI vector to e.g. 3- and 4-orbital correlations, would require larger numerical parameters for the approximate CI calculation as well as the actual construction of the corresponding RDMs. Additionally, the increased amount of data needs to be processed in the reconstruction of the configurations. Thus the restriction to 1- and 2-RDMs may provide a reasonable trade off between accuracy and computational cost. However, further research to support this statement is necessary.

The performance of the here proposed approach strongly depends on the initial CI calculation, on which the QIT analysis is based. The QIT analysis is known to yield qualitatively stable results with respect to a limited DMRG accuracy (number of blockstates). A similar argument is possible for FCIQMC, where the number of walkers may be kept fairly small. Although the resulting total energy estimate may be useless regarding their accuracy, the here proposed method can still leverage from the reduced computational cost: Only qualitative results are required for the QIT analysis, while high accuracy may be obtained by the multi-reference calculation in the final step. For the overall approach to be computationally more efficient than the conventional approach (CASSCF+MRCI), the new reference space needs to be small enough to compensate for additional the cost of the QIT analysis and preceding approximate CI calculation. However, the large scaling of the number of configurations that can be constructed based on an active space should be easy to overcome, especially for large active spaces.

As further extensions, an iterative optimization of the orbitals and QIT analysis of the wave function may be considered. So far, the QIT analysis was only performed on the initial ROHF orbitals. Performing a new QIT analysis of the MCSCF orbitals may further improve the description of the strong correlation. Especially if drastic changes between the HF and MCSCF orbitals occur, an iterative optimization may be required. The QIT based selection may also be applied to other multi-reference approaches, such as MRCC or the recently published tailored Coupled Cluster method [16]. And finally, different definitions and values for the threshold

parameters can be considered. In their current form, these values are highly system dependent and require a manual selection. Modification of these parameters, in a similar way as Stein and Reiher [121] did for measuring the multi-configurational character based on orbital entanglement, is possible and may result in a set system independent parameters.

4.3 Combining DMRG with the Incremental Approach

Both, DMRG and MoI, are established methods for treatment of electron correlation. Both are connected to approaches quantifying the electron correlation contributions. While QIT is strongly related to DMRG, in the MoI the individual increment of each center may be analyzed directly. In order to relate the increments to QIT, it is however required to assign each orbital to its own center. Similarities and differences between both measures have already been discussed in Section 2.5.3. In the following however, selected model systems will be investigated by applying QIT and the MoI to demonstrate, on a purely empirical bases, that there is indeed some correspondence between the two measures.

The selected model systems cover conjugated *trans*-polyacetylenes, more specifically hexatriene (C_6H_8), where different types of bonds (σ and π) can be compared, Be_6 rings at small and large separation providing an example of strong correlation, and the linear CoF_2 molecule as an open shell example. Results for the former two systems have already been published and discussed in Ref. [122]. For the DMRG calculations and QIT analyses the Budapest DMRG program [114] was used. The HF calculations, orbital localization and integral files (FCIDUMP) generation was done using the MOLPRO software package [94, 113].

4.3.1 Polyacetylene

Hexatriene (C_6H_8) provides a simple model system, featuring different kind of bonds, C–H and C–C σ bonds as well as C=C π bonds. All data in this section is taken

Table 4.19: Total energy and correlation energy for *trans*-hexatriene obtained with different methods using a cc-pVTZ basis set. All energies are in E_h . Table adopted from Ref. [122].

	Total Energy	Correlation Energy
HF	-231.883732	
DMRG(32,32)	-231.971288	-0.087556
CCSD	-232.891987	-1.008255

Table 4.20: Correlation energies obtained with various MoI variants for *trans*-hexatriene using a cc-pVTZ basis set. Occupied orbitals have been localized using the Pipek-Mezey method. All energies are in E_h . Table adopted from Ref. [122].

	Level	Correlation Energy	Summed Correlation Energy
CAS(32,32)-MoI (occupied)	1	-0.053475	-0.053475 (61.1 %) ^a
	2	-0.035636	-0.089111 (101.8 %) ^a
	3	+0.000988	-0.088122 (100.6 %) ^a
	4	+0.000393	-0.087729 (100.2 %) ^a
CAS(32,32)-MoI (virtual)	1	-0.022884	-0.022884 (26.1 %) ^a
	2	-0.063367	-0.086251 (98.5 %) ^a
	3	-0.003104	-0.089355 (102.1 %) ^a
	4	+0.001568	-0.087787 (100.3 %) ^a
CCSD-MoI (occupied)	1	-0.511070	-0.511070 (50.7 %) ^b
	2	-0.552483	-1.063553 (105.5 %) ^b
	3	+0.060588	-1.002969 (99.5 %) ^b

a) Correlation energy relative to DMRG(32,32) reference

b) Correlation energy relative to CCSD reference.

from Ref. [122].

The construction of the orbitals is described in Section 3.2 and yields a CAS(32,32), for which MoI and DMRG calculations have been performed. DMRG calculations are performed with the DMRG Budapest code [114]. Using DBSS with a density matrix cutoff of 1×10^{-6} and a maximum number of blockstates $M_{\max} = 2048$, highly accurate energies are obtained. For the QIT data however, using $M_{\max} = 128$ is sufficient.

Reference energies for HF (no correlation), DMRG(32,32) (static correlation) and CCSD (dynamic correlation) of the system are given in Table 4.19. Correlation

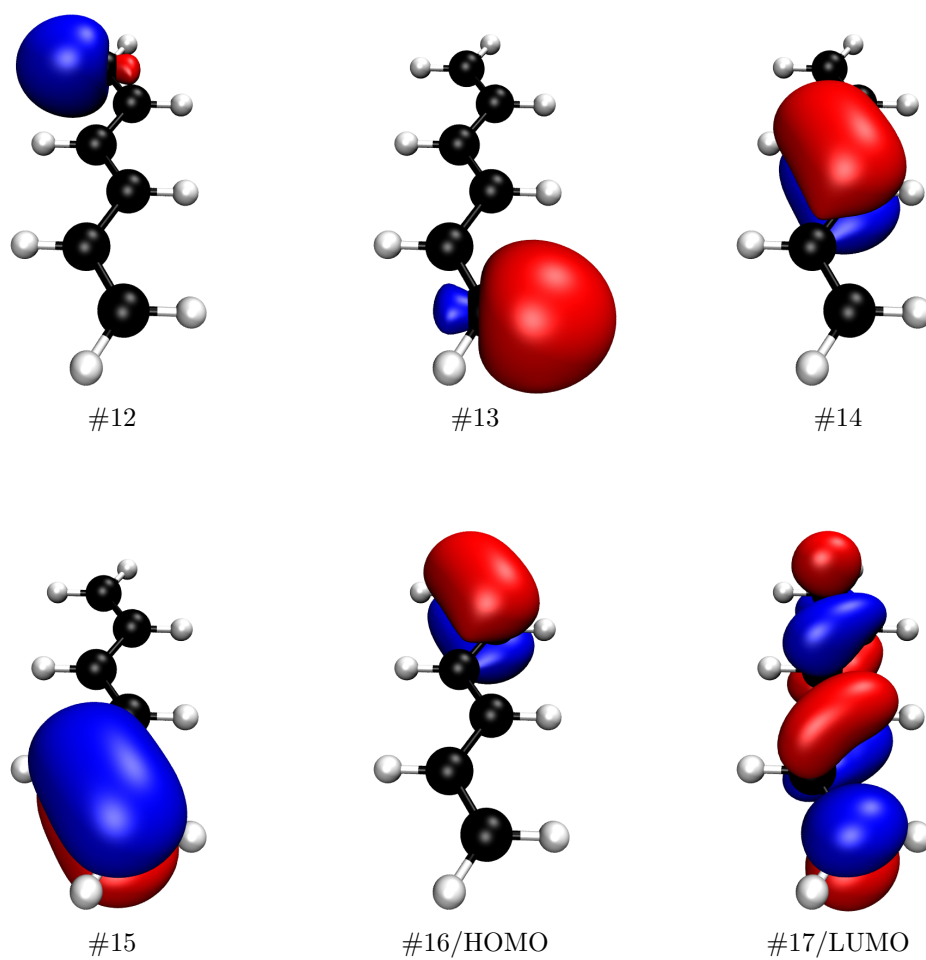


Figure 4.7: Isosurface plot ($|\psi(\vec{r})| = 0.05 a_0^{-1.5}$) for the localized occupied molecular orbitals #12 to #16 and the canonical virtual molecular orbital #17. Figure adopted from Ref. [122].

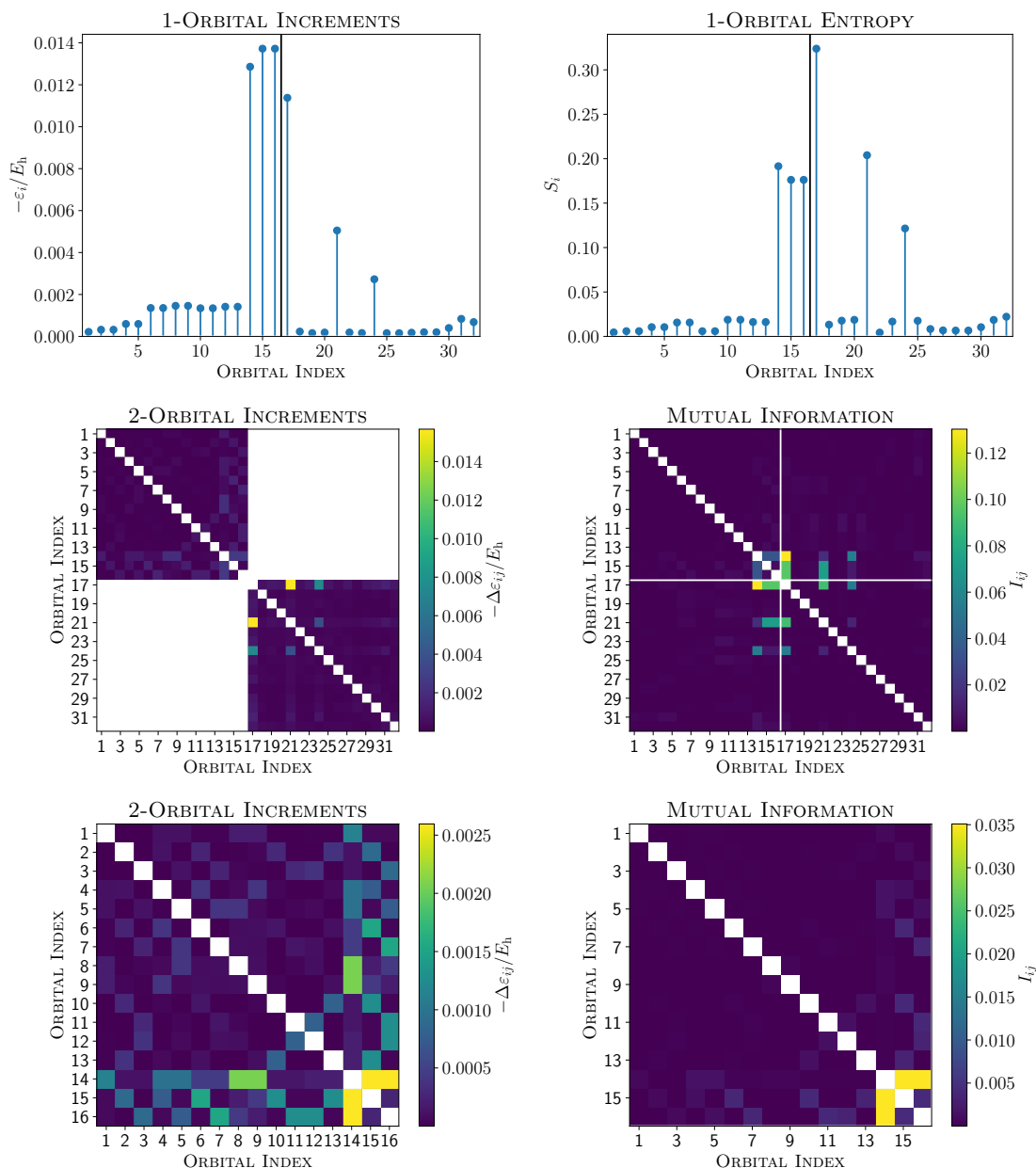


Figure 4.8: Polyacetylene: Comparison of Increments and Orbital Entropies for quantifying orbitals correlations. Left and right column show results based on Methods of Increments (MoI) and Quantum Information Theory (QIT) respectively. The upper and middle row show 1-orbital and 2-orbital correlations respectively. The Highest Occupied Molecular Orbital (HOMO) and Lowest Unoccupied Molecular Orbital (LUMO) are separated by black and white lines respectively. In the lower row the 2-orbital correlations among occupied orbitals are shown as a zoom in. MoI increments are based on CASCI(32,32)/cc-pVTZ calculations. Figure adopted from Ref. [122].

energies obtained from different MoI expansions are summarized in Table 4.20. The conventional CCSD-MoI approach, using CCSD to calculate each increment expanded in terms of occupied orbitals, converges within 1% of the corresponding reference energy at the 3-orbital increment level. The CAS(32,32)-MoI expansion in occupied orbitals converges at this level as well, only the virtual CAS(32,32)-MoI expansion requires 4-orbital increments to achieve the same level of accuracy.

To discuss the differences between the increments and QIT results, the 1- and 2-orbital measures of the CAS(32,32) calculations are presented in Fig. 4.8. A subset of the active space orbitals is depicted by their isosurfaces in Fig. 4.7. The data on the whole set of orbitals is available in the supplementary information of Ref. [122]. Note that the 2-orbital increments do not show pair correlations between occupied and virtual orbitals, as this data is not available by the incremental approach.

The 1-orbital measures (top row in Fig. 4.8) are very similar to each other. Although there are some qualitative differences, they are quantitatively small. For example according to the 1-orbital increments MO #14, representing the π bond on the center of the PAC molecule, is slightly less correlated than the terminal π bonds #15 and #16 on both ends of the chain. In reality however, one would expect the central π bond to be more correlated, as it has neighboring orbitals to correlate with. This is indeed reflected by the 1-orbital entropy, however the relative deviations between MO #14 and MOs #15 and #16 is rather small for both measures. Another, very obvious difference is the very large 1-orbital entropy of the LUMO (MO #17). Measured by the 1-orbital increments it is smaller than the HOMO. However the latter compares results for different MoI expansion (in terms of occupied and virtual orbitals) and direct comparison between those two sets of orbitals is not possible.

The 2-orbital measures (middle row in Fig. 4.8) show similar patterns as well. The major correlations which can be identified by the 2 measures yield the same orbital pairs, and both indicate same negligible pair-correlation. Although the 2-orbital increments seem to present more details and a better resolution of the values (colors) than the mutual information, this is mainly a problem of graphic representation. The zoom-in of the occupied orbitals in the lower row of Fig. 4.8 partially reconciles this issue. Overall, the trend of the most correlated orbitals is the same for the increments and QIT measure and results may therefore be translated from one approach to the other for this model system.

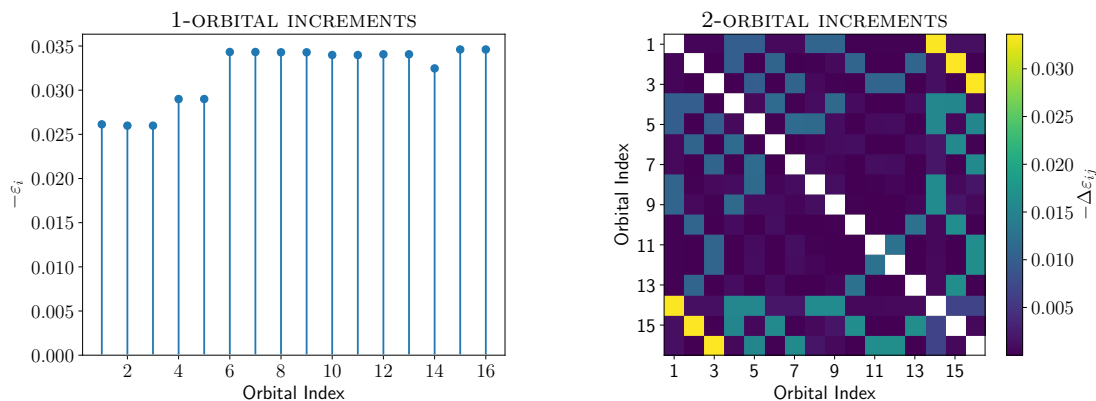


Figure 4.9: Polyacetylene: Occupied orbital increments including dynamical correlations based on CCSD/cc-pVTZ calculations. Figure adopted from Ref. [122].

The above results may also be chemically interpreted, at least for the occupied molecular orbitals. Most of the static correlation character is related to the (nearly) degenerated π orbitals of the C=C double bonds, while the contributions of all C-C and C-H σ bonds are much smaller. Furthermore the 2-orbital correlations show that neighboring orbitals have much more correlation than orbital being further apart from each other. For example MOs #13 and #15 are on the same end of the molecule and show medium values in the 2-orbital increments and mutual information, while correlations with MO #12 on the other end of the chain are negligible. For σ orbitals spatially overlapping with π orbitals, e.g. orbital pairs #1#14, #2#15 and #3#16, correlations of intermediate strength are observed. Those correlations represent the dynamic σ polarization which allows for more fluctuations in the π orbitals [123, 124].

The 1- and 2-orbital increments based on the CCSD-MoI in terms of occupied orbitals are shown in Fig. 4.9 and allow to compare the dynamical correlation effects to the static ones. No DMRG calculation has been performed, as this method is not suited or designed to treat the enormous number of configurations related to dynamic correlation. Although a QIT analysis based on other methods than DMRG is in principle possible, it is not readily implemented in the various codes available.

Compared to the static correlation, the 1- and 2-orbital increments related to dynamic correlation are much larger, which is consistent with the increased correlation energy. The smallest increments are the MOs #1 to #5, which correspond to the

C–C σ bonds, which is also observed in the CAS-MoI calculations. However, MOs #6 to #13, representing C–H bonds, are now on par with the C=C π bond orbitals #14 to #16.

4.3.2 Be₆ Rings

To demonstrate the above observations are not unique to weakly correlated systems, a further, more strongly correlated, example is provided by considering Be₆ rings. Two situations will be investigated in the following, with internuclear distance close to equilibrium distance ($R = 2.2 \text{ \AA}$) as well as at the dissociation limit ($R = 3.5 \text{ \AA}$). All data in this section is taken from Ref. [122].

The orbitals are constructed according to Section 3.3, i.e. an active space of 12 electrons in 78 orbitals is considered. Selecting virtual, localized orbitals for the active space is more difficult, as they have more abstract shapes and their chemical interpretation is less meaningful than for the occupied orbitals. DMRG calculations without prior knowledge of an optimized orbital ordering are possible, but cumbersome in this situation. The space of virtual orbital is therefore screened by calculating the corresponding 1-orbital increments, which yields a set of 78 individual calculations with a (12,7) active space each, i.e. only a single empty orbital needs to be correlated. A user-defined threshold for the 1-orbital increments is then used to select the virtual orbitals for a DMRG calculation on a smaller active space.

Similar to the polyacetylene calculations the DMRG Budapest code [114] was used. A density matrix cutoff for the DBSS approach of 1×10^{-6} is used and the maximum number of blockstates is restricted to $M_{\text{max}} = 1024$ as the larger active space requires more memory.

All 1-orbital increments are plotted in Fig. 4.10. For both situations, equilibrium distance and dissociation limit, a set of 24 orbitals with 1-orbital increments close to zero and a clear split to the next largest values can be found. Those orbitals are thus removed from the active space for the DMRG calculations.

Total energies and correlation energies for HF, CCSD(T), CAS(12,78)-MoI and DMRG(12,54) are summarized in Table 4.21. As a reference the CCSD(T) dissocia-

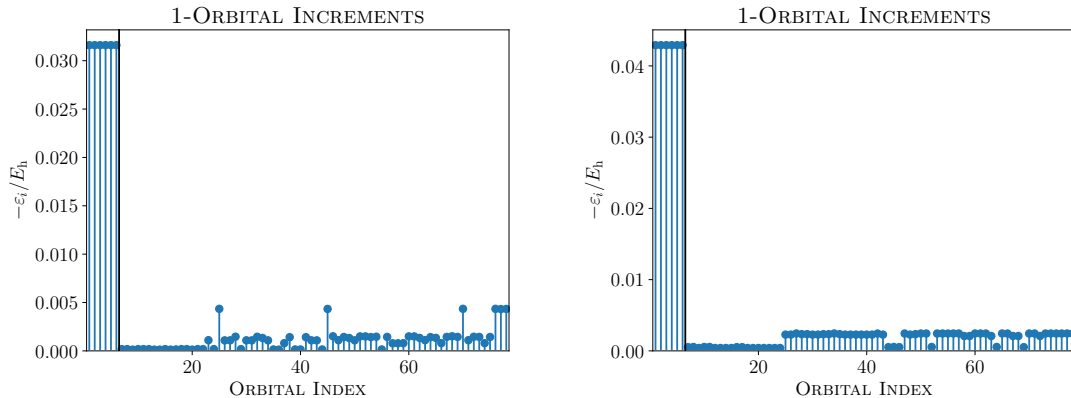


Figure 4.10: 1-Orbital increments for the Be_6 ring at equilibrium distance ($R = 2.2 \text{ \AA}$) and dissociation limit ($R = 3.5 \text{ \AA}$) to the left and right respectively. The black vertical line separates occupied and virtual orbitals. Virtual orbitals are in arbitrary order. Figure adopted from Ref. [122].

Table 4.21: Total energy and correlation energy for a Be_6 ring obtained with different methods using a cc-pVDZ basis set. All energies are in E_h . Table adopted from Ref. [122].

	Total Energy		Correlation Energy		Dissociation Energy
	$R = 2.2 \text{ \AA}$	$R = 3.5 \text{ \AA}$	$R = 2.2 \text{ \AA}$	$R = 3.5 \text{ \AA}$	
HF	-87.573755	-87.421411			0.152344
CCSD(T) (canonical)	-87.828746	-87.701393	-0.254991	-0.279981	0.127353
DMRG(12,54)	-87.777764	-87.644043	-0.204009	-0.222632	0.133721
CAS(12,78)-MoI (occ.)	-87.831646	-87.703778	-0.257890	-0.282367	0.127868
1-orbital			-0.189642	-0.257473	
2-orbital			-0.068249	-0.024894	
CAS(12,78)-MoI (virt.)	-87.824877	-87.694914	-0.251122	-0.273503	0.129963
1-orbital			-0.082232	-0.123687	
2-orbital			-0.131174	-0.091626	
3-orbital			-0.037715	-0.058190	

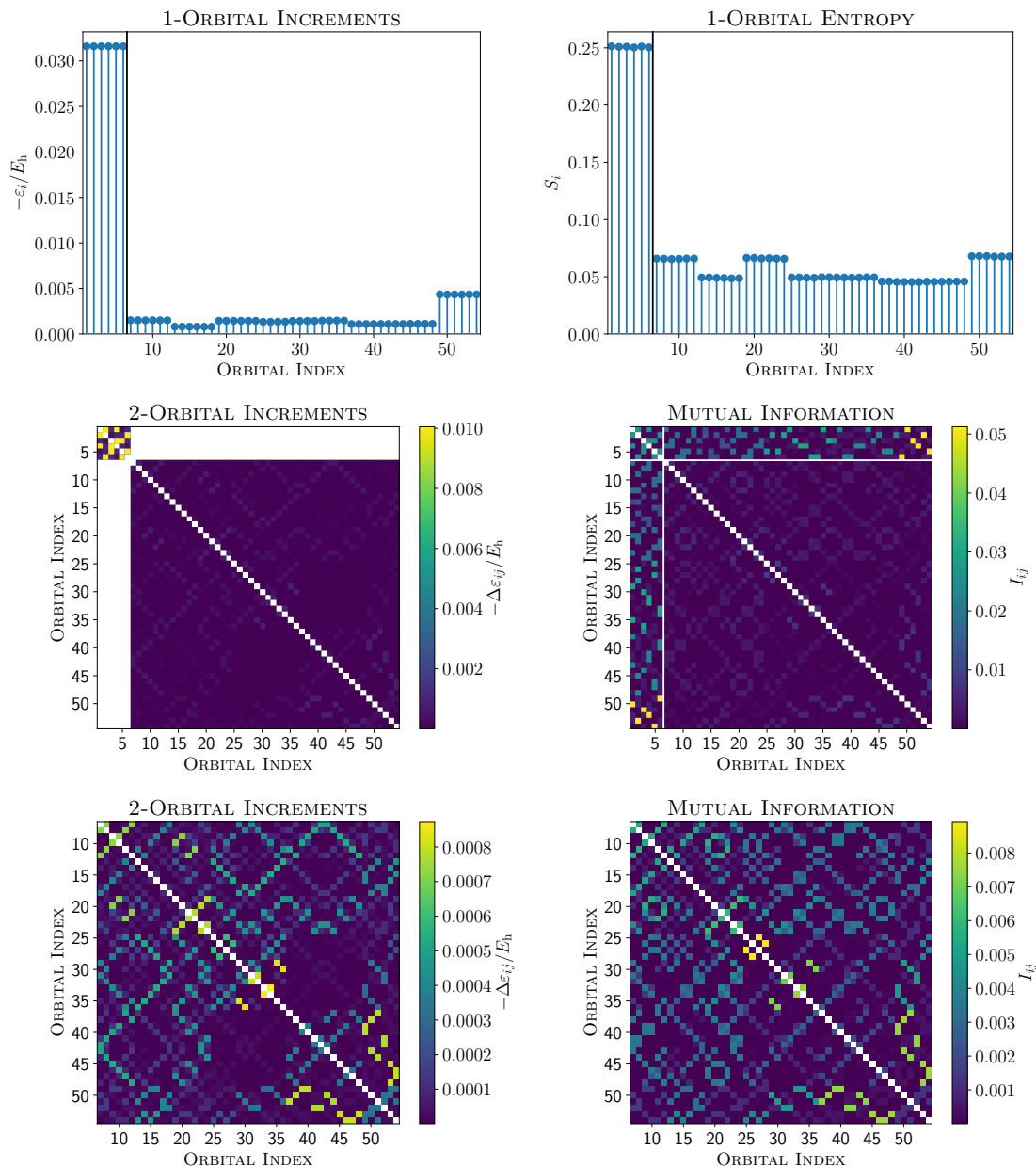


Figure 4.11: Be_6 at equilibrium distance ($R = 2.2 \text{ \AA}$). Comparison of Increments and Orbital Entropies for quantifying orbital correlations. Left and right column show results based on Methods of Increments (MoI) and Quantum Information Theory (QIT) respectively. The upper and middle row show 1-orbital and 2-orbital correlations respectively. The Highest Occupied Molecular Orbital (HOMO) and Lowest Unoccupied Molecular Orbital (LUMO) are separated by black and white lines respectively. In the lower row the 2-orbital correlations among virtual orbitals are shown. All orbitals are ordered by increasing diagonal Fock matrix element. Figure adopted from Ref. [122].

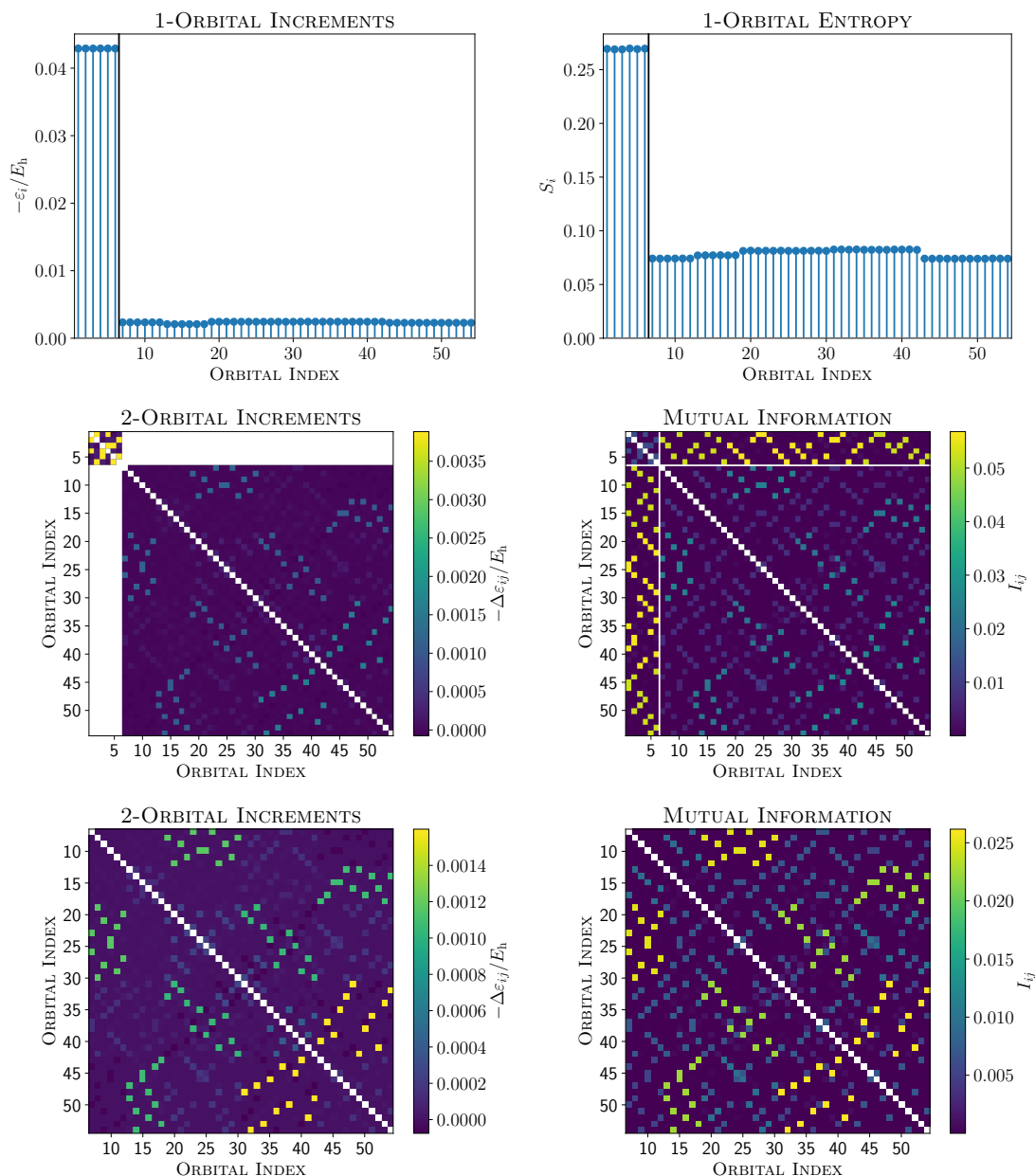


Figure 4.12: Be_6 at dissociation limit ($R = 3.5 \text{ \AA}$). Comparison of Increments and Orbital Entropies for quantifying orbital correlations. Left and right column show results based on Methods of Increments (MoI) and Quantum Information Theory (QIT) respectively. The upper and middle row show 1-orbital and 2-orbital correlations respectively. The Highest Occupied Molecular Orbital (HOMO) and Lowest Unoccupied Molecular Orbital (LUMO) are separated by black and white lines respectively. In the lower row the 2-orbital correlations among virtual orbitals are shown. All orbitals are ordered by increasing diagonal Fock matrix element. Figure adopted from Ref. [122].

tion energy is considered. The DMRG total energies are higher than for CCSD(T), as the reduced active space is missing dynamic correlation. However, the DMRG dissociation limit deviates only by $5 mE_h$. The MoI result, using the whole orbital space, are closer to the CCSD(T) reference. Similar to the polyacetylene example, convergence of the MoI expansion in terms of virtual orbitals is not as good as for the occupied orbital expansion and increments of higher order are required for similar accuracy.

The increments and QIT results for the Be_6 ring at equilibrium distance ($R = 2.2 \text{ \AA}$) and dissociation limit ($R = 3.5 \text{ \AA}$) are compared in Figs. 4.11 and 4.12 respectively. As before with the polyacetylene example, both measures yield roughly similar results. Similar patterns of the major/vanishing contributions can be identified, but quantitative deviations occur. Despite the 24 virtual orbitals removed from the active space, the mutual information is in well agreement with the 2-orbital increments. At the dissociation limit, the 6-fold degeneracy of all orbitals is clearly visible in all data (cf. Fig. 4.12). Different groups of 6 orbitals are easily identified. At equilibrium, the localization did not always yield perfectly degenerate orbitals (cf. SI of Ref. [122]). All groups of 6 (close)-degenerate orbitals can still be identified based on the 1-orbital correlation measures (ε_i and S_i), but not always in the 2-orbital correlation measures (cf. Fig. 4.11).

4.3.3 Open Shell CoF_2

As a final example the CoF_2 molecule in its open shell quartet ground-state (${}^4\Delta_g$) is considered. Applying the MoI scheme to open shell systems is challenging, since the original increment approach was formulated for closed shell cases only. The presence of singly occupied orbitals introduces a third set of orbitals, next to the doubly occupied (closed) and virtual (empty) orbitals of the HF reference wave function. In the approach chosen by Müller and Paulus [82] only one unpaired electron is considered and the singly occupied orbital is correlated with each increment. Thus a new 1-center increment is defined as

$$\tau_i = E_{i\star} - E_{\text{HF}} = \Delta\varepsilon_{i\star} + \varepsilon_i \quad (4.3)$$

where a one-center increment for the singly occupied orbital ε_{\star} vanishes. The MoI expansion Eq. (2.135) is then modified and expressed in terms of the increments τ to yield the correlation energy

$$E_{\text{corr}} = \sum_i \tau_i + \sum_i \sum_{j>i} \Delta\tau_{ij} + \sum_i \sum_{j>i} \sum_{k>j} \Delta\tau_{ijk} + \dots \quad (4.4)$$

However, for multiple unpaired electrons this approach does not work anymore. If \star represents a center with more than one singly occupied orbital, then ε_{\star} does not vanish anymore.

However, the correlation energy is not the main interest here. Instead the aim is to exploit the individual increments as a correlation measure. In analogy to the above concept, each increment will include all singly occupied orbitals, and the new increments are defined as

$$\tau_i^{\star} = \varepsilon_{i\star} - \varepsilon_{\star} \quad (4.5)$$

$$\tau_{ij}^{\star} = \varepsilon_{ij\star} - \varepsilon_{\star} \quad (4.6)$$

where \star indicates the set of all singly occupied orbitals. A corresponding expansion of the correlation energy will not be meaningful and is therefore not further considered here.

The localized orbitals are constructed as described in Section 3.4. Note that the localization is with respect to the total symmetric (A_g) component of the ${}^4\Delta_g$ ground state, while the other component (B_{1g}) is ignored. As a result the degeneracy in the #5#11 orbital pair, representing the Co $3d_{xy}$ and $3d_{x^2-y^2}$ orbitals respectively, is lifted. Isosurface plots of all valence and virtual orbitals are available in Figs. A.1 to A.8.

The 1-orbital correlations are then analyzed based on two approaches. As a reference, where all orbitals are entangled together, the entropies are first calculated with an active space of all 60 orbitals. For CoF_2 it is still feasible to perform this step using DMRG, but it becomes increasingly challenging for larger systems (more virtual orbitals). Additional to DMRG, the same entropies are obtained from an FCIQMC calculation. Qualitatively correct entropies may be obtained with only 1×10^6 walkers. The dependence on the number of walkers is illustrated

in Fig. 4.6 for the CoF₂ model using canonical orbitals. The energy expectation value of the 2-particle RDM sampled by FCIQMC ($-1581.006506 E_h$) is between the DMRG energy ($E_{\text{DMRG}} = -1580.986560 E_h$, DBSS DM cutoff 1×10^{-4}) and the converged FCIQMC energy ($E_{\text{FCIQMC}} = -1581.022471 E_h$, 1×10^8 walkers, 2 superinitiators).

For the MoI approach all 1-orbital increments are expanded in the virtual orbital space, i.e. each virtual orbital is correlated with the two sets of doubly and singly occupied orbitals. The individual increments are then calculated using DMRG. This is only for technical reasons, as it gives direct access to the 1-orbital entropies S_i^a , which are not implemented in MOLPRO. This however requires the 1- and 2-electron integrals ("FCIDUMP" files) which are different for each increment. Using a custom Python script, these integrals are obtained from the FCIDUMP file of the full active space of 60 orbitals. Also note, that this results in very cheap CASCI(2,14) calculations, where DMRG actually becomes inefficient due to the many iterations of the sweeping procedure. However, it does provide accurate energies. All DMRG calculations are performed with the DMRG Budapest code [114], while for the FCIQMC calculations the NECI code [70, 119, 120] was used.

As a result, four values are obtained for each virtual orbital, which are all plotted in Fig. 4.13. The DMRG-MoI increments τ_i^\star and DMRG-MoI entropies S_i^a are obtained from the same calculation for each orbital i and quantify the correlation in the agnostic case, i.e. the virtual orbitals are unaware of each other. The CASCI reference values (DMRG and FCIQMC based) show how the entropies S_i change if the virtual orbitals are correlated together. Note, that the CASCI entropies cover all orbitals, including the occupied ones, while in the incremental approach only the virtual orbitals are considered. The occupied increments would require much larger active spaces to calculate. Since their number is usually much smaller than the virtual orbitals and core orbitals can be efficiently excluded based on the orbital energies, identifying further occupied orbitals with negligible correlation contributions is thus unlikely and not of interest here.

The DMRG and FCIQMC entropies are in good agreement regarding the virtual orbitals. However the FCIQMC entropies are more stable. Entropies for degenerate orbitals (e.g. #15#16 or #45#46) show less fluctuations than in the DMRG results. For the occupied orbitals, which are not of main interest here, DMRG yields some

larger deviations: the degenerate orbital pair #3#4 (F p_z) shows a clear split in the DMRG-CASCI entropies, similar the four degenerate orbitals #7 to #10 (F p_x and p_y) perpendicular to the internuclear axis are not degenerate. For these cases the FCIQMC entropies are not degenerate as well, but the values are much closer to each other. In general the FCIQMC entropies are slightly larger than the DMRG entropies. This agrees with smaller total energy of FCIQMC, which indicates more overall correlation in the wave function.

Larger deviations are observed when comparing the DMRG-MoI increments with the CASCI entropies. However, analogous to the results of the first two examples considering polyacetylene and Be_6 , similar patterns can be found. Major differences are observed for orbitals #51 to #60, resembling the two sets of 3d orbitals on each F atom. Those orbitals have much larger relative contributions according to the increments τ_i^\star . The agnostic DMRG-MoI entropies S_i^a however are in agreement with the CASCI entropies. For all other orbitals, the increments and agnostic entropies are in rough agreement.

Another deviating orbital is #17, which is overestimated by the increments τ_i^\star and even more by the agnostic DMRG-MoI entropies S_i^a . According to the CASCI entropies it has one of the smallest correlation contributions. Furthermore the degenerate pair #15#16 (Co 4p) is underestimated by both agnostic measures, however the DMRG-MoI entropies show somewhat better agreement with the CASCI entropies. The presence of further virtual orbitals is thus of high importance here. This however does not necessarily indicate that the two orbitals primarily correlate with other virtual orbitals. Indeed the mutual information in Fig. 4.14 indicates most pair correlations connected to #15 and #16 include occupied orbitals. Thus they indirectly influence other orbitals correlation contribution.

The presented example shows that even for open shell systems an incremental approach may yield comparable 1-orbital correlation measures in most cases. Some orbitals are overestimated by the agnostic incremental approach while some further orbitals are underestimated. However, the DMRG-MoI entropies are a more reliable. In principle, exploiting the cheap scaling of the 1-orbital increments to screen an active space for CASCI calculations should thus be possible. Including overestimated orbitals may keep the computational scaling high, but will not sacrifice accuracy. The bigger issue is underestimating the correlation effects of orbital. Thus a rather

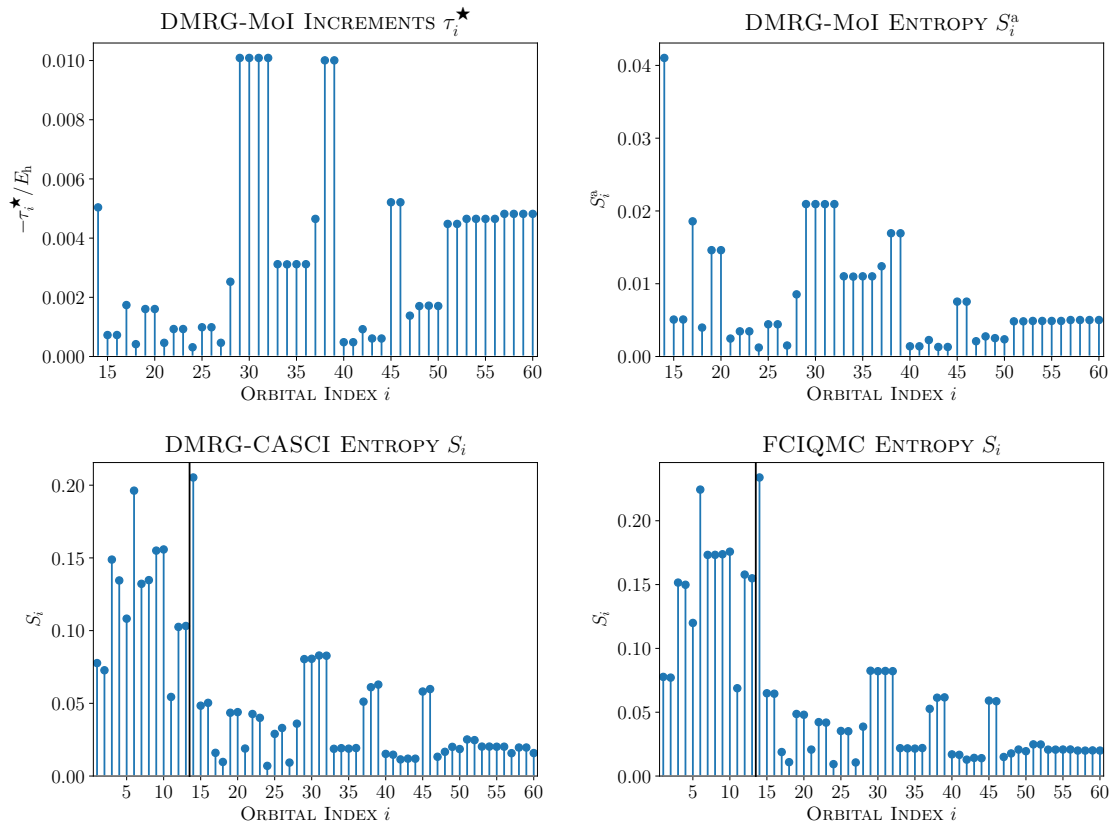


Figure 4.13: Comparison of 1-orbital increments and entropies for CoF_2 (localized orbitals), obtained with different approaches (DMRG-MoI, DMRG-CASCI, FCIQMC). Upper plots: DMRG-MoI increments and entropies for virtual orbitals only. Lower plots: CASCI entropies based on DMRG and FCIQMC calculations. The black vertical line indicates the split between occupied and virtual orbitals.

small threshold parameter to select the active space is advisable. Since the energy increments τ_i^\star are less reliable than the DMRG-MoI entropies S_i^a , only the latter should be considered.

4.3.4 Summary

In principle QIT and the MoI yield very similar results for negligible and major contributions to electron correlation. However, details may deviate. Especially in the open-shell example where only a generalized definition of the orbital increments is used, which does not yield a meaningful total energy anymore. As expected, the

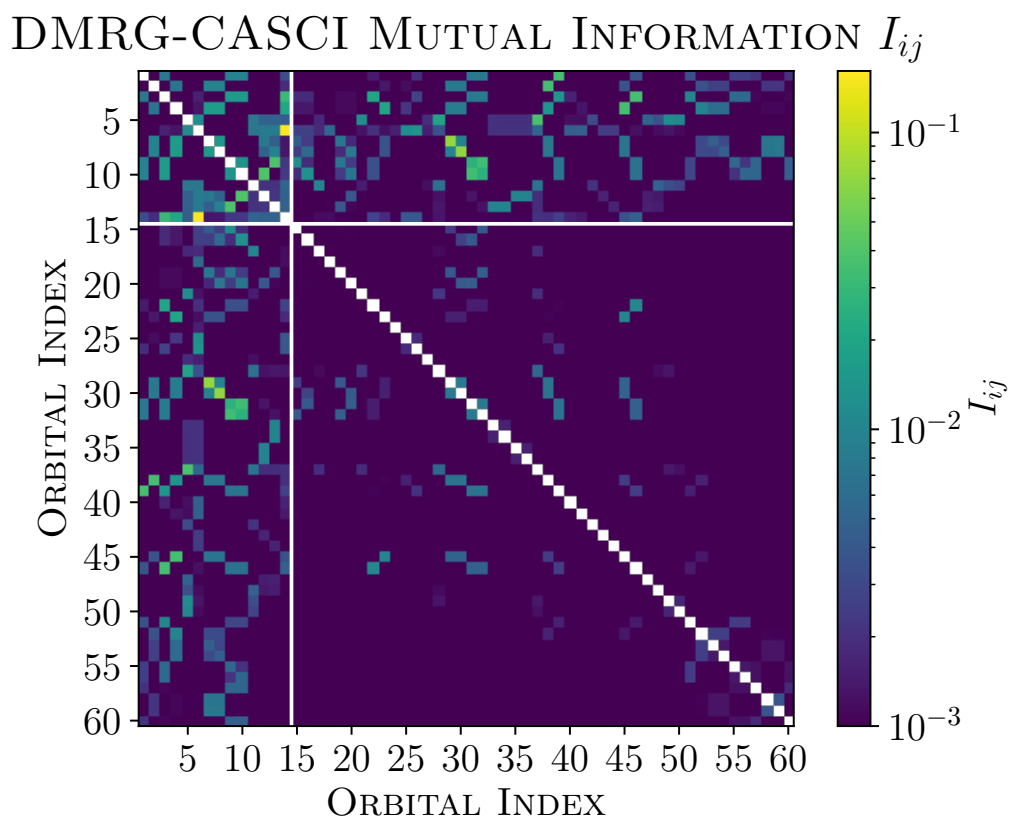


Figure 4.14: Mutual information I_{ij} for CoF_2 (localized orbitals) as obtained from a DMRG-CASCI calculation. The white horizontal and vertical lines indicate the split between occupied and virtual orbitals.

results can thus not directly be translated between the two approaches. However, the computationally extremely cheap 1-orbital increments, may still yield sufficient information to identify orbitals for an active space selection. An initial screening of all (virtual) orbitals, as here demonstrated for the Be_6 rings, may be used to select a more appropriate active space for DMRG. This may also be combined with the protocol for automated active space selection as recently introduced by Stein and Reiher [29].

As an outlook, the 1-orbital increments may yield useful information for choosing the orbital order in DMRG, which is typically based on the 1-orbital entropy and mutual information. This typically requires a preceding DMRG calculation (with small M), which in turn may critically depend on the initial orbital ordering. The MoI may thus present an alternative approach to pre-optimize the ordering for otherwise challenging systems. Unfortunately the 2-orbital increments, corresponding to the required mutual information, are more problematic. The 2-orbital increments are more expensive and greater in number. Furthermore, the off-diagonal block between occupied and virtual orbitals is not accessible. However, one may obtain the agnostic mutual information from the individual increment calculations. How to correctly use this information to reconstruct the (approximate) mutual information of the non-agnostic CI wave function remains an open question for future investigations.

Another possible approach to exploit the similarity between increments and entropies is to screen relevant higher order increments by a cheap DMRG calculation with a small number of blockstates. For the MoI only n -orbital increments corresponding to large n -orbital correlation in QIT would need to be calculated. This would however require implementation and analysis of the n -orbital entropies.

Finally, using the CoF_2 system, it was demonstrated that the 1-orbital entropies can easily be extracted from FCIQMC calculations. Similar to DMRG, a cheap FCIQMC run, i.e. small number of walkers, already yields qualitative correct energies. As before, this information may be useful for (automated) active space selection or screening of required n -orbital increments. In principle, the mutual information may be obtained from FCIQMC as well, but requires implementation of sampling the 4-particle reduced density matrix (in spin orbital basis). Once available, a cheap FCIQMC calculation may be used to construct an optimized orbital order for DMRG.

In general, the correspondence of values obtained from different methods (e.g. MoI, DMRG, FCIQMC) might be useful to exploit one method on a computationally cheap (yet inaccurate) level and facilitate the other method on a numerically accurate (yet expensive) level. Quantitatively incorrect energies or not fully converged wave functions at the first step are then not of primary interest, as those are obtained from the second step as long as qualitative agreement is maintained.

4.4 Analysis of Cobalt Fluorides

As described in Section 3.4, the CoF_2 and CoF_4 (D_{4h}) model systems can systematically be extended to linear chains of Co and O, with F terminating the ends. Information about the “monomers” CoF_2 and CoF_4 may potentially be transferred to the larger systems. In this last section, the correlation contributions of different cobalt fluorides (CoF_2 , CoF_3 , CoF_4 (D_{4h}) and CoF_4 (T_d)) are investigated to learn about the potentially most important contributions in the larger systems.

As a tool for the analysis QIT is applied, next to a systematic variation of the basis set, from minimal up to the cc-pVDZ basis set [99]. Accurate correlation energies for the smaller AO basis sets may be obtained by conventional FCI calculations as implemented in MOLPRO [94, 113, 125, 126], while for the larger basis sets FCIQMC [70, 119, 120] calculations are performed. Core orbitals (with eigenvalue $\epsilon_i \leq -3 E_h$) are not correlated in all cases. The molecular orbitals (FCIDUMP files) are constructed as described in Section 3.4, where canonical orbitals are used, i.e. no localization is applied.

4.4.1 Basis Set Dependence and Orbital Entropies

Table 4.22 shows the correlation energies of the isolated Co^{n+} and F^- ions at different AO basis sets. In Table 4.23 the HF, FCI and correlation energies for all four model systems at different basis sets are compared. The chosen basis set start with the minimal number of basis functions required to describe all electrons and then systematically add more shells on Co. Thus, increasingly more intra-atomic corre-

Table 4.22: HF, FCI and correlation energies (in E_h) for the different cobalt cations and F^- using different basis set. Systems without correlation energy at their minimal basis set are omitted.

	HF	FCI	E_{corr}
cc-pVDZ [6s,5p,3d,1f]			
Co^{2+}	-1380.596424	-1380.749118	-0.152694
Co^{3+}	-1379.432768	-1379.528192	-0.095423
Co^{4+}	-1377.606402	-1377.653136	-0.046734
cc-pVDZ [3s,2p,1d]			
F^-	-99.365984	-99.558917	-0.192934
minimal basis + 4sp [4s,3p,1d]			
Co^{2+}	-1380.532708	-1380.533252	-0.000544
Co^{3+}	-1379.112148	-1379.112396	-0.000248
Co^{4+}	-1376.890476	-1376.890552	-0.000076
minimal basis + 4s [4s,2p,1d]			
Co^{2+}	-1380.529043	-1380.529126	-0.000083
Co^{3+}	-1379.092596	-1379.092637	-0.000041
Co^{4+}	-1376.846931	-1376.846931	0.000000

lation effects on the Co are included. The largest basis set considers the complete set of cc-pVDZ functions on Co and F. Results for CoF_3 in the minimal basis set are missing as no reliable HF solution could be obtained. The last two columns in Table 4.23 represent the difference in the correlation energy between the combined molecule (CoF_n) and the isolated (dissociated) ionic fragments ($\text{Co}^{n+} + nF^-$). It is defined as

$$\Delta E_{\text{corr}} = E_{\text{corr}}(\text{CoF}_n) - E_{\text{corr}}(\text{Co}^{n+}) - nE_{\text{corr}}(F^-) \quad (4.7)$$

and represents the correlation energy contribution due to inter-atomic Co–F correlation. Note that for all basis sets except the largest one (cc-pVDZ on Co and F), the last term cancels out since there is no correlation energy for F^- in a minimal basis set.

The results are compared to the QIT data obtained from DMRG, using the Budapest DMRG code [114]. A DBSS DM cutoff of 1×10^{-5} has been used for all systems. The largest 1-orbital entropies S_i and mutual information I_{ij} for the studied model systems are summarized in Tables 4.26 to 4.30. The complete set of data and isosurface plots of the molecular orbitals are included in the appendix.

Table 4.23: HF, FCI and correlation energies (in E_h) for the cobalt fluorides using different basis set.^a FCIQMC correlation energy with standard deviation.

	HF	FCI	E_{corr}	Std. Dev.	ΔE_{corr}	ΔE_{corr} per F
cc-pVDZ (Co [6s,5p,3d,1f], F [3s,2p,1d])						
CoF ₂	-1580.389262	-1581.022206	-0.632944 ^a	3.2×10^{-5}	-0.094383	-0.047191
CoF ₃	-1679.813744	-1680.635657	-0.821913 ^a	1.6×10^{-4}	-0.147833	-0.049278
CoF ₄ D_{4h}	-1779.019872	-1780.124419	-1.104546 ^a	4.9×10^{-4}	-0.286078	-0.071520
CoF ₄ T_d	-1779.104549	-1780.211897	-1.107348 ^a	6.9×10^{-4}	-0.288879	-0.072220
cc-pVDZ on Co, minimal on F (Co [6s,5p,3d,1f], F [2s,1p])						
CoF ₂	-1580.361724	-1580.678793	-0.317070 ^a	4.4×10^{-5}	-0.164375	-0.082188
CoF ₃	-1679.770945	-1680.131453	-0.360508 ^a	1.1×10^{-4}	-0.265085	-0.088362
CoF ₄ D_{4h}	-1778.963170	-1779.455709	-0.492539 ^a	1.4×10^{-4}	-0.445805	-0.111451
CoF ₄ T_d	-1779.051622	-1779.541594	-0.489973 ^a	1.7×10^{-4}	-0.443239	-0.110810
minimal basis + Co 4sp (Co [4s,3p,1d], F [2s,1p])						
CoF ₂	-1580.219451	-1580.302693	-0.083241		-0.082697	-0.041349
CoF ₃	-1679.512361	-1679.699007	-0.186646		-0.186398	-0.062133
CoF ₄ D_{4h}	-1778.753694	-1778.992539	-0.238846		-0.238770	-0.059692
CoF ₄ T_d	-1778.806597	-1779.069714	-0.263116		-0.263040	-0.065760
minimal basis + Co 4s (Co [4s,2p,1d], F [2s,1p])						
CoF ₂	-1580.118522	-1580.179205	-0.060683		-0.060600	-0.030300
CoF ₃						
CoF ₄ D_{4h}	-1778.666630	-1778.843568	-0.176939		-0.176939	-0.044235
CoF ₄ T_d	-1778.701932	-1778.910543	-0.208612		-0.208612	-0.052153
minimal basis (Co [3s,2p,1d], F [2s,1p])						
CoF ₂	-1579.998988	-1580.010936	-0.011948		-0.011948	-0.005974
CoF ₃						
CoF ₄ D_{4h}	-1778.552226	-1778.788008	-0.235782		-0.235782	-0.058945
CoF ₄ T_d	-1778.696523	-1778.845614	-0.149091		-0.149091	-0.037273

Most correlation energies in Table 4.23 are systematically decreasing with the number of fluorine atoms and size of the basis set. Only the data based on the minimal basis set does not follow a systematic trend. Similar, the inter-atomic correlation energy ΔE_{corr} shows a decreasing trend, i.e. shows larger contributions. However, when employing the cc-pVDZ basis set on all atoms, it suddenly shows less contributions. This means that adding basis functions on F decreases inter-atomic correlations between Co and F, i.e. F–F correlations are preferred. This can be confirmed by the QIT data: For example in CoF_2 (cf. Tables 4.26 and 4.27) the mutual information between F 2p orbitals and orbitals mainly located on Co decreases (e.g. orbital pairs #2#5 and #2#6) when going from the smaller basis set (Co [6s,5p,3d,1f], F [2s,1p]) to the larger basis (Co [6s,5p,3d,1f], F [3s,2p,1d]). On the other hand, the mutual information between orbitals mainly located on the F atoms increases (e.g. #2#37 in the full cc-pVDZ basis, which corresponds to #2#28 in the smaller basis set). However, a direct correspondence of the QIT data to the AO basis functions is difficult, as the MOs are delocalized.

One can also observe, that the two larger basis sets (cc-pVDZ on Co) have very similar correlation energies for both CoF_4 geometries (difference in the order of $1 mE_h$), while the two smaller basis sets show a larger difference (in the order of $10 mE_h$). Thus, at the larger basis set, HF yields a quantitatively reasonable result for the energy difference between the D_{4h} and T_d geometries, even if only a minimal basis set on the F atoms is used. A larger basis set on the central Co atom is required however. The geometry is thus mainly influenced by the Co basis functions.

Furthermore, the inter-atomic correlation energy ΔE_{corr} per F atom at the larger two basis sets is very similar for CoF_2 and CoF_3 , while a different value for the two CoF_4 systems is observed. On the other hand, the smaller basis set (Co [4s,3p,1d], F [2s,1p]) groups CoF_3 with the two CoF_4 molecules and CoF_2 remains singular. A larger basis set on Co is thus required to yield a correct qualitative trend in the correlation energy contributions, while additional basis functions on F yield quantitative improvements.

Inspection of the molecular orbitals (isosurface plots are available in the appendix) reveals that for CoF_4 (T_d and D_{4h}) the Co 3d orbitals are part of delocalized MOs and are linearly combined with one 2p AO on each F. For CoF_2 however, the Co 3d orbitals remain much closer to their AO shape, while CoF_3 presents an intermediate

Table 4.24: Assignment of the Co 3d AO in CoF_n . The numbers indicate the index of the MOs with largest Co 3d AO contributions. Surface plots of all the MOs are available in the appendix. A single number indicates the corresponding 3d AO does not mix, while two numbers indicate the Co 3d orbital combines with F 2p orbitals, forming a pair of bonding and anti-bonding orbitals (i.e. whether there is a nodal plane perpendicular to the Co–F bonding axes). Numbers in parenthesis indicate only a small Co 3d contribution to the MO.

	$3d_{z^2}$	$3d_{x^2-y^2}$	$3d_{xy}$	$3d_{xz}$	$3d_{yz}$
CoF_2	3, (5)	4	32	48, (50)	54, (56)
CoF_3	6	4, 7	31, 34	66, (65)	52, (50)
$\text{CoF}_4 D_{4h}$	5, (4)	3, 6	50, 52	70, 71	77, 78
$\text{CoF}_4 T_d$	5, 7	75, 77	3, 8	34, 37	55, 58

situation. The 3d contributions to the MOs are summarized in Table 4.24. This trend is similar to the trend of the inter-atomic correlation energy mentioned above, and may therefore be connected. In case of CoF_2 the $3d_{z^2}$ sticks out of the trend, i.e. MO #3 shows some minor F 2p AO contributions. This maybe related to the state average including the ${}^4\Sigma_g$ where the $3d_{z^2}$ orbital is singly occupied (cf. Fig. 3.6). Consequently, in the CI vector for the ${}^4\Delta_g$ state, correlations to MO #5 (virtual orbital with Co $3d_{z^2}$ and F 2p contributions) try to counteract this effect.

In general, the orbital pairs of bonding and anti-bonding combinations including Co 3d and F 2p contributions give rise to the largest mutual information for each model system (cf. Tables 4.26 to 4.30). This is similar to the large $\pi_u + \pi_g$ correlations of the N_2 system in Section 4.1. These orbitals have large contributions in describing the chemical bonds, and the large correlations thus indicate systematic problems of HF in describing the bonding correctly. This then needs to be corrected at the CI level. This also agrees with the more important intra-atomic correlations, observed above based on the different basis sets. Similar arguments have been made a long time ago [127, 128, 129]. Furthermore this is supported by the recent study on the Be_6 ring, where the canonical, delocalized HF orbitals have been optimized by minimizing entropy and localized orbitals are obtained as a result [13].

Localizing the molecular orbitals thus seems beneficial. Unfortunately the tested localization schemes (Foster-Boys and Pipek-Mezey) had problems with convergence for the CoF_n systems and as a result the obtained orbitals are not always well

localized. A systematic study of the cobalt fluorides in terms of localized orbitals is thus not further considered here. Only for the CoF_2 system reasonable results are obtained with the Pipek-Mezey localization, as already presented in Section 4.3.3. A direct comparison of the QIT data for both sets of orbitals is shown in Fig. 4.15. One can observe a different, but similar distribution: some entropies and mutual information increase, others decrease. Similar the total correlation for both sets of orbitals do not change much (cf. Table 4.25). However, the DMRG total energy is drastically improved using the localized orbitals, despite using a much tighter DBSS DM cutoff for the delocalized orbitals (1×10^{-5} vs. 1×10^{-4}). Thus the correlation contributions are redistributed in a way that fewer orbitals with larger individual contributions exist, which can be described by fewer configurations.

The DMRG energies and total correlation due to QIT for all studied systems are compared in Table 4.25, while the 1-orbital entropies and mutual information is plotted in Figs. 4.15 and A.54. The general trend is that the total correlation I_{tot} is increasing with the number of atoms, but this also relates to more orbitals being present, that can be correlated. Furthermore the accuracy of DMRG decreases for larger systems, which is also expected as more orbitals means more dynamical correlation. The exception here is CoF_3 , where the error of DMRG is smaller than for CoF_2 using the delocalized basis. However, a direct comparison of the amount of correlation and the DMRG accuracy is only possible for same number of orbitals: As already mentioned, the localized orbitals for CoF_2 yield large improvements in the DMRG energy. The total correlation increases as the more compact CI vector allows to include more overall correlation, as indicated by the much lower correlation energy. Another direct comparison is possible for CoF_4 , where the DMRG energy of the T_d structure is closer to its FCIQMC estimate than the D_{4h} structure. The latter structure is more strongly correlated and thus shows larger total correlation. One would additionally expect its DMRG energy to be more accurate. However, numerical parameters like the orbital ordering have a large influence on the DMRG accuracy as well. Reliable DMRG energies are thus hard to obtain for the here used model systems. But qualitatively correct QIT data may still be obtained as may be confirmed by comparison with FCIQMC entropies. This was already demonstrated for the CoF_2 model using localized orbitals in Fig. 4.13.

Table 4.25: Summary of the DMRG results including the total energies and differences to FCIQMC ΔE (units in E_h) as well as the total correlation I_{tot} of the cobalt fluorides.

	FCIQMC	Std. Dev.	DMRG	ΔE	I_{tot}
CoF ₂ (cc-pVDZ, delocal)	-1581.0222	3.2×10^{-5}	-1580.8079	-0.2143	3.01
CoF ₂ (cc-pVDZ, local)			-1580.9866	-0.0357	3.24
CoF ₂ (min. basis on F)	-1580.6788	4.4×10^{-5}	-1580.5841	-0.0947	2.53
CoF ₃	-1680.6357	1.6×10^{-4}	-1680.4664	-0.1693	4.11
CoF ₄ D_{4h}	-1780.1244	4.9×10^{-4}	-1779.7190	-0.4054	5.51
CoF ₄ T_d	-1780.2119	6.9×10^{-4}	-1779.9149	-0.2970	5.23

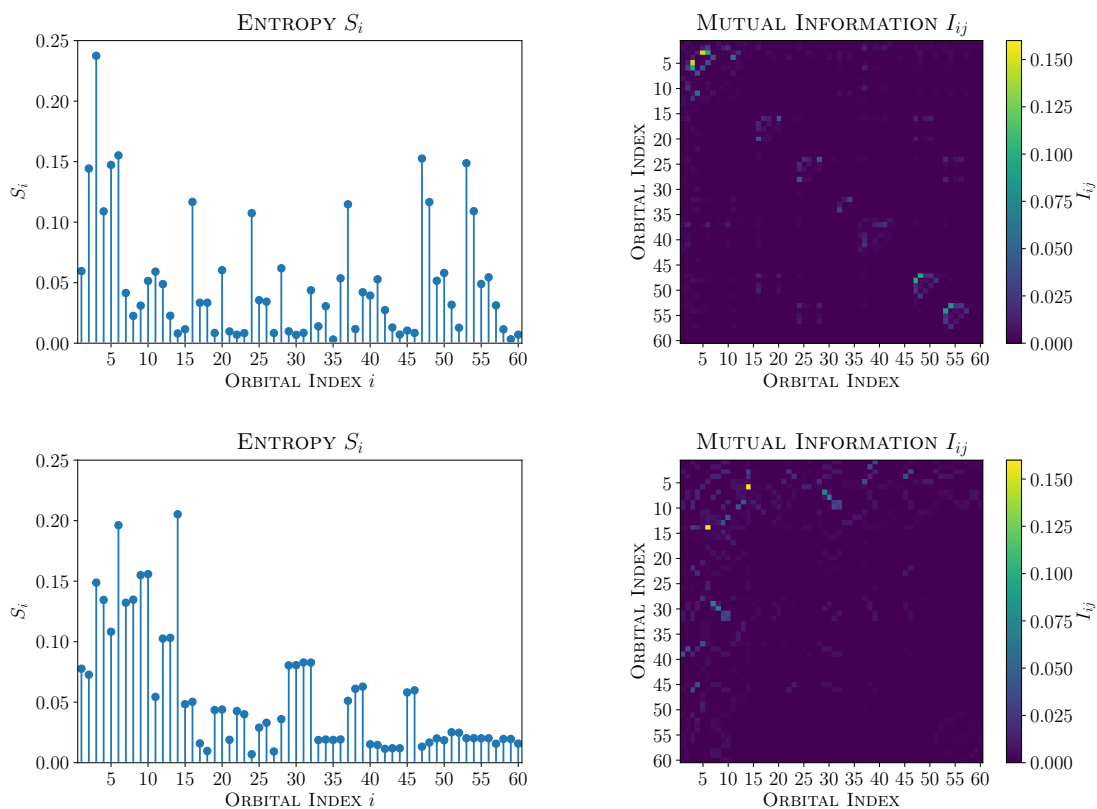


Figure 4.15: Comparison of 1-orbital entropy S_i and mutual information I_{ij} for the CoF₂ model in cc-pVDZ AO basis, using the delocalized (top) and localized (bottom) MOs.

Table 4.26: Largest entropies S_i and mutual information I_{ij} of selected orbital pairs ij for the **CoF₂** model in the full cc-pVDZ basis. The last column indicates which (type of) atoms the corresponding molecular orbital is located on. For occupied orbitals the atomic orbital most closely related to the molecular orbitals are indicated as well.

i	j	S_i	S_j	I_{ij}					
						40	0.0393	0.0170	Co + F
						41	0.0528	0.0230	F
2		0.1443				47	0.1525		F p _x
	5		0.1473	0.0119		16	0.1167	0.0134	F p _y
	6		0.1551	0.0293		20	0.0603	0.0117	F
	9		0.0310	0.0115		48	0.1166	0.0941	Co d _{xz} + F
	10		0.0514	0.0201		49	0.0516	0.0217	Co + F
	37		0.1147	0.0135		50	0.0580	0.0256	F
3		0.2375				48	0.1166		Co d _{xz} + F
	4		0.1089	0.0139		47	0.1525	0.0941	F p _x
	5		0.1473	0.1471		51	0.0317	0.0218	Co + F
	6		0.1551	0.0979		53	0.1487		F p _y
	12		0.0488	0.0227		24	0.1075	0.0168	F p _x
4		0.1089				28	0.0619	0.0134	F
	3		0.2375	0.0139		54	0.1090	0.0843	Co d _{yz} + F
	7		0.0415	0.0389		55	0.0489	0.0222	Co + F
	11		0.0591	0.0572		56	0.0544	0.0281	F
5		0.1473				54	0.1090		Co d _{yz} + F
	2		0.1443	0.0119		53	0.1487	0.0843	F p _y
	3		0.2375	0.1471		57	0.0313	0.0218	Co + F
	6		0.1551	0.0382					
6		0.1551							
	2		0.1443	0.0293					
	3		0.2375	0.0979					
	5		0.1473	0.0382					
	37		0.1147	0.0119					
16		0.1167							
	17		0.0334	0.0164					
	18		0.0334	0.0123					
	20		0.0603	0.0401					
	47		0.1525	0.0134					
	50		0.0580	0.0131					
24		0.1075							
	25		0.0355	0.0185					
	26		0.0343	0.0131					
	28		0.0619	0.0416					
	53		0.1487	0.0168					
	56		0.0544	0.0112					
37		0.1147							
	2		0.1443	0.0135					
	6		0.1551	0.0119					
	10		0.0514	0.0103					
	39		0.0421	0.0121					

Table 4.27: Largest entropies S_i and mutual information I_{ij} of selected orbital pairs ij for the CoF_2 model using the cc-pVDZ basis on Co but only a minimal basis set on F. The last column indicates which (type of) atoms the corresponding molecular orbital is located on. For occupied orbitals the atomic orbital most closely related to the molecular orbitals are indicated as well.

i	j	S_i	S_j	I_{ij}	
2		0.1221			F p_z
	5		0.1697	0.0145	Co + F
	6		0.1783	0.0433	Co + F
	28		0.0825	0.0104	F p_z
4		0.2566			Co d_{z^2}
	3		0.0604	0.0117	Co $d_{x^2-y^2}$
	5		0.1697	0.1623	Co + F
	6		0.1783	0.0960	Co + F
	11		0.0544	0.0311	Co + F
5		0.1697			Co + F
	2		0.1221	0.0145	F p_z
	4		0.2566	0.1623	Co d_{z^2}
	6		0.1783	0.0426	Co + F
6		0.1783			Co + F
	2		0.1221	0.0433	F p_z
	4		0.2566	0.0960	Co d_{z^2}
	5		0.1697	0.0426	Co + F
	28		0.0825	0.0208	F p_z
24		0.1006			Co d_{xy}
	25		0.0455	0.0429	Co
	26		0.0607	0.0598	Co
34		0.1405			F p_x + Co
	35		0.1436	0.1199	Co d_{xz} + F
	36		0.0651	0.0344	Co + F
35		0.1436			Co d_{xz} + F
	34		0.1405	0.1199	F p_x + Co
	37		0.0343	0.0261	Co
38		0.1301			F p_y
	39		0.1314	0.1053	Co d_{yz} + F
	40		0.0601	0.0353	Co + F
39		0.1314			Co d_{yz} + F
	38		0.1301	0.1053	F p_y
	41		0.0338	0.0259	Co

Table 4.28: Largest entropies S_i and mutual information I_{ij} of selected orbital pairs ij for the CoF_3 model in the full cc-pVDZ basis. The last column indicates which (type of) atoms the corresponding molecular orbital is located on. For occupied orbitals the atomic orbital most closely related to the molecular orbitals are indicated as well.

i	j	S_i	S_j	I_{ij}					
						50	0.1780	0.0941	F + Co
						55	0.0480	0.0135	F + Co
3		0.1385				59	0.0297	0.0207	F + Co
	10		0.0842	0.0134					F p + Co
					65	0.1469			F p + Co d
4		0.2184				51	0.1215	0.0106	F
	7		0.1970	0.1297		66	0.1083	0.0783	Co d + F p
	16		0.0672	0.0137		67	0.0409	0.0173	F + Co
5		0.1345				68	0.0577	0.0320	F
	7		0.1970	0.0132		66	0.1083		Co d + F p
	12		0.0747	0.0159		65	0.1469	0.0783	F p + Co d
	18		0.0505	0.0128		67	0.0409	0.0125	F + Co
7		0.1970				69	0.0286	0.0211	Co + F
	4		0.2184	0.1297					F p + Co d
	5		0.1345	0.0132					F p
	20		0.0402	0.0159					F + Co
31		0.2144							F p + Co d
	34		0.2056	0.1392					F p + Co d
	40		0.0658	0.0141					F
32		0.1386							F p
	34		0.2056	0.0172					F p + Co d
	36		0.0793	0.0160					F + Co
	39		0.0766	0.0122					F
	41		0.0538	0.0126					F
33		0.1334							F p
	39		0.0766	0.0205					F
34		0.2056							F p + Co d
	31		0.2144	0.1392					F p + Co d
	32		0.1386	0.0172					F p
	36		0.0793	0.0104					F + Co
	42		0.0399	0.0167					F + Co
50		0.1780							F + Co
	51		0.1215	0.0104					F
	52		0.1318	0.0941					F + Co
	55		0.0480	0.0157					F + Co
	57		0.0626	0.0135					F
	58		0.0676	0.0231					F
51		0.1215							F
	50		0.1780	0.0104					F + Co
	53		0.0457	0.0136					F + Co
	57		0.0626	0.0179					F
	58		0.0676	0.0145					F
	65		0.1469	0.0106					F p + Co d
52		0.1318							F + Co

Table 4.29: Largest entropies S_i and mutual information I_{ij} of selected orbital pairs ij for the CoF_4 D_{4h} model in the full cc-pVDZ basis. The last column indicates which (type of) atoms the corresponding molecular orbital is located on. For occupied orbitals the atomic orbital most closely related to the molecular orbitals are indicated as well.

i	j	S_i	S_j	I_{ij}					
						59	0.1366		F p
						60		0.1471 0.0148	F p
3		0.1926				61		0.0870 0.0353	Co + F
	6		0.2173	0.1047	F p + Co d	62		0.0452 0.0132	Co + F
4		0.1684			F p + Co	64		0.0683 0.0136	F
	5		0.1147	0.0405	Co d_{z^2}	65		0.0623 0.0145	Co + F
	8		0.0680	0.0126	Co + F	60	0.1471		F p
	11		0.0366	0.0111	Co	59		0.1366 0.0148	F p
5		0.1147			Co d_{z^2}	61		0.0870 0.0195	Co + F
	4		0.1684	0.0405	F p + Co	64		0.0683 0.0216	F
	7		0.0401	0.0143	Co	65		0.0623 0.0144	Co + F
	8		0.0680	0.0143	Co + F	70	0.3614		F p + Co d
	14		0.0315	0.0155	Co + F	71		0.3497 0.3796	F p + Co d
6		0.2173			F p + Co d	72		0.0658 0.0253	F + Co
	3		0.1926	0.1047	F p	73		0.0601 0.0188	F + Co
	15		0.0426	0.0157	Co + F	71	0.3497		F p + Co d
23		0.1087			F p	70		0.3614 0.3796	F p + Co d
	24		0.1121	0.0103	F p	72		0.0658 0.0238	F + Co
	27		0.0396	0.0128	Co + F	73		0.0601 0.0280	F + Co
	28		0.0555	0.0103	F	77	0.3774		F p + Co d
	29		0.0483	0.0100	F	78		0.3667 0.4066	F p + Co d
24		0.1121			F p	79		0.0666 0.0258	Co + F
	23		0.1087	0.0103	F p	80		0.0606 0.0194	Co + F
	28		0.0555	0.0151	F	81		0.0372 0.0100	Co + F
	29		0.0483	0.0104	F	78	0.3667		F p + Co d
37		0.1011			F p	77		0.3774 0.4066	F p + Co d
	41		0.0396	0.0130	Co + F	79		0.0666 0.0246	Co + F
	42		0.0575	0.0105	F	80		0.0606 0.0286	Co + F
	43		0.0490	0.0100	F				
38		0.1049			F p				
	42		0.0575	0.0157	F				
	43		0.0490	0.0103	F				
50		0.1853			F p + Co d				
	52		0.1967	0.1351	F p + Co d				
51		0.1168			F p				
	52		0.1967	0.0112	F p + Co d				
	53		0.0660	0.0180	Co + F				
	55		0.0511	0.0134	F				
52		0.1967			F p + Co d				
	50		0.1853	0.1351	F p + Co d				
	51		0.1168	0.0112	F p				
	53		0.0660	0.0101	Co + F				
	54		0.0558	0.0311	Co + F				

Table 4.30: Largest entropies S_i and mutual information I_{ij} of selected orbital pairs ij for the $\mathbf{CoF}_4 \mathbf{T}_d$ model in the full cc-pVDZ basis. The last column indicates which (type of) atoms the corresponding molecular orbital is located on. For occupied orbitals the atomic orbital most closely related to the molecular orbitals are indicated as well.

i	j	S_i	S_j	I_{ij}					
					58	0.2061			F p + Co d
3		0.2220			55	0.2003	0.1109		F p + Co d
	8		0.2300	0.1038	60	0.0687	0.0123		Co + F
4		0.1479			64	0.0592	0.0108		Co + F
					66	0.0384	0.0167		Co + F
	11		0.0884	0.0182	75	0.1677			F p + Co d
	15		0.0347	0.0114	77	0.1632	0.1093		F p + Co d
5		0.2588			78	0.0560	0.0126		Co + F
	7		0.2559	0.2096	79	0.0576	0.0102		Co + F
	13		0.0663	0.0122	76	0.1051			F p
6		0.1414			78	0.0560	0.0112		Co + F
	8		0.2300	0.0161	79	0.0576	0.0173		Co + F
	12		0.0761	0.0131	77	0.1632			F p + Co d
7		0.2559			75	0.1677	0.1093		F p + Co d
	5		0.2588	0.2096	78	0.0560	0.0142		Co + F
	13		0.0663	0.0160	80	0.0458	0.0301		Co + F
	17		0.0519	0.0315					
8		0.2300							
	3		0.2220	0.1038					
	6		0.1414	0.0161					
	12		0.0761	0.0105					
	22		0.0385	0.0158					
34		0.2322							
	37		0.2388	0.1289					
	43		0.0624	0.0163					
35		0.1144							
	39		0.0699	0.0128					
	44		0.0474	0.0107					
36		0.1342							
	42		0.0645	0.0178					
37		0.2388							
	34		0.2322	0.1289					
	39		0.0699	0.0114					
	43		0.0624	0.0112					
	45		0.0403	0.0171					
55		0.2003							
	58		0.2061	0.1109					
	64		0.0592	0.0180					
56		0.1068							
	60		0.0687	0.0134					
	65		0.0487	0.0116					
57		0.1156							
	63		0.0626	0.0191					

4.4.2 Diagonalized 2-Orbital Reduced Density Matrices ϕ_{ij}

In analogy to the QIT analysis of N_2 and N_2^+ in Section 4.1, the 2-orbital correlations are also investigated in terms of the diagonalized 2-orbitals RDM, i.e. the eigenvectors $\phi_{ij,\alpha}$ and their eigenvalues $\omega_{ij,\alpha}$. The main contributions for the most entangled orbital pairs are summarized in Tables 4.31 to 4.34.

According to the discussion at the end of Section 4.1, strong correlation effects are expected to yield large mutual information in connection with large contributions of multiple basis vectors ($|-, -\rangle$, $|-, \downarrow\rangle$, *etc.*) to the 2-orbital RDM ρ_{ij} . Recall, that according to the T_1 and D_1 diagnostics, the strong correlation character increases in the order of CoF_2 , CoF_3 , $CoF_4 (T_d)$, $CoF_4 (D_{4h})$ (cf. Table 3.2). Indeed, this can be observed for the two extreme cases CoF_2 and $CoF_4 (D_{4h})$ (Tables 4.31 and 4.33 respectively): The largest mutual information for CoF_2 are smaller (0.15 vs. 0.41 for the largest value) and largest eigenvalues $\omega_{ij,\alpha=1}$ for each orbital pair ij are in the range from 0.95 to 0.98. For $CoF_4 (D_{4h})$ the largest eigenvalues of each orbital pair are still close to 1, but slightly smaller (0.94 to 0.97). Additionally, almost all the shown eigenvectors for CoF_2 are dominated by a single basis vector (e.g. $\phi_{i=3,j=15,\alpha=2} = +0.06 \times |-, \uparrow\rangle - 1.00 \times | \downarrow, \uparrow \downarrow \rangle$), while for $CoF_4 (D_{4h})$ more contributing basis vectors can be identified (e.g. $\phi_{i=77,j=78,\alpha=2} = -0.51 \times | \uparrow \downarrow, \downarrow \rangle + 0.86 \times | \uparrow \downarrow, \uparrow \rangle$).

Similar, comparing CoF_4 in its D_{4h} and T_d geometry one finds, that the latter has smaller mutual information, similar largest eigenvalues ($\omega_{ij,\alpha=1}$) and the contributions of the eigenvectors are slightly more dominated by one of the basis vectors. Overall, this agrees with T_d being less strongly correlated than D_{4h} . The amount of correlation in CoF_3 is expected to be somewhere between CoF_2 and CoF_4 . Although the differences in the data shown is subtle, they are in agreement. The corresponding observation for the dissociation of N_2/N_2^+ can thus be confirmed, although the effect was much stronger pronounced for the dissociation.

4.4.3 Summary

In summary, the collected data suggests that most correlations are intra-atomic. Most of the inter-atomic correlation energies are related to the overly delocalized HF orbitals describing the chemical bond, which needs to be corrected for at the CI level. This suggests localized orbitals may yield improved results, which is confirmed by the CoF_2 example.

Furthermore, the cc-pVDZ basis functions on the 3d orbitals on Co allow a quantitative distinction between T_d and D_{4h} geometry already at HF, while a minimal basis set on F is sufficient. In general, a reasonable description of the electronic structure on Co seems more important than for F. When studying the larger CoO systems, one may thus try to reduce computational cost by using fewer basis functions on the O and F atoms. However, this observation does not necessarily translate from F to O and would need verification, for example based on Co_2OF_2 and $\text{Co}_2\text{O}_2\text{F}_4$ (cf. Fig. 3.5).

The trend of the strong correlation character in the CoF_n series is reflected by 2-orbital correlation measures (I_{ij} , $\omega_{ij,\alpha}$ and $\phi_{ij,\alpha}$), supporting the results of Section 4.1.

Table 4.31: Largest eigenvalues $\omega_{ij,\alpha}$ and corresponding eigenvectors $\phi_{ij,\alpha}$ of the 2-orbital RDMs of the orbital pairs ij with largest mutual information I_{ij} . Data is summarized for the **CoF₂** system.

i	j	S_i	S_j	I_{ij}	$\omega_{ij,\alpha}$	$\phi_{ij,\alpha}$
3	5	0.24	0.15	0.15	0.96	$+1.00 \times \downarrow, -\rangle$
					0.02	$+0.06 \times -\rangle + 1.00 \times \downarrow, \uparrow\rangle$
3	6	0.24	0.16	0.10	0.95	$+1.00 \times \downarrow, \uparrow\rangle$
					0.02	$-0.11 \times -\rangle + 0.99 \times \uparrow, -\rangle$
47	48	0.15	0.12	0.09	0.97	$+1.00 \times \uparrow\downarrow, \downarrow\rangle$
53	54	0.15	0.11	0.08	0.97	$+1.00 \times \uparrow\downarrow, \downarrow\rangle$
4	11	0.11	0.06	0.06	0.98	$+1.00 \times \downarrow, -\rangle$
24	28	0.11	0.06	0.04	0.98	$+1.00 \times \downarrow, -\rangle$
16	20	0.12	0.06	0.04	0.98	$+1.00 \times \downarrow, -\rangle$
4	7	0.11	0.04	0.04	0.98	$+1.00 \times \downarrow, -\rangle$
5	6	0.15	0.16	0.04	0.95	$+1.00 \times -\rangle$
					0.03	$+0.67 \times -\rangle + 0.74 \times \downarrow, -\rangle$
					0.01	$-0.78 \times -\rangle + 0.62 \times \downarrow, \downarrow\rangle$

Table 4.32: Largest eigenvalues $\omega_{ij,\alpha}$ and corresponding eigenvectors $\phi_{ij,\alpha}$ of the 2-orbital RDMS of the orbital pairs ij with largest mutual information I_{ij} . Data is summarized for the **CoF₃** system.

i	j	S_i	S_j	I_{ij}	$\omega_{ij,\alpha}$	$\phi_{ij,\alpha}$
31	34	0.21	0.21	0.14	0.95	$+1.00 \times \uparrow\downarrow, \uparrow\downarrow\rangle$
					0.01	$+0.07 \times \uparrow\downarrow, -\rangle - 1.00 \times \uparrow\downarrow, \downarrow\rangle$
					0.01	$-0.95 \times \downarrow, \uparrow\rangle + 0.32 \times \uparrow, \uparrow\rangle$
4	7	0.22	0.20	0.13	0.95	$+1.00 \times \uparrow\downarrow, \uparrow\downarrow\rangle$
					0.01	$+0.09 \times \uparrow\downarrow, -\rangle - 1.00 \times \uparrow\downarrow, \downarrow\rangle$
					0.01	$+0.95 \times \downarrow, \uparrow\rangle + 0.32 \times \uparrow, \uparrow\rangle$
50	52	0.18	0.13	0.09	0.96	$+1.00 \times \uparrow\downarrow, \downarrow\rangle$
65	66	0.15	0.11	0.08	0.97	$+1.00 \times \uparrow\downarrow, \downarrow\rangle$
6	19	0.09	0.05	0.03	0.99	$+1.00 \times \downarrow, -\rangle$
65	68	0.15	0.06	0.03	0.97	$+1.00 \times \downarrow, -\rangle$
					0.01	$-1.00 \times \uparrow\downarrow, -\rangle$

Table 4.33: Largest eigenvalues $\omega_{ij,\alpha}$ and corresponding eigenvectors $\phi_{ij,\alpha}$ of the 2-orbital RDMs of the orbital pairs ij with largest mutual information I_{ij} . Data is summarized for the **CoF₄** D_{4h} system.

i	j	S_i	S_j	I_{ij}	$\omega_{ij,\alpha}$	$\phi_{ij,\alpha}$
77	78	0.38	0.37	0.41	0.94	$+1.00 \times \uparrow\downarrow, \uparrow\downarrow\rangle$
					0.03	$-0.51 \times \uparrow\downarrow, \downarrow\rangle + 0.86 \times \uparrow\downarrow, \uparrow\rangle$
70	71	0.36	0.35	0.38	0.94	$+1.00 \times \uparrow\downarrow, \uparrow\downarrow\rangle$
					0.03	$+0.36 \times \uparrow\downarrow, -\rangle - 0.93 \times \uparrow\downarrow, \uparrow\rangle$
50	52	0.19	0.20	0.14	0.96	$+1.00 \times \uparrow\downarrow, \downarrow\rangle$
					0.02	$-0.13 \times \uparrow\downarrow, -\rangle + 0.99 \times \uparrow\downarrow, \uparrow\rangle$
3	6	0.19	0.22	0.10	0.95	$+1.00 \times \uparrow\downarrow, \uparrow\downarrow\rangle$
					0.02	$+0.07 \times \uparrow\downarrow, -\rangle + 1.00 \times \uparrow\downarrow, \downarrow\rangle$
					0.01	$+0.74 \times \downarrow, \uparrow\downarrow\rangle - 0.67 \times \uparrow, \downarrow\rangle$
4	5	0.17	0.11	0.04	0.96	$+1.00 \times \uparrow\downarrow, \uparrow\rangle$
					0.01	$-0.06 \times \uparrow, \uparrow\downarrow\rangle - 1.00 \times \uparrow\downarrow, \downarrow\rangle$
59	61	0.14	0.09	0.04	0.97	$+1.00 \times \downarrow, \uparrow\rangle$
52	54	0.20	0.06	0.03	0.95	$+1.00 \times -, \uparrow\downarrow\rangle$
					0.04	$-1.00 \times \uparrow, \downarrow\rangle$

Table 4.34: Largest eigenvalues $\omega_{ij,\alpha}$ and corresponding eigenvectors $\phi_{ij,\alpha}$ of the 2-orbital RDMs of the orbital pairs ij with largest mutual information I_{ij} . Data is summarized for the **CoF₄ T_d** system.

i	j	S_i	S_j	I_{ij}	$\omega_{ij,\alpha}$	$\phi_{ij,\alpha}$
5	7	0.26	0.26	0.21	0.95	$+1.00 \times \uparrow\downarrow, \downarrow\rangle$
					0.02	$+0.23 \times \uparrow\downarrow, -\rangle - 0.97 \times \uparrow\downarrow, \uparrow\rangle$
34	37	0.23	0.24	0.13	0.94	$+1.00 \times \uparrow\downarrow, \uparrow\downarrow\rangle$
					0.02	$-0.07 \times \uparrow\downarrow, -\rangle + 1.00 \times \uparrow\downarrow, \downarrow\rangle$
					0.01	$+0.87 \times \downarrow, \uparrow\downarrow\rangle + 0.50 \times \uparrow, \uparrow\rangle$
55	58	0.20	0.21	0.11	0.95	$+1.00 \times \uparrow\downarrow, \uparrow\rangle$
					0.02	$-0.14 \times \uparrow\downarrow, -\rangle - 0.99 \times \uparrow\downarrow, \downarrow\rangle$
75	77	0.17	0.16	0.11	0.96	$+1.00 \times \uparrow\downarrow, \downarrow\rangle$
					0.01	$+0.22 \times \uparrow\downarrow, -\rangle - 0.98 \times \uparrow\downarrow, \uparrow\rangle$
3	8	0.22	0.23	0.10	0.94	$+1.00 \times \uparrow\downarrow, \uparrow\downarrow\rangle$
					0.02	$+0.19 \times \uparrow\downarrow, -\rangle - 0.98 \times \uparrow\downarrow, \downarrow\rangle$
					0.01	$-0.85 \times \uparrow, -\rangle - 0.53 \times \uparrow, \downarrow\rangle$
					0.01	$-0.12 \times \downarrow, \downarrow\rangle - 0.10 \times \downarrow, \uparrow\downarrow\rangle - 0.99 \times \uparrow, \uparrow\rangle$
					0.01	$+0.98 \times \uparrow\downarrow, -\rangle + 0.19 \times \uparrow\downarrow, \downarrow\rangle$
7	17	0.26	0.05	0.03	0.94	$+1.00 \times -, \uparrow\rangle$
					0.05	$-1.00 \times \uparrow, \downarrow\rangle$
77	80	0.16	0.05	0.03	0.97	$+1.00 \times -, \uparrow\downarrow\rangle$
					0.03	$+1.00 \times \uparrow, \downarrow\rangle$

5 Conclusion and Outlook

This thesis exemplified on different model systems how correlation effects can systematically be analyzed to obtain insights on the structure of the electronic wave function. As a first example the dissociation of N_2 and N_2^+ in different electronic states was analyzed. The obtained QIT data can be related to and understood by chemical concepts such as bond breaking or different orbital types (σ/π , bonding/anti-bonding). Furthermore, different patterns in the mutual information and 2-orbital RDMs for orbital pairs mostly associated with weak and strong correlation are observed. While strong correlation can be associated with large mutual information and multiple 2-orbital occupation patterns (basis vectors) contributing to the related 2-orbital RDMs, weak correlation is associated with many such basis vectors of small weight each. These results are additionally confirmed by the cobalt fluorides in the last section.

Based on these observations a new approach to select the leading contributions for MCSCF and MRCI calculations was suggested and tested on the CoF_2 and CoF_4 (D_{4h}) model systems. Especially for the more strongly correlated CoF_4 model the computational effort can be drastically reduced, with accuracy remaining on the order of $1 mE_h$. Although the results are statistically limited, since only two models have been tested, they suggests large benefits for strongly correlated systems with large active spaces are possible. Systems previously unavailable due to the expensive scaling of MCSCF and MRCI may thus become accessible in the future. Further refinement of the method is possible and application to more systems may lead to empirical validation of the concept. Additionally, it was demonstrated that, depending on the system under study, an automated active space selection just based on the 1-orbital entropy does not always yield best results and the mutual information should be considered as well.

The equivalence of QIT and the MoI as a tool to quantify electron correlation effects of the different (groups of) orbitals was tested on different systems, including weakly (polyacetylen) and strongly correlated (Be_6 rings) systems as well as an open-shell (CoF_2) model. Although qualitative agreement in most cases can be observed, both approaches may yield very different quantitative values. Thus, results may in principle be transferred between both measures, but care should be taken to not accidentally exclude potentially important contributions, i.e. cutoff parameters to exclude orbitals should be kept small. The correspondence of both measures thus allows to exploit the different advantages of the related methods for treating electron correlation: Since the MoI is extremely cheap at the 1-orbital increment level, it may be used to screen a large space of virtual orbitals and then select an initial active space, without prior chemical knowledge or intuition. This will reduce the problem of large dynamical correlation contributions for a DMRG calculation. In turn, the fast convergence of the QIT data with respect to the number of blockstates in DMRG, or number of walkers in FCIQMC, may yield valuable information on the required and negligible n -orbital increments. In the context of FCIQMC it was further demonstrated how the 1-orbital entropies may be obtained.

Finally, the study of correlation effects in cobalt fluorides CoF_n shows, that the description of the electronic structure on the Co center critically depends on the AO basis set quality, while for F a smaller basis set may still yield qualitative trends. Additionally, orbital localization may significantly improve accuracy. The study of related extended systems should therefore use localized orbitals and may try to use a smaller basis set on the F and O than for Co.

Overall, the systematic study of correlation effects yielded insights stimulating a number of ideas on the improvement and combination of existing electron correlation methods for improved accuracy and/or reduced computational cost.

Bibliography

- [1] P. A. M. Dirac. “Quantum mechanics of many-electron systems”. *Proceedings of the Royal Society of London A: Mathematical, Physical and Engineering Sciences* 123 (1929), pp. 714–733. ISSN: 0950-1207. DOI: 10.1098/rspa.1929.0094.
- [2] E. Schrödinger. “Quantisierung als Eigenwertproblem”. *Ann. Phys.* 386 (1926), pp. 109–139. ISSN: 1521-3889. DOI: 10.1002/andp.19263861802.
- [3] P. A. M. Dirac. “The quantum theory of the electron”. *Proceedings of the Royal Society of London A: Mathematical, Physical and Engineering Sciences* 117 (1928), pp. 610–624. ISSN: 0950-1207. DOI: 10.1098/rspa.1928.0023.
- [4] P.-O. Löwdin. “Present Situation of Quantum Chemistry”. *The Journal of Physical Chemistry* 61 (1957), pp. 55–68. DOI: 10.1021/j150547a012.
- [5] P. Hohenberg and W. Kohn. “Inhomogeneous Electron Gas”. *Phys. Rev.* 136 (Nov. 1964), B864–B871. DOI: 10.1103/PhysRev.136.B864.
- [6] D. R. Hartree. “The Wave Mechanics of an Atom with a Non-Coulomb Central Field. Part I. Theory and Methods”. *Math. Proc. Cambridge Philos. Soc.* 24 (1928), pp. 89–110.
- [7] V. Fock. “Näherungsmethode zur Lösung des quantenmechanischen Mehrkörperproblems”. *Zeitschrift für Physik* 61 (Jan. 1930), pp. 126–148. ISSN: 0044-3328. DOI: 10.1007/BF01340294.
- [8] J. C. Slater. “Note on Hartree’s Method”. *Phys. Rev.* 35 (Jan. 1930), pp. 210–211. DOI: 10.1103/PhysRev.35.210.2.
- [9] J. D. Watts, J. Gauss, and R. J. Bartlett. “Coupled-cluster methods with noniterative triple excitations for restricted open-shell Hartree–Fock and other general single determinant reference functions. Energies and analytical gradients”. *The Journal of Chemical Physics* 98 (1993), pp. 8718–8733. DOI: 10.1063/1.464480.
- [10] J. Olsen, B. r. O. Roos, P. Joergensen, and H. J. A. Jensen. “Determinant based configuration interaction algorithms for complete and restricted configuration interaction spaces”. *The Journal of Chemical Physics* 89 (1988), pp. 2185–2192. DOI: 10.1063/1.455063.
- [11] S. F. Boys. “Construction of Some Molecular Orbitals to Be Approximately Invariant for Changes from One Molecule to Another”. *Rev. Mod. Phys.* 32 (Apr. 1960), pp. 296–299. DOI: 10.1103/RevModPhys.32.296.
- [12] J. Pipek and P. G. Mezey. “A fast intrinsic localization procedure applicable for ab initio and semiempirical linear combination of atomic orbital wave functions”. *The Journal of Chemical Physics* 90 (1989), pp. 4916–4926. DOI: 10.1063/1.456588.

- [13] C. Krumnow, L. Veis, Ö. Legeza, and J. Eisert. “Fermionic Orbital Optimization in Tensor Network States”. *Phys. Rev. Lett.* 117 (Nov. 2016), p. 210402. DOI: 10.1103/PhysRevLett.117.210402.
- [14] S. R. White. “Density matrix formulation for quantum renormalization groups”. *Phys. Rev. Lett.* 69 (Nov. 1992), pp. 2863–2866. DOI: 10.1103/PhysRevLett.69.2863.
- [15] S. R. White. “Density-matrix algorithms for quantum renormalization groups”. *Phys. Rev. B* 48 (Oct. 1993), pp. 10345–10356. DOI: 10.1103/PhysRevB.48.10345.
- [16] L. Veis et al. “Coupled Cluster Method with Single and Double Excitations Tailored by Matrix Product State Wave Functions”. *The Journal of Physical Chemistry Letters* 7 (2016). PMID: 27682626, pp. 4072–4078. DOI: 10.1021/acs.jpcllett.6b01908.
- [17] H. Stoll. “The correlation energy of crystalline silicon”. *Chem. Phys. Lett.* 191 (1992), pp. 548–552. ISSN: 0009-2614. DOI: [https://doi.org/10.1016/0009-2614\(92\)85587-Z](https://doi.org/10.1016/0009-2614(92)85587-Z).
- [18] H. Stoll. “Correlation energy of diamond”. *Phys. Rev. B* 46 (Sept. 1992), pp. 6700–6704. DOI: 10.1103/PhysRevB.46.6700.
- [19] B. M. Austin, D. Y. Zubarev, and W. A. Lester. “Quantum Monte Carlo and Related Approaches”. *Chem. Rev.* 112 (2012). PMID: 22196085, pp. 263–288. DOI: 10.1021/cr2001564.
- [20] G. H. Booth, A. J. W. Thom, and A. Alavi. “Fermion Monte Carlo without fixed nodes: A game of life, death, and annihilation in Slater determinant space”. *The Journal of Chemical Physics* 131 (2009), p. 054106. DOI: 10.1063/1.3193710.
- [21] A. Georges, G. Kotliar, W. Krauth, and M. J. Rozenberg. “Dynamical mean-field theory of strongly correlated fermion systems and the limit of infinite dimensions”. *Rev. Mod. Phys.* 68 (Jan. 1996), pp. 13–125. DOI: 10.1103/RevModPhys.68.13.
- [22] S. Wouters, C. A. Jiménez-Hoyos, Q. Sun, and G. K.-L. Chan. “A Practical Guide to Density Matrix Embedding Theory in Quantum Chemistry”. *J. Chem. Theory Comput.* 12 (2016). PMID: 27159268, pp. 2706–2719. DOI: 10.1021/acs.jctc.6b00316.
- [23] D. Ghosh, J. Hachmann, T. Yanai, and G. K.-L. Chan. “Orbital optimization in the density matrix renormalization group, with applications to polyenes and β -carotene”. *The Journal of Chemical Physics* 128 (2008), p. 144117. DOI: 10.1063/1.2883976.
- [24] T. Yanai, e. Y. Kurashig, D. Ghosh, and G. K.-L. Chan. “Accelerating convergence in iterative solution for large-scale complete active space self-consistent-field calculations”. *Int. J. Quant. Chem.* 109 (2009), p. 2178. DOI: 10.1002/qua.22099.
- [25] D. Zgid and M. Nooijen. “The density matrix renormalization group self-consistent field method: Orbital optimization with the density matrix renormalization group method in the active space”. *J. Chem. Phys.* 128 (2008), p. 144116. DOI: 10.1063/1.2883981.

- [26] S. Wouters, T. Bogaerts, P. Van Der Voort, V. Van Speybroeck, and D. Van Neck. “Communication: DMRG-SCF study of the singlet, triplet, and quintet states of oxo-Mn(Salen)”. *The Journal of Chemical Physics* 140 (2014), p. 241103. DOI: 10.1063/1.4885815.
- [27] G. Li Manni, S. D. Smart, and A. Alavi. “Combining the Complete Active Space Self-Consistent Field Method and the Full Configuration Interaction Quantum Monte Carlo within a Super-CI Framework, with Application to Challenging Metal-Porphyrins”. *J. Chem. Theory Comput.* 12 (2016). PMID: 26808894, pp. 1245–1258. DOI: 10.1021/acs.jctc.5b01190.
- [28] I. Bengtsson and K. Zyczkowski. *Geometry of Quantum States: An Introduction to Quantum Entanglement*. Cambridge University Press, 2007. ISBN: 9781139453462.
- [29] C. J. Stein and M. Reiher. “Automated Selection of Active Orbital Spaces”. *J. Chem. Theory Comput.* 12 (2016). PMID: 26959891, pp. 1760–1771. DOI: 10.1021/acs.jctc.6b00156.
- [30] D. J. Tannor. *Introduction to Quantum Mechanics: A Time-Dependent Perspective*. University Science Books, 2006. ISBN: 1891389238.
- [31] A. Szabo and N. S. Ostlund. *Modern Quantum Chemistry: Introduction to Advanced Electronic Structure Theory (Dover Books on Chemistry)*. Dover Publications, 1996. ISBN: 0486691861.
- [32] T. Helgaker, P. Jorgensen, and J. Olsen. *Molecular electronic-structure theory*. 1. Auflage. New York: Wiley, 2000. ISBN: 978-0-471-96755-2. DOI: 10.1002/9781119019572.
- [33] M. Born and R. Oppenheimer. “Zur Quantentheorie der Molekeln”. *Ann. Phys.* 389 (1927), pp. 457–484. DOI: 10.1002/andp.19273892002.
- [34] K. Fukui, T. Yonezawa, and H. Shingu. “A Molecular Orbital Theory of Reactivity in Aromatic Hydrocarbons”. *The Journal of Chemical Physics* 20 (1952), pp. 722–725. DOI: 10.1063/1.1700523.
- [35] R. B. Woodward and R. Hoffmann. “Stereochemistry of Electrocyclic Reactions”. *J. Am. Chem. Soc.* 87 (1965), pp. 395–397. DOI: 10.1021/ja01080a054.
- [36] J. C. Slater. “The Theory of Complex Spectra”. *Phys. Rev.* 34 (Nov. 1929), pp. 1293–1322. DOI: 10.1103/PhysRev.34.1293.
- [37] W. Pauli. “Über den Zusammenhang des Abschlusses der Elektronengruppen im Atom mit der Komplexstruktur der Spektren”. *Zeitschrift für Physik* 31 (Feb. 1925), pp. 765–783. ISSN: 0044-3328. DOI: 10.1007/BF02980631.
- [38] E. U. Condon. “The Theory of Complex Spectra”. *Phys. Rev.* 36 (Oct. 1930), pp. 1121–1133. DOI: 10.1103/PhysRev.36.1121.
- [39] C. C. J. Roothaan. “New Developments in Molecular Orbital Theory”. *Rev. Mod. Phys.* 23 (Apr. 1951), pp. 69–89. DOI: 10.1103/RevModPhys.23.69.
- [40] R. J. Bartlett and J. F. Stanton. *Reviews in Computational Chemistry: Applications of Post-Hartree-Fock Methods: A Tutorial*. Ed. by K. B. Lipkowitz and D. B. Boyd. Vol. 5. VCH Publishers, 1994, pp. 65–169.
- [41] R. J. Bartlett and M. Musiał. “Coupled-cluster theory in quantum chemistry”. *Rev. Mod. Phys.* 79 (Feb. 2007), pp. 291–352. DOI: 10.1103/RevModPhys.79.291.

- [42] D. I. Lyakh, M. Musiał, V. F. Lotrich, and R. J. Bartlett. “Multireference Nature of Chemistry: The Coupled-Cluster View”. *Chem. Rev.* 112 (2012). PMID: 22220988, pp. 182–243. DOI: 10.1021/cr2001417.
- [43] K. Andersson, P.-Å. Malmqvist, B. O. Roos, A. J. Sadlej, and K. Wolinski. “Second-order perturbation theory with a CASSCF reference function”. *The Journal of Physical Chemistry* 94 (1990), pp. 5483–5488. DOI: 10.1021/j100377a012.
- [44] K. Andersson, P. Malmqvist, and B. O. Roos. “Second-order perturbation theory with a complete active space self-consistent field reference function”. *The Journal of Chemical Physics* 96 (1992), pp. 1218–1226. DOI: 10.1063/1.462209.
- [45] C. Angeli, R. Cimiraglia, and J.-P. Malrieu. “N-electron valence state perturbation theory: a fast implementation of the strongly contracted variant”. *Chem. Phys. Lett.* 350 (2001), pp. 297–305. ISSN: 0009-2614. DOI: [https://doi.org/10.1016/S0009-2614\(01\)01303-3](https://doi.org/10.1016/S0009-2614(01)01303-3).
- [46] C. Angeli, R. Cimiraglia, S. Evangelisti, T. Leininger, and J.-P. Malrieu. “Introduction of n-electron valence states for multireference perturbation theory”. *The Journal of Chemical Physics* 114 (2001), pp. 10252–10264. DOI: 10.1063/1.1361246.
- [47] C. Angeli, R. Cimiraglia, and J.-P. Malrieu. “n-electron valence state perturbation theory: A spinless formulation and an efficient implementation of the strongly contracted and of the partially contracted variants”. *The Journal of Chemical Physics* 117 (2002), pp. 9138–9153. DOI: 10.1063/1.1515317.
- [48] P. G. Szalay, T. Müller, G. Gidofalvi, H. Lischka, and R. Shepard. “Multiconfiguration Self-Consistent Field and Multireference Configuration Interaction Methods and Applications”. *Chem. Rev.* 112 (2012). PMID: 22204633, pp. 108–181. DOI: 10.1021/cr200137a.
- [49] Sz. Szalay et al. “Tensor product methods and entanglement optimization for ab initio quantum chemistry”. *Int. J. Quant. Chem.* 115 (2015), pp. 1342–1391. ISSN: 1097-461X. DOI: 10.1002/qua.24898.
- [50] K. G. Wilson. “The renormalization group: Critical phenomena and the Kondo problem”. *Rev. Mod. Phys.* 47 (Oct. 1975), pp. 773–840. DOI: 10.1103/RevModPhys.47.773.
- [51] U. Schollwöck. “The density-matrix renormalization group”. *Rev. Mod. Phys.* 77 (Apr. 2005), pp. 259–315. DOI: 10.1103/RevModPhys.77.259.
- [52] U. Schollwöck. “The density-matrix renormalization group in the age of matrix product states”. *Ann. Phys.* 326 (2011). January 2011 Special Issue, pp. 96–192. ISSN: 0003-4916. DOI: <https://doi.org/10.1016/j.aop.2010.09.012>.
- [53] G. K.-L. Chan and S. Sharma. “The Density Matrix Renormalization Group in Quantum Chemistry”. *Annu. Rev. Phys. Chem.* 62 (2011), pp. 465–481. DOI: 10.1146/annurev-physchem-032210-103338.
- [54] S. Wouters and D. Van Neck. “The density matrix renormalization group for ab initio quantum chemistry”. *Eur. Phys. J. D* 68 (Sept. 2014), p. 272. ISSN: 1434-6079. DOI: 10.1140/epjd/e2014-50500-1.

- [55] E. Schmidt. “Zur Theorie der linearen und nichtlinearen Integralgleichungen”. *Mathematische Annalen* 63 (Dec. 1907), pp. 433–476. ISSN: 1432-1807. DOI: 10.1007/BF01449770.
- [56] G. Barcza, Ö. Legeza, K. H. Marti, and M. Reiher. “Quantum-information analysis of electronic states of different molecular structures”. *Phys. Rev. A* 83 (Jan. 2011), p. 012508. DOI: 10.1103/PhysRevA.83.012508.
- [57] V. Murg, F. Verstraete, Ö. Legeza, and R. M. Noack. “Simulating strongly correlated quantum systems with tree tensor networks”. *Phys. Rev. B* 82 (Nov. 2010), p. 205105. DOI: 10.1103/PhysRevB.82.205105.
- [58] N. Nakatani and G. K.-L. Chan. “Efficient tree tensor network states (TTNS) for quantum chemistry: Generalizations of the density matrix renormalization group algorithm”. *The Journal of Chemical Physics* 138, 134113 (2013), p. 134113. DOI: 10.1063/1.4798639.
- [59] V. Murg, F. Verstraete, R. Schneider, P. R. Nagy, and Ö. Legeza. “Tree Tensor Network State with Variable Tensor Order: An Efficient Multireference Method for Strongly Correlated Systems”. *J. Chem. Theory Comput.* 11 (2015). PMID: 25844072, pp. 1027–1036. DOI: 10.1021/ct501187j.
- [60] K. Gunst, F. Verstraete, S. Wouters, Ö. Legeza, and D. Van Neck. “T3NS: Three-Legged Tree Tensor Network States”. *J. Chem. Theory Comput.* 14 (2018). PMID: 29481743, pp. 2026–2033. DOI: 10.1021/acs.jctc.8b00098.
- [61] Ö. Legeza and J. Sólyom. “Optimizing the density-matrix renormalization group method using quantum information entropy”. *Phys. Rev. B* 68 (Nov. 2003), p. 195116. DOI: 10.1103/PhysRevB.68.195116.
- [62] Ö. Legeza, J. Röder, and B. A. Hess. “Controlling the accuracy of the density-matrix renormalization-group method: The dynamical block state selection approach”. *Phys. Rev. B* 67 (Mar. 2003), p. 125114. DOI: 10.1103/PhysRevB.67.125114.
- [63] Ö. Legeza and J. Sólyom. “Quantum data compression, quantum information generation, and the density-matrix renormalization-group method”. *Phys. Rev. B* 70 (Nov. 2004), p. 205118. DOI: 10.1103/PhysRevB.70.205118.
- [64] J. J. Eriksen, F. Lipparini, and J. Gauss. “Virtual Orbital Many-Body Expansions: A Possible Route towards the Full Configuration Interaction Limit”. *The Journal of Physical Chemistry Letters* 8 (2017). PMID: 28892390, pp. 4633–4639. DOI: 10.1021/acs.jpcllett.7b02075.
- [65] H. Flyvbjerg and H. G. Petersen. “Error estimates on averages of correlated data”. *The Journal of Chemical Physics* 91 (1989), pp. 461–466. DOI: 10.1063/1.457480.
- [66] G. H. Booth, D. Cleland, A. J. W. Thom, and A. Alavi. “Breaking the carbon dimer: The challenges of multiple bond dissociation with full configuration interaction quantum Monte Carlo methods”. *The Journal of Chemical Physics* 135 (2011), p. 084104. DOI: 10.1063/1.3624383.
- [67] D. Cleland, G. H. Booth, and A. Alavi. “Communications: Survival of the fittest: Accelerating convergence in full configuration-interaction quantum Monte Carlo”. *The Journal of Chemical Physics* 132 (2010), p. 041103. DOI: 10.1063/1.3302277.

- [68] A. Lozovoi, K. Guther, and A. Alavi. *to be published* ().
- [69] F. R. Petruzielo, A. A. Holmes, H. J. Changlani, M. P. Nightingale, and C. J. Umrigar. “Semistochastic Projector Monte Carlo Method”. *Phys. Rev. Lett.* 109 (Dec. 2012), p. 230201. DOI: 10.1103/PhysRevLett.109.230201.
- [70] N. S. Blunt et al. “Semi-stochastic full configuration interaction quantum Monte Carlo: Developments and application”. *The Journal of Chemical Physics* 142 (2015), p. 184107. DOI: 10.1063/1.4920975.
- [71] C. E. Shannon. “A mathematical theory of communication”. *The Bell System Technical Journal* 27 (July 1948), pp. 379–423. ISSN: 0005-8580. DOI: 10.1002/j.1538-7305.1948.tb01338.x.
- [72] C. E. Shannon. “A mathematical theory of communication”. *The Bell System Technical Journal* 27 (Oct. 1948), pp. 623–656. ISSN: 0005-8580. DOI: 10.1002/j.1538-7305.1948.tb00917.x.
- [73] T. D. Schneider. “A brief review of molecular information theory”. *Nano Commun. Networks* 1 (2010). Fundamentals of Nanoscale Communications, pp. 173–180. ISSN: 1878-7789. DOI: <https://doi.org/10.1016/j.nancom.2010.09.002>.
- [74] E. Gibson et al. “A Noisy-Channel Account of Crosslinguistic Word-Order Variation”. *Psychological Science* 24 (2013). PMID: 23649563, pp. 1079–1088. DOI: 10.1177/0956797612463705.
- [75] J. D. Bekenstein. “Black Holes and Entropy”. *Phys. Rev. D* 7 (Apr. 1973), pp. 2333–2346. DOI: 10.1103/PhysRevD.7.2333.
- [76] S. Ghosh. “Black Hole Entropy: From Shannon to Bekenstein”. *Int. J. Theor. Phys.* 50 (2011), pp. 3512–3520. DOI: 10.1007/s10773-011-0859-y.
- [77] A. Rényi. “On Measures of Entropy and Information”. *Proceedings of the Fourth Berkeley Symposium on Mathematical Statistics and Probability, Volume 1: Contributions to the Theory of Statistics*. Berkeley, Calif.: University of California Press, 1961, pp. 547–561.
- [78] J. v. Neumann. “Mathematische Begründung der Quantenmechanik”. *Nachrichten von der Gesellschaft der Wissenschaften zu Göttingen, Mathematisch-Physikalische Klasse 1927* (1927), pp. 1–57.
- [79] Ö. Legeza and J. Sólyom. “Two-Site Entropy and Quantum Phase Transitions in Low-Dimensional Models”. *Phys. Rev. Lett.* 96 (Mar. 2006), p. 116401. DOI: 10.1103/PhysRevLett.96.116401.
- [80] J. Rissler, R. M. Noack, and S. R. White. “Measuring orbital interaction using quantum information theory”. *Chem. Phys.* 323 (2006), pp. 519–531. ISSN: 0301-0104. DOI: 10.1016/j.chemphys.2005.10.018.
- [81] S. Szalay, G. Barcza, T. Szilvási, L. Veis, and Ö. Legeza. “The correlation theory of the chemical bond”. *Sci. Rep.* 7 (May 2017). DOI: 10.1038/s41598-017-02447-z.
- [82] C. Müller and B. Paulus. “Wavefunction-based electron correlation methods for solids”. *Phys. Chem. Chem. Phys.* 14 (2012), pp. 7605–7614. DOI: 10.1039/C2CP24020C.

- [83] H. Bethe. “Zur Theorie der Metalle”. *Zeitschrift für Physik* 71 (Mar. 1931), pp. 205–226. ISSN: 0044-3328. DOI: 10.1007/BF01341708.
- [84] J. Hubbard and B. H. Flowers. “Electron correlations in narrow energy bands”. *Proceedings of the Royal Society of London. Series A. Mathematical and Physical Sciences* 276 (1963), pp. 238–257. DOI: 10.1098/rspa.1963.0204.
- [85] A. Roche and H. Lefebvre-Brion. “Some ab initio calculations related to the predissociation of the $C^2\Sigma_u^+$ state of N_2^+ ”. *Chem. Phys. Lett.* 32 (Apr. 1975), pp. 155–158. ISSN: 0009-2614. DOI: 10.1016/0009-2614(75)85190-6.
- [86] S. R. Langhoff, C. W. Bauschlicher, and H. Partridge. “Theoretical study of the N_2^+ Meinel system”. *J. Chem. Phys.* 87 (1987), p. 4716. ISSN: 0021-9606. DOI: 10.1063/1.452835.
- [87] S. R. Langhoff and C. W. Bauschlicher. “Theoretical study of the first and second negative systems of N_2^+ ”. *J. Chem. Phys.* 88 (1988), p. 329. ISSN: 0021-9606. DOI: 10.1063/1.454604.
- [88] P. Baltzer, M. Larsson, L. Karlsson, B. Wannberg, and M. Carlsson Göthe. “Inner-valence states of N_2^+ studied by uv photoelectron spectroscopy and configuration-interaction calculations”. *Phys. Rev. A* 46 (Nov. 1992), pp. 5545–5553. ISSN: 1094-1622. DOI: 10.1103/physreva.46.5545.
- [89] C. van de Runstraat, F. de Heer, and T. Govers. “Excitation and decay of the $C^2\Sigma_u^+$ state of N_2^+ in the case of electron impact on N_2 ”. *Chem. Phys.* 3 (1974), pp. 431–450. ISSN: 0301-0104. DOI: [http://dx.doi.org/10.1016/0301-0104\(74\)87010-2](http://dx.doi.org/10.1016/0301-0104(74)87010-2).
- [90] T. Govers, C. van de Runstraat, and F. de Heer. “Excitation and decay of the $C^2\Sigma_u^+$ state of N_2^+ following collisions of He^+ ions with N_2 isotopes”. *Chem. Phys.* 9 (1975), pp. 285–299. ISSN: 0301-0104. DOI: [http://dx.doi.org/10.1016/0301-0104\(75\)80068-1](http://dx.doi.org/10.1016/0301-0104(75)80068-1).
- [91] P. Erman. “Direct Measurement of the N_2^+ C State Predissociation Probability”. *Phys. Scr.* 14 (July 1976), pp. 51–54. ISSN: 1402-4896. DOI: 10.1088/0031-8949/14/1-2/010.
- [92] T. Aoto et al. “Inner-valence states of N_2^+ and the dissociation dynamics studied by threshold photoelectron spectroscopy and configuration interaction calculation”. *J. Chem. Phys.* 124, 234306 (2006). DOI: <http://dx.doi.org/10.1063/1.2206586>.
- [93] M. Lucchini et al. “Autoionization and ultrafast relaxation dynamics of highly excited states in N_2 ”. *Phys. Rev. A* 86 (Oct. 2012), p. 043404. DOI: 10.1103/PhysRevA.86.043404.
- [94] H.-J. Werner et al. *MOLPRO, version 2015.1, a package of ab initio programs*. see <http://www.molpro.net>. Cardiff, UK, 2015.
- [95] H.-J. Werner and P. J. Knowles. “A Second Order MCSCF Method with Optimum Convergence”. *J. Chem. Phys.* 82 (1985), p. 5053. DOI: 10.1063/1.448627.
- [96] P. J. Knowles and H.-J. Werner. “An Efficient Second Order MCSCF Method for Long Configuration Expansions”. *Chem. Phys. Letters* 115 (1985), pp. 259–267. DOI: 10.1016/0009-2614(85)80025-7.

- [97] C. Stemmler, B. Paulus, and Ö. Legeza. “Analysis of electron-correlation effects in strongly correlated systems (N_2 and N_2^+) by applying the density-matrix renormalization-group method and quantum information theory”. *Phys. Rev. A* 97 (Feb. 2018), p. 022505. DOI: 10.1103/PhysRevA.97.022505.
- [98] M. Yu, S. Kalvoda, and M. Dolg. “An incremental approach for correlation contributions to the structural and cohesive properties of polymers. Coupled-cluster study of trans-polyacetylene”. *Chem. Phys.* 224 (1997), pp. 121–131. ISSN: 0301-0104. DOI: [https://doi.org/10.1016/S0301-0104\(97\)00257-7](https://doi.org/10.1016/S0301-0104(97)00257-7).
- [99] R. A. Kendall, T. H. Dunning, and R. J. Harrison. “Electron affinities of the first-row atoms revisited. Systematic basis sets and wave functions”. *J. Chem. Phys.* 96 (1992), pp. 6796–6806. DOI: 10.1063/1.462569.
- [100] E. Fertitta, B. Paulus, G. Barcza, and Ö. Legeza. “Investigation of metal–insulator-like transition through the *ab initio* density matrix renormalization group approach”. *Phys. Rev. B* 90 (2014), p. 245129. DOI: 10.1103/PhysRevB.90.245129.
- [101] D. Koch, E. Fertitta, and B. Paulus. “Calculation of the static and dynamical correlation energy of pseudo-one-dimensional beryllium systems via a many-body expansion”. *The Journal of Chemical Physics* 145 (2016), p. 024104. DOI: 10.1063/1.4955317.
- [102] T. Schlöder. “Matrix Isolation and Quantum-chemical Study of Molecules containing Transition Metals in High Oxidation States”. PhD thesis. Albert-Ludwigs-Universität Freiburg, 2013.
- [103] J. V. Rau, S. Nunziante Cesaro, N. S. Chilingarov, and G. Balducci. “Identification of Gaseous Cobalt Tetrafluoride: MS and FTIR Spectroscopic Studies”. *Inorg. Chem.* 38 (1999), pp. 5695–5697. DOI: 10.1021/ic990294t.
- [104] M. Korobov, L. Savinova, and L. Sidorov. “Stabilities of CoF_4 and CrF_5 in the gas phase”. *The Journal of Chemical Thermodynamics* 25 (1993), pp. 1161–1168. ISSN: 0021-9614. DOI: 0.1006/jcht.1993.1113.
- [105] V. V. Sliznev, N. V. *, and J. Vogt. “Ab initio study of the ground and lower-lying excited electronic states of CoF_2 , $CoCl_2$, $CoBr_2$ and CoI_2 ”. *Mol. Phys.* 102 (2004), pp. 1767–1776. DOI: 10.1080/00268970412331287043.
- [106] J. H. Yates and R. M. Pitzer. “Molecular and electronic structures of transition metal trifluorides”. *The Journal of Chemical Physics* 70 (1979), pp. 4049–4055. DOI: 10.1063/1.438027.
- [107] A. Popovic, A. Lesar, J. V. Rau, and L. Bencze. “Sublimation properties of CoF_3 : mass spectrometric and quantum chemical studies”. *Rapid Commun. Mass Spectrom.* 15 (2001), pp. 749–757. DOI: 10.1002/rcm.292.
- [108] S. Riedel and M. Kaupp. “The highest oxidation states of the transition metal elements”. *Coord. Chem. Rev.* 253 (2009). Theory and Computing in Contemporary Coordination Chemistry, pp. 606–624. ISSN: 0010-8545. DOI: 10.1016/j.ccr.2008.07.014.
- [109] R. Fowler et al. “Synthesis of Fluorocarbons”. *Industrial & Engineering Chemistry* 39 (1947), pp. 292–298. DOI: 10.1021/ie50447a612.

- [110] P. Ferstl et al. “Self-Organized Growth, Structure, and Magnetism of Monatomic Transition-Metal Oxide Chains”. *Phys. Rev. Lett.* 117 (July 2016), p. 046101. DOI: 10.1103/PhysRevLett.117.046101.
- [111] P. Ferstl, F. Mittendorfer, J. Redinger, M. A. Schneider, and L. Hammer. “Monatomic Co, CoO₂, and CoO₃ nanowires on Ir(100) and Pt(100) surfaces: Formation, structure, and energetics”. *Phys. Rev. B* 96 (Aug. 2017), p. 085407. DOI: 10.1103/PhysRevB.96.085407.
- [112] W. Jiang, N. J. DeYonker, and A. K. Wilson. “Multireference Character for 3d Transition-Metal-Containing Molecules”. *J. Chem. Theory Comput.* 8 (2012). PMID: 26596596, pp. 460–468. DOI: 10.1021/ct2006852.
- [113] H.-J. Werner, P. J. Knowles, G. Knizia, F. R. Manby, and M. Schütz. “Molpro: a general purpose quantum chemistry program package”. *WIREs Comput Mol Sci* 2 (2012), pp. 242–253.
- [114] Ö. Legeza. *QC-DMRG-Budapest, A Program for Quantum Chemical DMRG Calculations*. HAS RISSPO Budapest. 2000-2016.
- [115] H.-J. Werner and P. J. Knowles. “An Efficient Internally Contracted Multiconfiguration Reference CI Method”. *J. Chem. Phys.* 89 (1988), pp. 5803–5814. DOI: 10.1063/1.455556.
- [116] P. J. Knowles and H.-J. Werner. “An Efficient Method for the Evaluation of Coupling Coefficients in Configuration Interaction Calculations”. *Chem. Phys. Letters* 145 (1988), pp. 514–522. DOI: 10.1016/0009-2614(88)87412-8.
- [117] K. Boguslawski, P. Tecmer, G. Barcza, Ö. Legeza, and M. Reiher. “Orbital Entanglement in Bond-Formation Processes”. *J. Chem. Theory Comput.* 9 (2013), pp. 2959–2973. DOI: 10.1021/ct400247p.
- [118] C. Overy et al. “Unbiased reduced density matrices and electronic properties from full configuration interaction quantum Monte Carlo”. *The Journal of Chemical Physics* 141 (2014), p. 244117. DOI: 10.1063/1.4904313.
- [119] *NECI, Code available at https://github.com/ghb24/NECI_STABLE*.
- [120] G. H. Booth, S. D. Smart, and A. Alavi. “Linear-scaling and parallelisable algorithms for stochastic quantum chemistry”. *Mol. Phys.* 112 (2014), pp. 1855–1869. DOI: 10.1080/00268976.2013.877165.
- [121] C. J. Stein and M. Reiher. “Measuring multi-configurational character by orbital entanglement”. *Mol. Phys.* 115 (2017), pp. 2110–2119. DOI: 10.1080/00268976.2017.1288934.
- [122] C. Stemmler and B. Paulus. “Quantification of electron correlation effects: Quantum Information Theory versus Method of Increments”. *Int. J. Quantum Chem.* (2019). DOI: 10.1002/qua.26007.
- [123] P.-Å. Malmqvist and B. O. Roos. “Inclusion of dynamic σ - π polarization in π -electron ab initio calculations”. *Theor. Chim. Acta* 83 (May 1992), pp. 191–199. ISSN: 1432-2234. DOI: 10.1007/BF01132828.
- [124] C. Angeli. “An analysis of the dynamic σ polarization in the V state of ethene”. *Int. J. Quantum Chem.* 110 (2010), pp. 2436–2447. DOI: 10.1002/qua.22597.

- [125] P. J. Knowles and N. C. Handy. “A New Determinant-based Full Configuration Interaction Method”. *Chem. Phys. Letters* 111 (1984), pp. 315–321.
- [126] P. J. Knowles and N. C. Handy. “A Determinant Based Full Configuration Interaction Program”. *Comput. Phys. Commun.* 54 (1989), pp. 75–83. DOI: 10.1016/0010-4655(89)90033-7.
- [127] S. Diner, J. P. Malrieu, and P. Claverie. “Localized bond orbitals and the correlation problem”. *Theor. Chim. Acta* 13 (Jan. 1969), pp. 1–17. ISSN: 1432-2234. DOI: 10.1007/BF00527316.
- [128] O. Sinanoğlu. “Many-Electron Theory of Atoms, Molecules and Their Interactions”. *Advances in Chemical Physics*. John Wiley & Sons, Ltd, 1964, pp. 315–412. ISBN: 9780470143520. DOI: 10.1002/9780470143520.ch7.
- [129] R. K. Nesbet. “Electronic Correlation in Atoms and Molecules”. *Advances in Chemical Physics*. John Wiley & Sons, Ltd, 1965, pp. 321–363. ISBN: 9780470143551. DOI: 10.1002/9780470143551.ch4.

Appendix

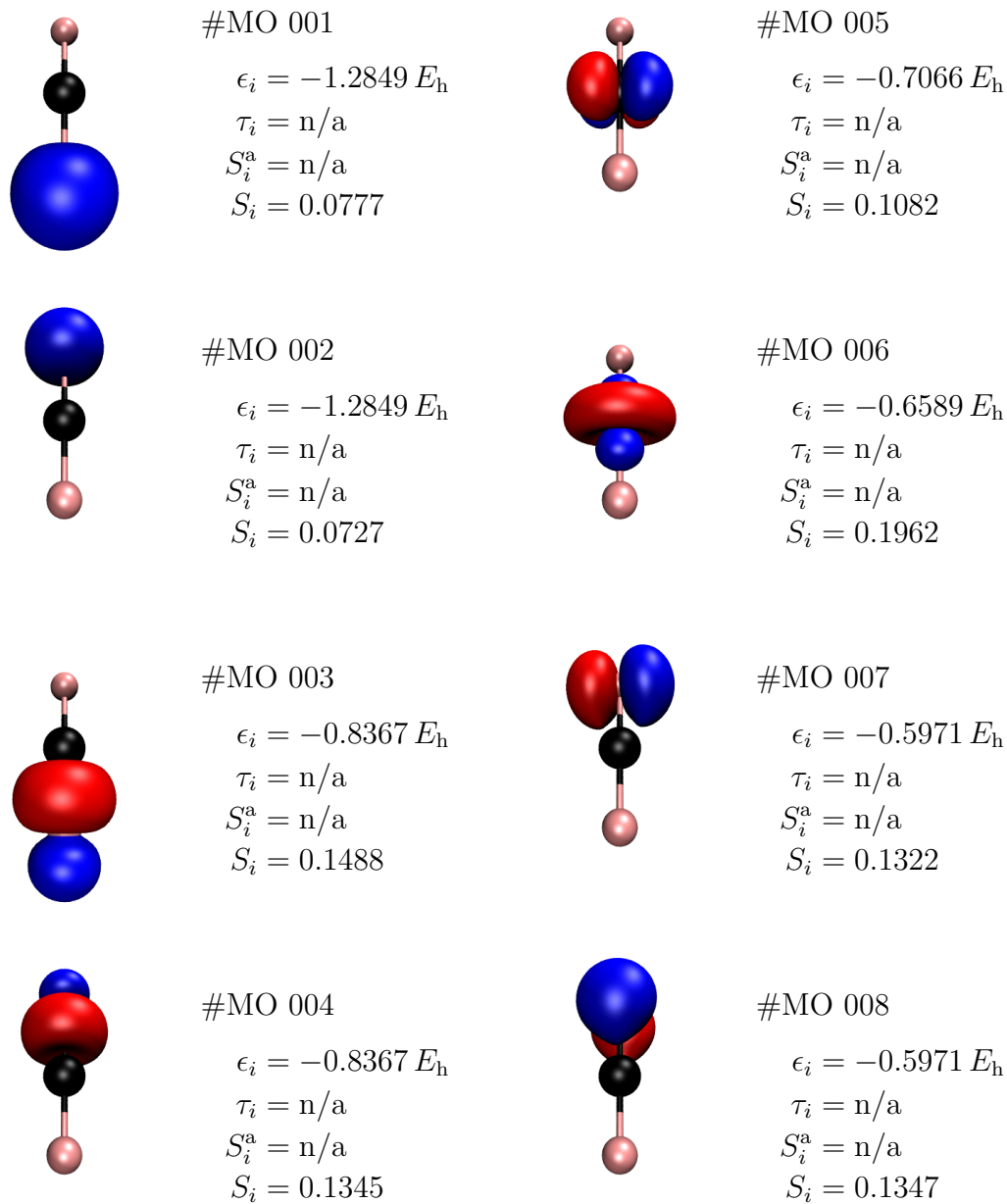


Figure A.1: Pipek-Mezey localized active space molecular orbitals #1 to #8 for CoF_2 . Their corresponding diagonal Fock matrix element ϵ_i , 1-orbital increment ε_i as well as the agnostic and non-agnostic 1-orbital entropies S_i^a and S_i are given as well. Isosurfaces are plotted at $|\psi(\vec{r})| = 0.05 a_0^{-1.5}$.

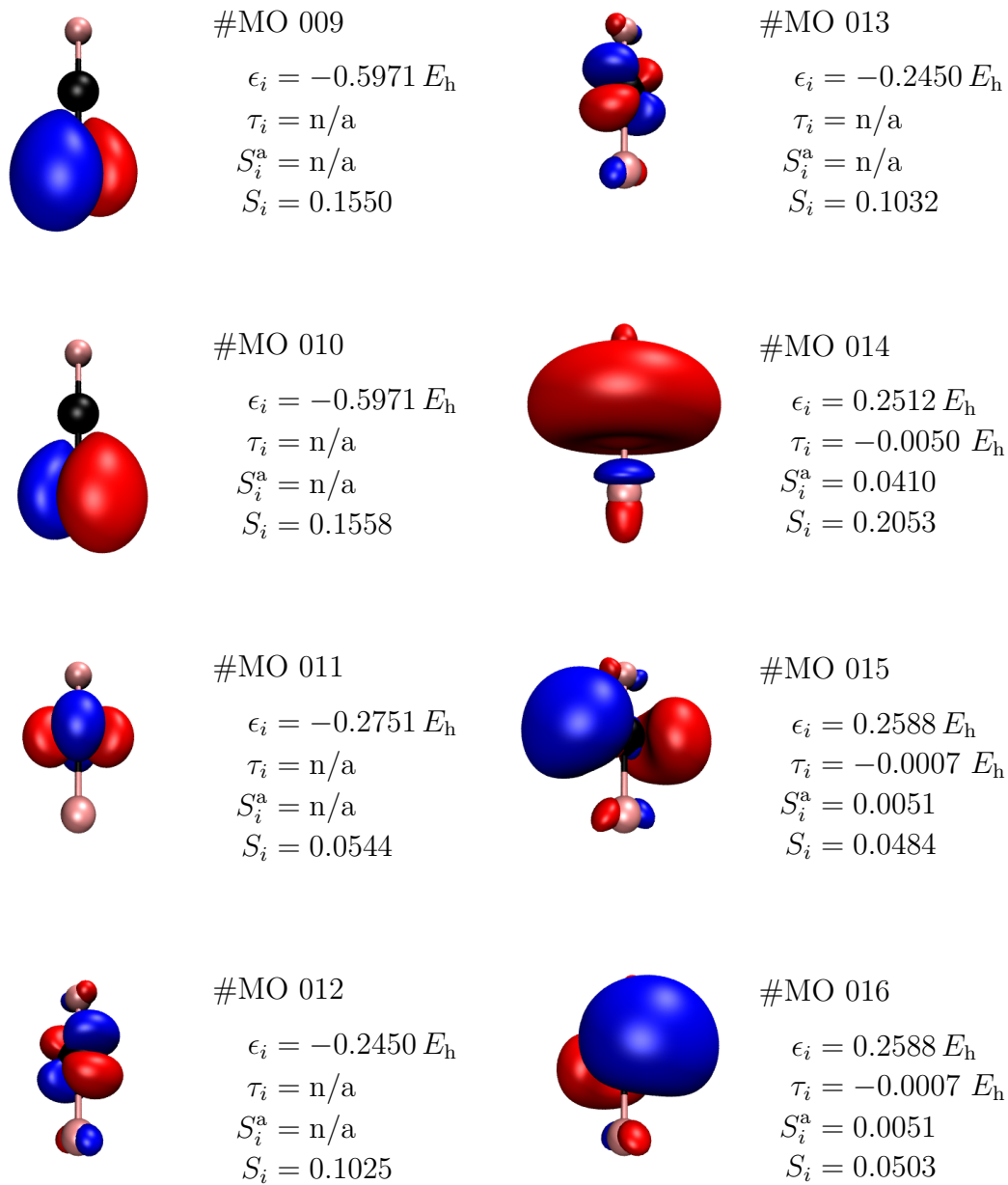


Figure A.2: Pipek-Mezey localized active space molecular orbitals #9 to #16 for CoF_2 . Their corresponding diagonal Fock matrix element ϵ_i , 1-orbital increment ε_i as well as the agnostic and non-agnostic 1-orbital entropies S_i^a and S_i are given as well. Isosurfaces are plotted at $|\psi(\vec{r})| = 0.05 a_0^{-1.5}$.

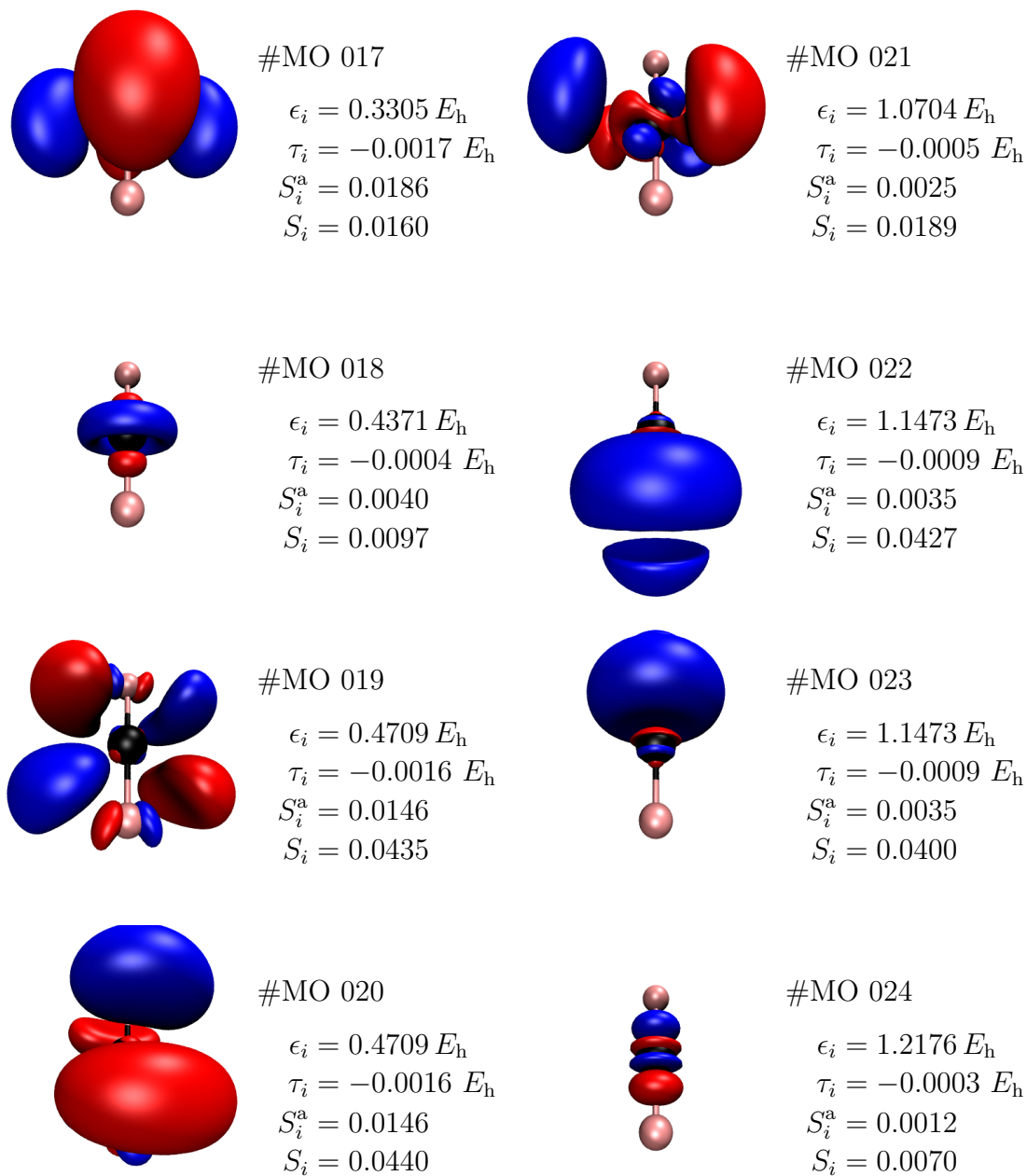


Figure A.3: Pipek-Mezey localized active space molecular orbitals #17 to #24 for CoF_2 . Their corresponding diagonal Fock matrix element ϵ_i , 1-orbital increment ε_i as well as the agnostic and non-agnostic 1-orbital entropies S_i^a and S_i are given as well. Isosurfaces are plotted at $|\psi(\vec{r})| = 0.05 a_0^{-1.5}$.

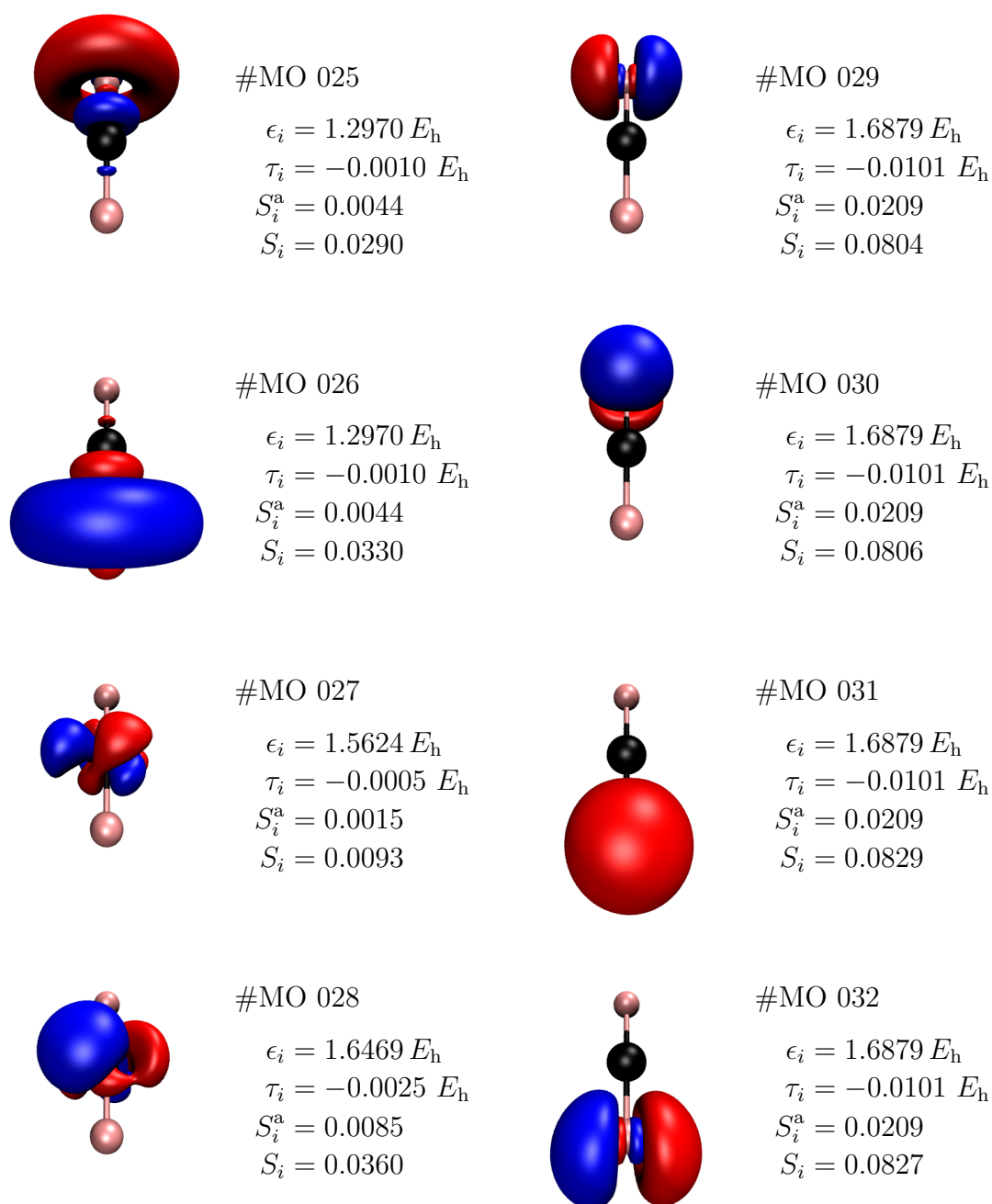


Figure A.4: Pipek-Mezey localized active space molecular orbitals #25 to #32 for CoF_2 . Their corresponding diagonal Fock matrix element ϵ_i , 1-orbital increment ε_i as well as the agnostic and non-agnostic 1-orbital entropies S_i^a and S_i are given as well. Isosurfaces are plotted at $|\psi(\vec{r})| = 0.05 a_0^{-1.5}$.

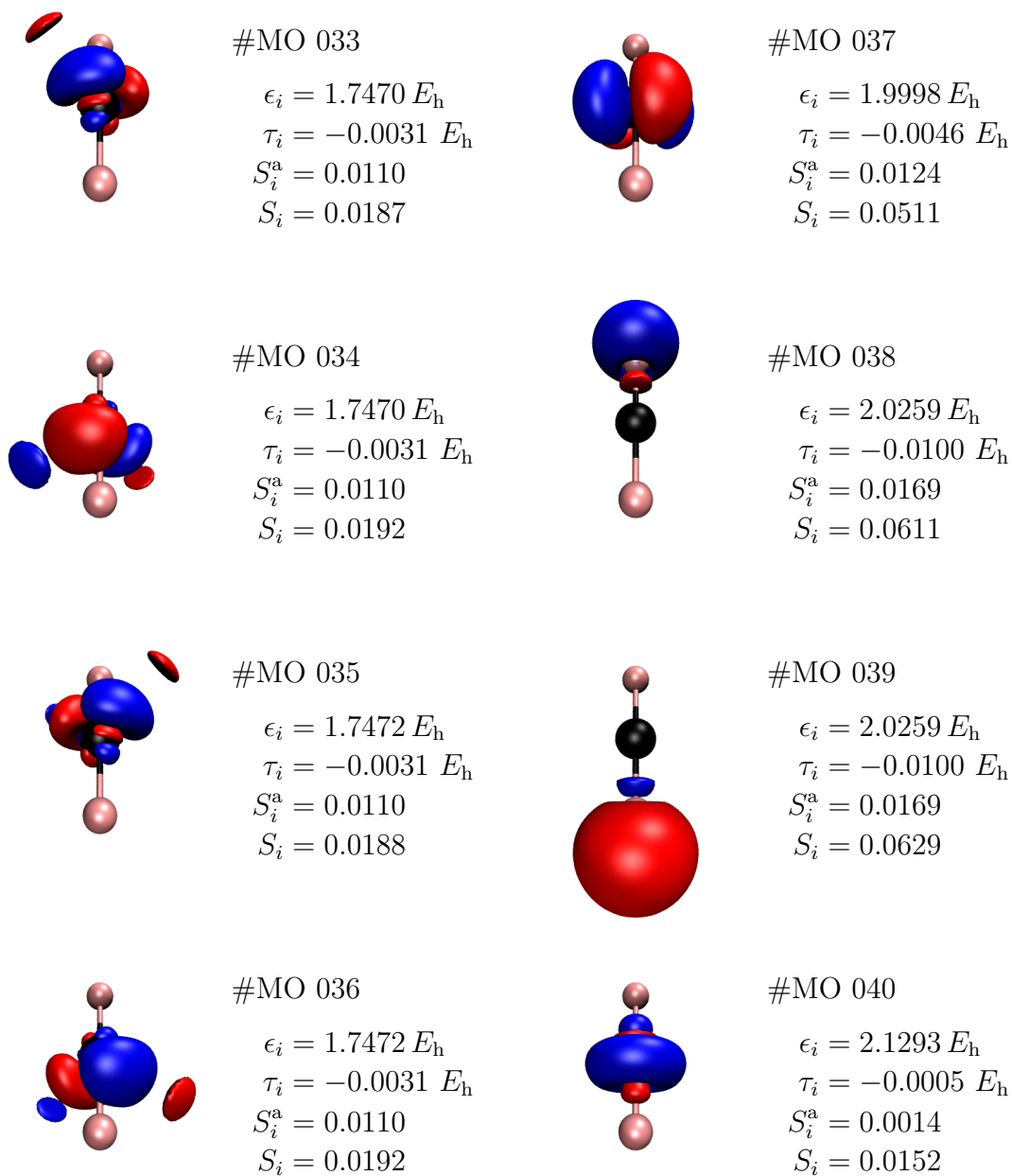


Figure A.5: Pipek-Mezey localized active space molecular orbitals #33 to #40 for CoF_2 . Their corresponding diagonal Fock matrix element ϵ_i , 1-orbital increment τ_i as well as the agnostic and non-agnostic 1-orbital entropies S_i^a and S_i are given as well. Isosurfaces are plotted at $|\psi(\vec{r})| = 0.05 a_0^{-1.5}$.

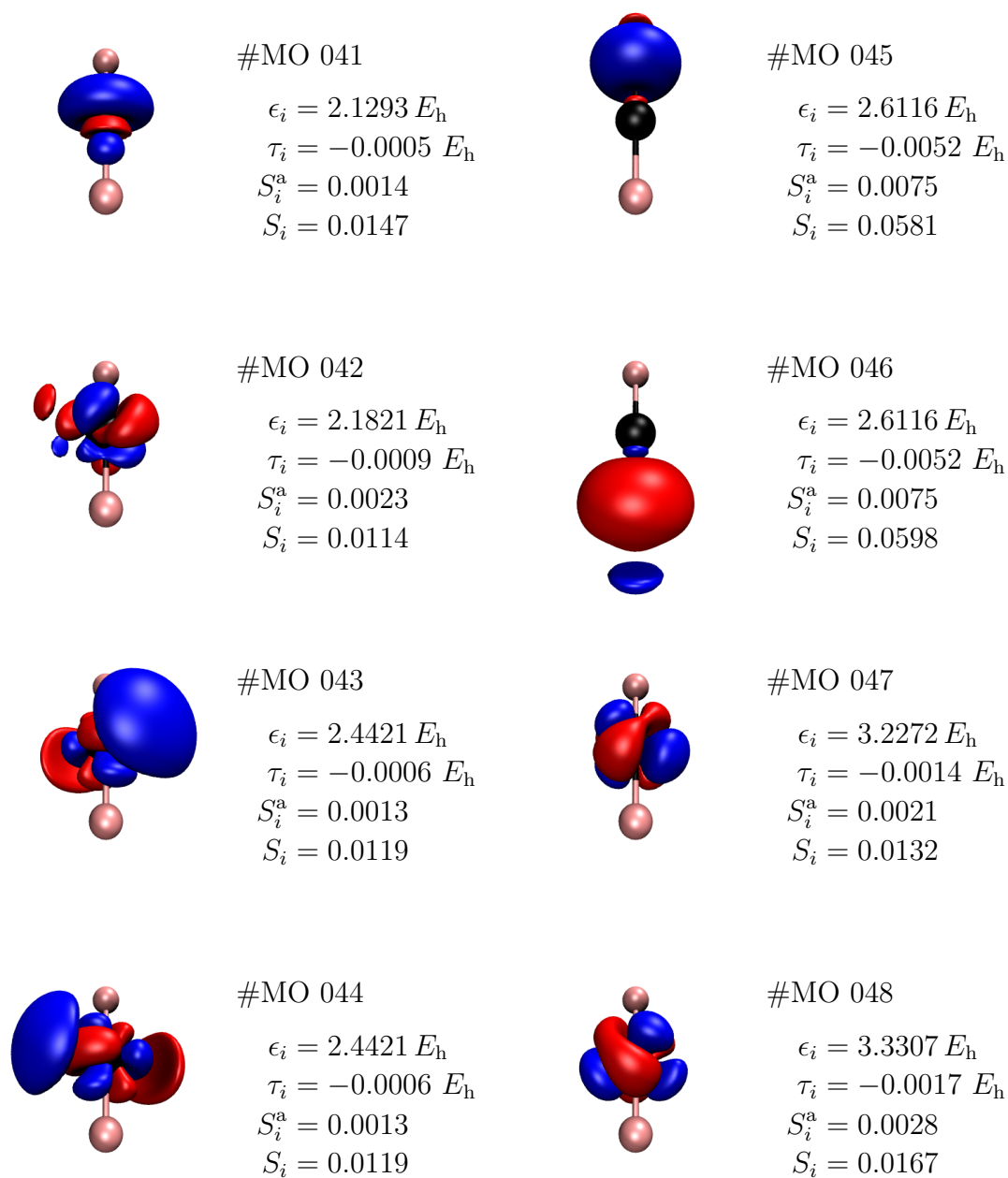


Figure A.6: Pipek-Mezey localized active space molecular orbitals #41 to #48 for CoF_2 . Their corresponding diagonal Fock matrix element ϵ_i , 1-orbital increment ε_i as well as the agnostic and non-agnostic 1-orbital entropies S_i^a and S_i are given as well. Isosurfaces are plotted at $|\psi(\vec{r})| = 0.05 a_0^{-1.5}$.

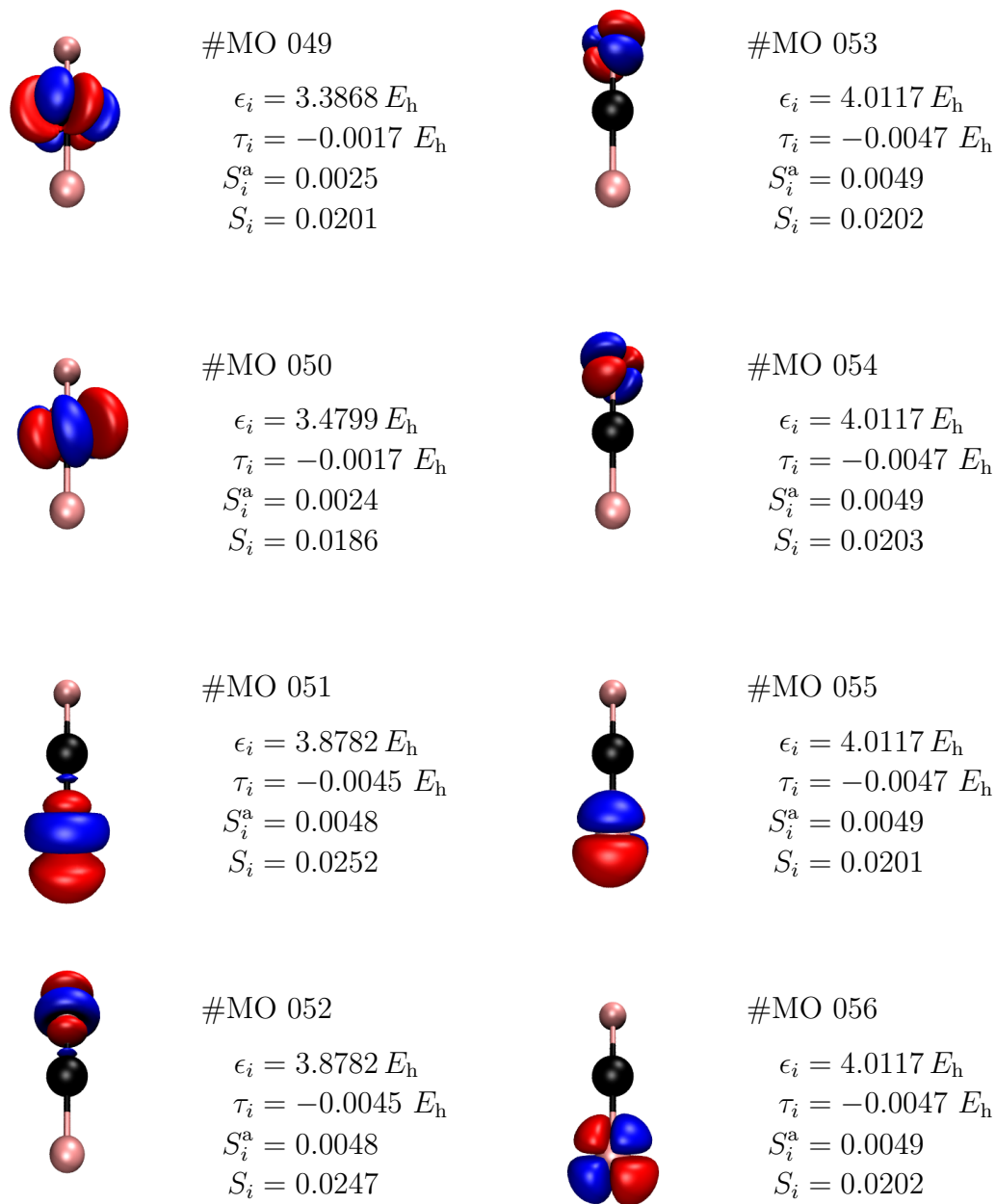


Figure A.7: Pipek-Mezey localized active space molecular orbitals #49 to #56 for CoF_2 . Their corresponding diagonal Fock matrix element ϵ_i , 1-orbital increment ε_i as well as the agnostic and non-agnostic 1-orbital entropies S_i^a and S_i are given as well. Isosurfaces are plotted at $|\psi(\vec{r})| = 0.05 a_0^{-1.5}$.

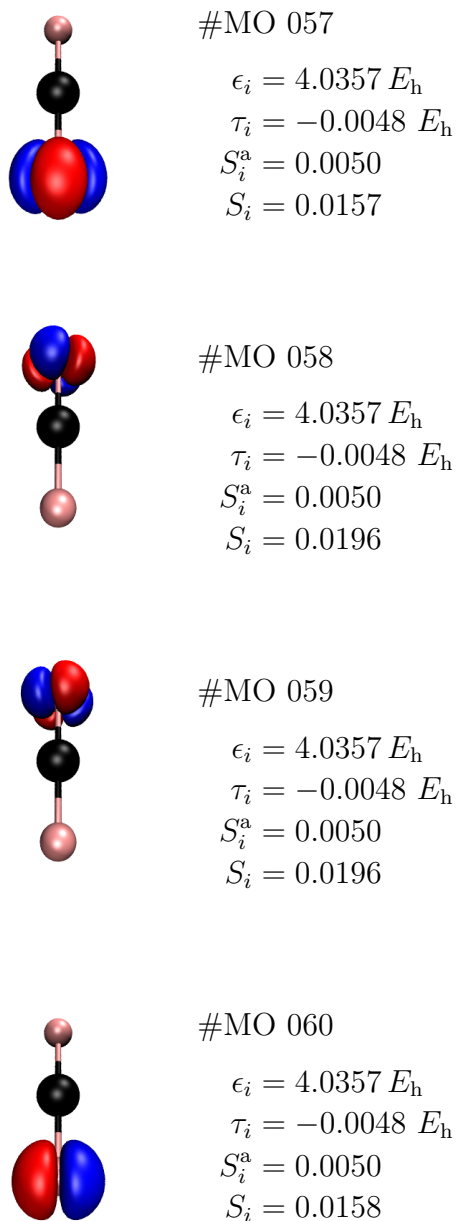


Figure A.8: Pipek-Mezey localized active space molecular orbitals #57 to #60 for CoF_2 . Their corresponding diagonal Fock matrix element ϵ_i , 1-orbital increment ε_i as well as the agnostic and non-agnostic 1-orbital entropies S_i^a and S_i are given as well. Isosurfaces are plotted at $|\psi(\vec{r})| = 0.05 a_0^{-1.5}$.

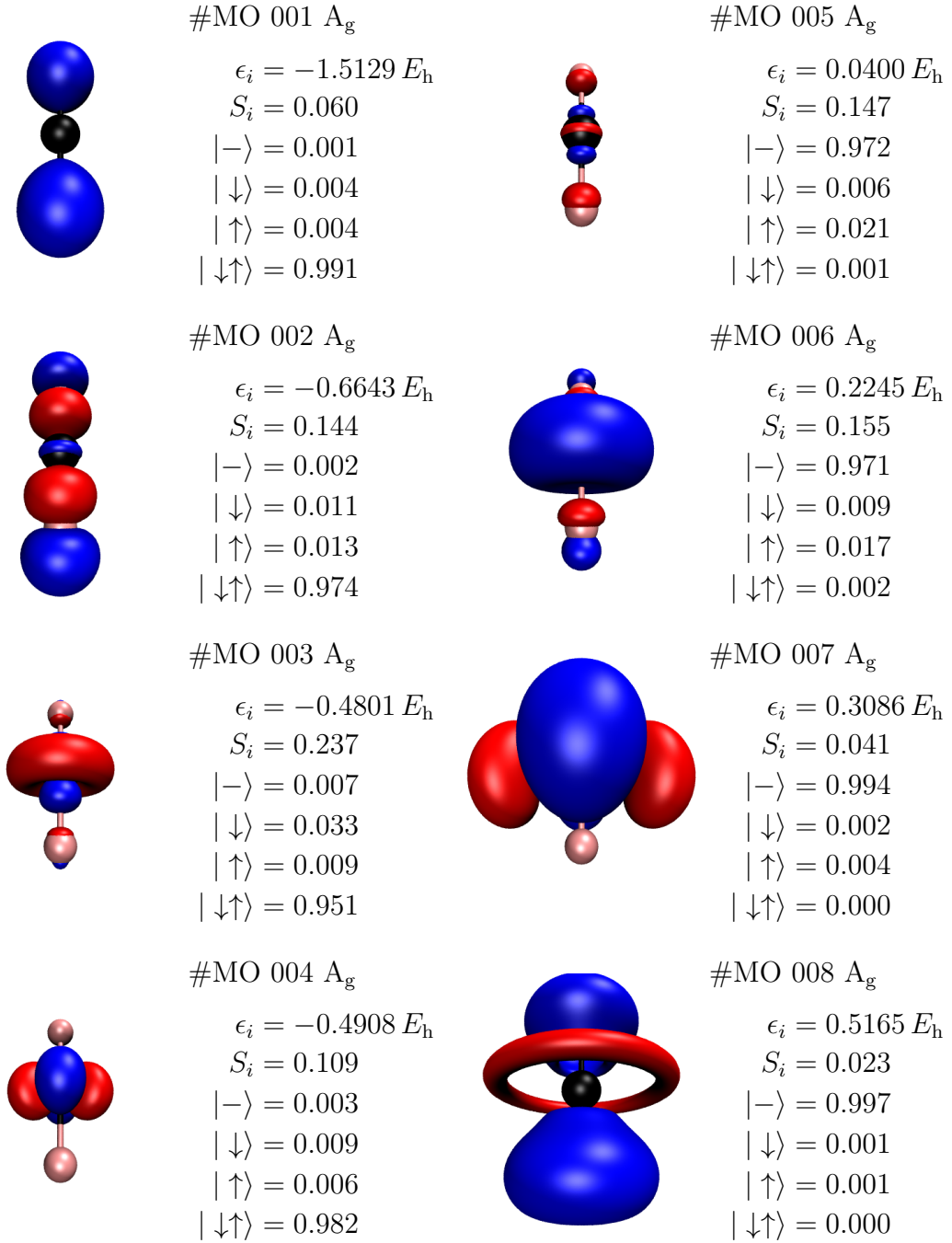


Figure A.9: Molecular orbitals #1 to #8 for CoF_2 with their eigenenergy ϵ_i , 1-orbital entropy S_i and orbital occupations $\omega_{i,\alpha} = \{ |-\rangle, |\downarrow\rangle, |\uparrow\rangle, |\downarrow\uparrow\rangle \}$. Isosurfaces are plotted at $|\psi(\vec{r})| = 0.05 a_0^{-1.5}$.

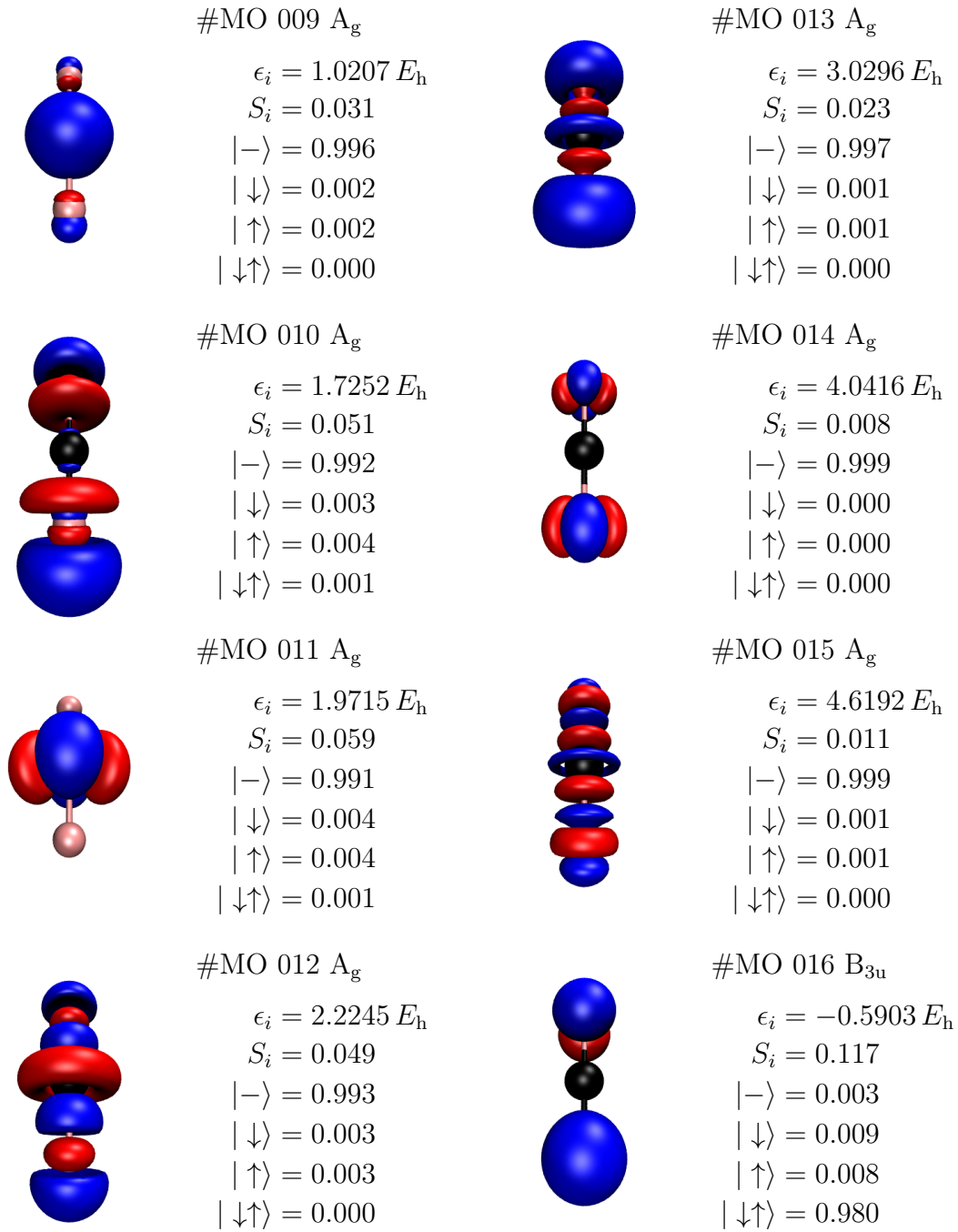


Figure A.10: Molecular orbitals #9 to #16 for CoF_2 with their eigenenergy ϵ_i , 1-orbital entropy S_i and orbital occupations $\omega_{i,\alpha} = \{ |- \rangle, |\downarrow \rangle, |\uparrow \rangle, |\downarrow\uparrow \rangle \}$. Isosurfaces are plotted at $|\psi(\vec{r})| = 0.05 a_0^{-1.5}$.

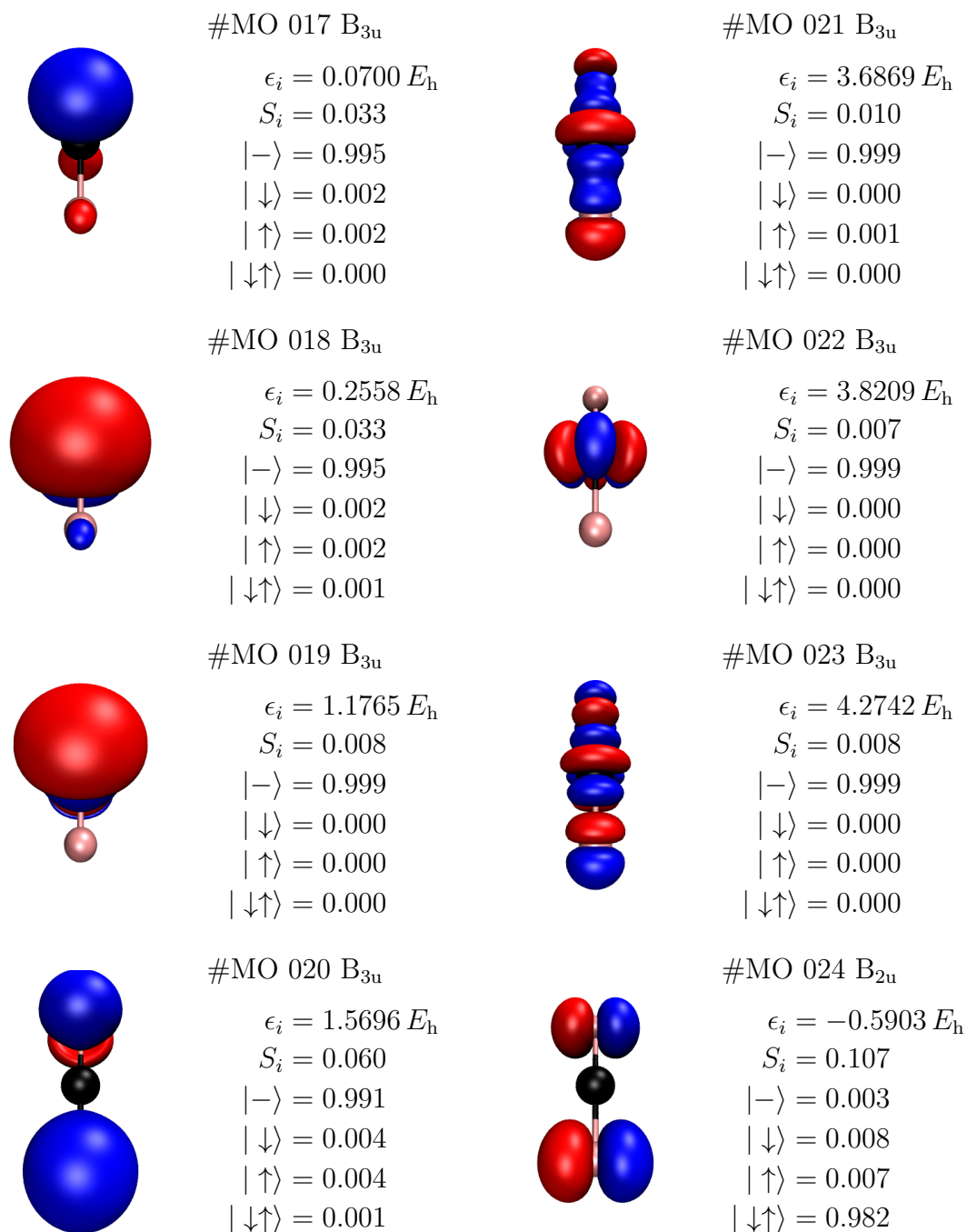


Figure A.11: Molecular orbitals #17 to #24 for CoF₂ with their eigenenergy ϵ_i , 1-orbital entropy S_i and orbital occupations $\omega_{i,\alpha} = \{ |- \rangle, |\downarrow \rangle, |\uparrow \rangle, |\downarrow\uparrow \rangle \}$. Isosurfaces are plotted at $|\psi(\vec{r})| = 0.05 a_0^{-1.5}$.

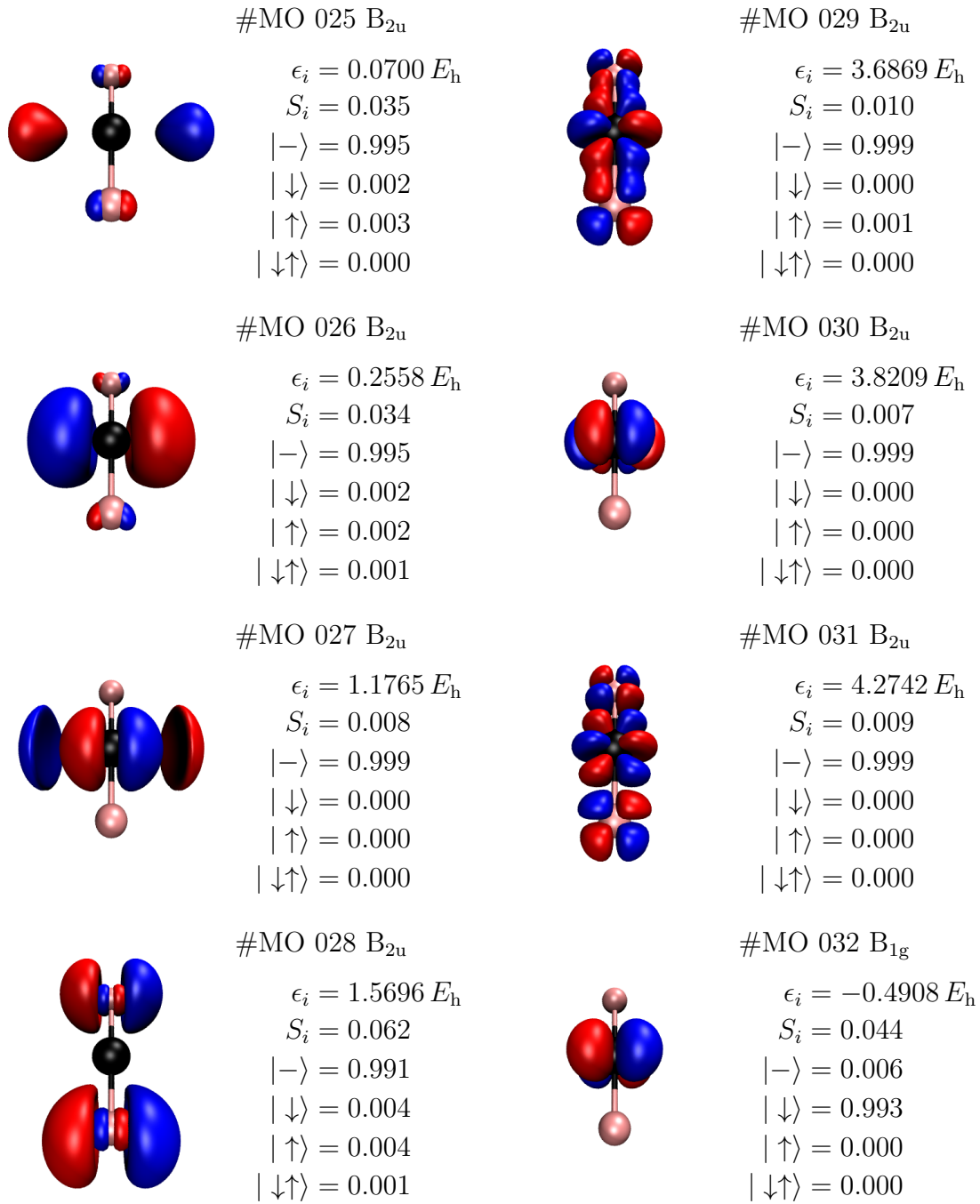


Figure A.12: Molecular orbitals #25 to #32 for CoF₂ with their eigenenergy ϵ_i , 1-orbital entropy S_i and orbital occupations $\omega_{i,\alpha} = \{ |- \rangle, |\downarrow \rangle, |\uparrow \rangle, |\downarrow\uparrow \rangle \}$. Isosurfaces are plotted at $|\psi(\vec{r})| = 0.05 a_0^{-1.5}$.

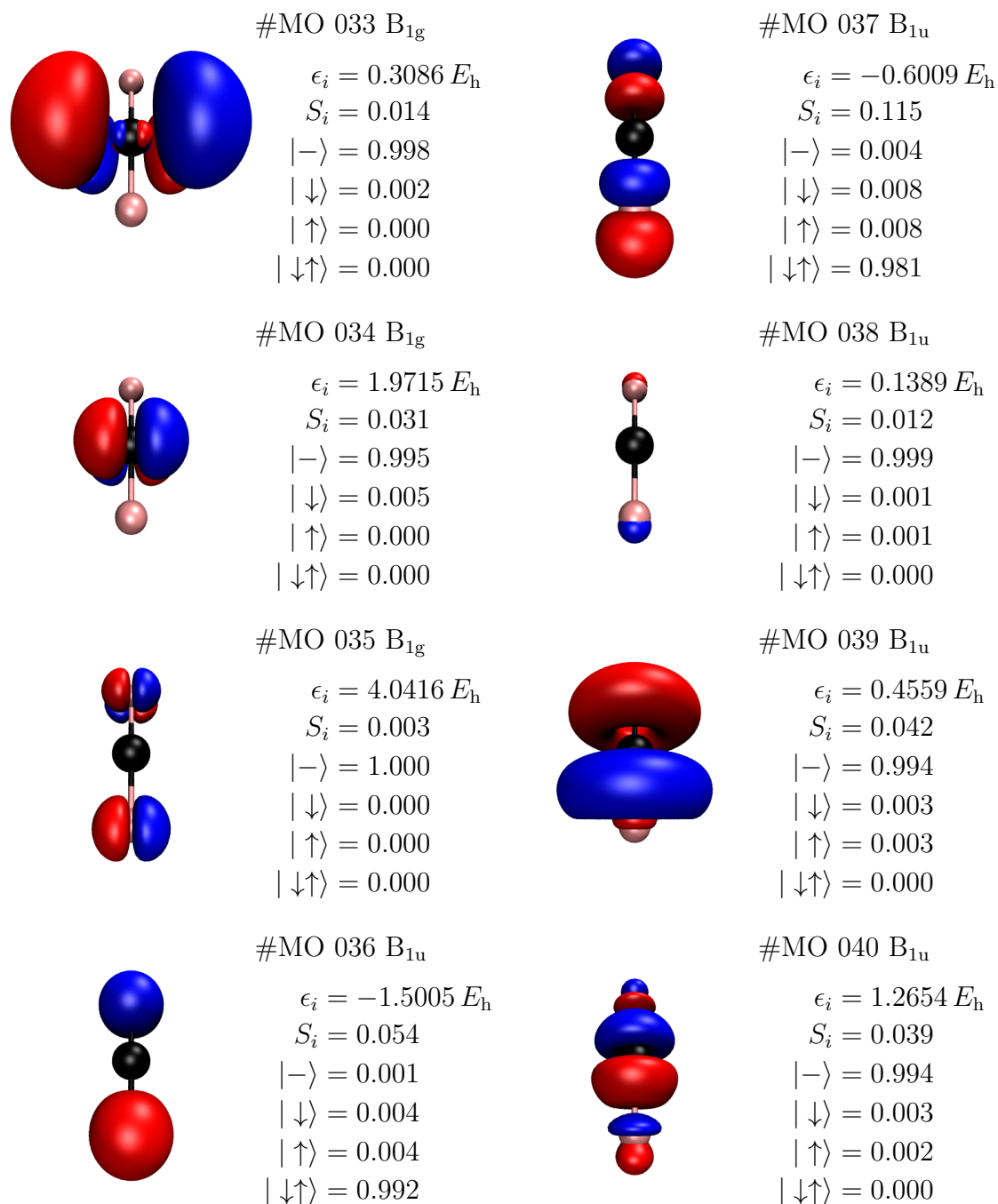


Figure A.13: Molecular orbitals #33 to #40 for CoF₂ with their eigenenergy ϵ_i , 1-orbital entropy S_i and orbital occupations $\omega_{i,\alpha} = \{ |- \rangle, |\downarrow \rangle, |\uparrow \rangle, |\downarrow\uparrow \rangle \}$. Isosurfaces are plotted at $|\psi(\vec{r})| = 0.05 a_0^{-1.5}$.

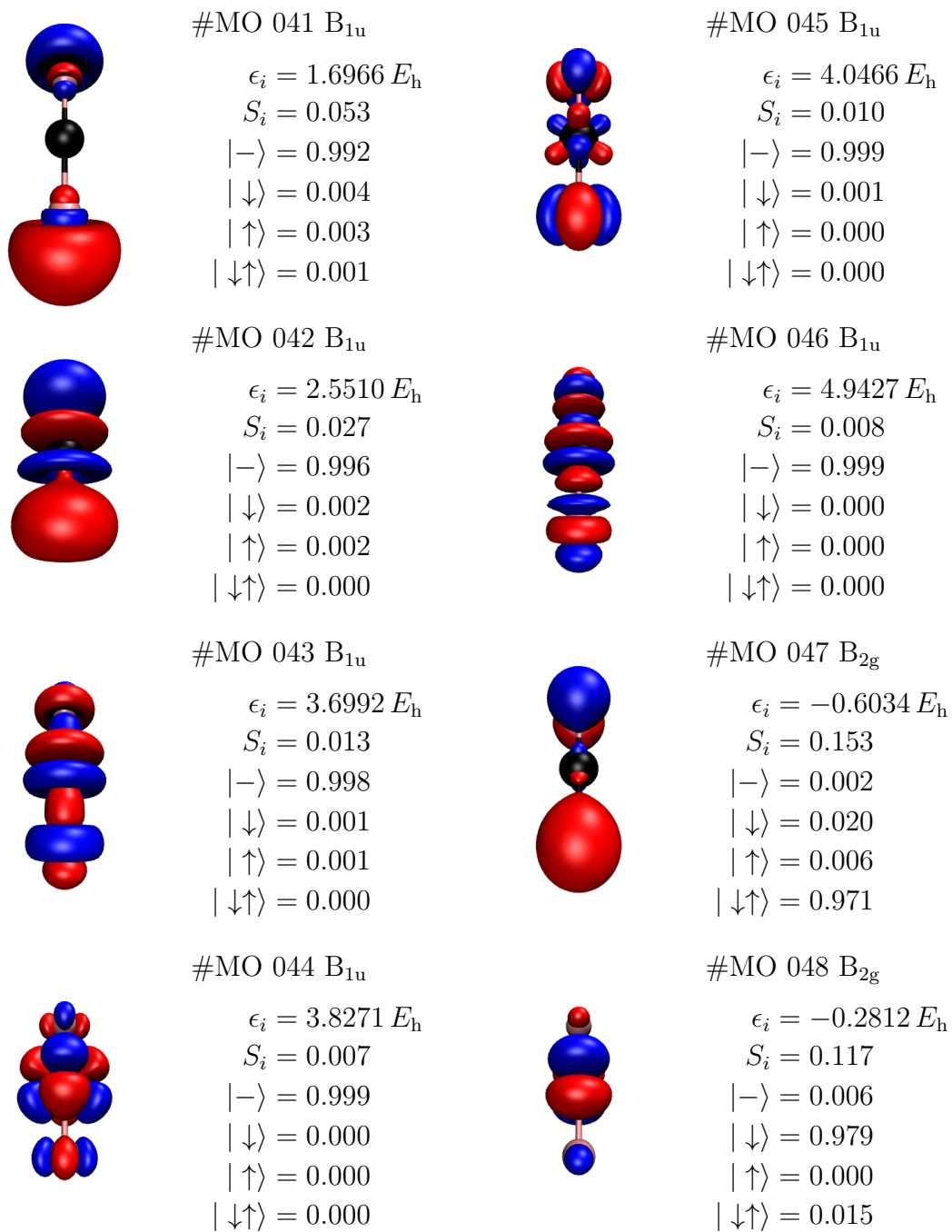


Figure A.14: Molecular orbitals #41 to #48 for CoF₂ with their eigenenergy ϵ_i , 1-orbital entropy S_i and orbital occupations $\omega_{i,\alpha} = \{ |- \rangle, |\downarrow \rangle, |\uparrow \rangle, |\downarrow\uparrow \rangle \}$. Isosurfaces are plotted at $|\psi(\vec{r})| = 0.05 a_0^{-1.5}$.

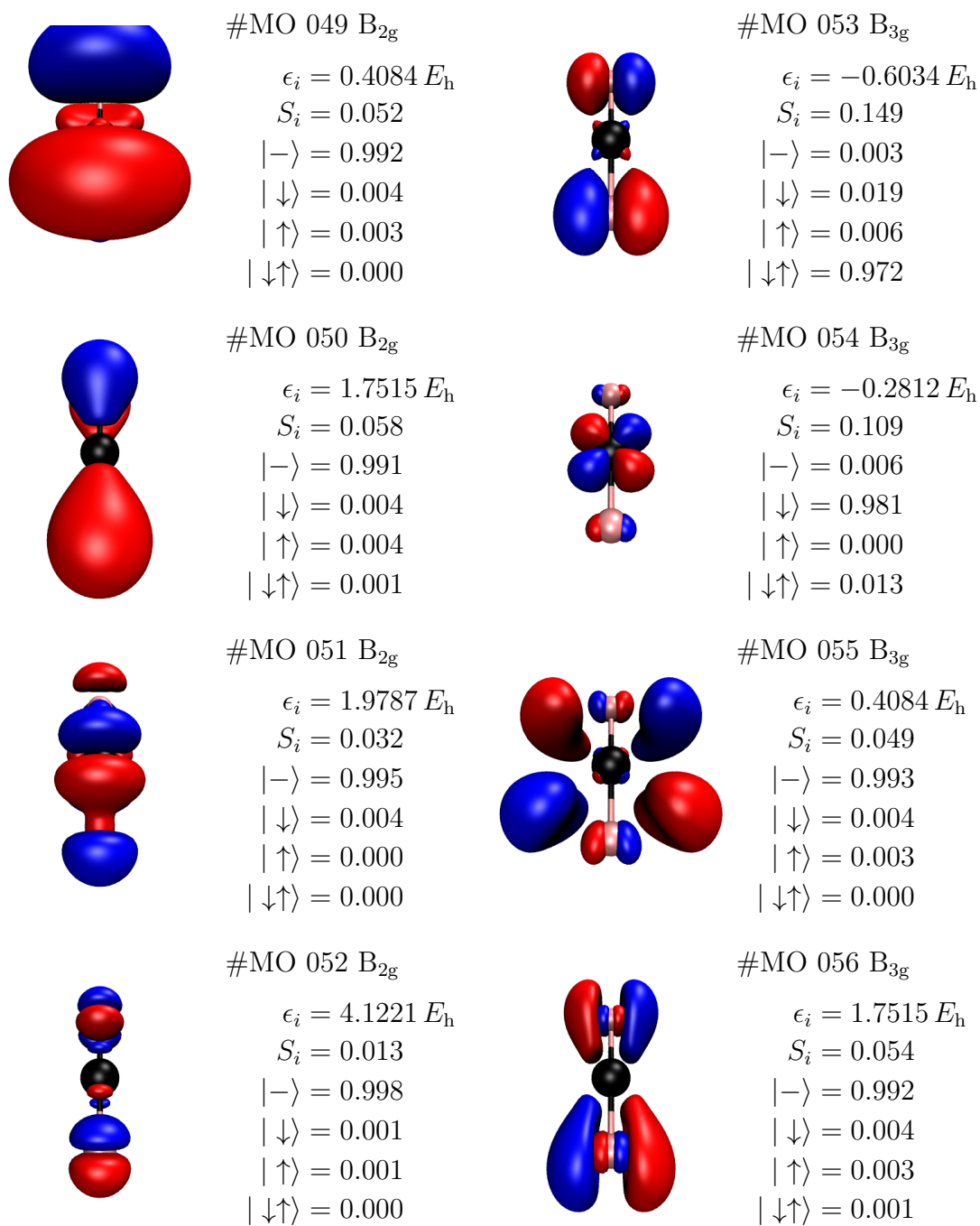


Figure A.15: Molecular orbitals #49 to #56 for CoF₂ with their eigenenergy ϵ_i , 1-orbital entropy S_i and orbital occupations $\omega_{i,\alpha} = \{ |- \rangle, |\downarrow \rangle, |\uparrow \rangle, |\downarrow\uparrow \rangle \}$. Isosurfaces are plotted at $|\psi(\vec{r})| = 0.05 a_0^{-1.5}$.

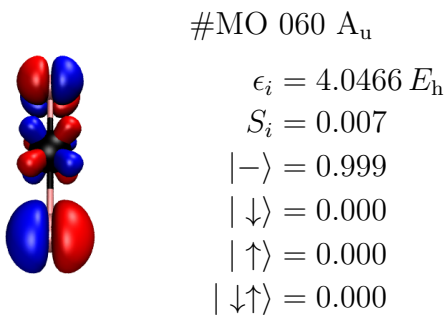
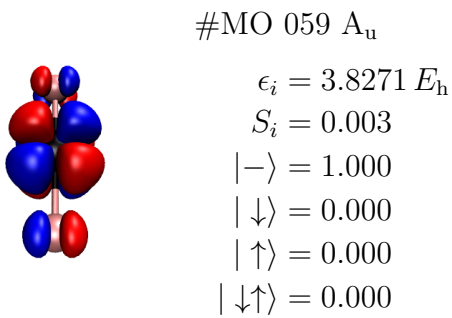
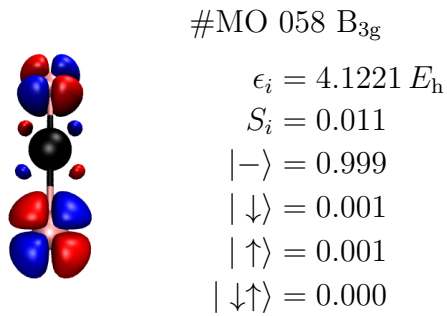
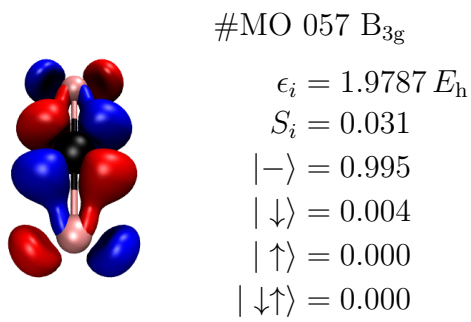


Figure A.16: Molecular orbitals #57 to #60 for CoF₂ with their eigenenergy ϵ_i , 1-orbital entropy S_i and orbital occupations $\omega_{i,\alpha} = \{|-\rangle, |\downarrow\rangle, |\uparrow\rangle, |\downarrow\uparrow\rangle\}$. Isosurfaces are plotted at $|\psi(\vec{r})| = 0.05 a_0^{-1.5}$.

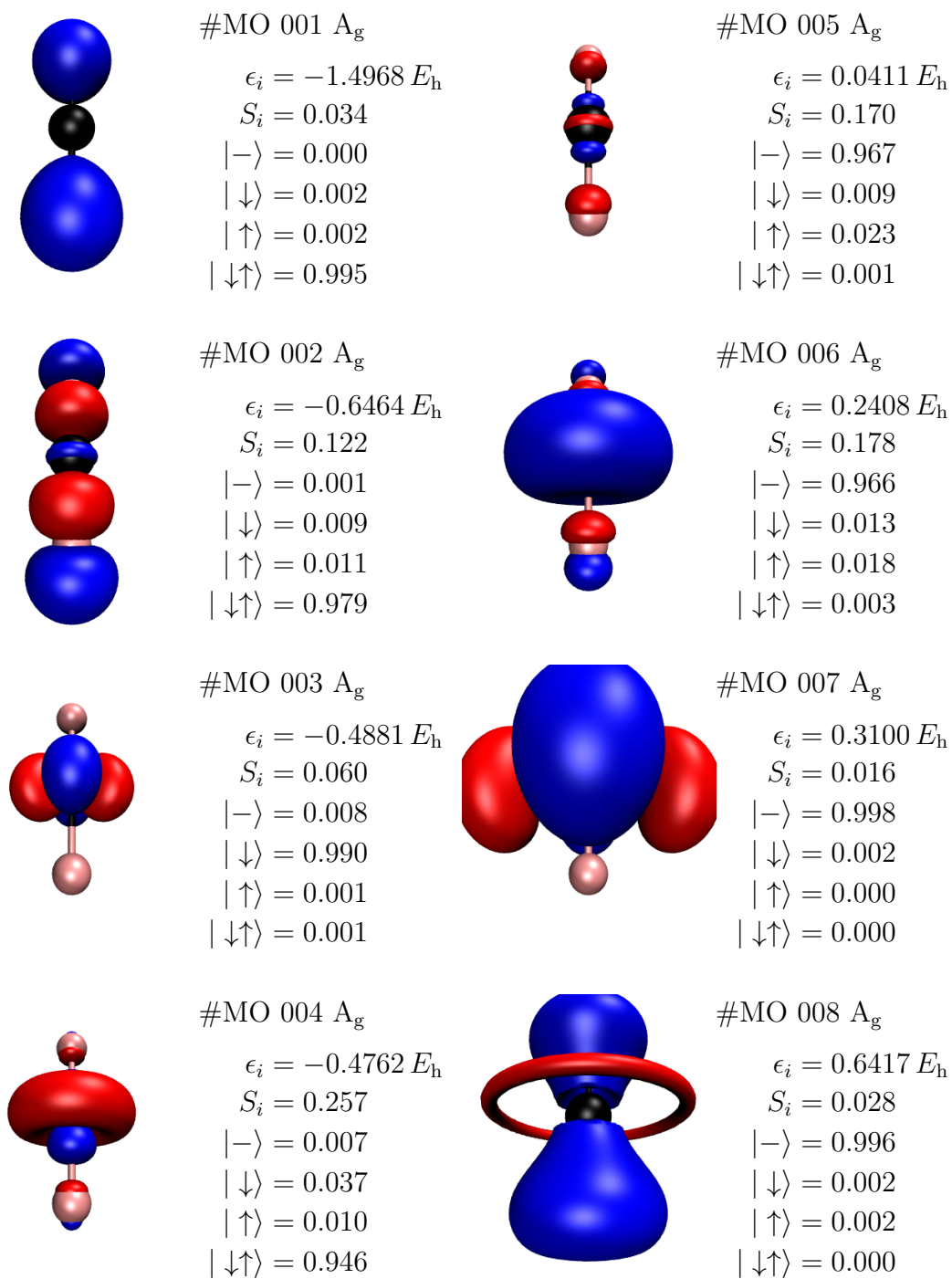


Figure A.17: Molecular orbitals #1 to #8 for CoF_2 (min. basis at F) with their eigenenergy ϵ_i , 1-orbital entropy S_i and orbital occupations $\omega_{i,\alpha} = \{ |- \rangle, |\downarrow \rangle, |\uparrow \rangle, |\downarrow\uparrow \rangle \}$. Isosurfaces are plotted at $|\psi(\vec{r})| = 0.05 a_0^{-1.5}$.

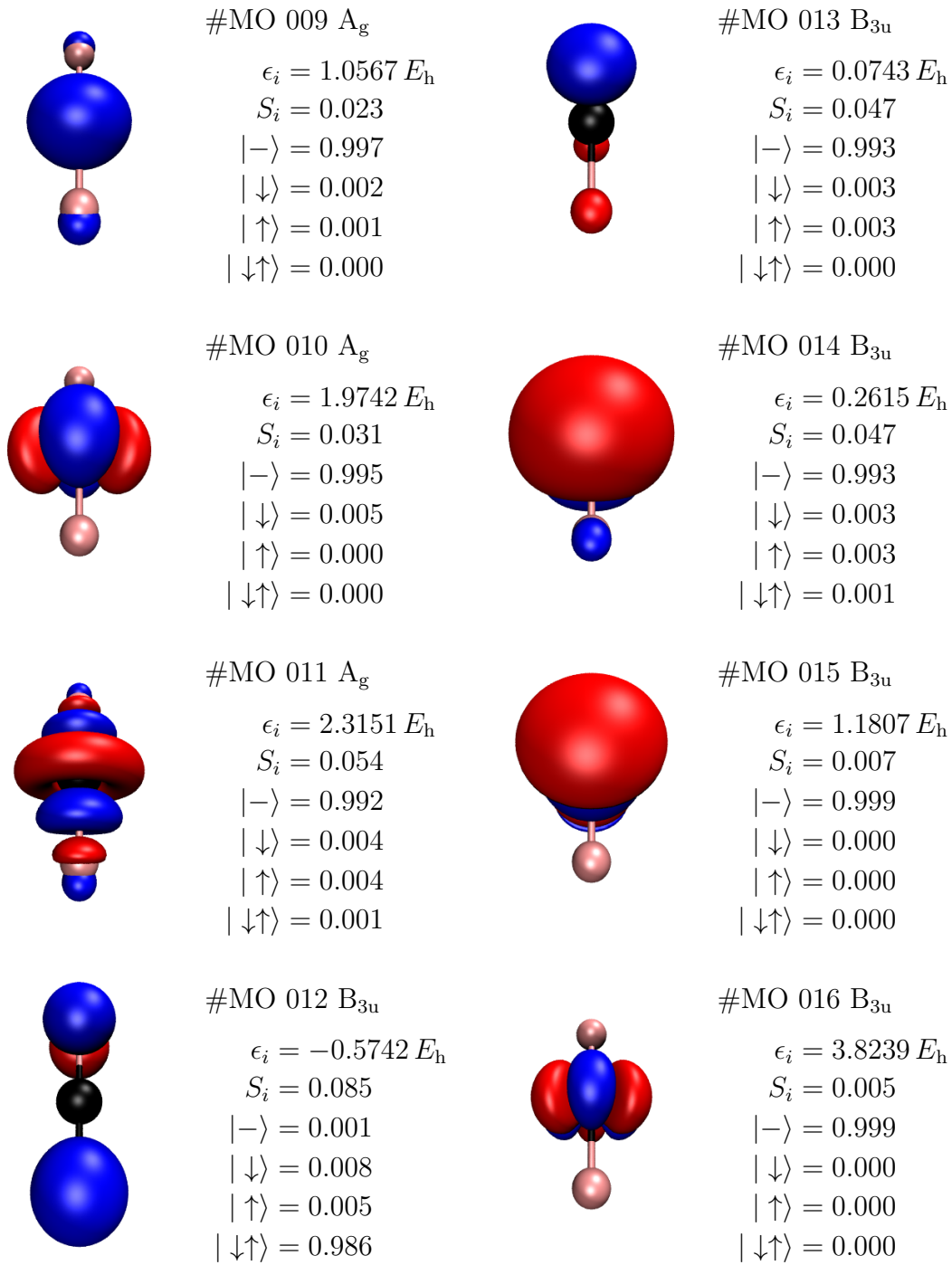


Figure A.18: Molecular orbitals #9 to #16 for CoF₂ (min. basis at F) with their eigenenergy ϵ_i , 1-orbital entropy S_i and orbital occupations $\omega_{i,\alpha} = \{ |-\rangle, |\downarrow\rangle, |\uparrow\rangle, |\downarrow\uparrow\rangle \}$. Isosurfaces are plotted at $|\psi(\vec{r})| = 0.05 a_0^{-1.5}$.

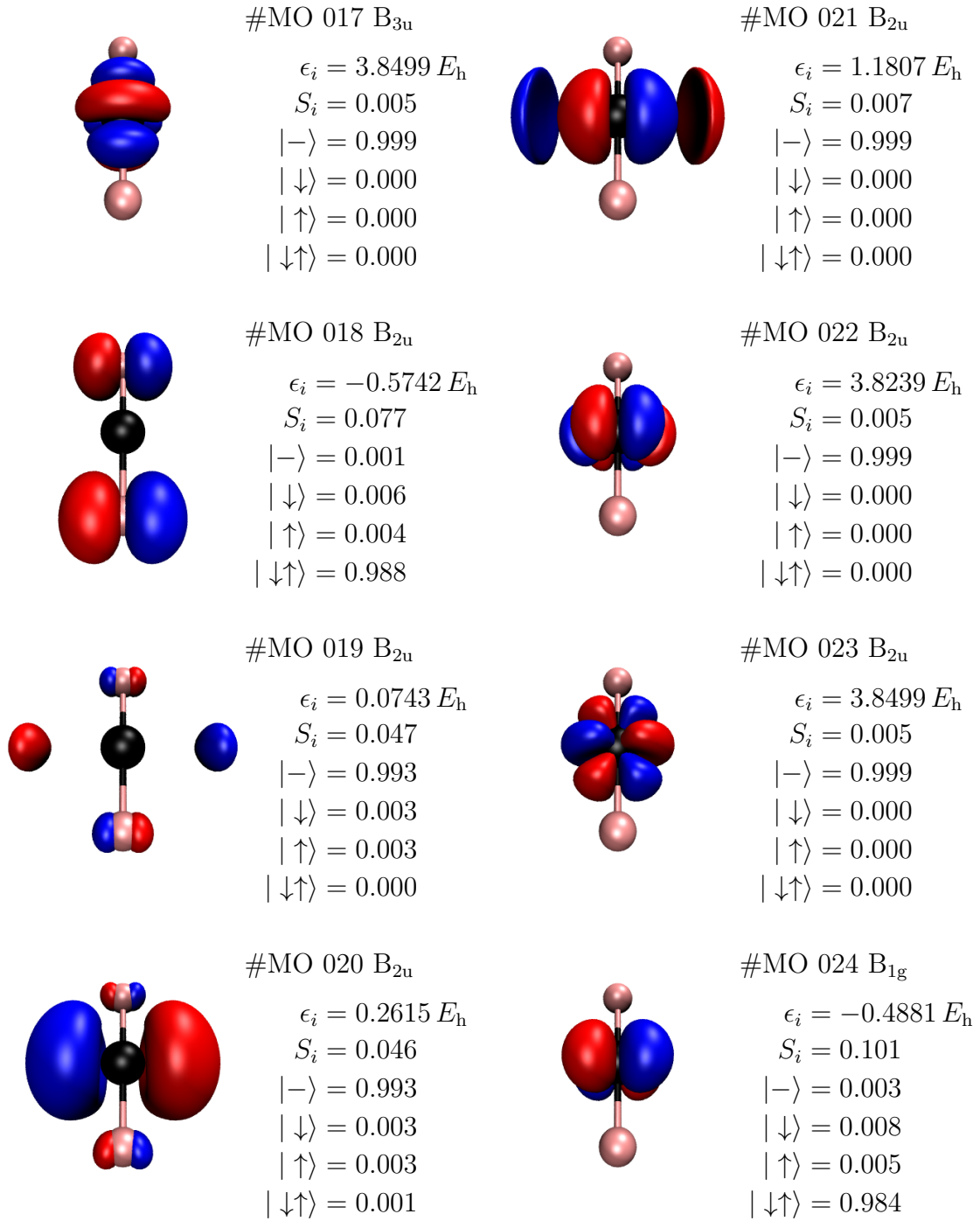


Figure A.19: Molecular orbitals #17 to #24 for CoF₂ (min. basis at F) with their eigenenergy ϵ_i , 1-orbital entropy S_i and orbital occupations $\omega_{i,\alpha} = \{ |- \rangle, |\downarrow \rangle, |\uparrow \rangle, |\downarrow\uparrow \rangle \}$. Isosurfaces are plotted at $|\psi(\vec{r})| = 0.05 a_0^{-1.5}$.

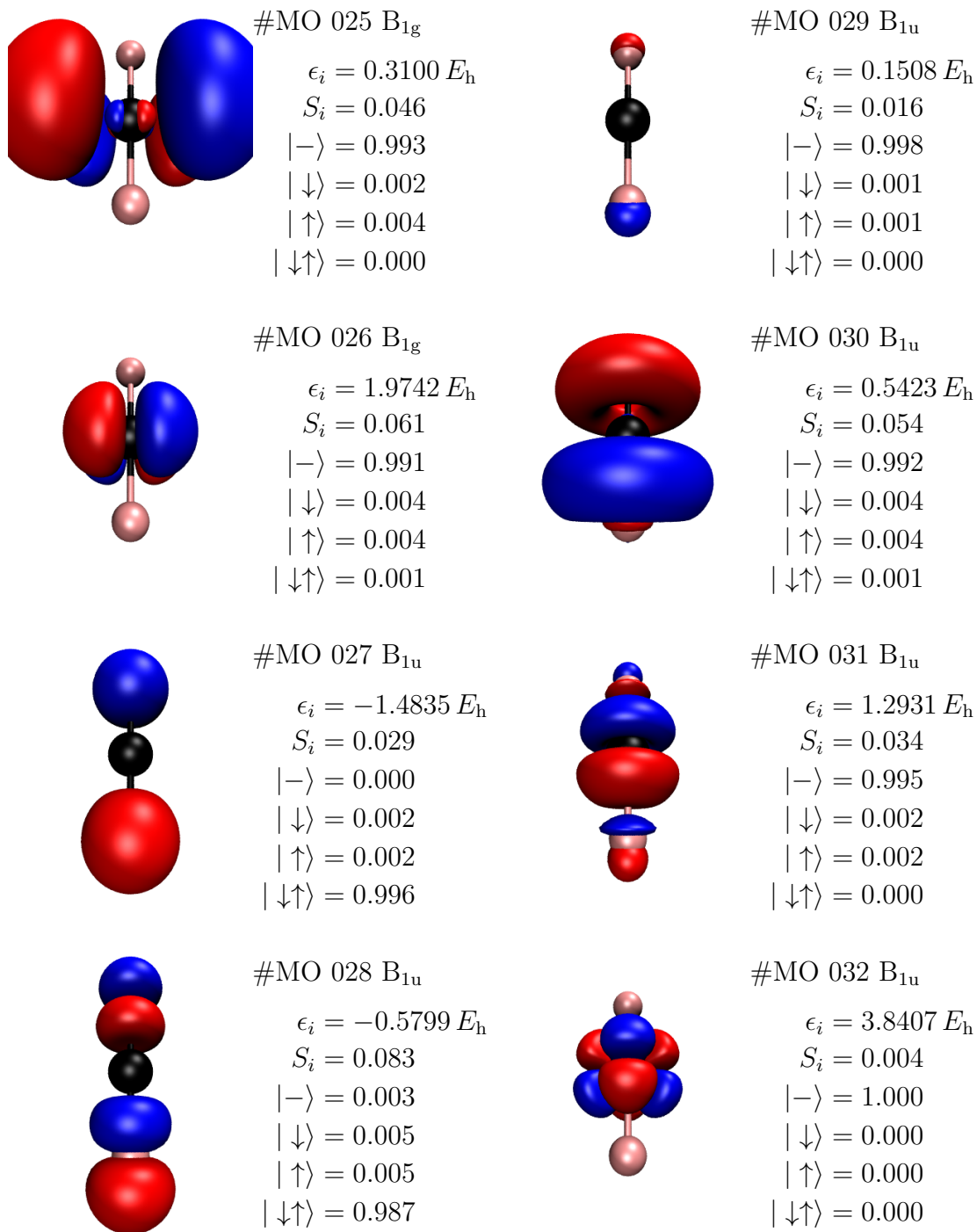


Figure A.20: Molecular orbitals #25 to #32 for CoF₂ (min. basis at F) with their eigenenergy ϵ_i , 1-orbital entropy S_i and orbital occupations $\omega_{i,\alpha} = \{ |- \rangle, |\downarrow \rangle, |\uparrow \rangle, |\downarrow\uparrow \rangle \}$. Isosurfaces are plotted at $|\psi(\vec{r})| = 0.05 a_0^{-1.5}$.

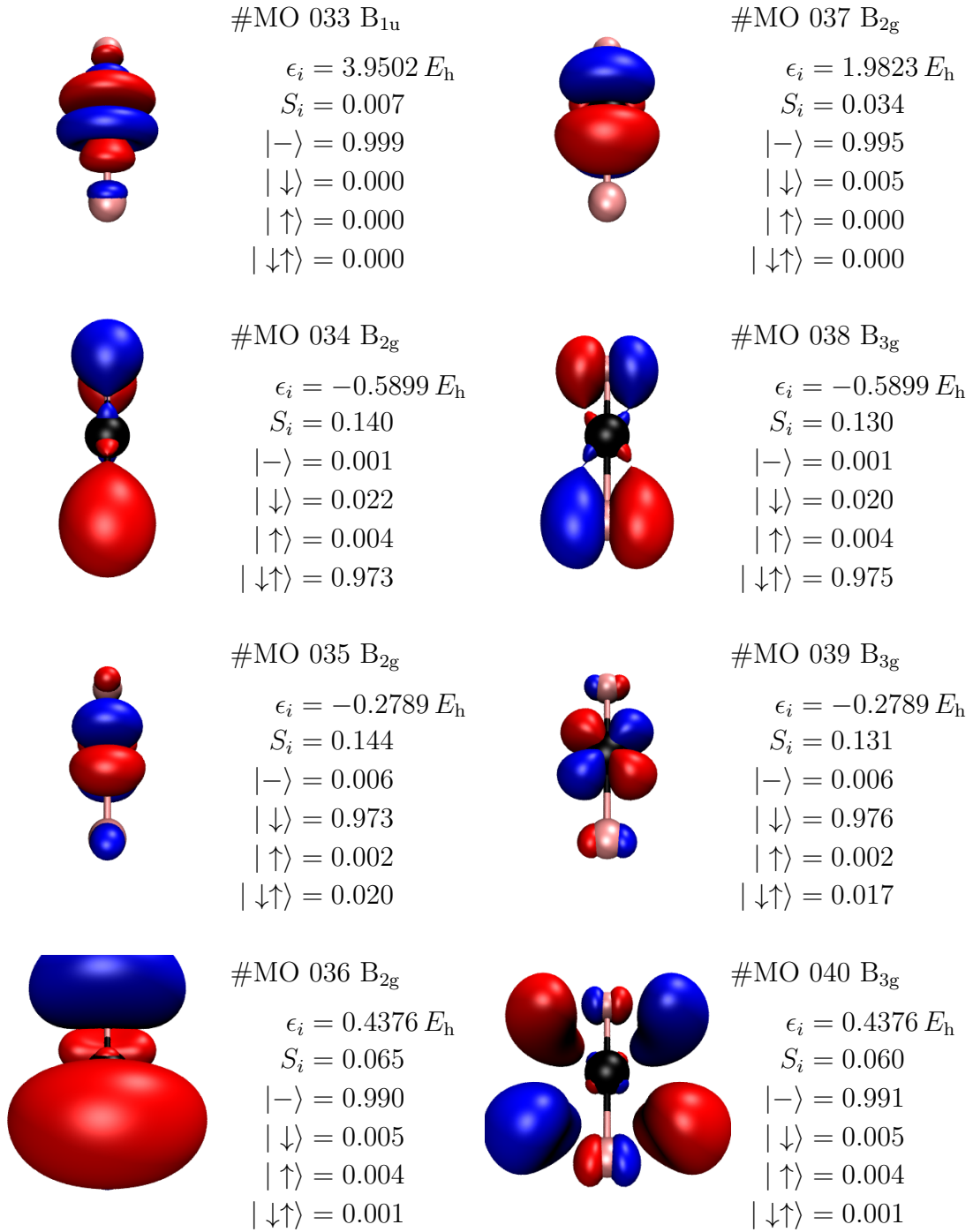


Figure A.21: Molecular orbitals #33 to #40 for CoF₂ (min. basis at F) with their eigenenergy ϵ_i , 1-orbital entropy S_i and orbital occupations $\omega_{i,\alpha} = \{ |- \rangle, |\downarrow \rangle, |\uparrow \rangle, |\downarrow\uparrow \rangle \}$. Isosurfaces are plotted at $|\psi(\vec{r})| = 0.05 a_0^{-1.5}$.

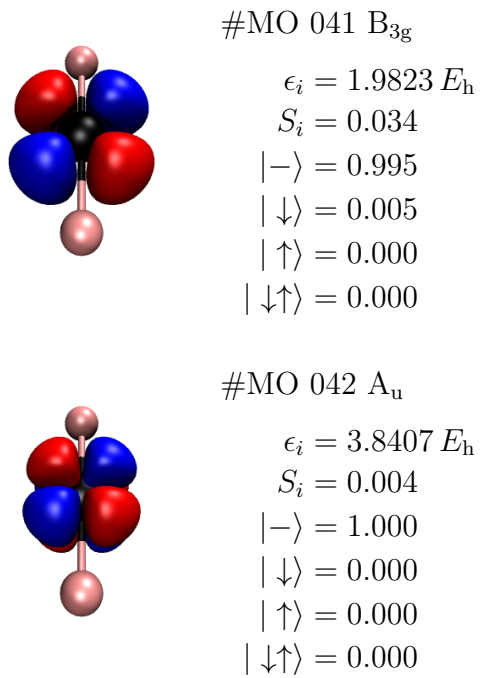


Figure A.22: Molecular orbitals #41 to #42 for CoF₂ (min. basis at F) with their eigenenergy ϵ_i , 1-orbital entropy S_i and orbital occupations $\omega_{i,\alpha} = \{|\rightarrow\rangle, |\downarrow\rangle, |\uparrow\rangle, |\downarrow\uparrow\rangle\}$. Isosurfaces are plotted at $|\psi(\vec{r})| = 0.05 a_0^{-1.5}$.

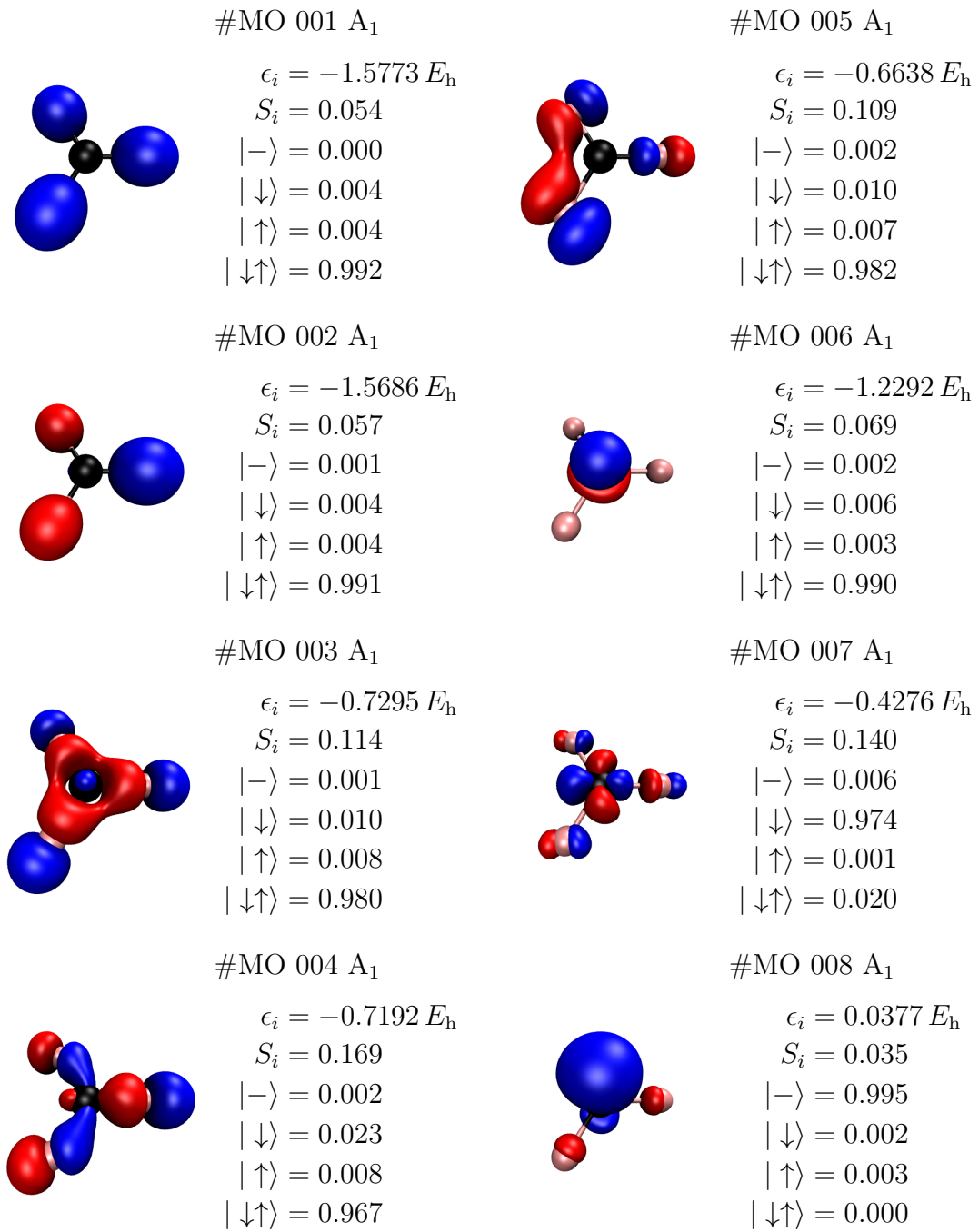


Figure A.23: Molecular orbitals #1 to #8 for CoF₃ with their eigenenergy ϵ_i , 1-orbital entropy S_i and orbital occupations $\omega_{i,\alpha} = \{ |-\rangle, |\downarrow\rangle, |\uparrow\rangle, |\downarrow\uparrow\rangle \}$. Isosurfaces are plotted at $|\psi(\vec{r})| = 0.05 a_0^{-1.5}$.

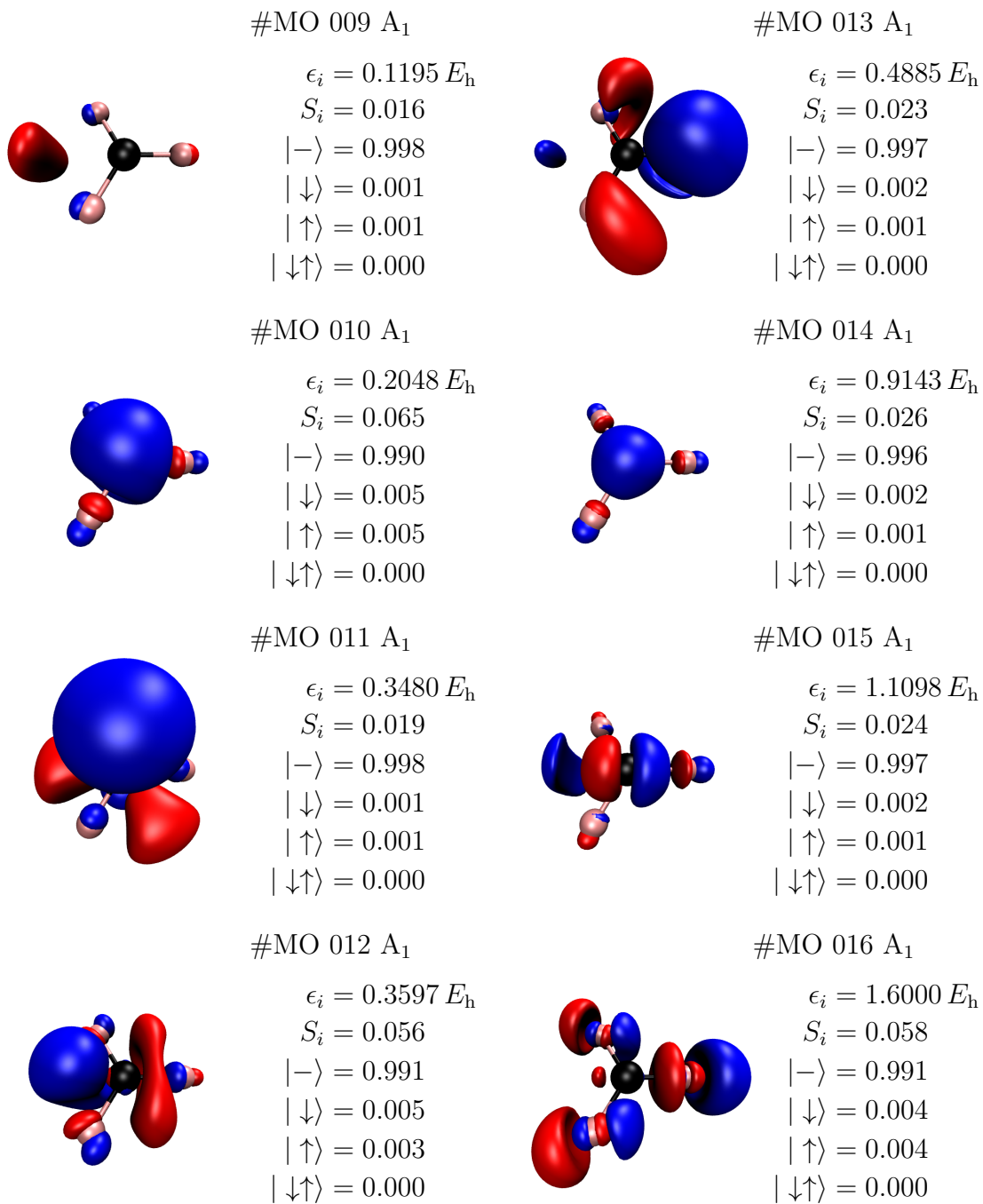


Figure A.24: Molecular orbitals #9 to #16 for CoF₃ with their eigenenergy ϵ_i , 1-orbital entropy S_i and orbital occupations $\omega_{i,\alpha} = \{ |- \rangle, |\downarrow \rangle, |\uparrow \rangle, |\downarrow\uparrow \rangle \}$. Isosurfaces are plotted at $|\psi(\vec{r})| = 0.05 a_0^{-1.5}$.

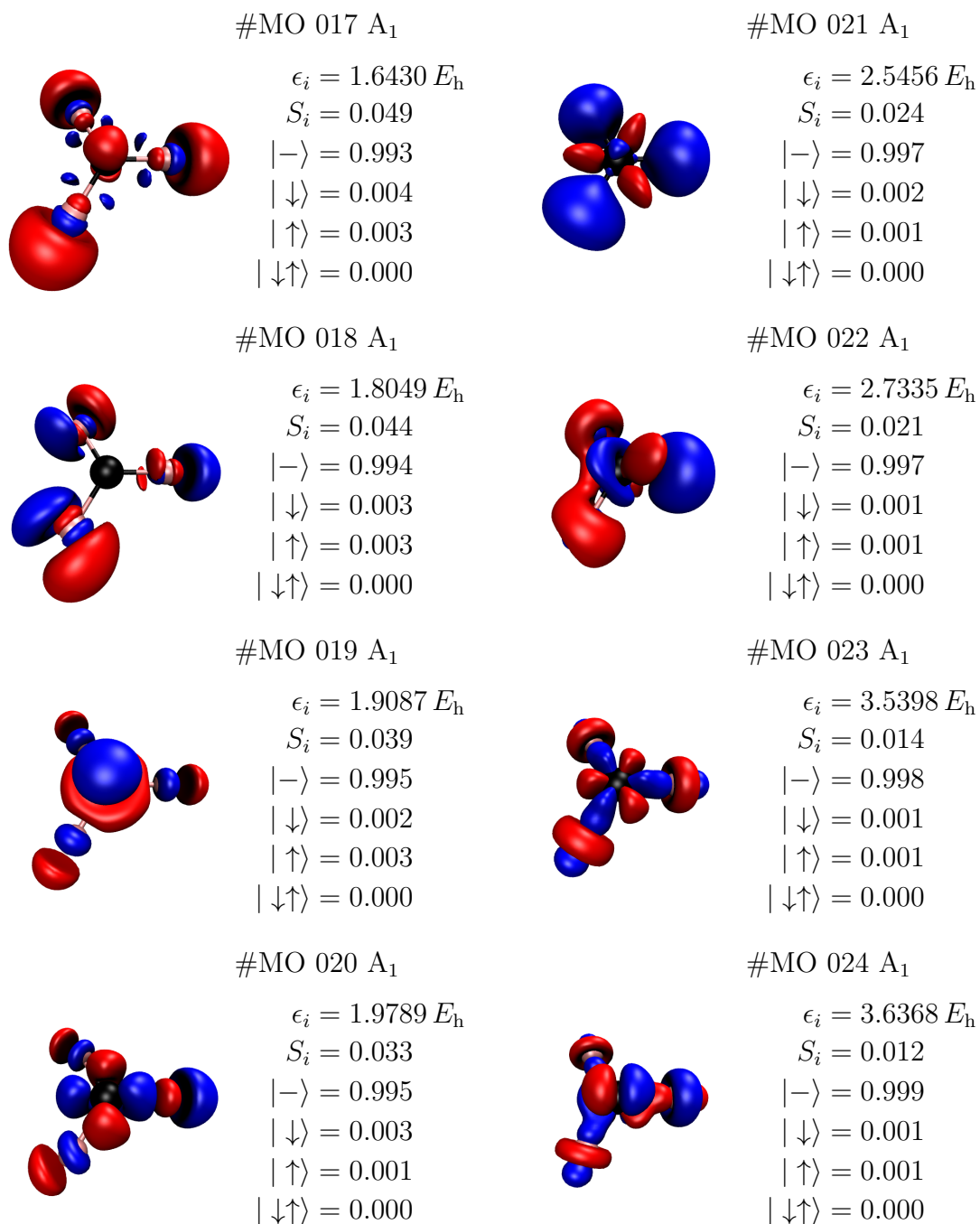


Figure A.25: Molecular orbitals #17 to #24 for CoF₃ with their eigenenergy ϵ_i , 1-orbital entropy S_i and orbital occupations $\omega_{i,\alpha} = \{ |- \rangle, |\downarrow \rangle, |\uparrow \rangle, |\downarrow\uparrow \rangle \}$. Isosurfaces are plotted at $|\psi(\vec{r})| = 0.05 a_0^{-1.5}$.

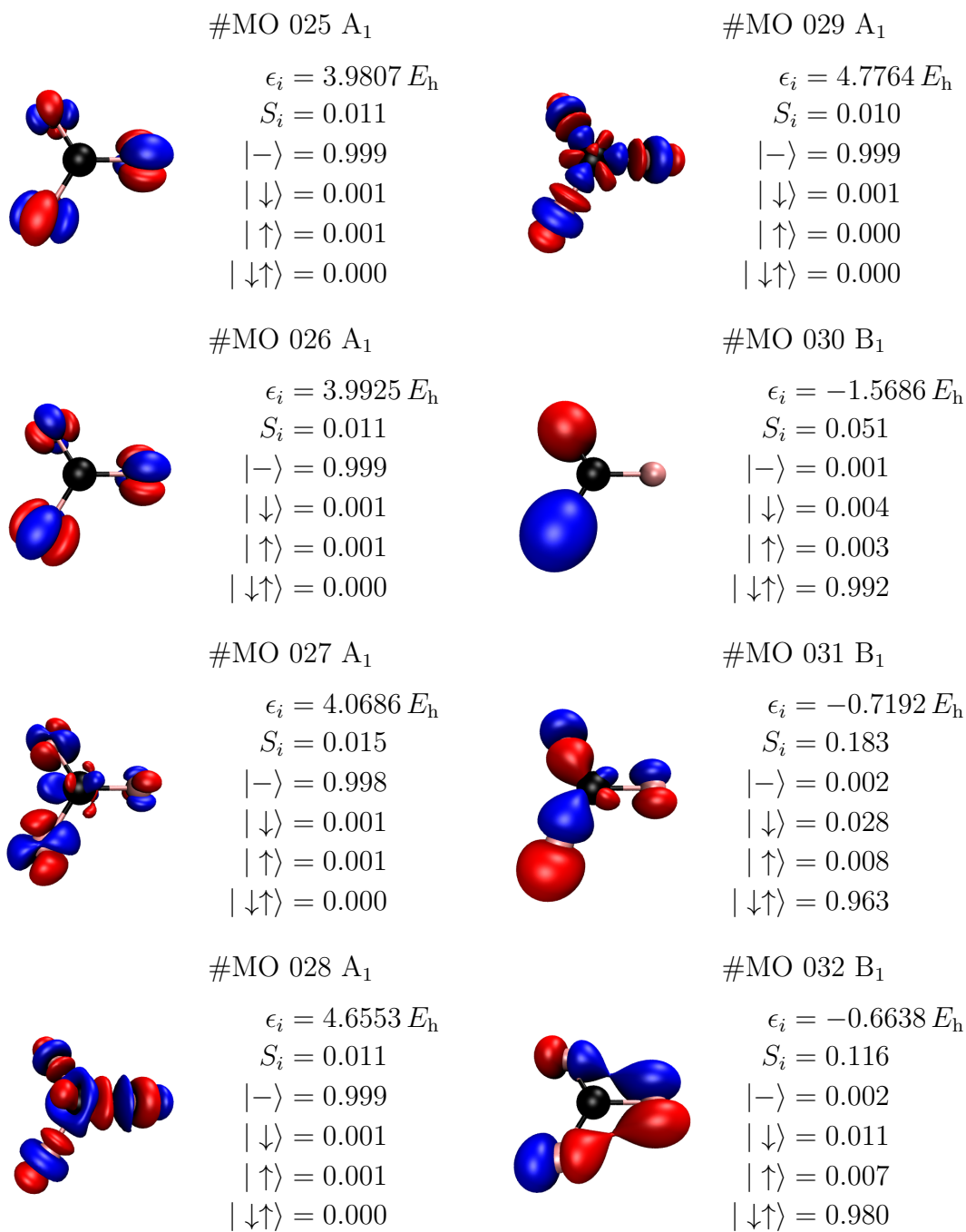


Figure A.26: Molecular orbitals #25 to #32 for CoF_3 with their eigenenergy ϵ_i , 1-orbital entropy S_i and orbital occupations $\omega_{i,\alpha} = \{ |- \rangle, |\downarrow \rangle, |\uparrow \rangle, |\downarrow\uparrow \rangle \}$. Isosurfaces are plotted at $|\psi(\vec{r})| = 0.05 a_0^{-1.5}$.

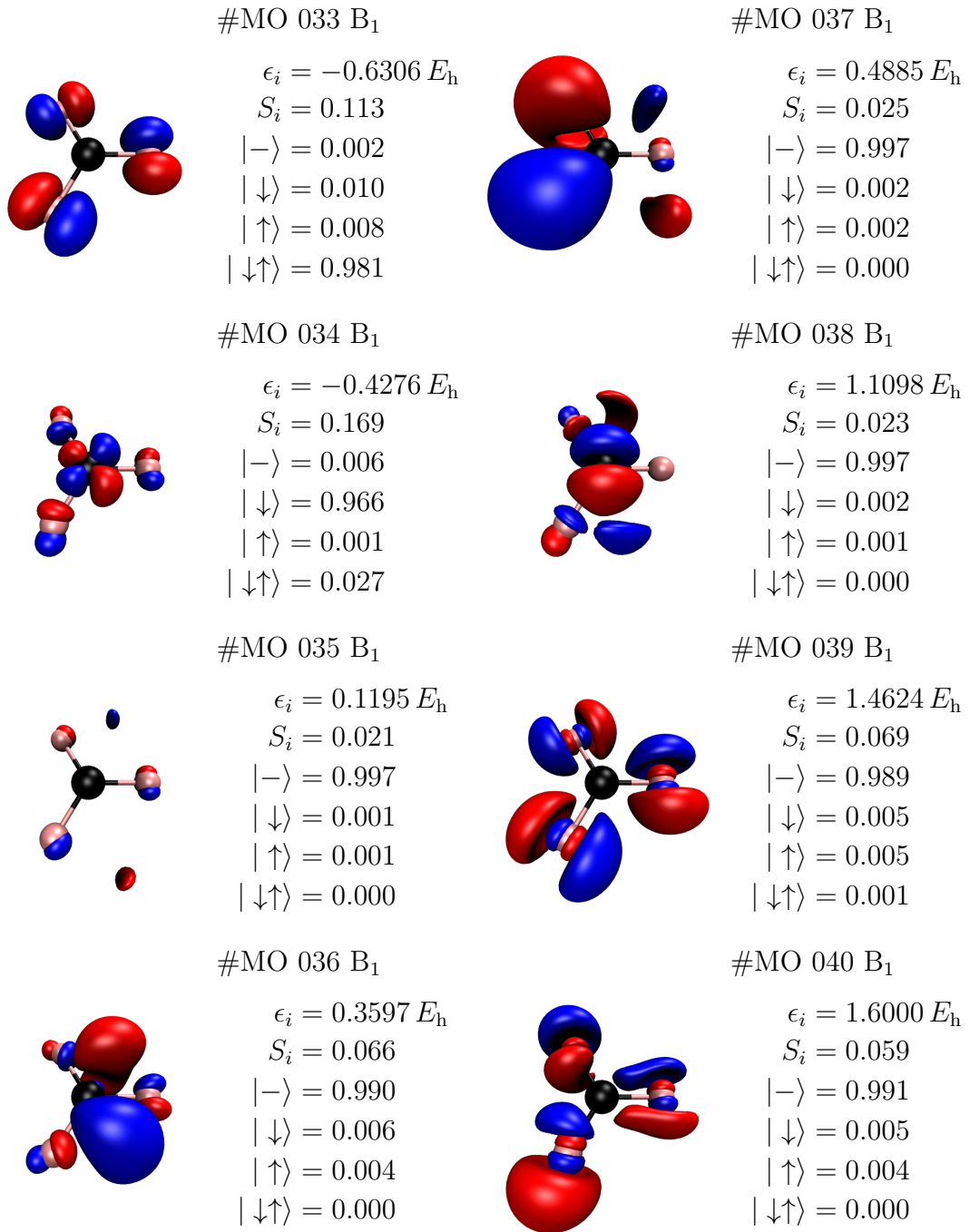


Figure A.27: Molecular orbitals #33 to #40 for CoF₃ with their eigenenergy ϵ_i , 1-orbital entropy S_i and orbital occupations $\omega_{i,\alpha} = \{|\rightarrow\rangle, |\downarrow\rangle, |\uparrow\rangle, |\downarrow\uparrow\rangle\}$. Isosurfaces are plotted at $|\psi(\vec{r})| = 0.05 a_0^{-1.5}$.

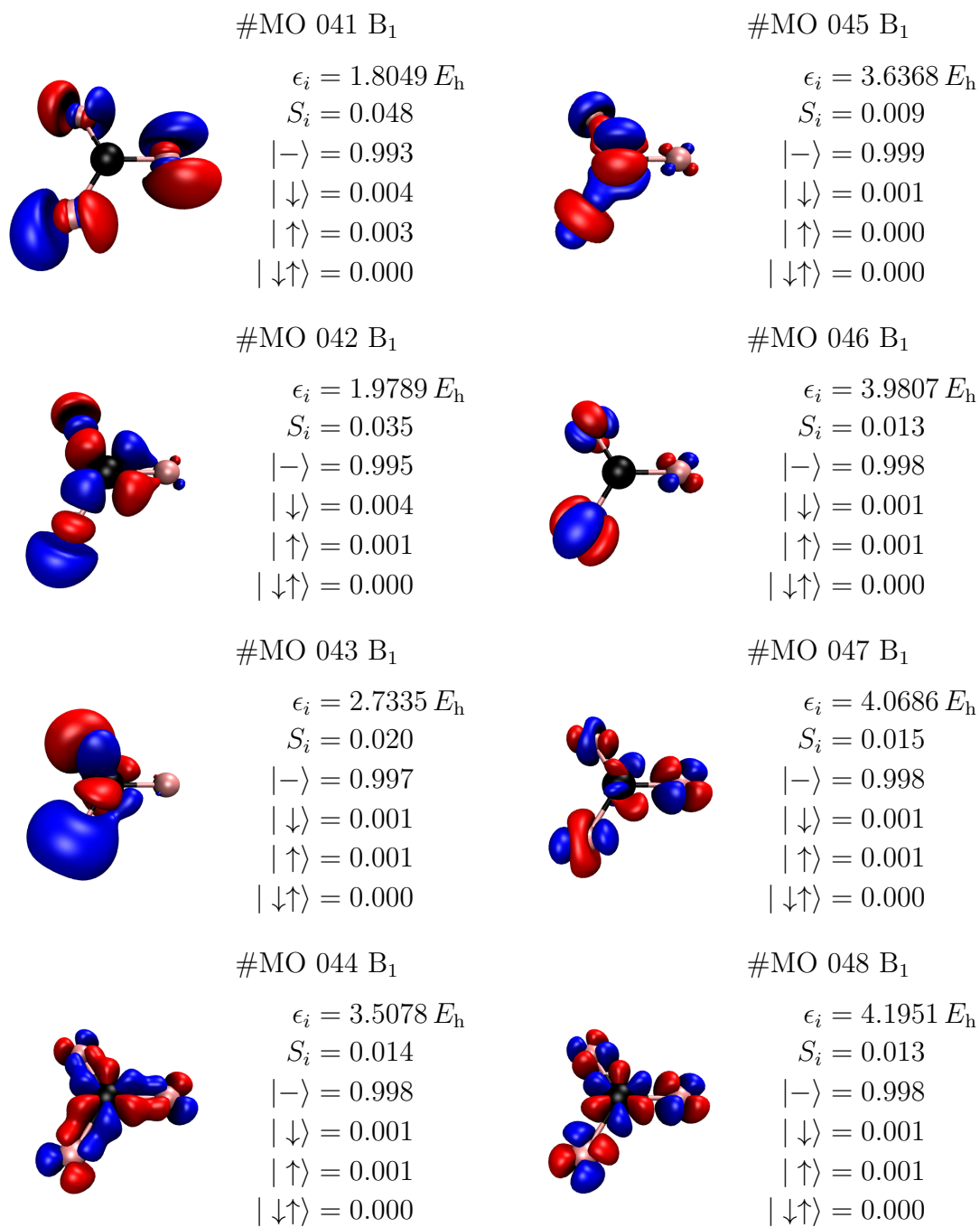


Figure A.28: Molecular orbitals #41 to #48 for CoF₃ with their eigenenergy ϵ_i , 1-orbital entropy S_i and orbital occupations $\omega_{i,\alpha} = \{ |- \rangle, |\downarrow \rangle, |\uparrow \rangle, |\downarrow\uparrow \rangle \}$. Isosurfaces are plotted at $|\psi(\vec{r})| = 0.05 a_0^{-1.5}$.

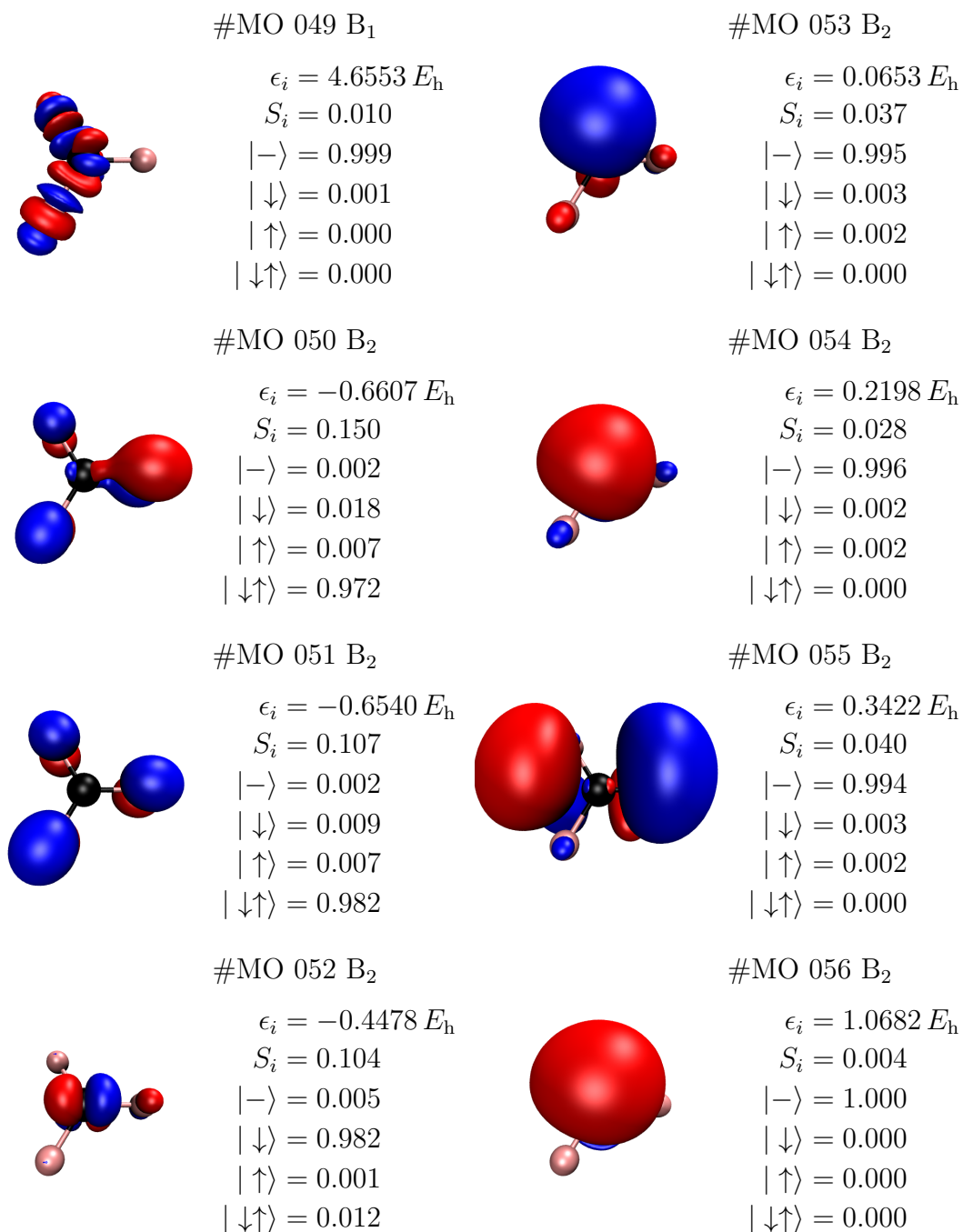


Figure A.29: Molecular orbitals #49 to #56 for CoF₃ with their eigenenergy ϵ_i , 1-orbital entropy S_i and orbital occupations $\omega_{i,\alpha} = \{ |- \rangle, |\downarrow \rangle, |\uparrow \rangle, |\downarrow\uparrow \rangle \}$. Isosurfaces are plotted at $|\psi(\vec{r})| = 0.05 a_0^{-1.5}$.

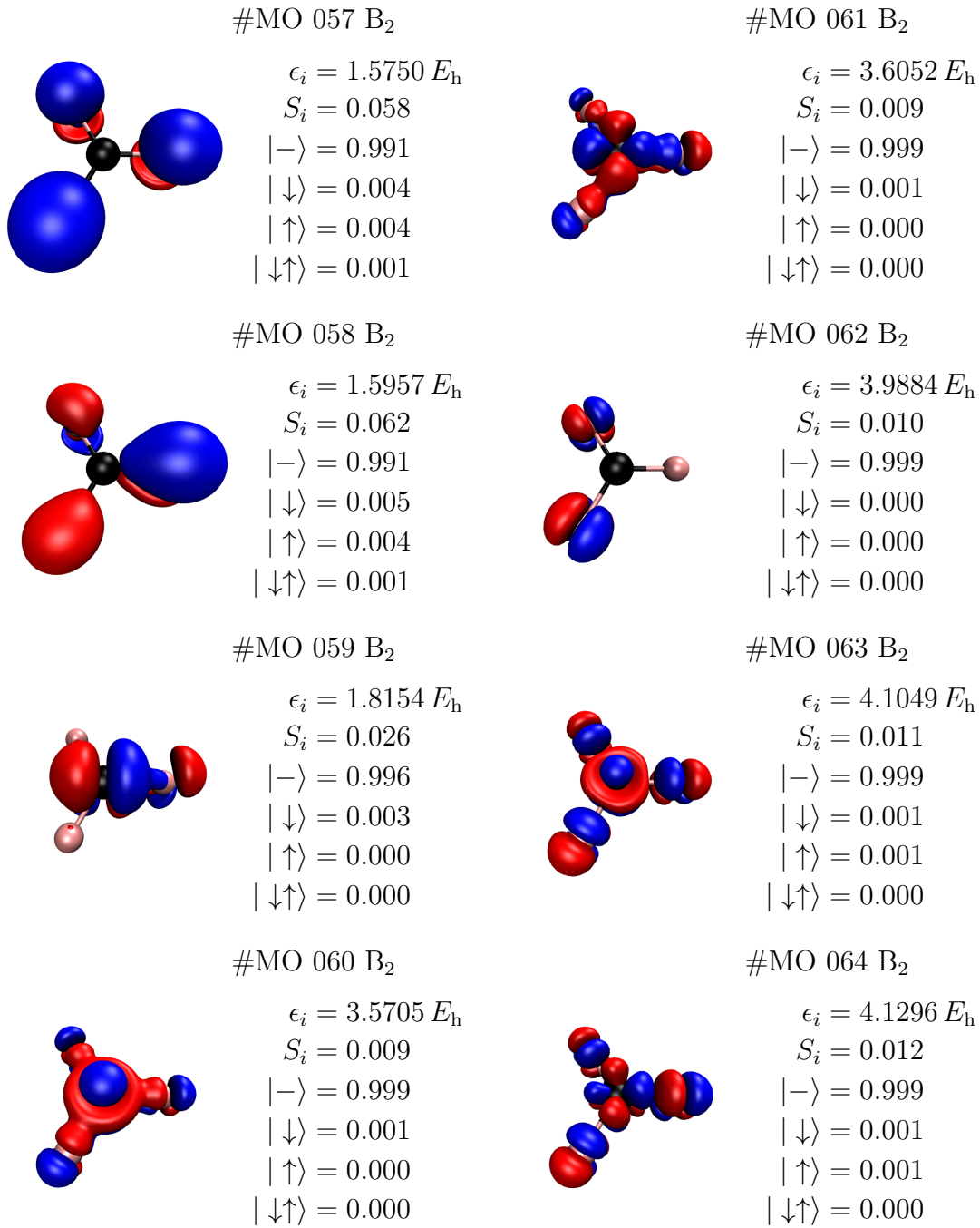


Figure A.30: Molecular orbitals #57 to #64 for CoF₃ with their eigenenergy ϵ_i , 1-orbital entropy S_i and orbital occupations $\omega_{i,\alpha} = \{ |- \rangle, |\downarrow \rangle, |\uparrow \rangle, |\downarrow\uparrow \rangle \}$. Isosurfaces are plotted at $|\psi(\vec{r})| = 0.05 a_0^{-1.5}$.

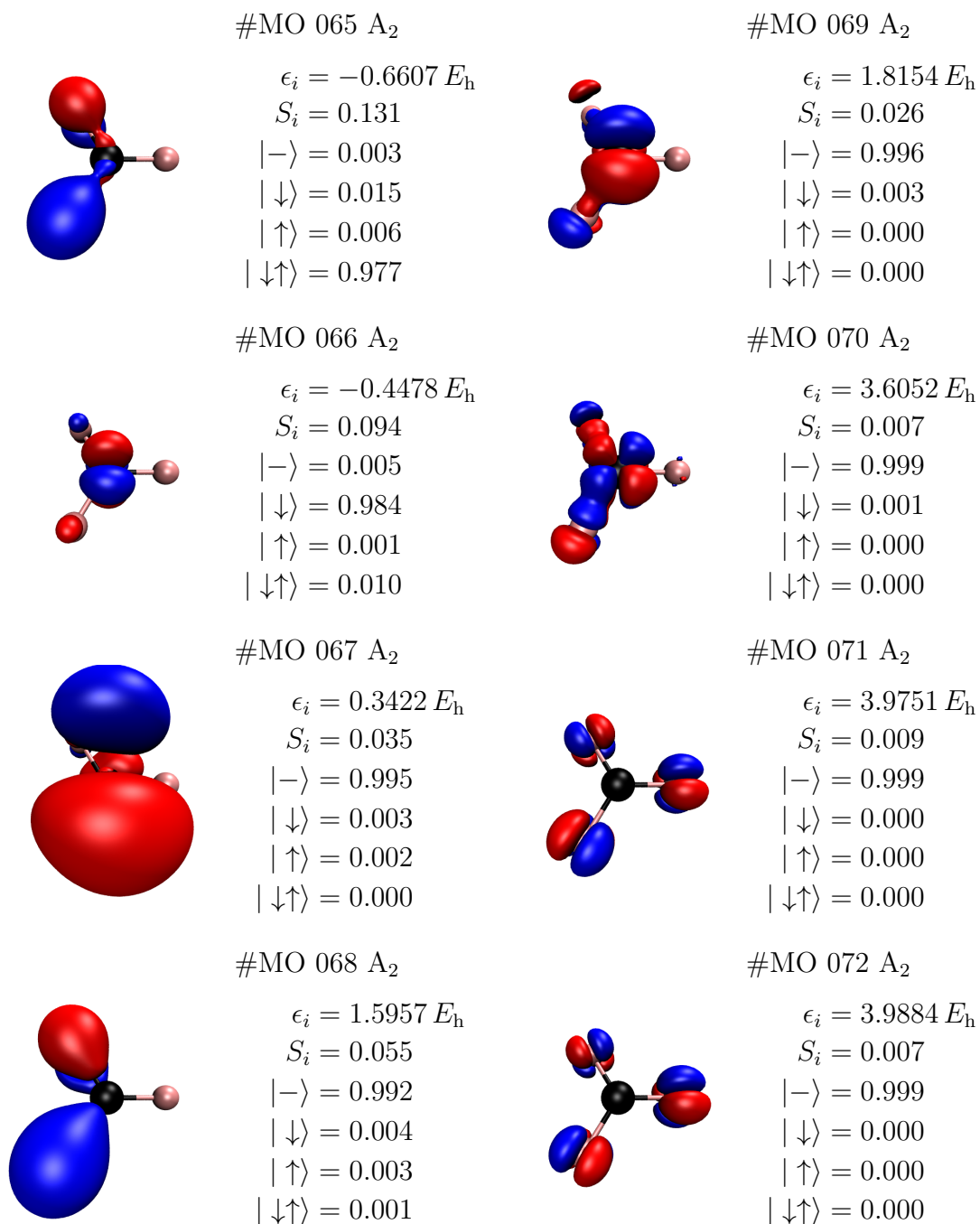


Figure A.31: Molecular orbitals #65 to #72 for CoF₃ with their eigenenergy ϵ_i , 1-orbital entropy S_i and orbital occupations $\omega_{i,\alpha} = \{ |- \rangle, |\downarrow \rangle, |\uparrow \rangle, |\downarrow\uparrow \rangle \}$. Isosurfaces are plotted at $|\psi(\vec{r})| = 0.05 a_0^{-1.5}$.

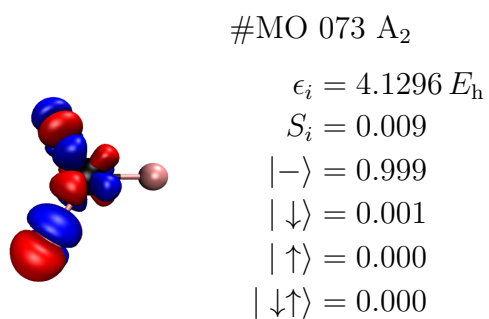


Figure A.32: Molecular orbitals #73 to #73 for CoF₃ with their eigenenergy ϵ_i , 1-orbital entropy S_i and orbital occupations $\omega_{i,\alpha} = \{|-\rangle, |\downarrow\rangle, |\uparrow\rangle, |\downarrow\uparrow\rangle\}$. Isosurfaces are plotted at $|\psi(\vec{r})| = 0.05 a_0^{-1.5}$.

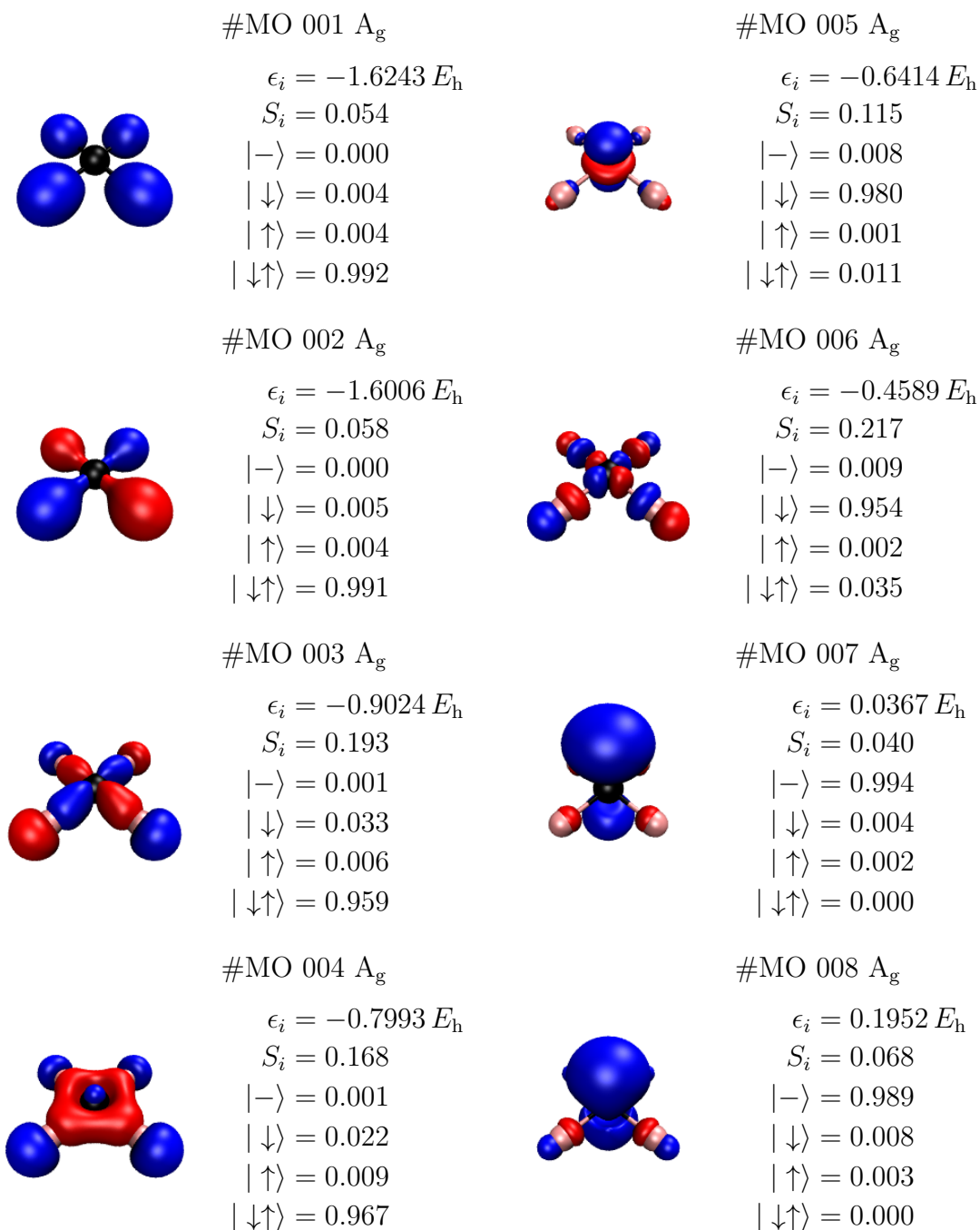


Figure A.33: Molecular orbitals #1 to #8 for CoF_4 D_{4h} with their eigenenergy ϵ_i , 1-orbital entropy S_i and orbital occupations $\omega_{i,\alpha} = \{ |-\rangle, |\downarrow\rangle, |\uparrow\rangle, |\downarrow\uparrow\rangle \}$. Isosurfaces are plotted at $|\psi(\vec{r})| = 0.05 a_0^{-1.5}$.

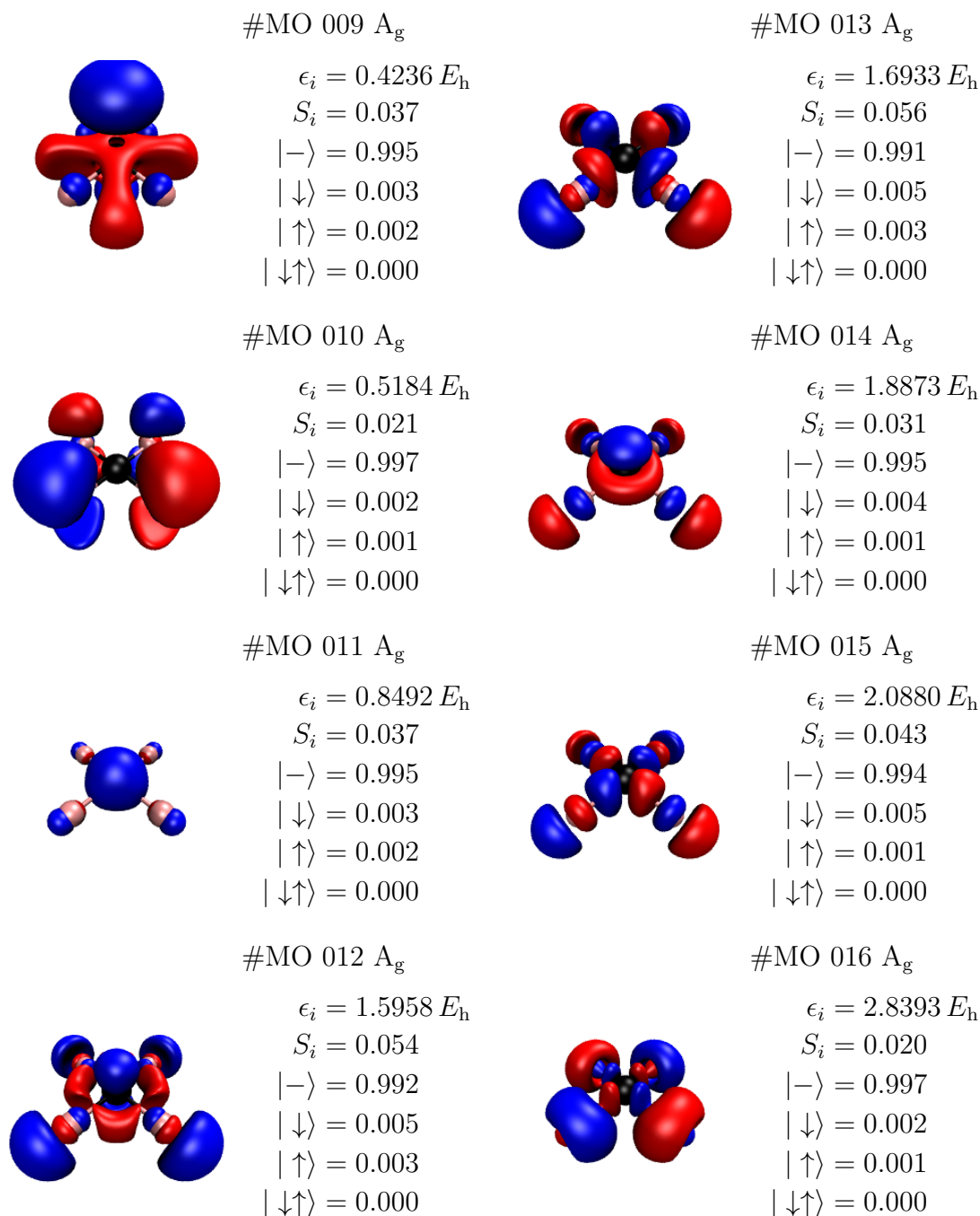


Figure A.34: Molecular orbitals #9 to #16 for CoF_4 D_{4h} with their eigenenergy ϵ_i , 1-orbital entropy S_i and orbital occupations $\omega_{i,\alpha} = \{ |- \rangle, |\downarrow \rangle, |\uparrow \rangle, |\downarrow\uparrow \rangle \}$. Isosurfaces are plotted at $|\psi(\vec{r})| = 0.05 a_0^{-1.5}$.

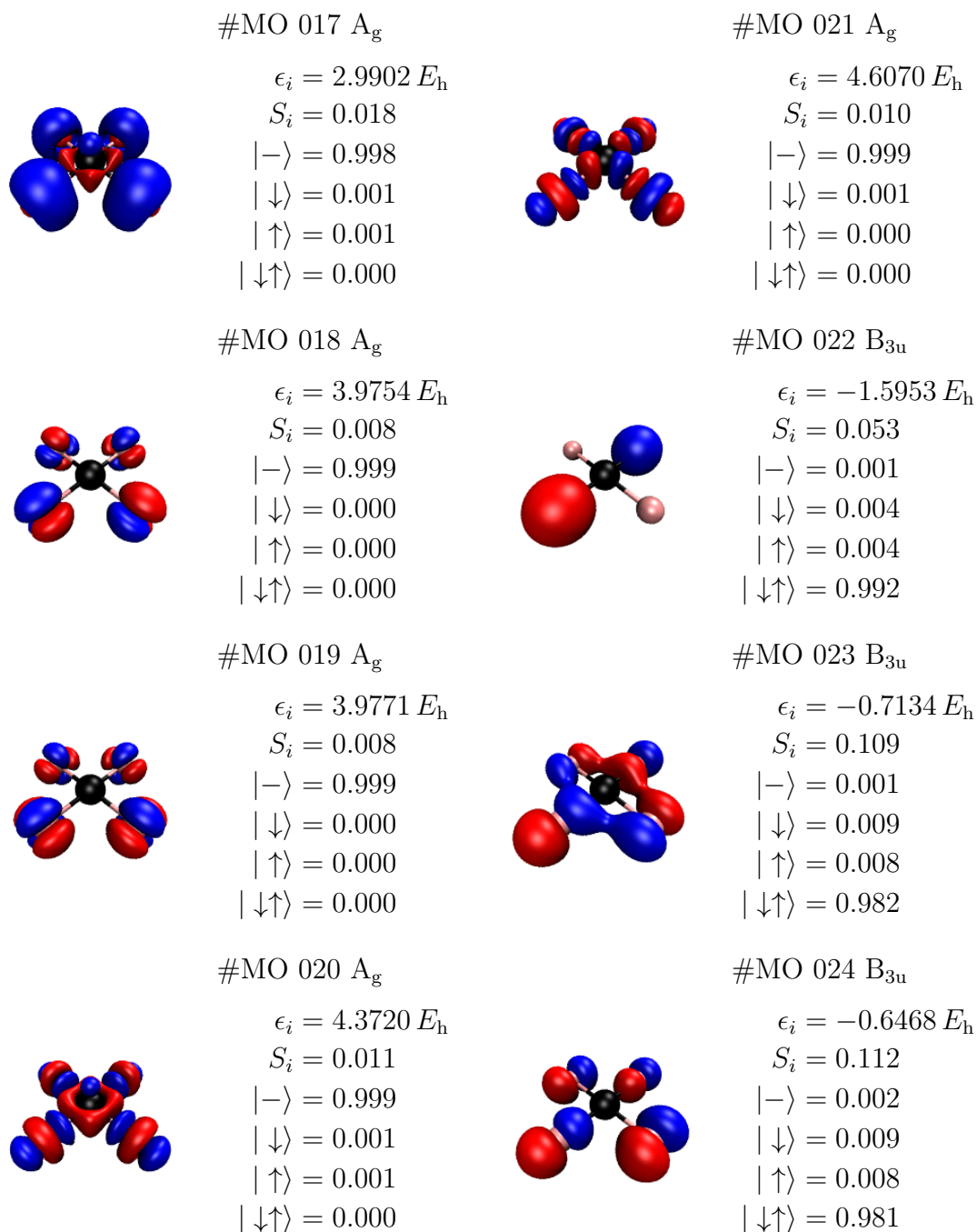


Figure A.35: Molecular orbitals #17 to #24 for CoF_4 D_{4h} with their eigenenergy ϵ_i , 1-orbital entropy S_i and orbital occupations $\omega_{i,\alpha} = \{|\rightarrow\rangle, |\downarrow\rangle, |\uparrow\rangle, |\downarrow\uparrow\rangle\}$. Isosurfaces are plotted at $|\psi(\vec{r})| = 0.05 a_0^{-1.5}$.

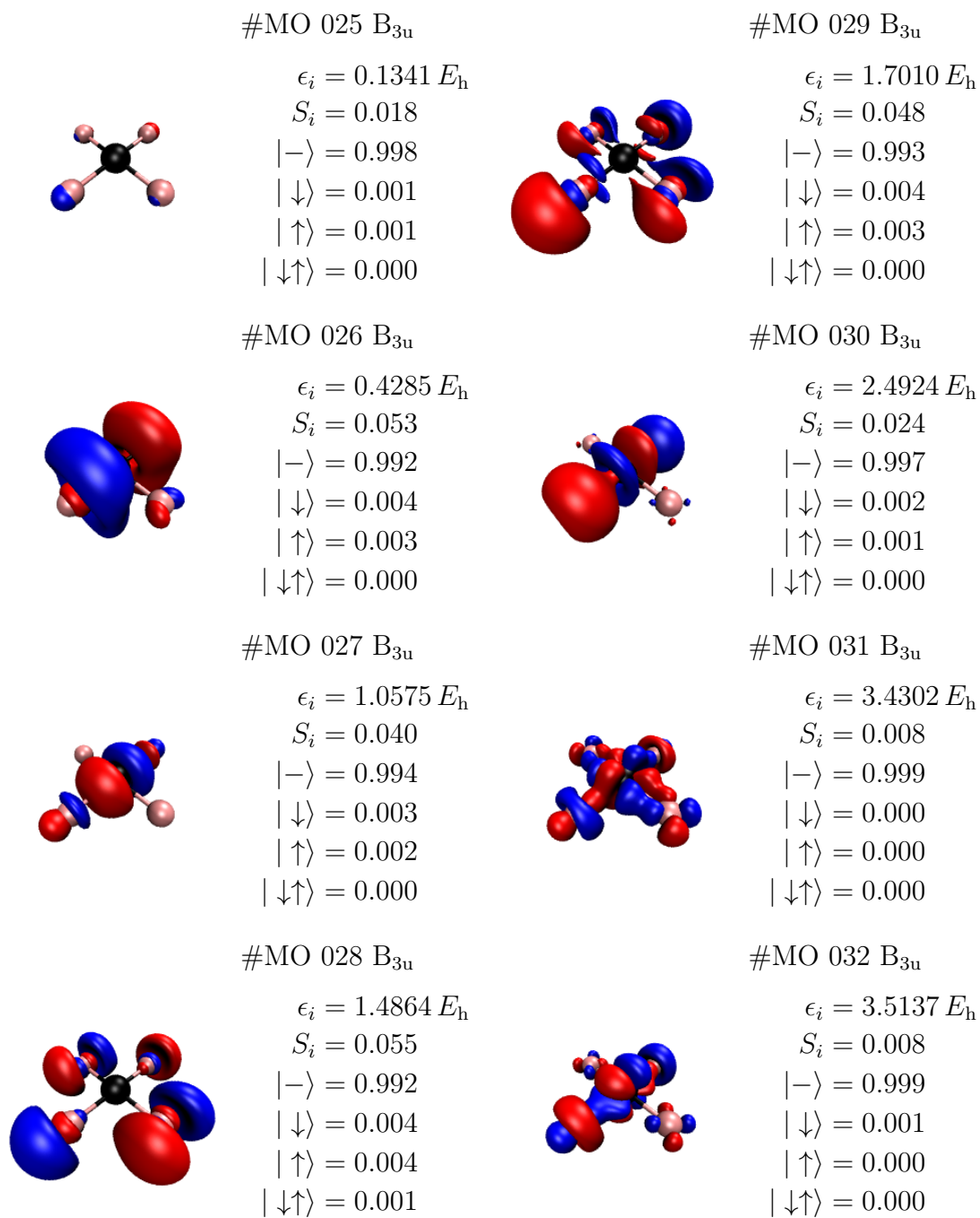


Figure A.36: Molecular orbitals #25 to #32 for CoF₄ D_{4h} with their eigenenergy ϵ_i , 1-orbital entropy S_i and orbital occupations $\omega_{i,\alpha} = \{|-\rangle, |\downarrow\rangle, |\uparrow\rangle, |\downarrow\uparrow\rangle\}$. Isosurfaces are plotted at $|\psi(\vec{r})| = 0.05 a_0^{-1.5}$.

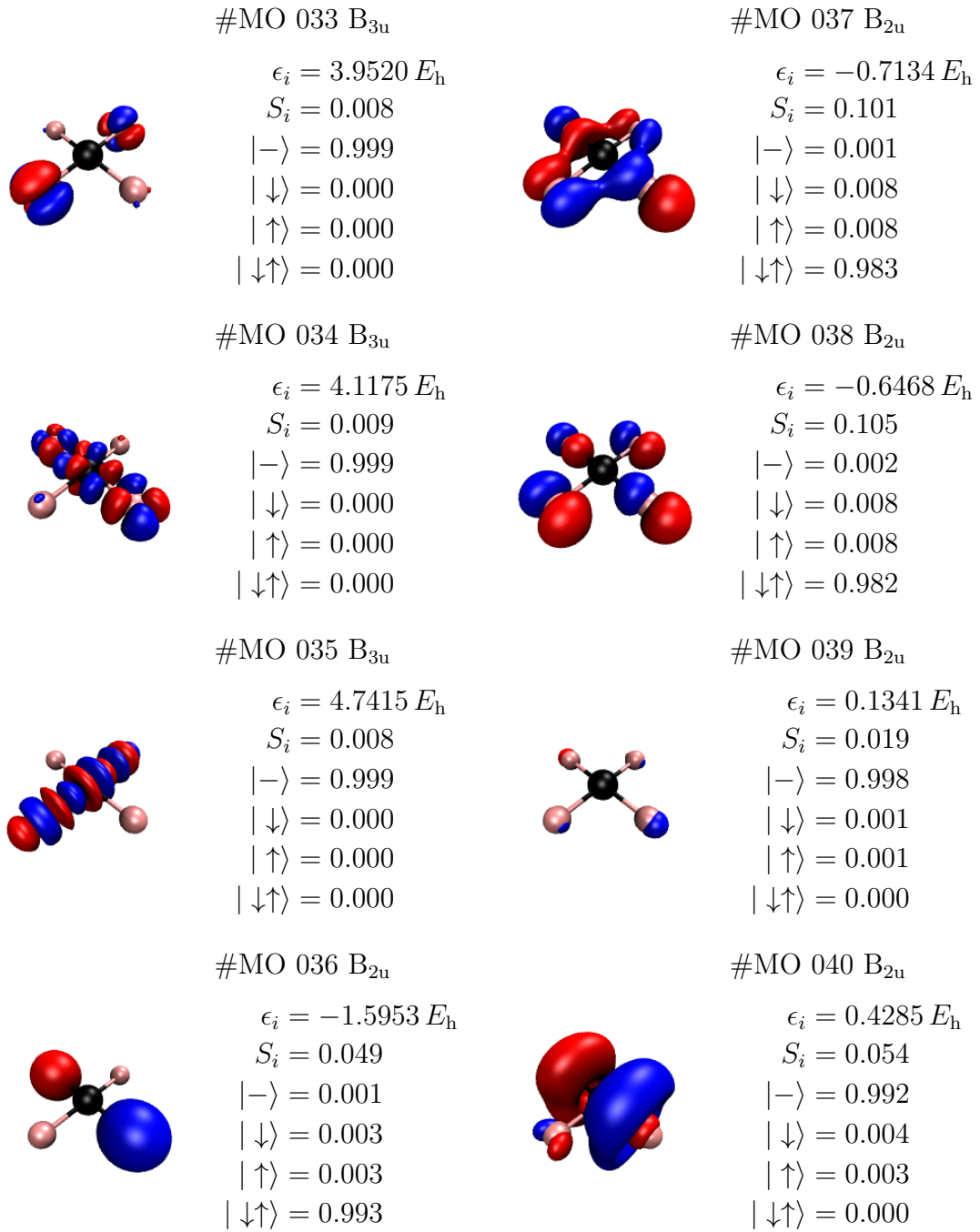


Figure A.37: Molecular orbitals #33 to #40 for CoF₄ D_{4h} with their eigenenergy ϵ_i , 1-orbital entropy S_i and orbital occupations $\omega_{i,\alpha} = \{ |- \rangle, |\downarrow \rangle, |\uparrow \rangle, |\downarrow\uparrow \rangle \}$. Isosurfaces are plotted at $|\psi(\vec{r})| = 0.05 a_0^{-1.5}$.

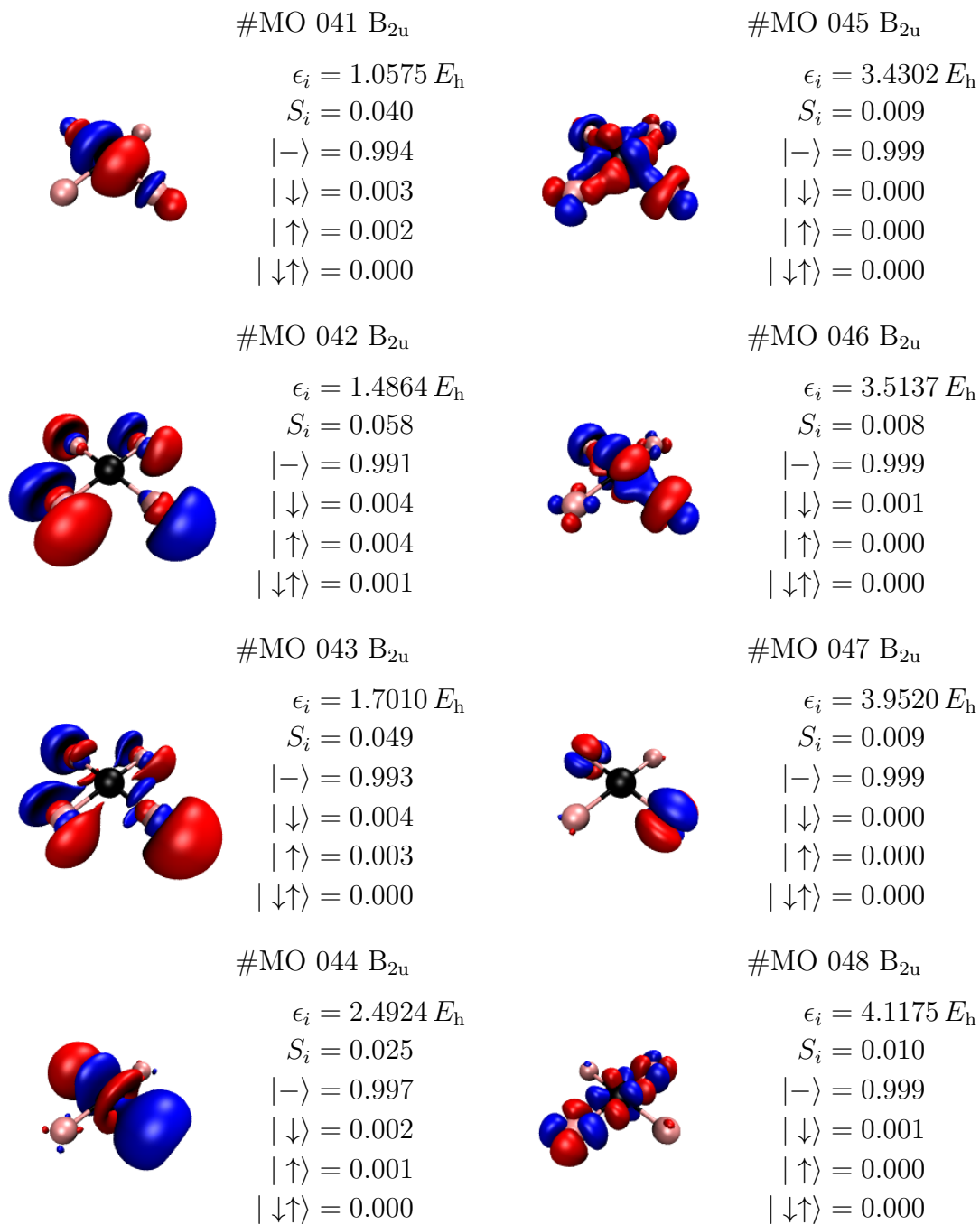


Figure A.38: Molecular orbitals #41 to #48 for CoF₄ D_{4h} with their eigenenergy ϵ_i , 1-orbital entropy S_i and orbital occupations $\omega_{i,\alpha} = \{|-\rangle, |\downarrow\rangle, |\uparrow\rangle, |\downarrow\uparrow\rangle\}$. Isosurfaces are plotted at $|\psi(\vec{r})| = 0.05 a_0^{-1.5}$.

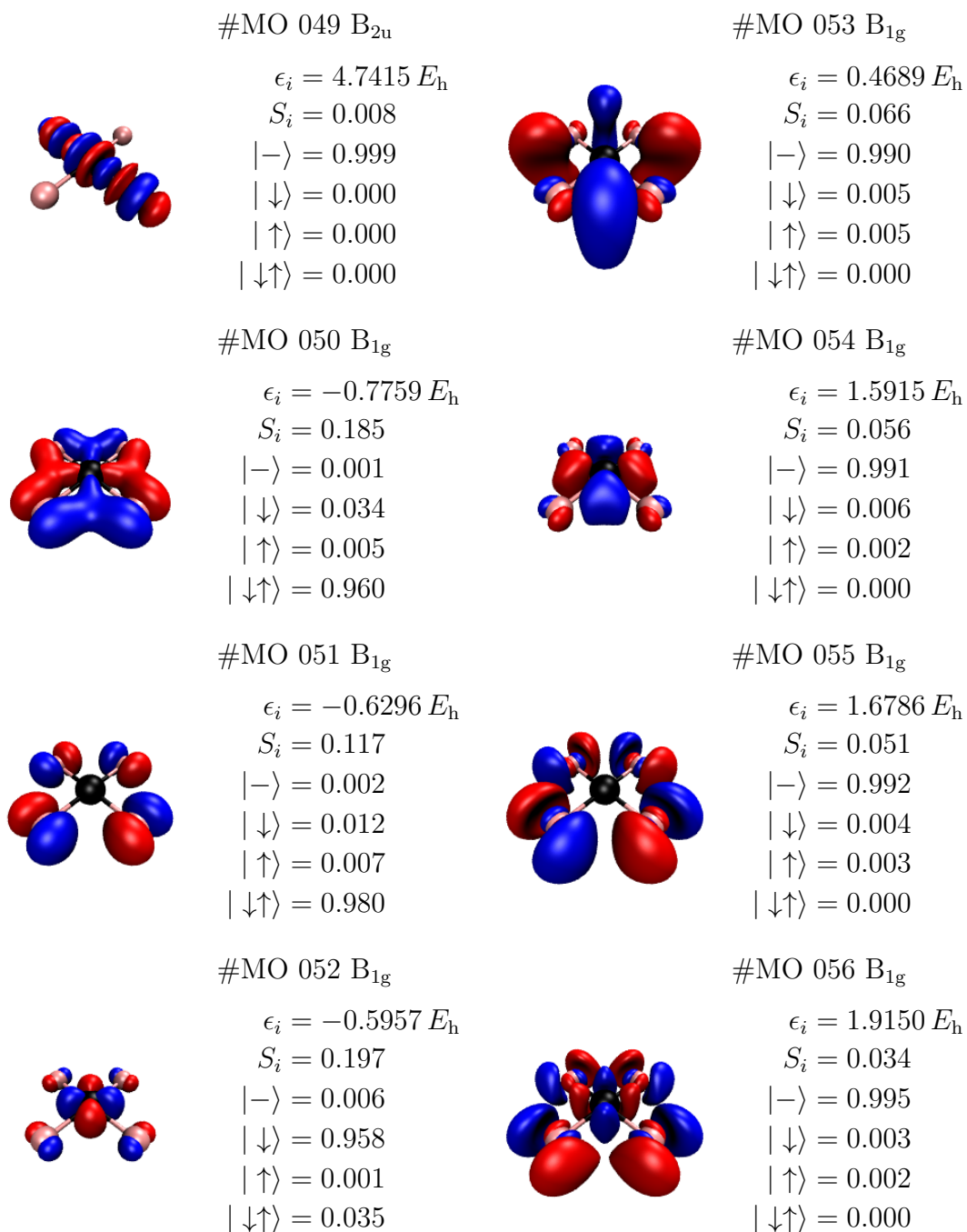


Figure A.39: Molecular orbitals #49 to #56 for CoF₄ D_{4h} with their eigenenergy ϵ_i , 1-orbital entropy S_i and orbital occupations $\omega_{i,\alpha} = \{ |- \rangle, |\downarrow \rangle, |\uparrow \rangle, |\downarrow\uparrow \rangle \}$. Isosurfaces are plotted at $|\psi(\vec{r})| = 0.05 a_0^{-1.5}$.

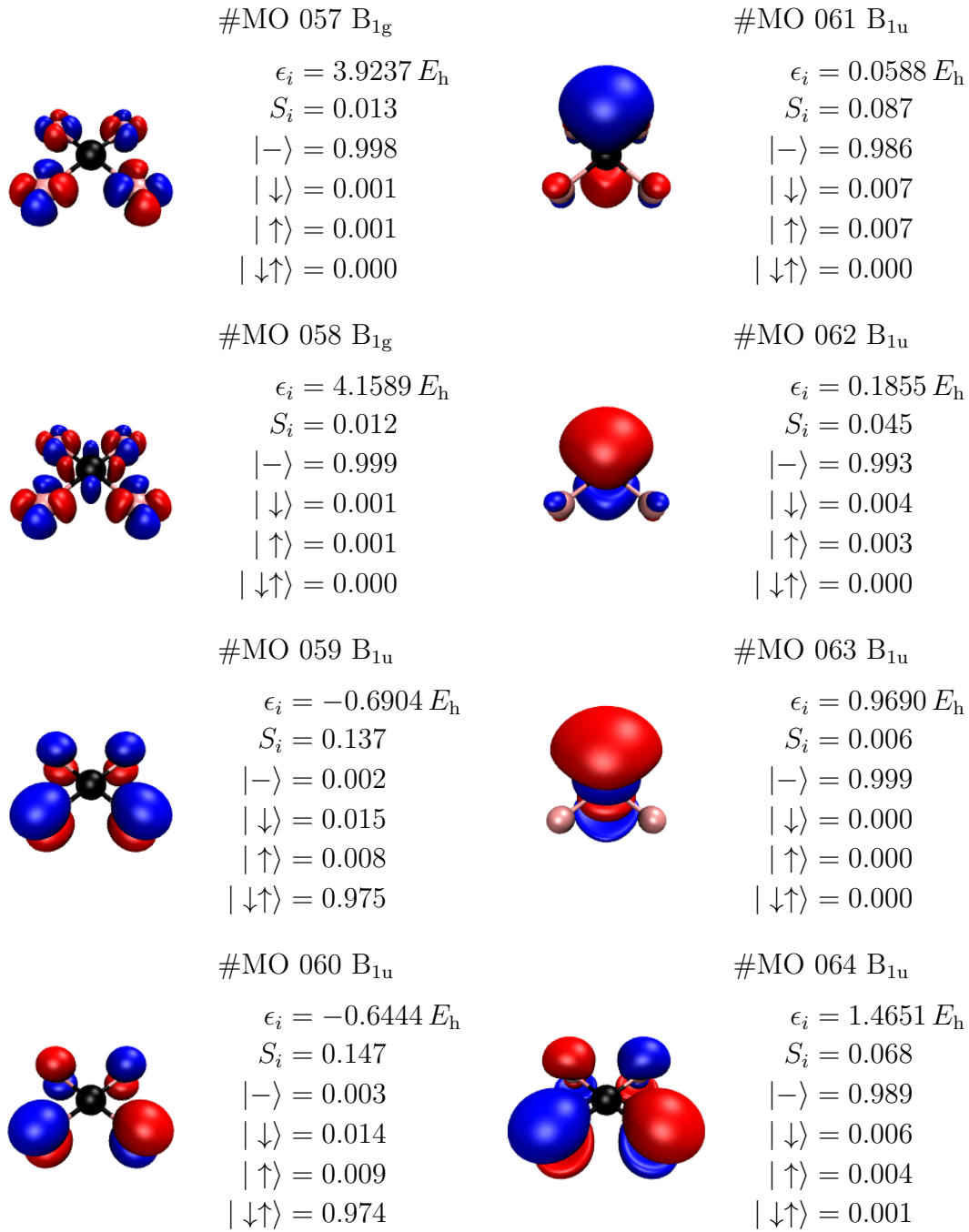


Figure A.40: Molecular orbitals #57 to #64 for CoF₄ D_{4h} with their eigenenergy ϵ_i , 1-orbital entropy S_i and orbital occupations $\omega_{i,\alpha} = \{ |- \rangle, |\downarrow \rangle, |\uparrow \rangle, |\downarrow\uparrow \rangle \}$. Isosurfaces are plotted at $|\psi(\vec{r})| = 0.05 a_0^{-1.5}$.

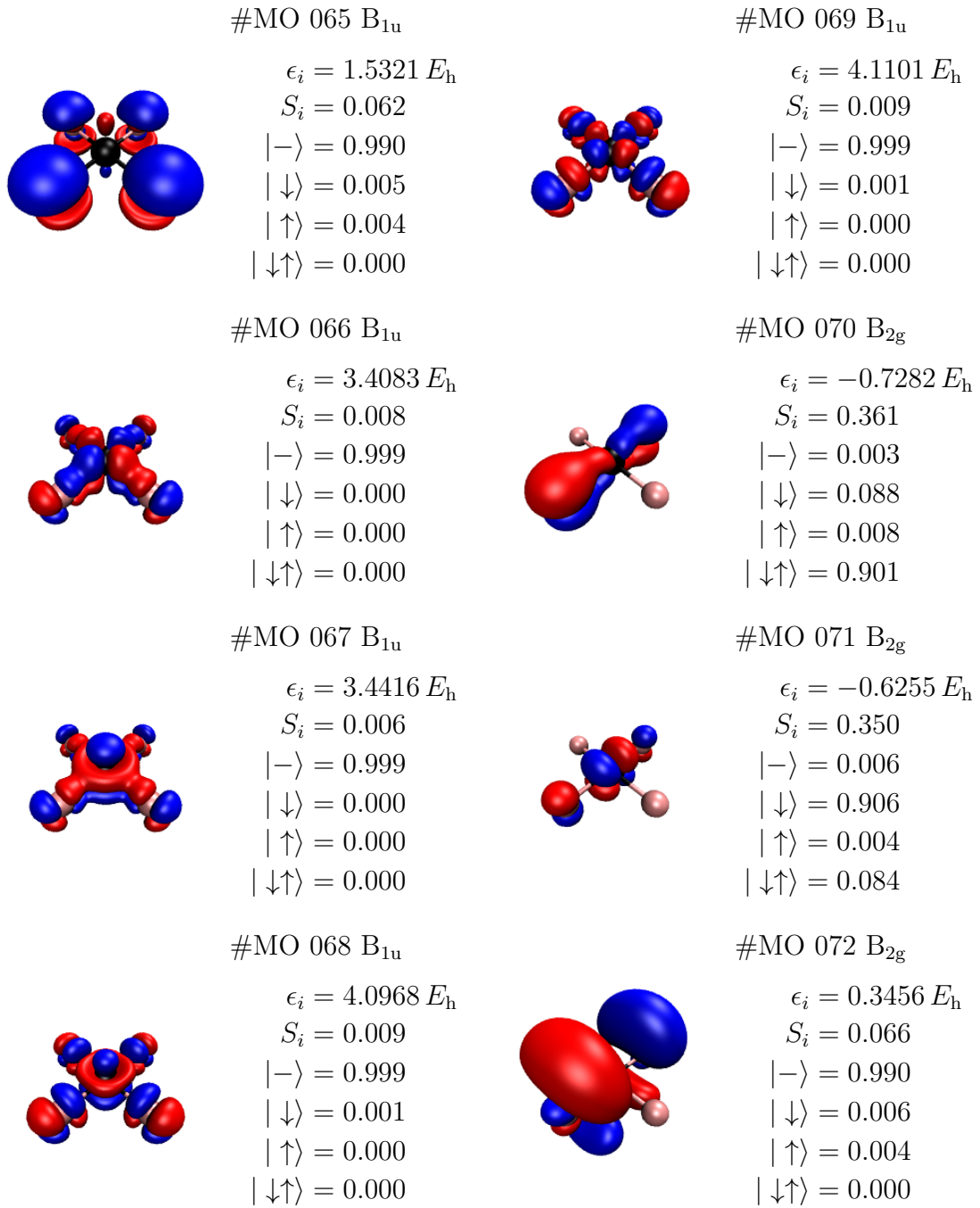


Figure A.41: Molecular orbitals #65 to #72 for CoF₄ D_{4h} with their eigenenergy ϵ_i , 1-orbital entropy S_i and orbital occupations $\omega_{i,\alpha} = \{ |- \rangle, |\downarrow \rangle, |\uparrow \rangle, |\downarrow\uparrow \rangle \}$. Isosurfaces are plotted at $|\psi(\vec{r})| = 0.05 a_0^{-1.5}$.

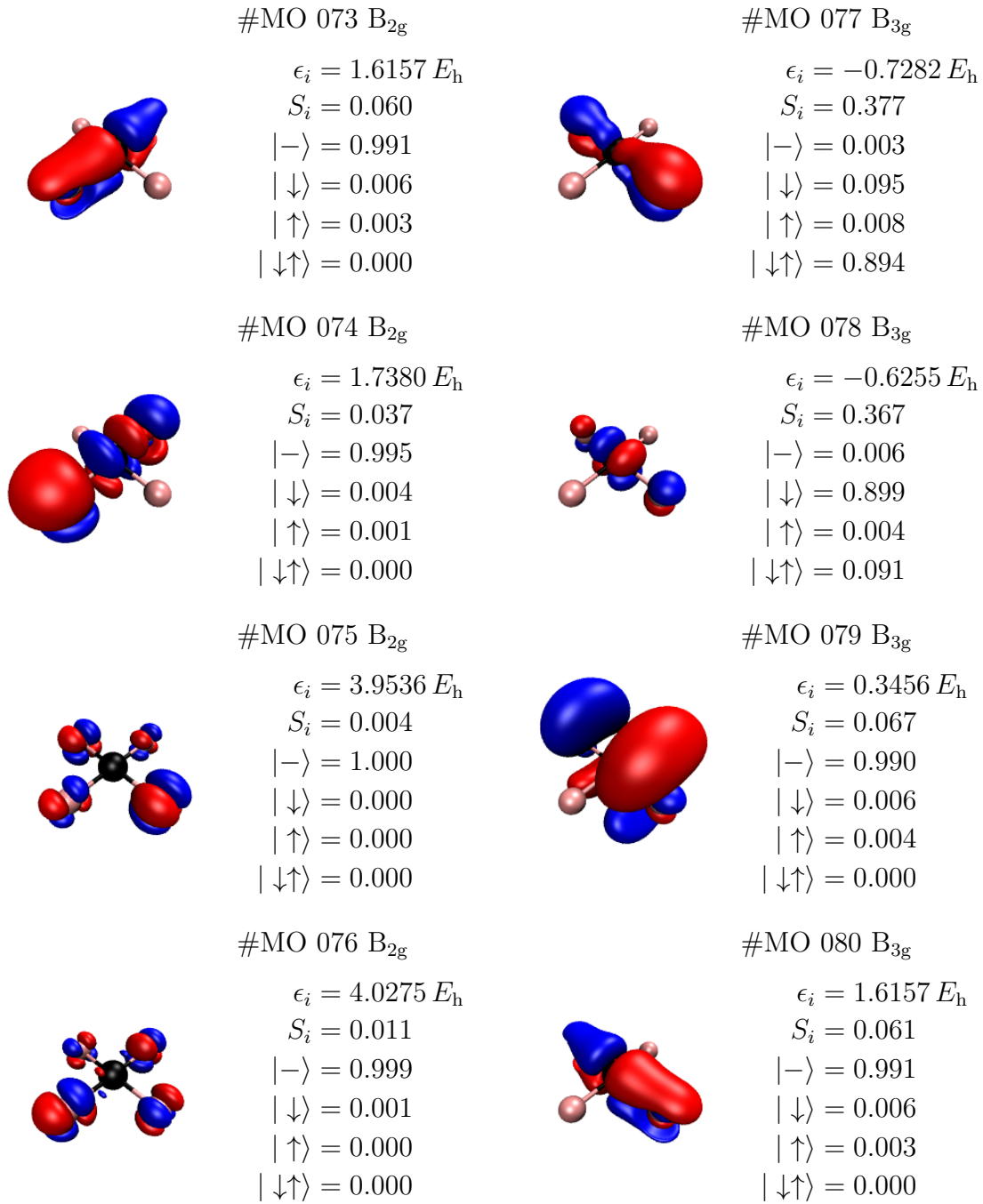


Figure A.42: Molecular orbitals #73 to #80 for CoF₄ D_{4h} with their eigenenergy ϵ_i , 1-orbital entropy S_i and orbital occupations $\omega_{i,\alpha} = \{|\rightarrow\rangle, |\downarrow\rangle, |\uparrow\rangle, |\downarrow\uparrow\rangle\}$. Isosurfaces are plotted at $|\psi(\vec{r})| = 0.05 a_0^{-1.5}$.

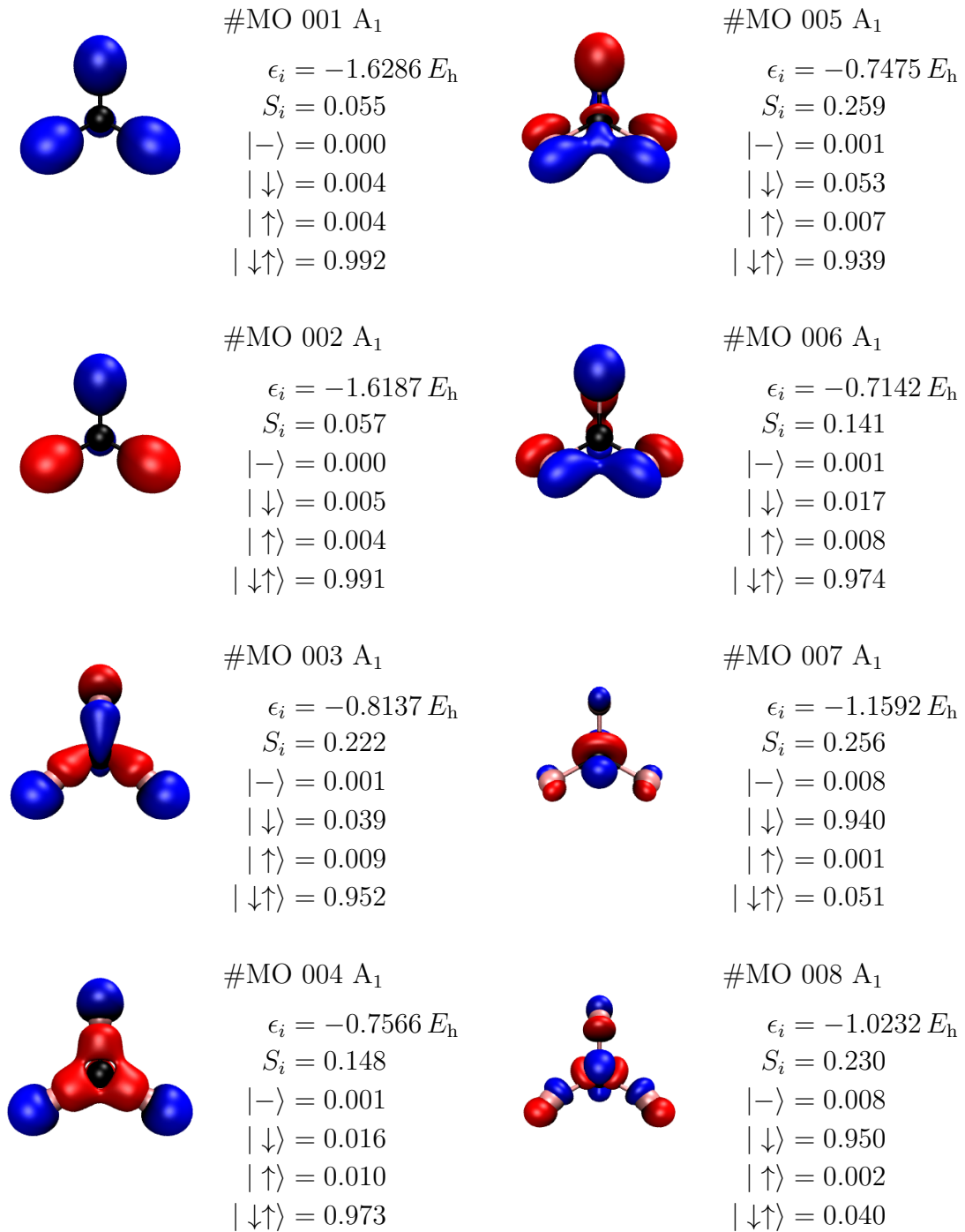


Figure A.43: Molecular orbitals #1 to #8 for CoF_4 T_d with their eigenenergy ϵ_i , 1-orbital entropy S_i and orbital occupations $\omega_{i,\alpha} = \{ |- \rangle, |\downarrow \rangle, |\uparrow \rangle, |\downarrow\uparrow \rangle \}$. Isosurfaces are plotted at $|\psi(\vec{r})| = 0.05 a_0^{-1.5}$.

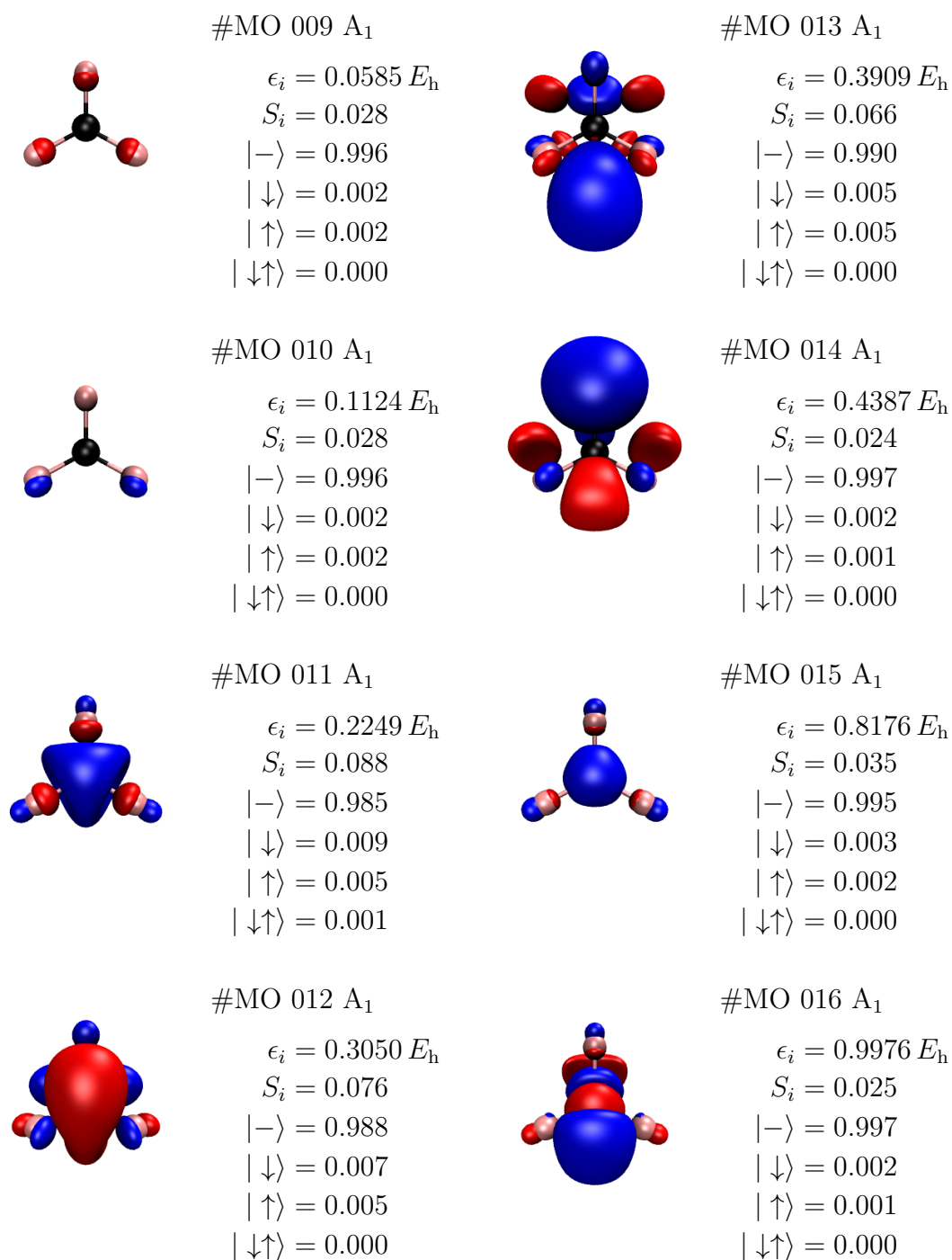


Figure A.44: Molecular orbitals #9 to #16 for $\text{CoF}_4 T_d$ with their eigenenergy ϵ_i , 1-orbital entropy S_i and orbital occupations $\omega_{i,\alpha} = \{ |- \rangle, |\downarrow \rangle, |\uparrow \rangle, |\downarrow\uparrow \rangle \}$. Isosurfaces are plotted at $|\psi(\vec{r})| = 0.05 a_0^{-1.5}$.

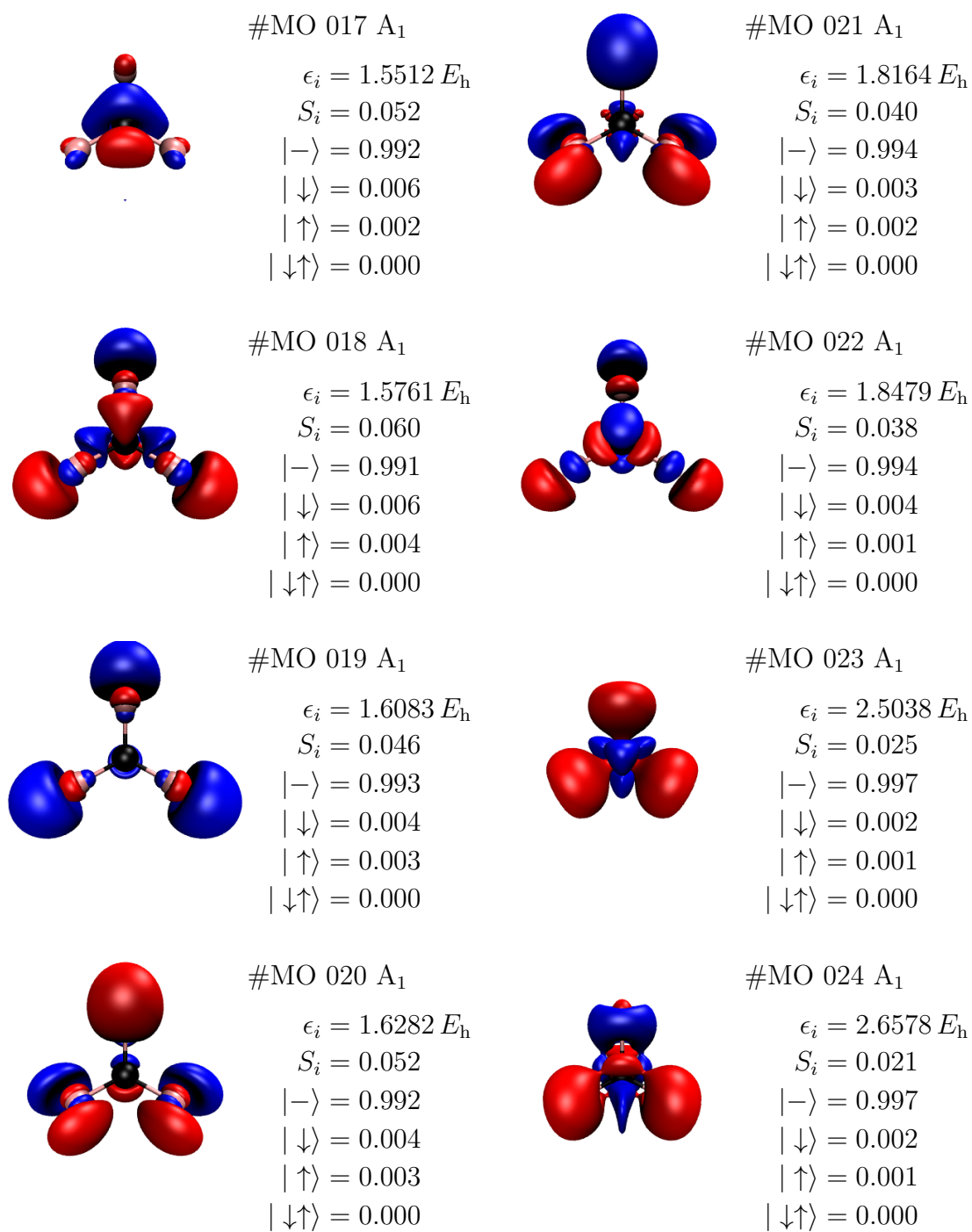


Figure A.45: Molecular orbitals #17 to #24 for $\text{CoF}_4 T_d$ with their eigenenergy ϵ_i , 1-orbital entropy S_i and orbital occupations $\omega_{i,\alpha} = \{ |- \rangle, |\downarrow \rangle, |\uparrow \rangle, |\downarrow\uparrow \rangle \}$. Isosurfaces are plotted at $|\psi(\vec{r})| = 0.05 a_0^{-1.5}$.

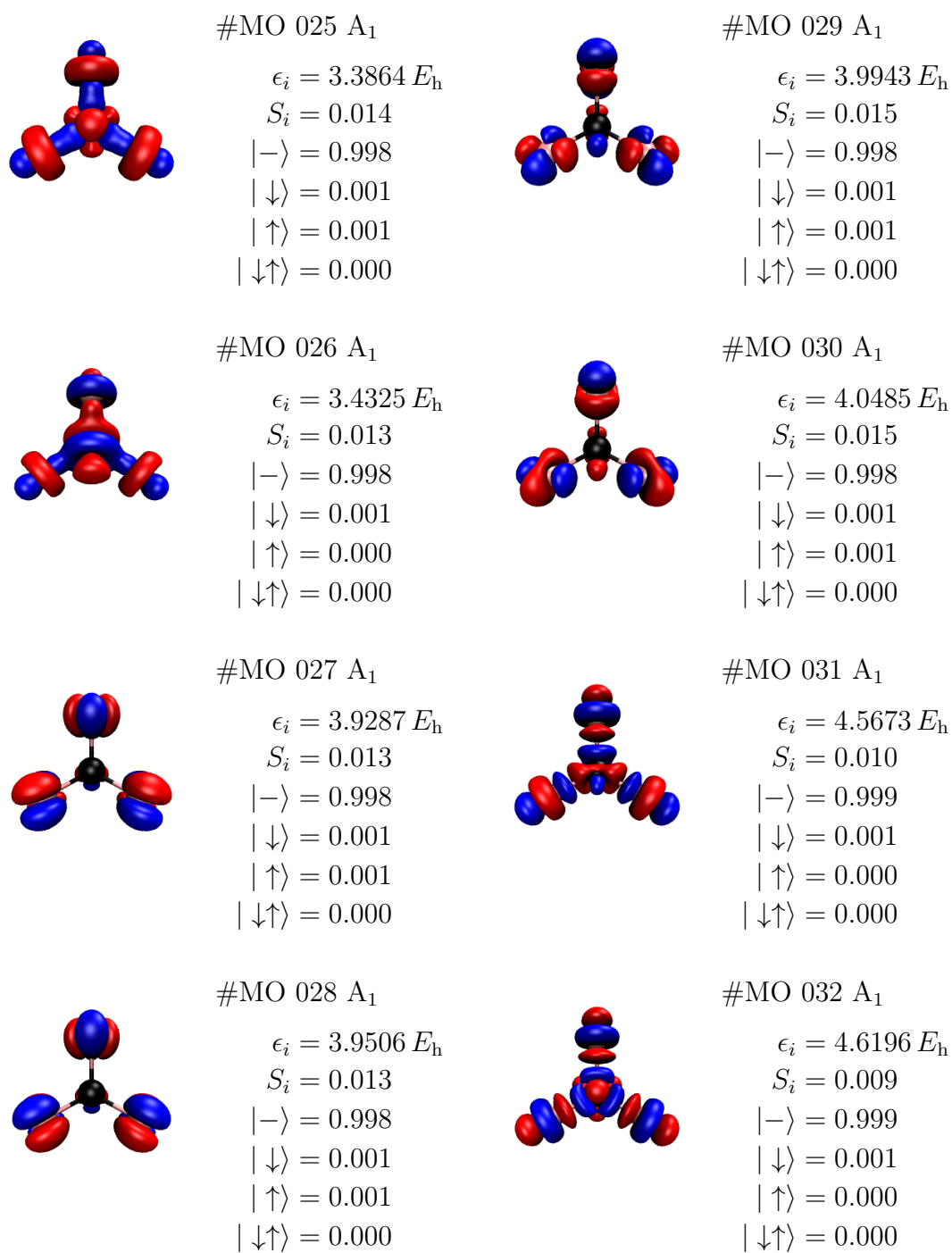


Figure A.46: Molecular orbitals #25 to #32 for $\text{CoF}_4 T_d$ with their eigenenergy ϵ_i , 1-orbital entropy S_i and orbital occupations $\omega_{i,\alpha} = \{|\rightarrow\rangle, |\downarrow\rangle, |\uparrow\rangle, |\downarrow\uparrow\rangle\}$. Isosurfaces are plotted at $|\psi(\vec{r})| = 0.05 a_0^{-1.5}$.

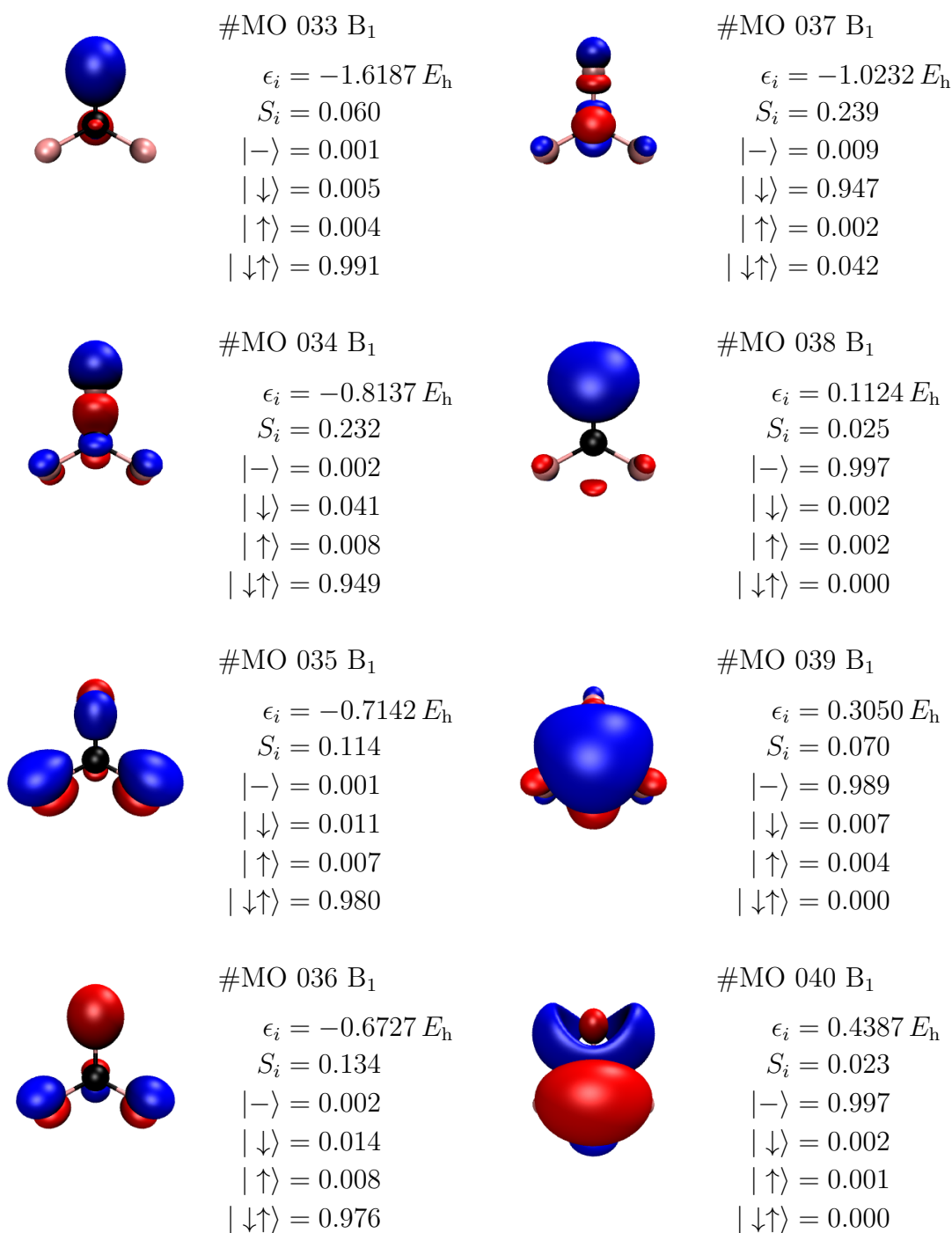


Figure A.47: Molecular orbitals #33 to #40 for $\text{CoF}_4 T_d$ with their eigenenergy ϵ_i , 1-orbital entropy S_i and orbital occupations $\omega_{i,\alpha} = \{ |- \rangle, |\downarrow \rangle, |\uparrow \rangle, |\downarrow\uparrow \rangle \}$. Isosurfaces are plotted at $|\psi(\vec{r})| = 0.05 a_0^{-1.5}$.

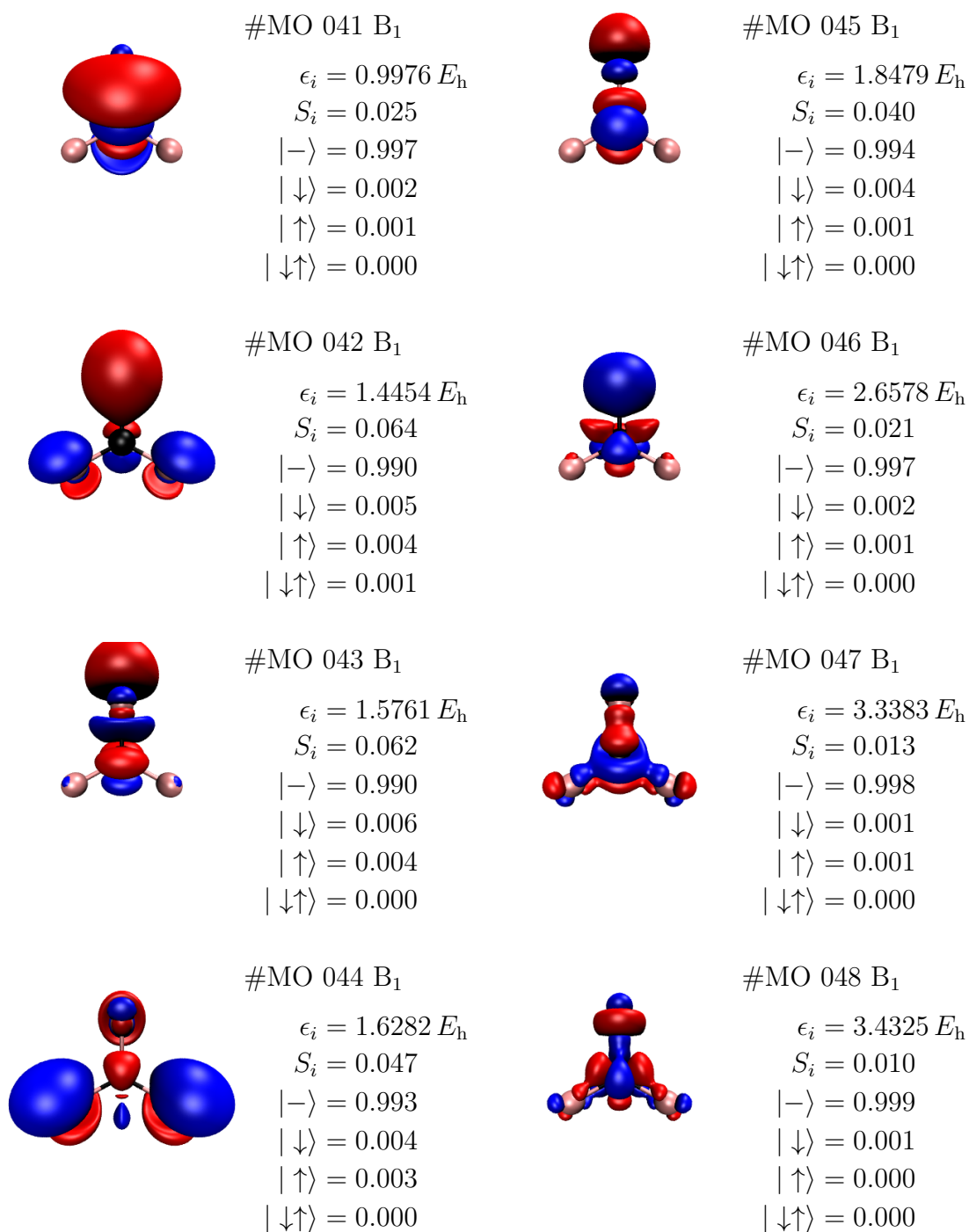


Figure A.48: Molecular orbitals #41 to #48 for CoF₄ T_d with their eigenenergy ϵ_i , 1-orbital entropy S_i and orbital occupations $\omega_{i,\alpha} = \{|\rightarrow\rangle, |\downarrow\rangle, |\uparrow\rangle, |\downarrow\uparrow\rangle\}$. Isosurfaces are plotted at $|\psi(\vec{r})| = 0.05 a_0^{-1.5}$.

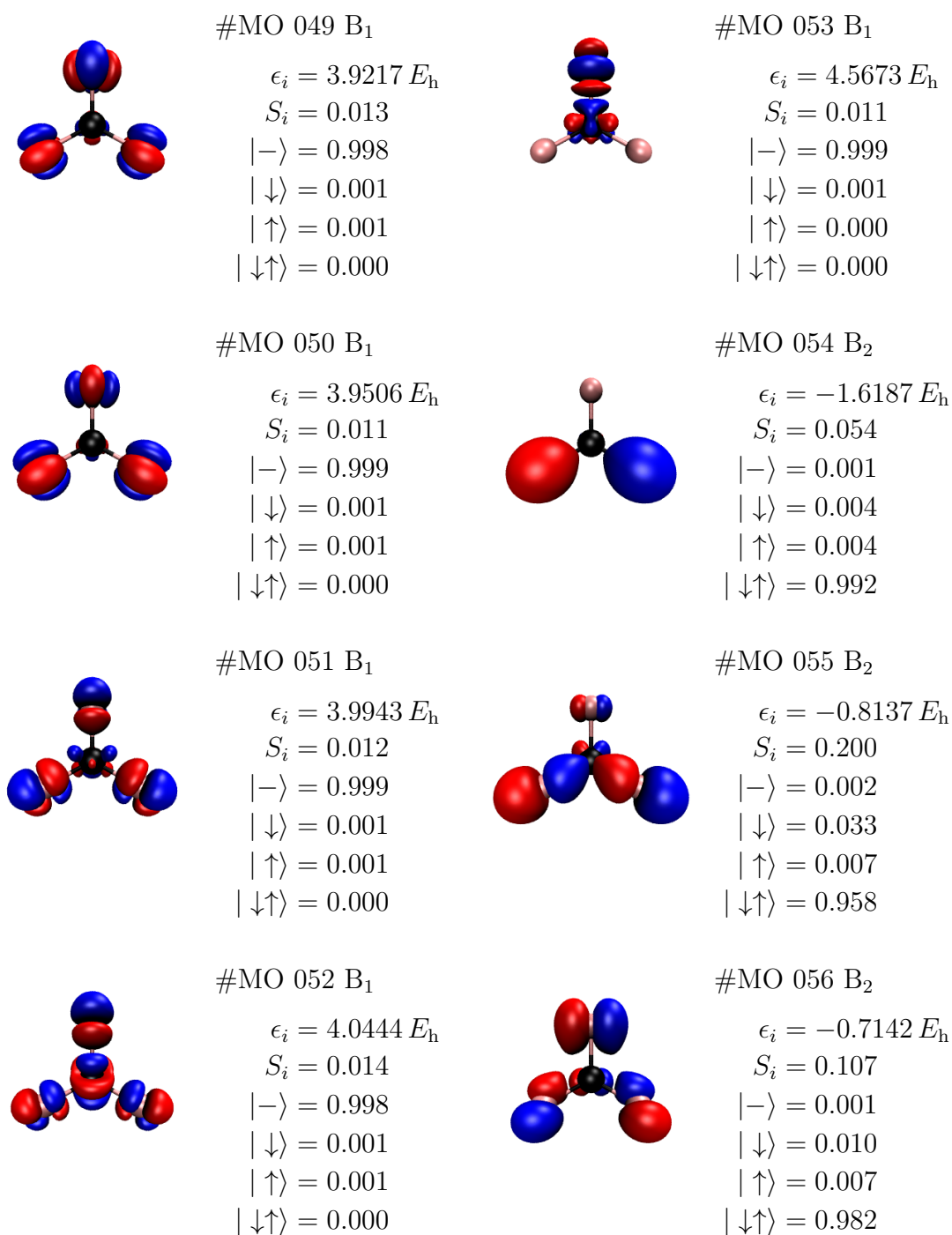


Figure A.49: Molecular orbitals #49 to #56 for $\text{CoF}_4 T_d$ with their eigenenergy ϵ_i , 1-orbital entropy S_i and orbital occupations $\omega_{i,\alpha} = \{|\rightarrow\rangle, |\downarrow\rangle, |\uparrow\rangle, |\downarrow\uparrow\rangle\}$. Isosurfaces are plotted at $|\psi(\vec{r})| = 0.05 a_0^{-1.5}$.

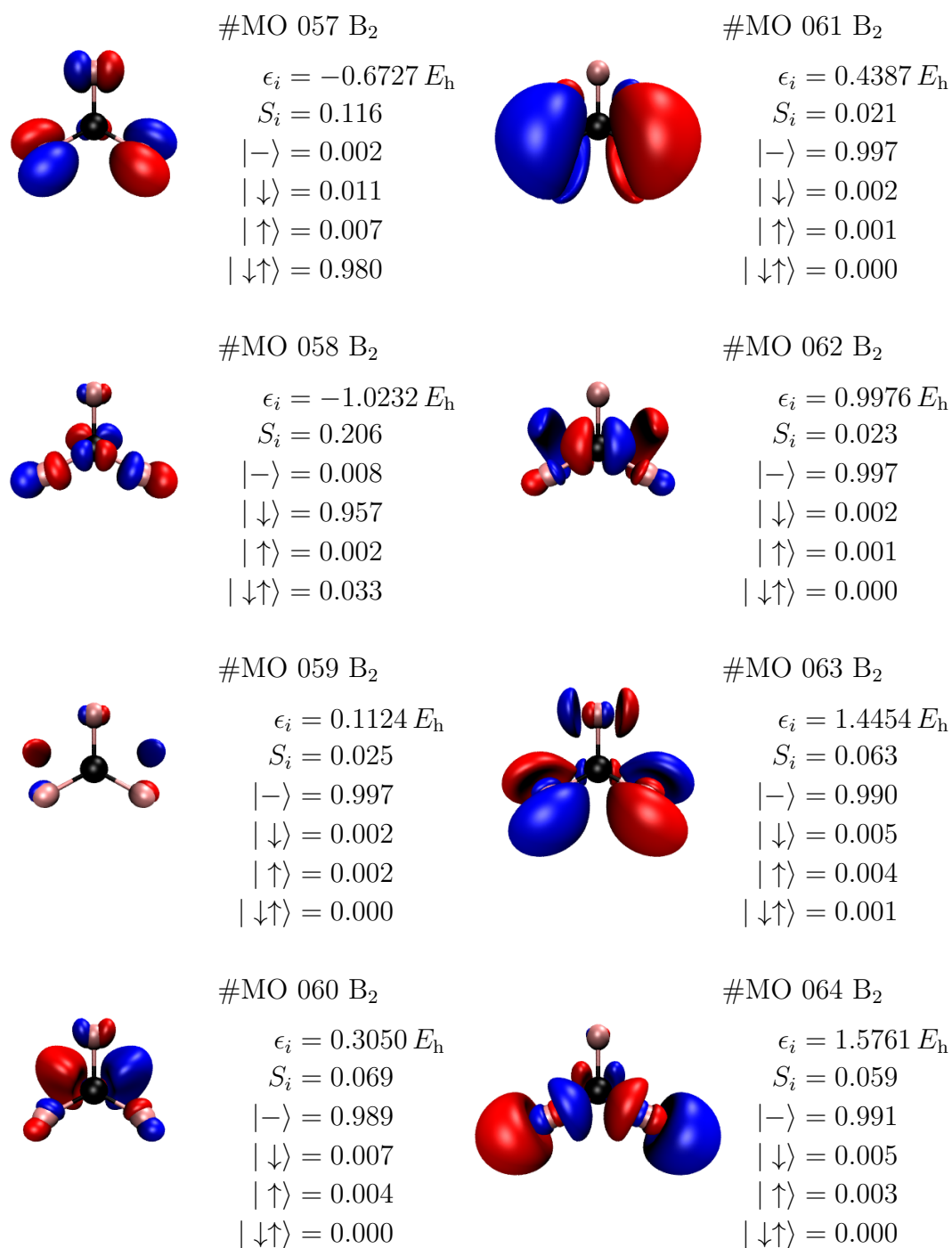


Figure A.50: Molecular orbitals #57 to #64 for CoF₄ T_d with their eigenenergy ϵ_i , 1-orbital entropy S_i and orbital occupations $\omega_{i,\alpha} = \{ |- \rangle, |\downarrow \rangle, |\uparrow \rangle, |\downarrow\uparrow \rangle \}$. Isosurfaces are plotted at $|\psi(\vec{r})| = 0.05 a_0^{-1.5}$.

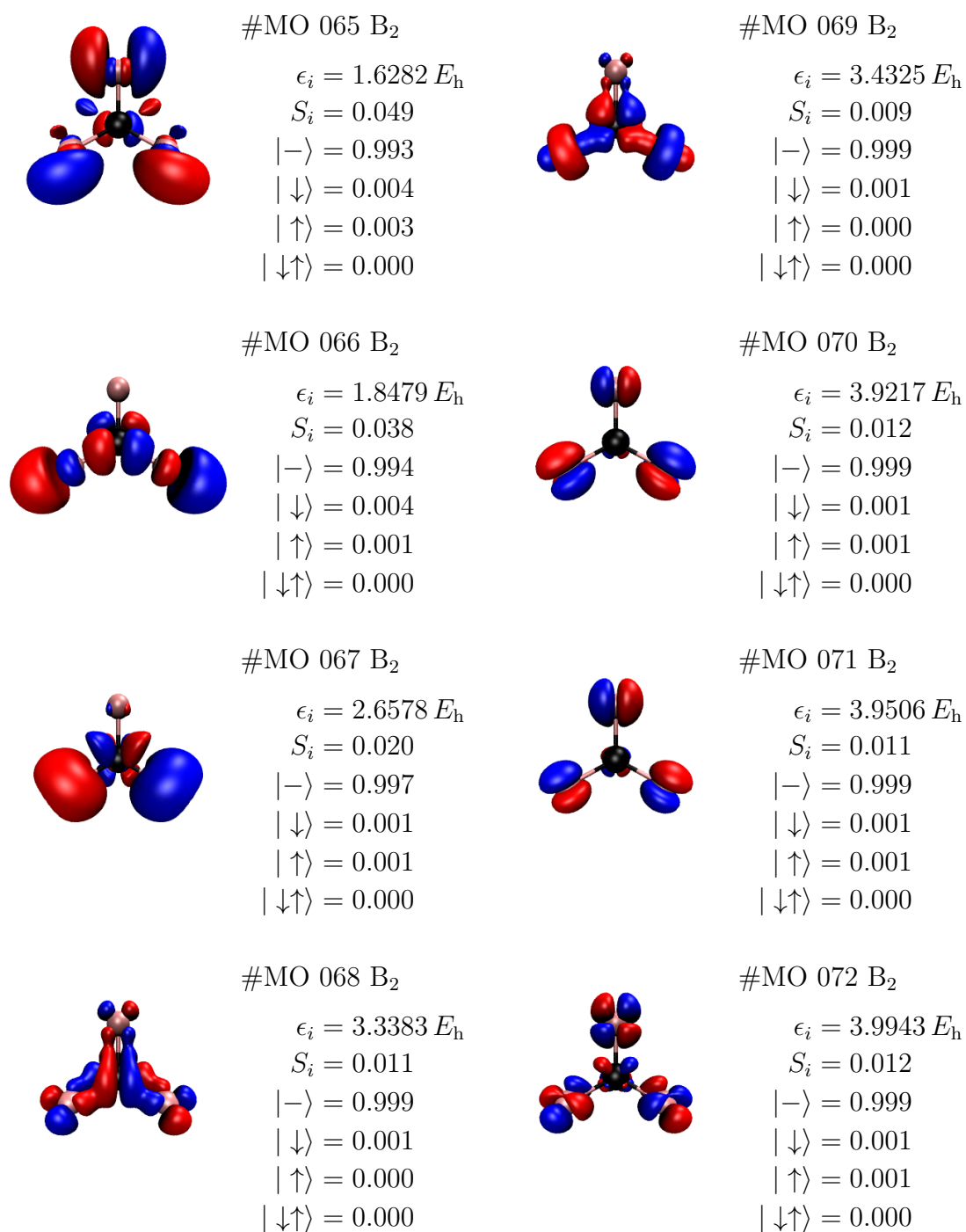


Figure A.51: Molecular orbitals #65 to #72 for CoF₄ T_d with their eigenenergy ϵ_i , 1-orbital entropy S_i and orbital occupations $\omega_{i,\alpha} = \{ |- \rangle, |\downarrow \rangle, |\uparrow \rangle, |\downarrow\uparrow \rangle \}$. Isosurfaces are plotted at $|\psi(\vec{r})| = 0.05 a_0^{-1.5}$.

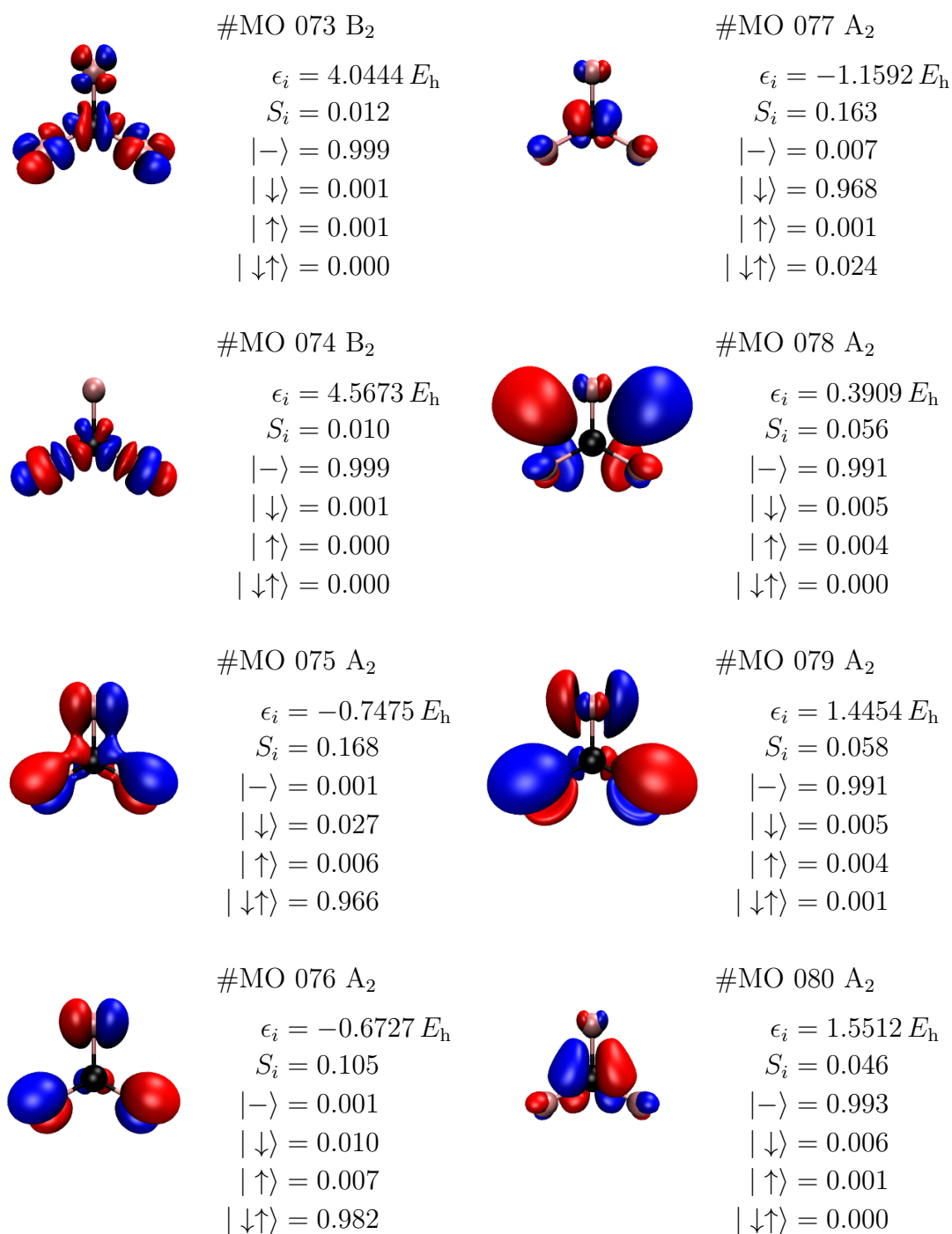


Figure A.52: Molecular orbitals #73 to #80 for $\text{CoF}_4 T_d$ with their eigenenergy ϵ_i , 1-orbital entropy S_i and orbital occupations $\omega_{i,\alpha} = \{ |- \rangle, |\downarrow \rangle, |\uparrow \rangle, |\downarrow\uparrow \rangle \}$. Isosurfaces are plotted at $|\psi(\vec{r})| = 0.05 a_0^{-1.5}$.

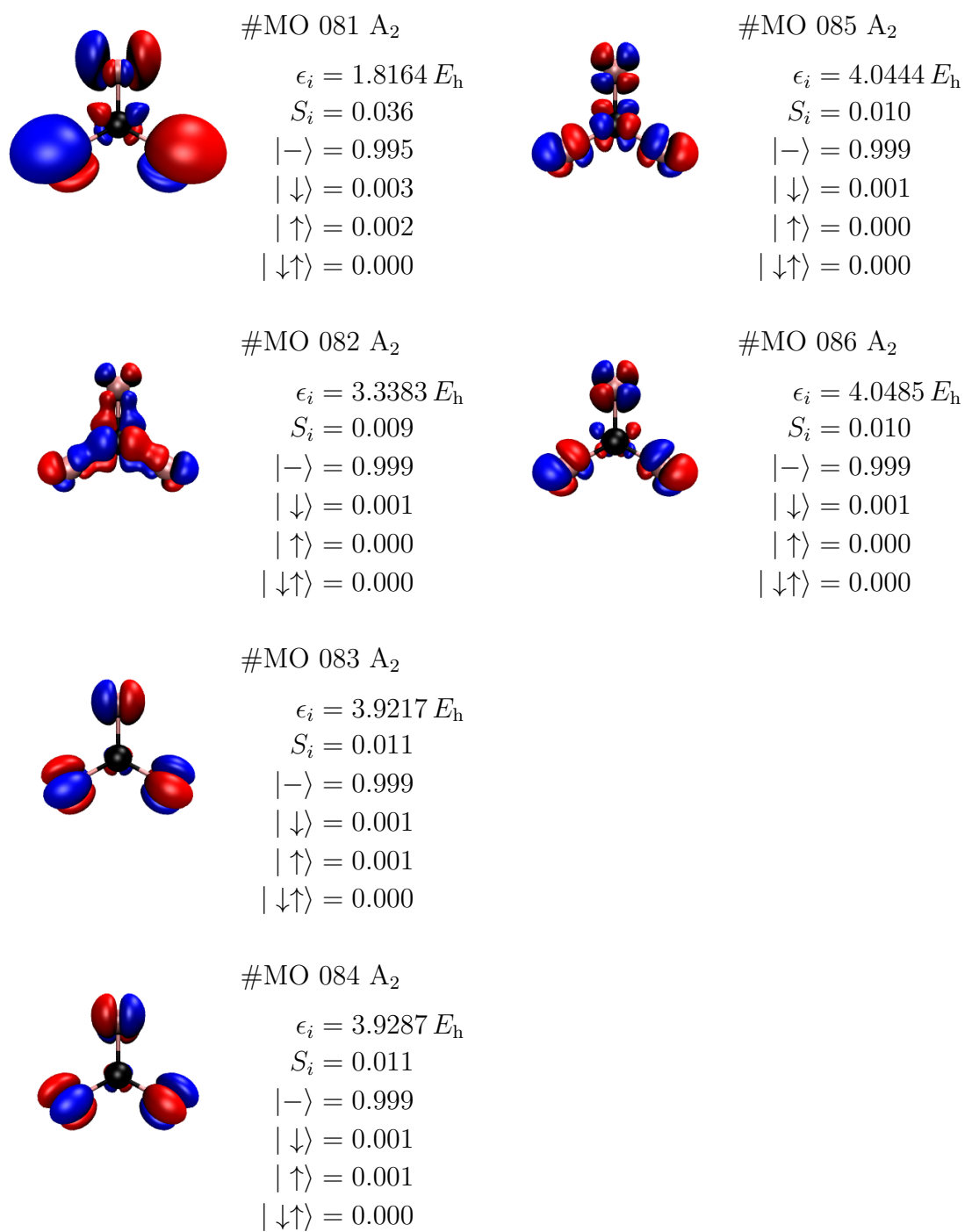


Figure A.53: Molecular orbitals #81 to #86 for $\text{CoF}_4 T_d$ with their eigenenergy ϵ_i , 1-orbital entropy S_i and orbital occupations $\omega_{i,\alpha} = \{ |- \rangle, |\downarrow \rangle, |\uparrow \rangle, |\downarrow\uparrow \rangle \}$. Isosurfaces are plotted at $|\psi(\vec{r})| = 0.05 a_0^{-1.5}$.

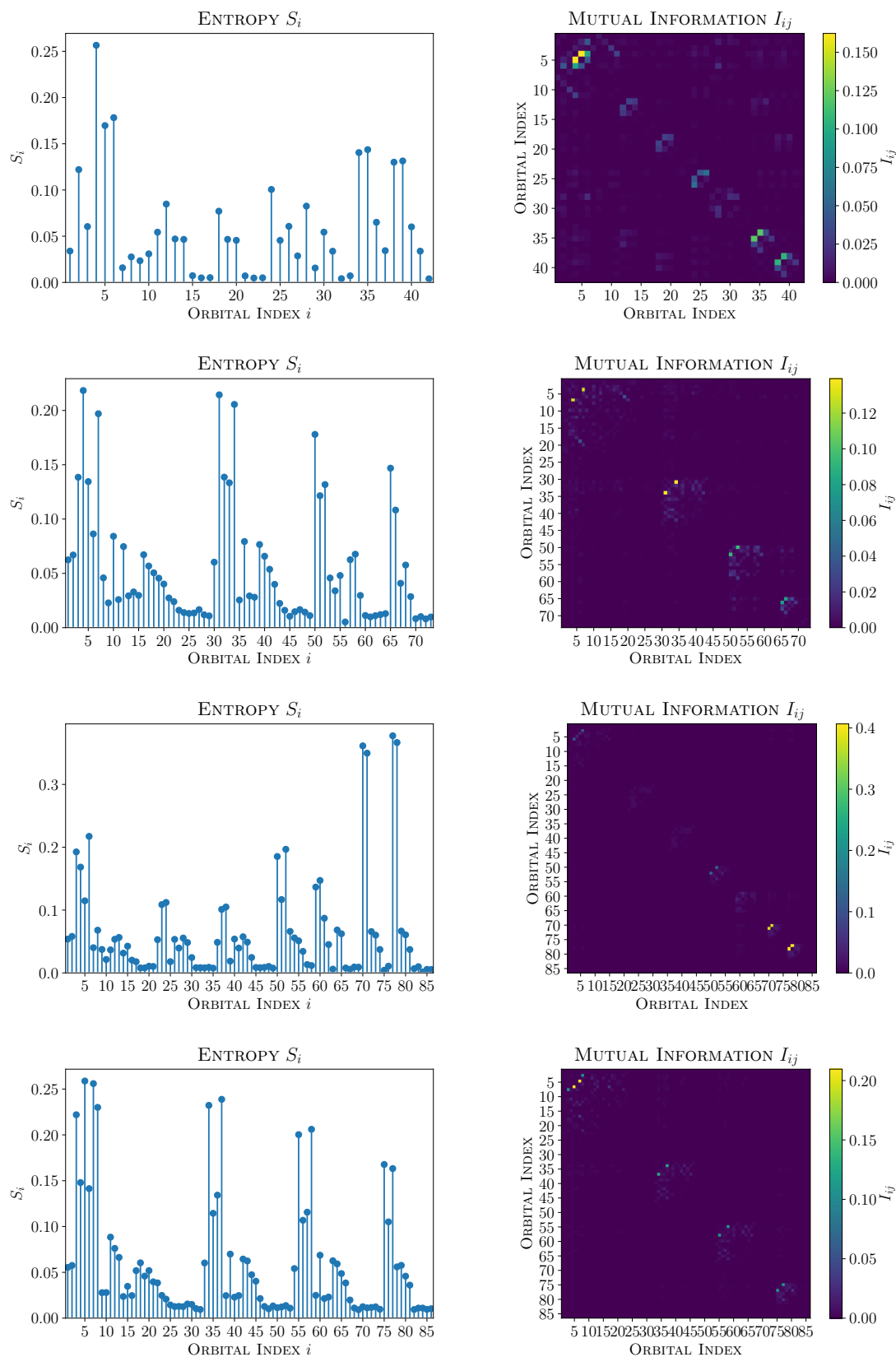


Figure A.54: QIT data (1-orbital entropy S_i and mutual information I_{ij}). From top to bottom: CoF₂ (Co [6s,5p,3d,1f], F [2s,1p]), CoF₃, CoF₄ D_{4h} and CoF₄ T_d (cc-pVDZ).

